Mechanisms of Catalysis and Inhibition of Chlorite Dismutase

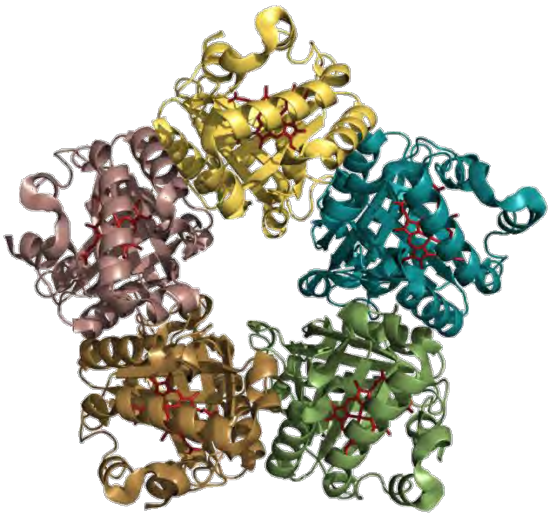

PhD Thesis

Stefan Hofbauer

April 2014

Supervisor: Prof. Christian Obinger

Protein Biochemistry Group

Department of Chemistry, Division of Biochemistry

BOKU - University of Natural Resources and Life Sciences

Muthgasse 18, 1190 Vienna, Austria

FWF

BioToP Biomolecular Technology of Proteins

BOKU

Declaration

All the laboratory work was carried out by the author of this thesis in the laboratory of Christian Obinger at Muthgasse 18, 1190 Vienna, in the laboratory of Gianantonio Battistuzzi at via Campi 183, 41100 Modena, and in the laboratory of Giulietta Smulevich at via della Lastruccia 3/13, 50019 Sesto Fiorentino.

Most of the cloning procedures and X-ray crystallography were performed in the facility of Kristina Djinović-Carugo by Kira Gysel, Andreas Hagmüller, Georg Mlynek and Julius Kostan (MFPL, Dr. Bohrgasse 9, 1030 Vienna)

Some spectroelectrochemical measurements were performed by Marzia Bellei (UniMoRe, via Campi 183, 41100 Modena)

Mass spectrometry was performed by Clemens Gruber (BOKU, Muthgasse 18, 1190 Wien).

Some kinetic measurements and phylogenetic analyses were done by Irene Schaffner and Markus Dobersberger (BOKU, Muthgasse 18, 1190 Wien).

Molecular Dynamics Simulations were mainly performed by Axel Sündermann and Chris Oostenbrink (BOKU, Muthgasse 18, 1190 Wien).

Electron Paramagnetic Resonance spectroscopy was supervised by Katharina F. Pirker (BOKU, Muthgasse 18, 1190 Wien).

Table of Content

Abstract 3

Chapter 1 5

Introduction - Chlorite dismutases - a heme enzyme family for use in bioremediation and generation of molecular oxygen

Chapter 2 23

Aims of the thesis

Chapter 3 25

Impact of subunit and oligomeric structure on the thermal and conformational stability of chlorite dismutases

Chapter 4 34

Redox thermodynamics of high-Spin and low-Spin forms of chlorite dismutases with diverse subunit and oligomeric structures

Chapter 5 50

Manipulating conserved heme cavity residues of chlorite dismutase: effect on structure, redox chemistry, and reactivity

Chapter 6 72

Transiently produced hypochlorite is responsible for the irreversible inhibition of chlorite dismutase

Chapter 7 93

Investigation of the structural implications of ion binding in chlorite dismutases by means of molecular dynamics simulations

Chapter 8 110

Conclusion

Appendix I 116

Inactivation of human myeloperoxidase by hydrogen peroxide

Appendix II 129

Mechanism of reaction of chlorite with mammalian heme peroxidases

Acknowledgements 144

Abstract

Chlorite is an anthropogenic environmental pollutant of increasing concern, as rising concentrations of this compound have been detected in groundwater, drinking water, and soil. The heme-dependent enzyme chlorite dismutase (Cld) is able to convert chlorite into chloride and molecular oxygen thereby forming a covalent oxygen-oxygen bond. Originally, Clds were discovered in perchlorate reducing bacteria (PCRB) but in the meanwhile it was demonstrated that they are widely distributed among Archaea and Bacteria.

In the beginning of the thesis the biophysical and biochemical properties of Clds from the nitrite-oxidizing bacteria "*Candidatus* Nitrospira defluvii" (NdCld) and *Nitrobacter winogradskyi* (NwCld) were investigated. They differ in oligomerization as well as subunit architecture but show very similar kinetic properties. Furthermore, the reduction potentials of the high-spin and low-spin (cyanide-bound) forms of NdCld and NwCld as well as their temperature dependence were determined spectro-electrochemically and yielded very similar $E°'$ values for the Fe(III)/Fe(II) couple for both proteins being -120 mV (high-spin) and -400 mV (low-spin), respectively. This suggests a high similarity in architecture of both the heme cavity and the substrate channel. However, pentameric NdCld has a significantly higher conformational and thermal stability and thus was selected as model enzyme for further investigations.

Based on analyses of available X-ray structures and phylogenetic data highly conserved amino acid residues in close proximity to the heme co-factor of NdCld were selected for site-directed mutagenesis. The effect of mutagenesis on the structure, redox chemistry and reactivity was elucidated in twelve single and double mutants. In detail, the (i) crystal structures of five mutants, (ii) UV-vis spectra of all NdCld variants in the ferric and ferrous state, (iii) Michaelis-Menten parameters, (iv) reduction potentials of the Fe(III)/Fe(II) couple as well as (v) the kinetics of cyanide binding to the respective ferric proteins have been determined. The obtained data clearly show that the hydrogen bonding network on the proximal side of the heme is very susceptible to perturbation. As a consequence of mutations the reduction potential shifts to more positive values and lowers the catalytic efficiency. Upon exchange of the only charged residue on the distal heme side (i.e. Arg173 in NdCld) the catalytic efficiency (k_{cat}/K_m) is decreased by more than 90 % whereas only a modest increase of the Michaelis constant is observed. Its role in chlorite binding seems to be negligible.

During degradation of chlorite NdCld becomes irreversibly inactivated. It is demonstrated that the transiently formed intermediate hypochlorite can escape from the reaction sphere and oxidatively modify both the protein and the prosthetic group. Traps of hypochlorite, like methionine, significantly decelerate this process. Inactivation is more pronounced at pH values aside from the pH optimum as well as in variants that lack R173. This suggests that this conserved amino acid is important to keep hypochlorite in close vicinity to the ferryl-oxygen of Compound I in order to allow the rebound mechanism that finally leads to the release of dioxygen and chloride. A mechanism of Cld-mediated chlorite degradation is proposed.

Abstract

Chlorit ist eine anthropogene, umweltverschmutzende Substanz, die in immer größeren Mengen im Grund- und Trinkwasser, sowie in Böden nachgewiesen wird. Das Hämenzym Chloritdismutase (Cld) kann Chlorit in Chlorid und molekularen Sauerstoff umwandeln und dabei auch die Bildung einer Sauerstoff-Sauerstoff Doppelbindung katalysieren. Clds wurden ursrpünglich in perchloratreduzierenden Bakterien entdeckt, inzwischen wurde jedoch gezeigt, dass sie im Reich der Bakterien und Archaebakterien weit verbreitet sind.

Am Anfang dieser Arbeit wurden die biochemischen und biophysikalischen Eigenschaften der Clds von den nitrit-oxidierenden Bakterien „*Candidatus* Nitrospira defluvii“ (NdCld) und *Nitrobacter winogradskyi* (NwCld) untersucht. Diese unterscheiden sich in ihrer oligomeren Struktur und in der Struktur ihrer Untereinheiten, sind kinetisch aber sehr ähnlich. Die hohe Homologie der Architektur der Substratkanäle und der reaktiven Zentren in NdCld und NwCld wurde durch die Bestimmung der Redox Potentiale und deren Temperaturabhängigkeit der Fe(III)/Fe(II) Paare von NdCld und NwCld in ihrem high und low-spin (Cyanid-Addukt) Zustand verdeutlicht. NdCld hat jedoch eine deutlich höhere intrinsische chemische und thermische Stabilität und wurde daher als Modellenzym für weitere Untersuchungen ausgewählt.

Hochkonservierte Aminosäurereste in der Nähe des aktiven Zentrums wurden, basierend auf den vorhandenen strukturellen und phylogenetischen Daten, ausgewählt um zielgerichtete Mutationen in NdCld einzuführen. Die Auswirkungen dieser Mutationen auf die Redox-Chemie, die Struktur und die Reaktivität wurden untersucht. Neben der Aufklärung der Röntgenstrukturen von fünf Mutanten, wurden alle Mutanten spektroskopisch und kinetisch untersucht. Die vorhandenen Daten zeigen, dass das Wasserstoffbrückenbindungsnetzwerk an der proximalen Hämseite bei Veränderung sehr störunganfällig ist. Dies wird durch eine Änderung der Redoxpotentiale und einer Verminderung der katalytischen Effizienz deutlich. Wenn die einzige geladene Aminosäure auf der distalen Seite des Häms ausgetauscht wird (z. B. Arg173 in NdCld), dann sinkt die katalytische Effizienz (k_{cat}/K_m) um 90% bei nur minimaler Erhöung der Michaelis Konstante. Die Rolle des distalen Arginins bei der Substratbindung scheint daher vernachlässigbar zu sein.

Während des Chloritabbaus wird NdCld irreversibel inaktiviert. Verantwortlich dafür ist Hypochlorit, das während der enzymatischen Reaktion als Zwischenprodukt gebildet wird. Dieses Hypochlorit kann das aktive Zentrum verlassen und dadurch wird das Enzym und die prostethische Gruppe oxidativ modifiziert. Dieser Inaktivierungprozess kann durch Zugabe von Substanzen, die Hypochlorit effektiv binden können, wie z. B. Methionin, verlangsamt werden. In Abwesenheit des distalen Arginins ist die Inaktivierung stärker ausgeprägt. Dies verdeutlicht die Bedeutung dieses Aminosäurenrestes, um Hypochlorit im Reaktionszentrum zu halten, um Mechanismus zu ermöglichen, der letztendlich zur Freigabe von Chlorid und Sauerstoff führt. Abschließend wird ein Mechanismus für den Chloritabbau durch Chloritdismutasen vorgeschlagen.

Chapter 1

Introduction

Chlorite dismutases - a heme enzyme family for use in bioremediation and generation of molecular oxygen

Stefan Hofbauer, Irene Schaffner, Paul G. Furtmüller, Christian Obinger

Review Article

Biotechnology Journal (2014), 9, 461-473

Biotechnology Journal
www.biotechnology-journal.com

Biotechnol. J. 2014, 9

DOI 10.1002/biot.201300210

Review

Chlorite dismutases – a heme enzyme family for use in bioremediation and generation of molecular oxygen

Stefan Hofbauer, Irene Schaffner, Paul G. Furtmüller and Christian Obinger

Department of Chemistry, Division of Biochemistry, Vienna Institute of BioTechnology, BOKU, University of Natural Resources and Life Sciences, Vienna, Austria

Chlorite is a serious environmental concern, as rising concentrations of this harmful anthropogenic compound have been detected in groundwater, drinking water, and soil. Chlorite dismutases (Clds) are therefore important molecules in bioremediation as Clds catalyze the degradation of chlorite to chloride and molecular oxygen. Clds are heme *b*-containing oxidoreductases present in numerous bacterial and archaeal phyla. This review presents the phylogeny of functional Clds and Cld-like proteins, and demonstrates the close relationship of this novel enzyme family to the recently discovered dye-decolorizing peroxidases. The available X-ray structures, biophysical and enzymatic properties, as well as a proposed reaction mechanism, are presented and critically discussed. Open questions about structure-function relationships are addressed, including the nature of the catalytically relevant redox and reaction intermediates and the mechanism of inactivation of Clds during turnover. Based on analysis of currently available data, chlorite dismutase from "*Candidatus* Nitrospira defluvii" is suggested as a model Cld for future application in biotechnology and bioremediation. Additionally, Clds can be used in various applications as local generators of molecular oxygen, a reactivity already exploited by microbes that must perform aerobic metabolic pathways in the absence of molecular oxygen. For biotechnologists in the field of chemical engineering and bioremediation, this review provides the biochemical and biophysical background of the Cld enzyme family as well as critically assesses Cld's technological potential.

Received 16 JUL 2013
Revised 06 DEC 2013
Accepted 14 JAN 2014

Supporting information available online

Keywords: Bioremediation · Chlorite degradation · Chlorite dismutase · Enzymology · Metalloprotein

1 Introduction

In 1996 van Ginkel and co-workers [1] discovered, in perchlorate-reducing bacteria (PCRB), the heme *b*-containing oxidoreductase chlorite dismutase (Cld), which catalyzes the decomposition of chlorite (ClO_2^-) into chloride (Cl^-) and molecular oxygen (O_2). During turnover a covalent oxygen-oxygen bond is formed, an uncommon biochemical reaction that is also catalyzed by the water-splitting manganese complex of photosystem II of oxygenic organisms (cyanobacteria and plants) and an enzyme of an anaerobic methane-oxidizing bacterium [2].

Perchlorate-reducing bacteria are facultative anaerobes that can utilize perchlorate (ClO_4^-) and chlorate (ClO_3^-) as terminal electron acceptors [3] in the absence of oxygen. In this way they intracellularly produce the strong oxidant chlorite [$E°'$ (ClO_2^-/ClO^-) = 1.175 V] [4], which exhibits strong cell-damaging effects [5]. The

Correspondence: Prof. Christian Obinger, Department of Chemistry, Division of Biochemistry, Vienna Institute of BioTechnology, BOKU, University of Natural Resources and Life Sciences, Muthgasse 18, A-1190 Vienna, Austria
E-mail: christian.obinger@boku.ac.at

Abbreviations: **AoCld**, Cld from *Azospira oryzae*; **Cld**, chlorite dismutase; **DaCld**, chlorite dismutase from *Dechloromonas aromatica*; **DyP**, dye-decolorizing peroxidase; ***E°'***, standard reduction potential; **ECD**, electronic circular dichroism; **EPR**, electron paramagnetic resonance; **GsCld**, Cld from *Geobacillus stearothermophilus*; **HS**, high-spin; **IdCld**, Cld from *Ideonella dechloratans*; **LS**, low-spin; **NdCld**, Cld from "*Candidatus* Nitrospira defluvii"; **NwCld**, Cld from *Nitrobacter winogradskyi*; **PcCld**, Cld from *Pseudomonas chloritidismutans*; **PDB**, Protein Data Bank; **RR**, resonance Raman; **TaCld**, Cld from *Thermus acidophilum*; **TtCld**, Cld from *Thermus thermophilis*; **5c**, five-coordinated; **6c**, six-coordinated

high two-electron reduction potentials of perchlorate [$E°$ (ClO_4^-/ClO_3^-) = 0.79 V] and chlorate [$E°'$ (ClO_3^-/ClO_2^-) = 0.71 V] make them ideal electron acceptors for microbial respiratory electron chains [6]. The transiently formed chlorite is degraded to harmless chloride and O_2 by chlorite dismutases. As will be discussed in section 4, the denomination "dismutase" is chemically incorrect and should be eliminated in future terminology.

The first biophysical and biochemical studies of Clds were performed on the perchlorate-reducing bacteria *Azospira oryzae* (GR-1) [1, 4], *Ideonella dechloratans* [7], *Dechloromonas aromatica* [8], and *Pseudomonas chloritidismutans* [9]. Additionally, homologous enzymes with chlorite dismutase activity have been found and characterized in the nitrite-oxidizing bacteria *Candidatus* Nitrospira defluvii [10] and *Nitrobacter winogradskyi* [11]. Further phylogenetic analysis showed that *cld* genes are present in numerous bacterial and archaeal phyla indicating that they represent ancient sequences [12]. The question regarding the natural substrate for Clds and Cld-like proteins, as well as their physiological role(s), remains unanswered, since (i) except in PCRBs chlorite is not a metabolic intermediate in prokaryotes, (ii) reservoirs of chlorite on Earth are very rare [13], and (iii) most chlorite present in our environment is of anthropogenic origin [6, 14].

Structurally, Clds and Cld-like proteins form a superfamily together with recently discovered dye-decolorizing peroxidases (DyPs) suggesting common phylogenetic roots (see section 2) [15]. DyPs are heme *b*-containing peroxidases with histidine as the proximal ligand but secondary and tertiary structures, as well as heme cavity architecture, show no homology to the two main heme peroxidase superfamilies, i.e. the peroxidase-catalase and the peroxidase-cyclooxygenase superfamilies [16, 17]. DyPs exhibit a very broad substrate range. Originally, they were found to degrade anthraquinone derivatives, such as Reactive Blue 5, a synthetic dye, as well as relatively bulky compounds used in the textile industry [18]. From these early observations the denomination dye-decolorizing peroxidase was derived. Later on, DyPs were found also to be able to metabolize artificial electron donors such as ABTS [19], non-phenolic lignin model compounds [20], azo-dyes [21], aromatic sulfides [22], and manganese [23]. It was also reported that DyPs efficiently degrade β-carotene [24]. DyPs are found in a variety of prokaryotes and – in contrast to Clds – also in eukaryotes (mainly fungi). DyPs cluster into four subfamilies [25].

In recent years, insightful findings have been published regarding both chlorite dismutases and dye-decolorizing peroxidases including: protocols of recombinant production; mutational analyses; three-dimensional structures; and biochemical and biophysical properties. This information will enable rational engineering strategies to be devised in the near future in order to apply these novel iron enzymes in chemical and biotechnological processes as well as in bioremediation. This review focuses on chlorite dismutases and discusses – where necessary – relationships with DyPs. We present an updated phylogenetic tree of Clds and DyPs. We analyze, compare, and critically discuss all available biophysical and biochemical data. Based on this information, the biotechnological potential of these oxidoreductases as well as engineering strategies will be discussed.

2 Phylogeny of chlorite dismutases and dye-decolorizing peroxidases

In 2010, Kostan and co-workers presented a Maximum Likelihood tree of Clds and Cld-like proteins that demonstrated a wide distribution of the *cld* gene across *Bacteria* and *Archaea* [12]. It showed that proteins from the same phylogenetic lineage (phylum) – based on 16S rRNA-phylogeny – group together to a high degree and that several lateral gene transfer events occurred during evolution, reflecting functional diversification. We have updated this analysis using a selection of 120 Clds and Cld-like proteins as well as 86 DyP sequences (July 2013) collected from public databases (Uniprot, NCBI). After separate multiple sequence alignments [26] and reconstruction of phylogenetic trees for Cld/Cld-like proteins and DyPs, a common phylogenetic Maximum Likelihood tree was constructed (Fig. 1A) [27].

Figure 1A shows that all Clds with chlorite decomposition activity (i.e. functional Clds) deriving from different phyla (*Proteobacteria, Cyanobacteria, Nitrospirae*) cluster together. The fact that bacterial phyla with distinct metabolism group together, and Clds are not randomly distributed over *Bacteria*, might suggest that these metalloenzymes play similar physiological role(s) in these organisms. This hypothesis is underlined by mapping the homologous amino acid residues at position 173 (Cld from *Candidatus* Nitrospira defluvii [NdCld] numbering), which was shown to be important for efficient degradation of chlorite [12, 15]. However, it is important to note that the physiological substrate of these heme enzymes is unknown. For example, *Cyanobacteria* and *Nitrospirae* possess functional Clds but do not produce chlorite intracellularly. Possible clues for physiological role(s) of Clds might result from future comparative studies of Clds and DyPs. The phylogeny of the latter has been studied recently using different algorithms and four subfamilies have been defined [25, 28]. Moreover, in 2011 Goblirsch and co-workers showed, for the first time, the phylogenetic relationship between Clds and DyPs suggesting a common ancestor [15].

The updated phylogenetic tree presented in Fig. 1A represents all relevant branches of DyPs, chlorite dismutases, and chlorite-dismutase-like proteins, i.e. Clds missing the distal arginine (Arg173 in NdCld) known to be important for efficient chlorite degradation. The overall categorization into Cld and DyP sequences is obvious and

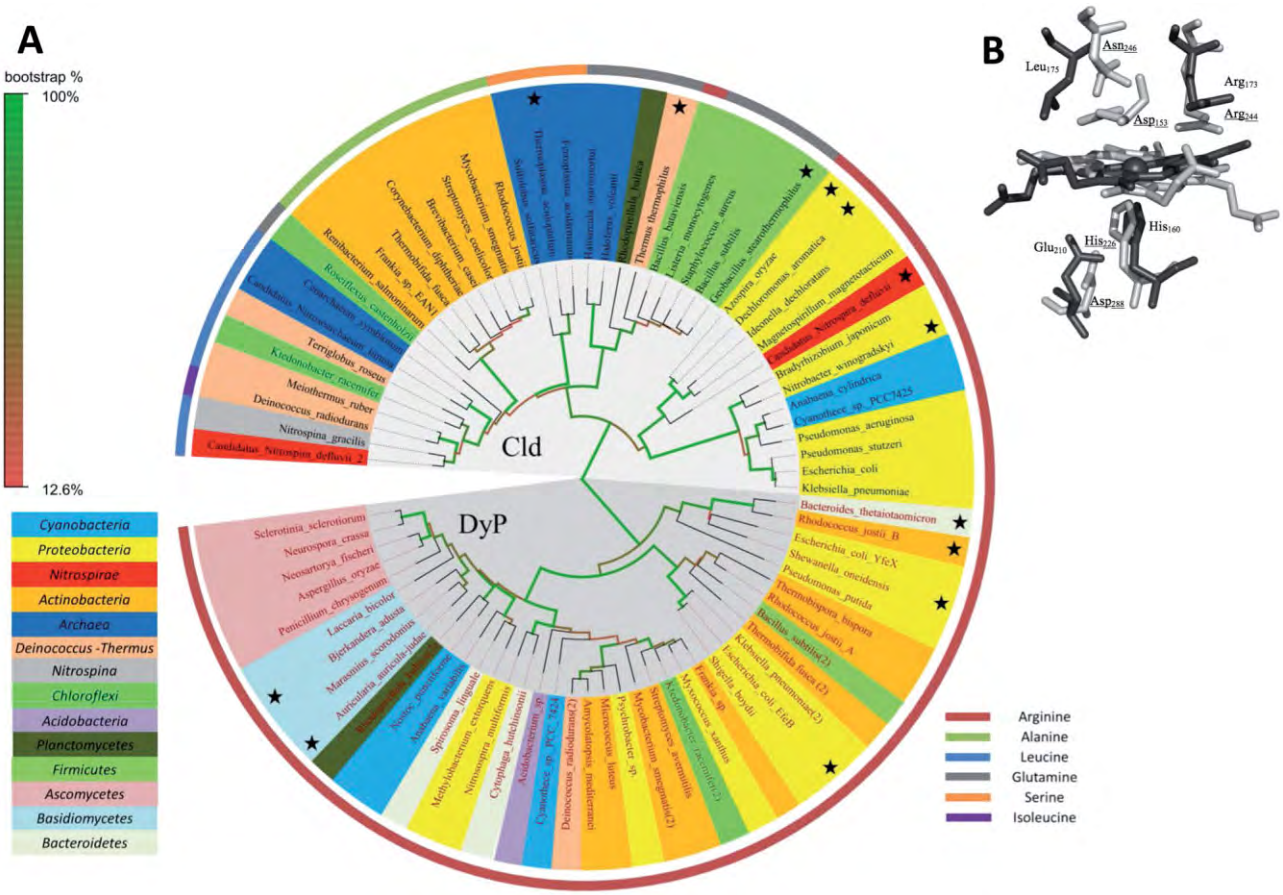

Figure 1. Phylogeny and active site architecture of clorite dismutase (Cld) and dye-decolorizing peroxidase (DyP). (**A**) Maximum likelihood tree based on amino acid sequences of Clds, Cld-like proteins and DyPs. Sequences marked with an asterisk represent proteins of known X-ray structure. Colors highlighting the species name indicate the affiliations of the respective organisms to bacterial and archaeal phylae based on 16S rRNA phylogeny. Color of the stripe, bordering the figure, define the residues at the position which is homologous to Arg173 of NdCld, in the respective proteins. This residue is fully conserved in functional (i.e. chlorite degrading) Clds. The circular tree was drawn using FigTree v1.4 (http://tree.bio.ed.ac.uk/software/figtree/). (**B**) Overlay of active site of Cld and DyP. Cld from "*Candidatus* Nitrospira defluvii" (NdCld, PDB: 3NN1) is depicted in dark gray, and DypB from *Rhodococcus jostii* (PDB: 3QNS) in light gray; Amino acid numbering follows NdCld and DypB from *Rhodococcus jostii* (underlined). Figure was generated using PyMOL (http://www.pymol.org/).

each of these protein families can be rooted against the other, suggesting a common ancestor. All functional Clds have an arginine residue at the distal side of heme *b* and can be further divided into two lineages [11] differing in overall sequence length. From the group of "short Clds" (Lineage II) only Cld from *Nitrobacter winogradskyi* has been studied so far, whereas several representatives from the group of "long Clds" (Lineage I) were characterized in more detail (see Sections 3–6).

Little is known about the physiological role of the Cld-like proteins. Cld-like proteins from *Bacillus subtilis*, *Mycobacterium tuberculosis* [29], and *Staphylococcus aureus* [30] have been reported to play a (yet undefined) role in heme biosynthesis. The Cld-like protein from *Haloferax volcanii* was shown to have a role in antibiotic biosynthesis. Its gene is located together with a monooxygenase-like protein within a single open reading frame [31]. It was interesting to see that in the updated tree the sequence of *Bacillus bataviensis,* which represents a functional Cld, clusters together with all *Firmicutes* and sequences from other phyla having a glutamine residue on the distal side of the heme *b*. But this seems to be an exception. Typically, Cld-like proteins having the distal arginine exchanged for a distinct amino acid, mainly occur in one phylum. Figure 1A clearly demonstrates that Cld-like proteins in *Firmicutes* and *Actinobacteria* have a glutamine and an alanine, respectively, instead of the Arg173 in NdCld. By contrast, enzymes having leucine at this position are found in diverse phyla. This might indicate a more general functionality for this group of enzymes.

In contrast to Clds, the family of DyPs shows minimal grouping of organisms from the same phylogenetic lineage (with the exception of subfamily D), indicating

numerous lateral gene transfer events. The sequences show a higher degree of similarity throughout the whole family and all sequences have the catalytic arginine residue (present in functional chlorite dismutases) structurally conserved (Fig. 1). The previously described four subfamilies (A-D) [15] can be roughly identified but the pattern of distribution seems to be more complicated and needs further evaluation in the future. Bacterial representatives of subfamily B seem to be closely related to the common ancestor of Clds and DyPs. The first node divides the representatives of subfamily B from other DyPs. The next node divides bacterial sequences of subfamily A from subfamilies C and D. Subfamily C is comprised of bacterial heme proteins, whereas subfamily D also contains sequences of fungal origin. In subfamily D, sequences of distinct phyla (e.g. *Ascomycetes* and *Basidiomycetes*) clearly cluster together.

3 Crystal structures of chlorite dismutases

All currently available (up to July 2013) crystal structures in the Protein Data Bank (PDB)-database (www.rsbc.org) of Clds and Cld-like proteins are listed in Supporting information, Table S1. Figure 1B shows a comparison of the active site of the Cld from *Candidatus* Nitrospira defluvii (PDB-code 3NN1) [12] and of DyP from *Rhodococcus jostii* (PDB-code 3QNS) [19]. The latter is a member of subfamily B and thus closest to the common origin of Clds and DyPs. Both structures show the conserved catalytically important distal arginine at similar positions [12, 19]. In both enzyme families, a histidine is the proximal heme ligand. Due to hydrogen bonding with an acidic amino acid (glutamate in Clds and aspartate in DyPs) the histidine has some imidazolate characteristics. In functional Clds, the distal arginine is the only charged amino acid [12], whereas in DyPs a fully conserved aspartate is found at the distal heme cavity. Furthermore, the orientation of the prosthetic group and its substituents is different (Fig. 1B) with the propionate-, vinyl- and methyl-substituents being tilted by 90° with respect to each other.

Figure 2 shows all of the structures of Clds and Cld-like proteins solved so far, with those having the same set of amino acids in the heme cavity being grouped and represented by a single structure (distal heme ligands deriving from crystallization liquids are omitted for clarity). To date

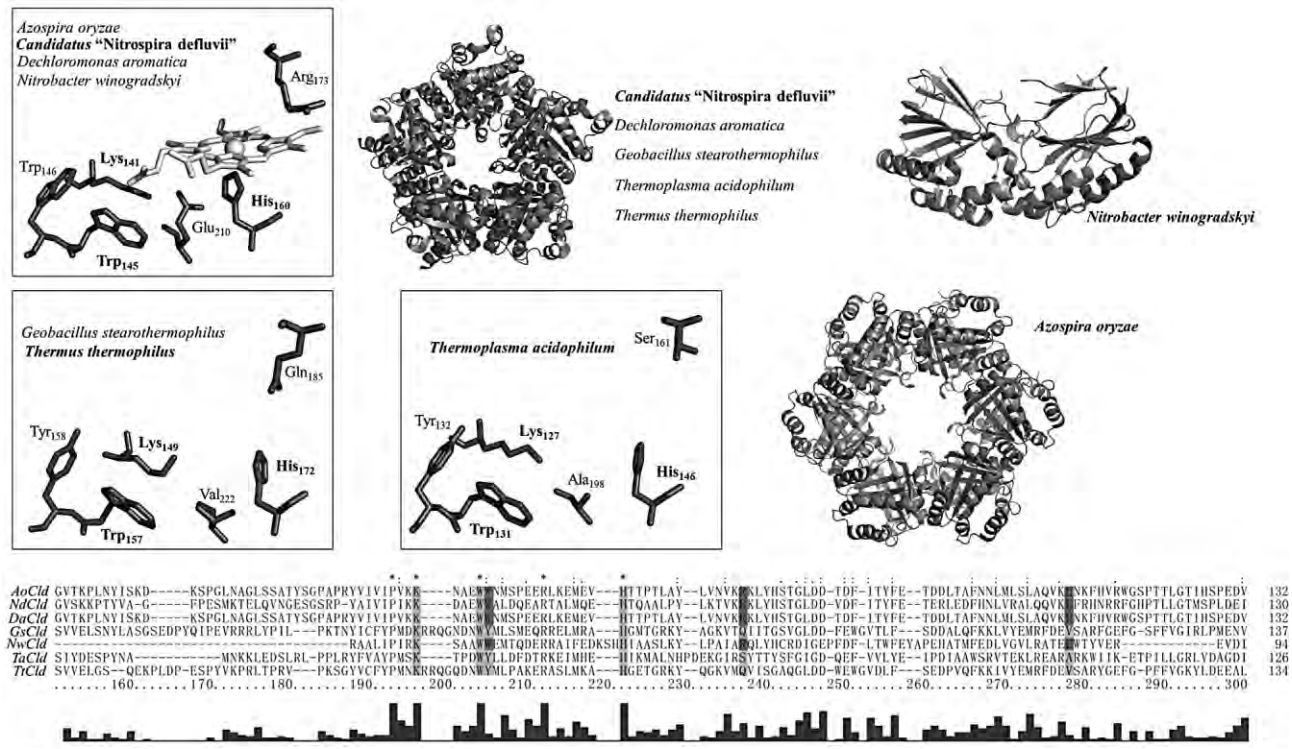

Figure 2. Crystal structures and sequence alignment of Clds and Cld-like proteins. Oligomeric structures and active site residues of Clds from *Azospira oryzae* (2VXH), *Candidatus* Nitrospira defluvii (3NN1), *Dechloromonas aromatica* (3Q08, 3Q09), and *Nitrobacter winogradskyi* (3QPI). Oligomeric structures and heme cavity residues in Cld-like proteins from *Geobacillus stearothermophilus* (1T0T), *Thermus thermophilus* (1VDH) and *Thermoplasma acidophilum* (3DTZ). Note that these X-ray structures do not contain the prosthetic group. Cld structures from species written in bold are depicted. Residues in the sequence alignment of the C-terminal domains , which are depicted in the structures, are highlighted in light gray; depicted residues unique for Clds with chlorite decomposition activity are highlighted in dark gray. Bar graph shows conserved amino acids. Figures were generated using PyMOL (http://www.pymol.org/).

three-dimensional structures of Clds and Cld-like proteins from seven different organisms have been published, revealing a high structural conservation of the subunit fold. Two distinct subunit topologies have been identified. The first topology ("long Clds") includes Clds from Lineage I and Cld-like representatives from *Azospira oryzae* strain GR-1 (AoCld) [32], *Dechloromonas aromatica* (DaCld) [33], *Candidatus* Nitrospira defluvii (NdCld) [12], *Thermus thermophilus* (TtCld) [34], *Thermoplasma acidophilum* (TaCld) (PDB-code: 3DTZ), and *Geobacillus stearothermophilus* (GsCld) (PDB-code: 1T0T). These proteins have a subunit topology consisting of an N-terminal and a C-terminal ferredoxin-like fold. The N-terminal fold is always heme free, whereas in functional Clds the C-terminal fold has a heme *b* bound. The second subunit topology ("short Clds") is only found in functional Clds of Lineage II. The only representative with known X-ray structure is the Cld from *Nitrobacter winogradskyi* (NwCld) [11]. It has a smaller subunit size, lacking almost the entire N-terminal domain of the first group described above. However, the heme-binding ferredoxin-like fold is highly similar to the C-terminal domain of "long Clds".

All Clds and Cld-like proteins form oligomers. NwCld forms a dimer [11], AoCld [32] crystallizes as a hexamer, but appears to be a pentamer in solution. All other Clds show pentameric crystal structures stabilized by hydrogen bonds and salt bridges. Neither inter- nor intra-subunit disulphide bonds are found, due to the complete absence of cysteines in "long Clds" and the presence of a maximum of a single cysteine in "short Clds". Oligomerization of some Clds depends on conditions like pH and ionic strength [35]. AoCld was reported to be a homotetramer [1] or homopentamer in solution [32] and to crystallize as a hexamer [32]. Cld from *Pseudomonas chloritidismutans* (PcCld) [9] and DaCld were described as homotetramers in solution [8] but DaCld crystallized as a pentamer [33]. Recently, Blanc and co-workers proposed the existence of dimeric DaCld depending on buffer conditions and protein concentration [35]. It is worth mentioning, that AoCld and DaCld have a sequence identity of 94.3 % (Supporting information, Table S2) with just a few amino acids differing in the heme free N-terminal domain and 100% identity in the heme-bound catalytic C-terminal domain (Fig. 2). Additionally, there are two structures of NdCld variants having point mutations of the catalytically important arginine 173. They exhibit subunit and oligomeric structures almost identical to the wild-type protein.

The distal ligand of ferric Clds is typically a water molecule. In the crystal structures it can be exchanged with molecules of the crystallization liquid. In some structures thiocyanate, nitrite and cyanide act as the distal ligand. Whereas cyanide is a typical low-spin ligand that inhibits heme proteins, SCN^- and NO_2^- was found to act as a ligand and substrate of heme oxidoreductases. Whether Clds can use thiocyanate and/or nitrite as a substrate is unknown.

4 Spectral properties

Several Clds and Cld-like proteins have been analyzed by UV-vis electronic absorption, electron paramagnetic resonance (EPR), electronic circular dichroism (ECD), and resonance Raman (RR) spectroscopy. Despite the fact of almost identical heme cavity architecture (see Section 3), large differences in spectral signatures have been reported at comparable pH-values. This becomes obvious by inspection of Table 1 that summarizes the UV-vis absorbance maxima of Clds and Cld-like proteins in the respective ferric and ferrous state and in the low-spin cyanide complex.

Closely related AoCld, DaCld and IdCld (Table 1) exhibit a relatively broad Soret maximum at around 393 nm and charge transfer bands at around 510 and 645 nm with a Q_v band at approximately 535 nm at neutral pH. These bands indicate the presence of 5-coordinated high-spin (5cHS) heme iron. All three proteins show a clear pH dependence of the UV-visible spectral signatures. At alkaline pH, the resulting spectra indicate the presence of a hydroxyl 6-coordinated low-spin (6cLS) complex with Q-bands around 540 and 575 nm and a sharpened red-shifted Soret band. This alkaline transition is stated to be irreversible [36] and has pK_a – values of 8.2 for AoCld [4], 8.5 for IdCld [7], and 8.7 for DaCld [36]. These findings are also reflected by the RR data of DaCld. In the acidic pH region DaCld loses its heme at around pH 4, exhibiting a spectrum of free heme with a Soret maximum at 375 nm [36]. Resonance Raman spectroscopy of wild-type DaCld also demonstrated that the hydrogen bond between the proximal histidine and the conserved glutamate is rather weak compared to other His-coordinated heme proteins. RR data on carbon monoxide binding suggest no significant electrostatic interactions of CO with residues in the distal heme pocket.

Interestingly, ferric PcCld, which has more than 90% sequence identity to AoCld and DaCld (Table 1), has a Soret maximum at 411 nm [9]. Furthermore, NdCld, NwCld, SaCld, and TtCld show Soret maxima between 403–408 nm and CT1 bands between 630 and 640 nm, indicating dominating high-spin iron heme species at pH 7. The Soret bands of these proteins are sharper than those of AoCld, IdCld and DaCld and comparable with other His-ligated heme *b* protein families. One reason for the significant differences in spectral properties between these two groups of Clds could be the relatively low conformational and thermal stability of AoCld, IdCld and DaCld, which will be discussed in Section 6.

Spectra of the ferrous state of Clds are characteristic of 5cHS Fe(II), with the exception of ferrous TtCld, which has a blue-shifted Soret maximum at 429 nm, indicative of a 6cLS ferrous heme iron. TtCld and SaCld are Cld-like proteins with no or very limited chlorite dismutase activity [30, 34].

Table 1. Spectral parameters of recombinant wild-type chlorite dismutases and variants in the ferric and ferrous states as well as low-spin complex with cyanide

	ferric						ferrous			CN^-	
	pH	Soret (nm)	CT2 (nm)	Q_v (nm)	Q_0 (nm)	CT1 (nm)	Soret (nm)	Q_v (nm)	Q_0 (nm)	Soret (nm)	reference
AoCld	7.2 7.0	392 394	–	–	–	–	432	560	–	–	[1, 4, 32]
DaCld	6.8 8.0 10	392 400 408	506 – –	536 538 539	– – 576	644 650 608	433 – –	556 – –	587 – –	419 – –	[8, 35, 36, 38]
IdCld	7.0	392	509	–	–	648	434	555	586	–	[7]
NdCld	7.0	408	–	533	570	640	435	556	590	422	[12, 37]
NwCld	7.0	405	506	543	–	640	435	556	590	420	[11, 37]
PcCld	6.0	411	–	–	–	–	433	–	–	420	[9]
SaHemQ (Cld)	6.8	406	510	–	–	630	433	558	–	420	[30]
TtCld	7.0	403	495	–	–	634	429	558	–	420	[34]
DaCld R183A	6.8 10	391 391	509	530 530	– –	644 625					[38]
DaCld R183K	6.8 10	410 410	–	530 530	560 560	– –					[38]
DaCld R183Q	6.8 10	403 403	509 509	530 530	– –	635 640					[38]
DaCld W227F	6.0 8.0	402 409	– –	538 540	– 576	650 650					[35]
DaCld W156F	6.0 8.0	411 412	– –	534 535	– 575	– 650					[35]
DaCld W155F	6.0 8.0	413 413	– –	– 535	– 565	660 660					[35]
NdCld R173A	7.0	410	–	535	570	640					[12]
NdCld R173K	7.0	412	–	535	565	–					[12]

In recombinant heme proteins, occupancy of the active site with the prosthetic group is reflected by the Reinheitszahl (R_z-value or purity number, A_{Soret}/A_{280nm}). Typical R_z-values for functional recombinant Clds are 2.1 (NdCld) [37], 1.1 (DaCld) [35], and 1.5 (AoCld) [4]. Low R_z-values are often found in Cld-like proteins and might reflect weaker or hindered binding of the prosthetic group compared to Clds. Most probably this was the reason why the crystal structures of GsCld, TaCld and TtCld were obtained without the prosthetic group (Supporting information, Table S1).

Mutations at the active site were shown to have an impact on spectral properties in DaCld [35, 38]. UV-visible electronic absorption spectroscopy as well as Soret excited RR spectroscopy show the importance of the distal arginine residue for keeping the enzyme in the catalytically active 5cHS Fe(III) state (Table 2). Especially the R183K variant of DaCld exhibits spectral features indicative of a 6cLS heme iron at pH 6.8 [38]. Exchange of proximal amino acids in DaCld severely diminished heme-binding, and also modified the oligomerization and the conformational stability of the protein [35].

Electronic circular dichroism spectroscopy in the far UV-region of ferric NdCld, apo-NdCld, DaCld [39], and proximal tryptophan variants of DaCld [35] show minima at 208 and 222 nm typical for a-helical proteins (NdCld and DaCld). In Lineage II Clds such as NwCld, the four N-terminal a-helices present in "long Clds" are lacking [40], which is reflected by the ECD spectrum in the far-UV region. Consequently, the dichroic minimum typical for β-sheets between 212 and 214 nm is observed [40]. For recombinant SaCld, minima in the ECD-spectrum at

Table 2. Steady-state kinetic parameters of chlorite degradation[a)]

	pH	K_M (μM)	k_{cat} (s^{-1})	k_{cat}/K_M (M^{-1} s^{-1})	E°' (mV)	reference
AoCld	7.2[b)]	170	1200	7.1×10^6	–23 ± 9 –158 ± 9	[1, 4, 32]
DaCld	5.2[c)] 6.8[d)] 7.6[c)]	620 212 430	20000 7500 3000	3.2×10^7 3.5×10^7 6.9×10^6	–23	[8, 36, 38]
IdCld	7.0[e)]	260	1800	6.9×10^6	–21	[7]
NdCld	7.0[f)]	69	43.0	6.2×10^5	–113 ± 5	[12, 37]
NwCld	7.0[g)]	90	190	2.1×10^6	–119 ± 5	[11, 37]
PcCld	6.0[h)]	84	230	2.7×10^6	–	[9]
SaHemQ (Cld)	6.8[i)]	NA	NA	NA	–	[30]
TtCld	7.0[j)]	13	0.77	59	–	[34]
DaCld R183A	6.8[k)]	14600	91	6.2×10^3	–4	[38]
DaCld R183K	6.8[k)]	42000	1000	2.5×10^4	–18	[38]
DaCld R183Q	6.8[k)]	50000	350	6.9×10^3	–34	[38]
DaCld W227F	6.0[j)] 8.0[j)]	210 620	1300 440	6.1×10^6 7.1×10^5	–	[35]
DaCld W156F	6.0[j)] 8.0[j)]	160 130	2100 470	1.3×10^7 3.7×10^6	–	[35]
DaCld W155F	6.0[j)] 8.0[j)]	NA NA	NA NA	NA NA	–	[35]
NdCld R173A	7.0[l)]	90	2.8	3.1×10^4	–	[12]
NdCld R173K	7.0[l)]	898	14.0	1.5×10^4	–	[12]

a) Please note (i) the varying pH-values; (ii) that chlorite dismutases are inactivated during chlorite degradation; and (iii) the different chlorite concentration regimes used in the various laboratories. Additionally, standard reduction potentials of the Fe(III)/Fe(II) couple for some Clds have been published. NA, no activity detected.
b) $[ClO_2^-]$ up to 15 mM
c) $[ClO_2^-]$ 0.08–21 mM
d) $[ClO_2^-]$ 0.08–2 mM
e) $[ClO_2^-]$ 0.2–1.5 mM
f) $[ClO_2^-]$ 0.05–80 mM
g) $[ClO_2^-]$ 0.05–100 mM
h) $[ClO_2^-]$ 0.001–0.5 mM
i) $[ClO_2^-]$ up to 20 mM
j) $[ClO_2^-]$ not reported
k) $[ClO_2^-]$ 0.08–2 mM
l) $[ClO_2^-]$ 0.05–80 mM

227 nm for the apo-form and at 234 nm for the holo-form were reported [30]. These minima cannot be assigned to secondary structure elements and are probably resulting from misfolded protein [41].

ECD spectra in the near UV- and visible regions are only reported for NdCld and NwCld [40]. These spectra show positive ellipticity maxima for the heme region at 417 (NdCld) and 416 nm (NwCld), and clear differences in the fingerprint region suggesting slightly different heme environments in solution.

Electron paramagnetic resonance (EPR) spectroscopy was also used to determine the spin-state and electron distribution at the heme iron. IdCld shows a rhombically distorted high-spin spectrum at neutral pH and a low-spin dominated spectrum at alkaline pH [7]. AoCld and DaCld show a similar rhombic high-spin signal at pH 6 and pH 9 [4, 42]. The EPR spectrum of NdCld shows an axial and a rhombic high-spin form and also a low-spin form at pH 7, whereas the high-spin species of NwCld gives a completely axial signal next to a weak low-spin signal [37]. These data clearly show that the electron distribution of the ferric heme iron might differ in Clds, which cannot be seen in the respective crystal structures. Still, one has to be cautious about comparing the above mentioned results since EPR spectroscopy is a very sensitive method and results can be influenced by buffer- and cryo-condi-

tions [43] as well as experimental setup. Buffer or cryo-components can interact with the active site. Furthermore, the ferric low-spin signal saturates at much lower microwave power (i.e. approximately 1 mW at 10 K) than the high-spin signal [37]. Spectra discussed above have been taken at significantly different micro-wave powers; 0.2 mW for NdCld and NwCld [37], 2 mW for IdCld [7], 50 mW for DaCld [42], and 80 mW for AoCld [4].

5 Enzymatic activity and redox chemistry

Originally, chlorite dismutases were discovered in PCRBs and were shown to degrade chlorite to chloride and O_2. This reactivity attracted the attention of environmental biotechnologists, since chlorite is an anthropogenic environmental pollutant abundant in bleaching agents. Its occurrence in ground waters is a severe problem in the USA [6, 14]. Additionally, functional Clds fascinated enzymologists, since they represent the only soluble enzyme family known that is able to catalyze the formation of a covalent oxygen-oxygen bond, which has been proven by ^{18}O-labeling studies [42]. This can also be of interest from a biotechnological point of view, since it enables the local and controlled generation of O_2 in an oxygen-free environment. In studies on O_2-utilizing enzymes such as monooxygenases, Dassama and co-workers [44] applied DaCld for in situ generation of molecular oxygen.

In order to use Clds for bioremediation and biotechnological application, it is important to understand structure-function relationships. Interesting and still open questions concern substrate specificity, electron structure of the catalytic redox intermediates, substrate and intermediate binding and oxidation/reduction, as well as the origin of the mechanism-based inactivation of Clds during chlorite degradation.

The ability to degrade chlorite to chloride and produce molecular oxygen has been shown for several functional Clds that all have the distal arginine residue fully conserved (Fig. 1B). All currently published steady-state kinetic parameters of functional Clds are listed in Table 2. Cld-like proteins (SaCld, TaCld, GsCld) do not show any or very weak (TtCld) chlorite dismutase activity. It is important to mention that catalytic efficiencies are problematic to compare, since the various enzymes were probed at different chlorite concentrations, pH-values, and temperatures. Especially at high chlorite concentrations, Clds are irreversibly inactivated which does not allow the determination of reliable kinetic parameters [8]. We strongly suggest working with micromolar up to 1 mM chlorite concentrations and only using the initial linear phase of polarographically measured O_2 release within the first 30 s for rate calculation. The inhibition mechanism itself is not yet understood, but heme bleaching is observed when Clds are treated with high molar (~1000 eq) excess of chlorite [8]. Formation of a tryptophanyl radical at the proximal heme site was hypothesized [33] but later it was shown that mutations of tryptophans close to the catalytic center do not prevent inhibition [35]. So far, published temperature optima for characterized Clds are between 20–30°C, and pH optima for chlorite degradation activity are between pH 5.0–6.0 [10, 11, 36]. The published K_M values at pH 7.0 vary from 69 to 260 μM, k_{cat} values from 43 to 7500 s^{-1} and k_{cat}/K_M values from 6.2×10^5 to 3.5×10^7 M^{-1} s^{-1} (Table 2). Generally, exchange of the distal arginine decreased the affinity for chlorite as well as the catalytic efficiency, but these effects were more pronounced in DaCld compared to NdCld. In DaCld, the effects of mutations of tryptophans at the proximal heme cavity on the chlorite degradation activity were relatively small (Table 2).

The redox potential of the Fe(III)/Fe(II)-couple of the heme protein determines the stable oxidation state of the native protein in solution. In addition, it reflects the redox properties of higher intermediate oxidation states of the respective protein family and therefore gives hints on substrate specificities [45]. Performing these redox measurements at variable temperatures allows determination of the enthalpic and entropic contribution to the reduction reaction [46]. Determined redox potentials of Clds are listed in Table 2.

AoCld, DaCld, and IdCld have a redox potential of the Fe(III)/Fe(II) couple of about –20 mV [4, 7, 38], which has been determined via indirect dye-mediated [47, 48] or dye- and enzyme-mediated [49] methods. Recombinant AoCld shows a redox potential of –158 mV. DaCld variants R173A, R173K, and R173Q have reduction potentials of –4, –18, and –34 mV, respectively, similar to the wild-type protein. The redox potentials and redox thermodynamics of pentameric NdCld (Lineage I) and dimeric NwCld (Lineage II) were determined spectroelectrochemically under identical conditions. In this method, the sample is directly reduced and oxidized by applied potentials and not by addition of dithionite or xanthine oxidase for reduction and ferricyanide for oxidation. Redox potentials for both proteins are around –120 mV for the ferric high-spin enzymes and about -400 mV for the respective cyanide complexes [37]. The ferric forms of the high-spin enzymes are enthalpically favored, while the entropic contribution partly compensates for enthalpic stabilization. This suggests that despite different subunit and oligomeric architecture of NdCld and NwCld, the redox properties and active site architectures are very similar in solution, as was suggested by the crystal structures [11, 12]. Differences in $E°'$ values as described above might be derived from different applied electrochemical methods. It would be interesting to measure the $E°'$ values of the Fe(III)/Fe(II) couple of DaCld and closely related AoCld under the same conditions used for NdCld and NwCld.

A few mechanistic investigations of AoCld and DaCld have been performed. AoCld was shown to react with H_2O_2 possibly forming Compound I- or Compound II-like

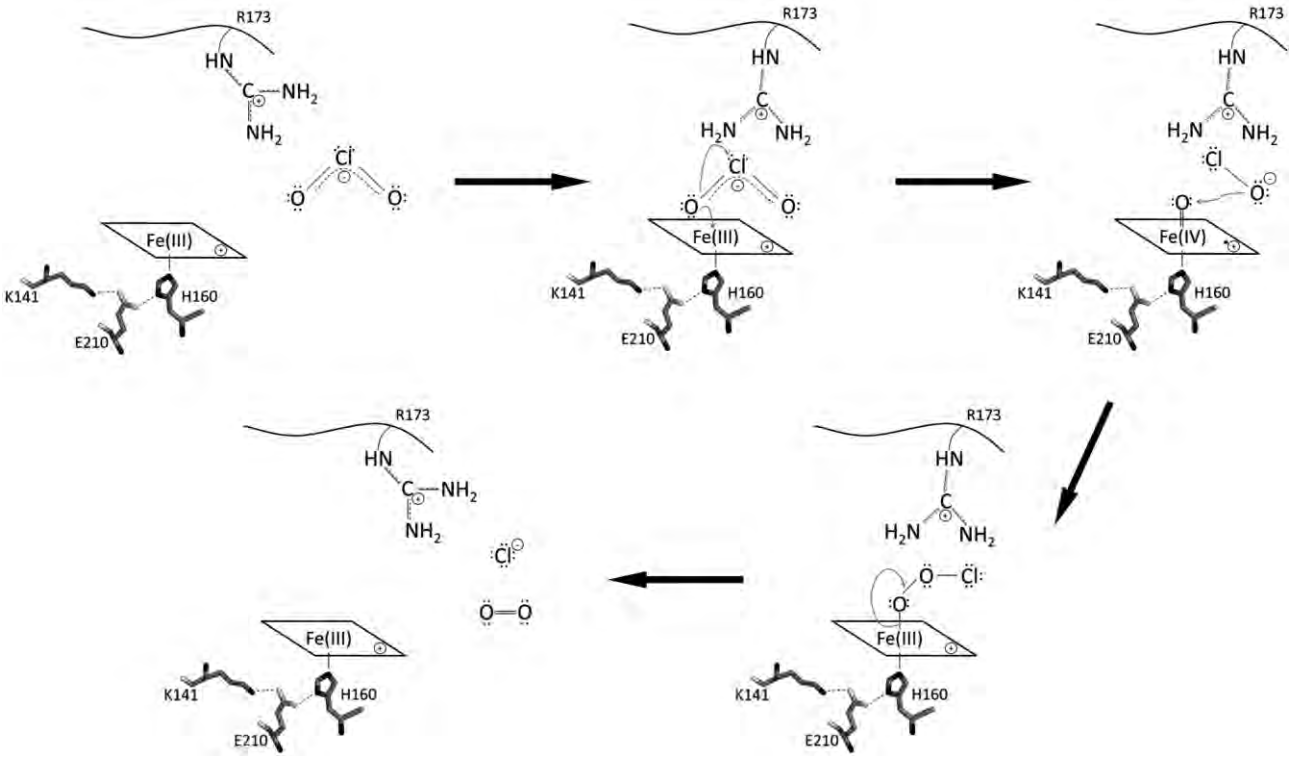

Figure 3. Proposed reaction mechanism of chlorite dismutase. The reaction starts with the attack of anionic chlorite at ferric heme *b*. After formation of the Fe(III)-chlorite complex, heterolytic cleavage of one covalent oxygen-chlorine bond in chlorite leads to the formation of hypochlorite and the redox intermediate compound I [oxoiron(IV) porphyrin cation radical]. Finally, upon nucleophilic attack of intermediate anionic hypochlorite at the ferryl oxygen, compound I is reduced to the resting state and dioxygen and chloride are released. In addition, the scheme shows the putative role of distal arginine (fully conserved in functional Clds) in the orientation and stabilization of the substrate as well as the postulated intermediate(s). On the proximal site the conserved triad H160-E210-K141 that forms a H-bonding network is depicted.

intermediates [4]. Similarly, DaCld reacted with peracetic acid to the same redox states. Compound II was reduced back to the ferric state using ascorbate, whereas putative Compound I was reported to interact weakly with the two-electron reductant thioanisole in a monooxygenase-like reaction [42]. Freeze-quench EPR using chlorite as substrate showed the formation of radicals at remote sites associated with Compound I and Compound II formation [35, 42]. Chlorite at higher concentrations, but also hypochlorite, hydrogen peroxide, and peracetic acid promote heme bleaching [4, 42].

Based on all these findings, a reaction mechanism was proposed by Lee and co-workers [42] and is summarized in Fig. 3. The conserved and (as the X-ray structures suggest) mobile distal arginine supports binding of the anionic chlorite to the ferric resting state of Cld. Chlorite immediately oxidizes the enzyme to the Compound I state, which, most probably, is an oxoiron(IV) porphyryl radical intermediate. Thereby, hypochlorite is formed as an intermediate that is kept in the reaction sphere by the distal arginine. Finally, hypochlorite attacks the ferryl oxygen and chloride and O_2 are released. It is important to note that so far the formation of Compound I and hypochlorite is not fully proven. Moreover, the role of a Compound II state in this reactivity as well as the mechanism of inactivation are unknown so far.

Figure 1 demonstrates the close relationship between Clds and DyPs. Nevertheless, so far there is no study on the use of chlorite as substrate for DyPs and only a few data are available about the peroxidase activity of Clds. In the presence of hydrogen peroxide, DaCld and SaCld show weak peroxidase reactivity towards artificial one-electron donors such as guaiacol and ABTS with catalytic efficiencies around $10^2 - 10^3\ M^{-1}\ s^{-1}$ [30, 35, 38, 42]. A very poor catalase activity has been reported for Clds from *Mycobacterium tuberculosis*, *Bacillus subtilis* [29], and *Staphylococcus aureus* [30]. As outlined above, the endogenous substrate and/or physiological role of most Clds and Cld-like proteins is yet unknown.

From both, an enzymatic and mechanistic point of view, the structural and phylogenetic relationship between Clds and DyPs is interesting and needs further investigation. Recently mutational analysis has demonstrated that the distal arginine in DyP (subfamily B) from *Rhodococcus jostii*, which is structurally conserved in all functional Clds and DyPs, is essential for the peroxidase

activity of this enzyme (just as the distal arginine in Clds is crucial for chlorite-dismutase activity) [50]. Since recombinant enzymes from both families can be produced in high yields, these biochemical relationships should be addressed now in more detail.

6 Conformational and thermal stability

Biotechnologically applied enzymes are often required to withstand elevated temperatures, acidic or alkaline environments, and the presence of denaturing agents, while at the same time maintaining their catalytic efficiency. In the case of chlorite dismutases, studies on conformational and thermal stability as well as enzymatic activity at higher temperatures have mainly been performed with NdCld and NwCld. Pentameric NdCld of Lineage I has been shown to be a highly thermostable enzyme with a melting temperature at around 90°C compared to less stable dimeric NwCld (Lineage II) which denatures at around 50°C [40]. Moreover, NdCld also shows high stability in acidic and alkaline conditions. Furthermore, NdCld is able to detoxify chlorite even at 80°C [40].

Compared to NwCld, the pentameric protein also has a higher chemical stability probed by guanidinium hydrochloride [40]. Both NdCld and NwCld have similar activities and redox properties as discussed above but differ in subunit and oligomeric structure. Heme *b* bound to the heme cavity has a stabilizing effect, since apo-NdCld has a significantly lower T_m-value than the holoprotein.

DaCld was incubated at different pH values prior to activity measurements at pH 6.8 and showed loss of activity below pH 4.5 and above pH 10 [36]. Also spectroscopic data suggest inactivation due to an irreversibly formed 6cLS heme-iron of DaCld [36] and closely related AoCld [4]. Mutational studies of conserved tryptophan residues of DaCld showed a significant impact on protein stability [35]. The authors hypothesized that in solution oligomerization state of DaCld is dependent on different buffer conditions and protein concentrations [35].

Although the crystal structures of DaCld and NdCld are almost superposable, there appears to be a difference in stability, indicated by the fact that DaCld changes its oligomeric structure depending on pH or ionic strength, a phenomenon not observed with NdCld [12, 35, 37, 40]. Examination of the crystal structures of DaCld (PDB-code: 3Q09) and NdCld (PDB-code: 3NN1) by PDBePISA (Protein Interfaces, Surfaces and Assemblies; http://www.ebi.ac.uk/msd-srv/prot_int/cgi-bin/piserver) of EMBL-EBI shows that 17 residues at the N-terminus of NdCld are involved in inter-subunit hydrogen bonds and salt bridges, whereas only 11 residues at the N-terminus of DaCld stabilize the oligomeric structure. The contribution of the C-terminal region to subunit interaction is similar in both proteins. This observation might indicate that the heme free N-terminal domain of functional Lineage I proteins ("long Clds") is important for modulation of the overall stability of the enzyme. Clearly, more detailed studies need to be performed to fully understand the interplay between oligomerization and stability, which could then be the basis for rational stability engineering.

7 Conclusion

Since their discovery in 1996 [1], several Clds and Cld-like proteins from different organisms have been investigated. Functional Clds cluster into two lineages with Lineage I containing (mainly) homopentameric metalloproteins with subunits consisting of an N-terminal and a C-terminal heme *b* containing ferredoxin-like fold, and Lineage II containing homodimeric enzymes with subunits lacking almost the entire N-terminal domain of Lineage I proteins. The heme cavity architecture of both lineages is almost identical and this is reflected by similar redox properties and catalytic efficiencies. Oligomerization seems to have an impact on conformational and thermal stability. All functional Clds have only one prominent and fully conserved arginine residue at the distal heme side that supports chlorite binding and oxidation, and (possibly) keeps the postulated intermediate hypochlorite in the reaction sphere (Fig. 3). Since the final product of ClO_2^- (Cl: +III) degradation is Cl^- (Cl: –I) with OCl^- (Cl: +I) as intermediate, this reaction is clearly not a dismutation reaction as the misleading name suggests. Due to the occurrence of Clds in many different bacterial and archaeal phyla (and not only in PCRBs), it is reasonable to assume that chlorite is not the endogenous substrate. Future studies on the biochemistry and physiology of Cld-like proteins (that lack the distal arginine and have no or very poor chlorite degradation activity) as well as a better understanding of the phylogenetic and biochemical relationship between Clds and DyPs will contribute to identifying the endogenous substrate of these enzymes.

Our comparative analyses of biochemical and biophysical data on Clds and Cld-like proteins show that, at the moment, NdCld is the best candidate for use in biotechnological applications. NdCld has a high conformational and thermal stability over a broad pH range and shows chlorite degradation activity even at very high temperatures. The oligomerization state of NdCld is independent of pH and ionic strength, and a high resolution crystal structure is available. Moreover, NdCld is the only functional Cld where X-ray structures of mutants have been solved. Nevertheless, before NdCld can be efficiently used in bioremediation of chlorite, several questions must be solved. It is important to understand: (i) the proposed reaction sequence and the involved redox intermediates (Fig. 3); and (ii) the mechanism of inhibition during chlorite degradation. This knowledge will provide the basis for rational enzyme engineering and/or modification

of reaction conditions. Simultaneously, the heterologous expression and purification in *E. coli* must be improved to obtain high yields. Principally, as demonstrated in the recent years, this will not be the bottleneck for application in biotechnology. Successful overexpression and purification of recombinant chlorite dismutases in *E. coli* has been reported for AoCld [32], IdCld [51, 52], DaCld [8, 36], NdCld [10, 12, 37], and NwCld [11].

The biotechnological potential of Cld is very high due to its unique chlorite detoxifying activity. Together with perchlorate and chlorate, chlorite is a serious environmental concern as rising concentrations of these harmful compounds have been detected in ground water, drinking water, and soils [6]. Environmental contamination with perchlorate and chlorate results from its extensive use as oxidizer in pyrotechnics and rocket fuel, and its presence in certain fertilizers. Chlorite is used as bleaching agent in the textile, pulp and paper industries, as a disinfectant and component of cleaning solutions, and in pesticides. Intake of chlorite by humans occurs mainly via drinking water, milk and consuming certain plants, and should be minimized. Due to its oxidative nature cholrite reacts easily with organic material and thus has toxic effects on living cells [5].

Besides chloride, the second reaction product of chlorite degradation is molecular oxygen. Nature seems to use Cld as O_2 generator. For example, in halophilic archaea a fusion protein consisting of a Cld and a monooxygenase was found [31]. Moreover, it has been suggested that PCRBs, which are facultative anaerobes, and other microbes, use Clds for metabolisms in anoxia. Several examples of aerobic pathways, e.g. of aromatic or aliphatic hydrocarbon degradation, have been reported that function in microbes in the absence of external O_2. It might be possible that these organisms use molecular oxygen formed by Cld. Exploitation of this Cld activity in various biochemical or biotechnological applications depends on further investigation of the reaction mechanism and the use of alternative oxidants instead of chlorite.

This project was supported by the Austrian Science Foundation, FWF [Doctoral program BioToP–Molecular Technology of Proteins (W1224) and the FWF-project P25270-B22].

All authors declare no commercial or financial conflict of interest.

8 References

[1] van Ginkel, C.G., Rikken, G.B., Kroon, A.G.M., Kengen, S.W.M., Purification and characterization of chlorite dismutase: a novel oxygen-generating enzyme. *Arch. Microbiol.* 1996, *166,* 321–326.

[2] Ettwig, K. F., Butler, M. K., Le Paslier, D., Pelletier, E. et al., Nitrite-driven anaerobic methane oxidation by oxygenic bacteria. *Nature* 2010, *464*, 543–548.

[3] Rikken, G.B., Kroon, A.G.M. van Ginkel, C.G., Transformation of (per) chlorate into chloride by a newly isolated bacterium: reduction and dismutation. *Appl.Microbiol. Biotechnol.* 1996, *45*, 420–426.

[4] Hagedoorn, P. L., de Geus, D. C., and Hagen, W. R., Spectroscopic characterization and ligand-binding properties of chlorite dismutase from the chlorate respiring bacterial strain GR-1. *Eur. J. Biochem.* 2002, *269*, 4905–4911.

[5] Ueno, H., Oishi, K., Sayato, Y., Nakamuro, K., Oxidative cell damage in Kat-sod assay of oxyhalides as inorganic disinfection by-products and their occurrence by ozonation. *Arch. Environ. Contam. Toxicol.* 2000, *38*, 1–6.

[6] Coates, J. D., Achenbach, L. A., Microbial perchlorate reduction: rocket-fueled metabolism. *Nat. Rev. Microbiol.* 2004, *2*, 569–580.

[7] Stenklo, K., Thorell, D., Bergius, H., Aasa, R., Nilsson, T., Chlorite dismutase from *Ideonella dechloratans*. *J. Biol. Inorg. Chem.* 2001, *6*, 601–607.

[8] Streit, B. R., DuBois, J. L., Chemical and steady-state analysis of a heterologously expressed heme dependent chlorite dismutase. *Biochemistry* 2008, *47*, 5271–5280.

[9] Mehboob, F., Wolterink, A. F., Vermeulen, A. J., Jiang, B. et al., Purification and characterization of a chlorite dismutase from *Pseudomonas chloritidismutans*. *FEMS Microbiol. Lett.* 2009, *293*, 115–121.

Stefan Hofbauer holds an M.Sc. degree in Biotechnology from BOKU – University of Natural Resources and Life Sciences, Vienna, where he is currently a PhD student at the Department of Chemistry within the international PhD-Program BioToP (Biomolecular Technology of Proteins; http://biotop.boku.ac.at). His research focuses on heme enzymes, and he is particularly interested in structure-function relationships and the reaction mechanism of chlorite dismutases.

Christian Obinger studied Chemistry and Biochemistry and performed his doctoral thesis at the Institute of Physical Chemistry at the University of Vienna. In 1992 he became Assistant Professor at the Department of Chemistry at BOKU–University of Natural Resources and Life Sciences. In 1999 he was promoted to Associate Professor (habilitation) for Biochemistry, and in 2011 to Full Professor for Protein Biochemistry. He is interested in structure-function relationships of heme-containing oxidoreductases including peroxidases, peroxidasins, catalases, chlorite dismutases and related systems. His reseach focuses on the impact of the protein matrix and post-translational modifications on catalytically relevant redox intermediates and electron-transfer reactions.

[10] Maixner, F., Wagner, M., Lücker, S., Pelletier, E. et al., Environmenteal genomics reveals a functional chlorite dismutase in the nitrite-oxidizing bacterium "*Candidatus* Nitrospira defluvii". *Environ. Microbiol.* 2008, *10*, 3043 Environmenteal genomics reveals a functional chlorite dismutase in the nitrite-oxidizing bacterium 3056.

[11] Mlynek, G., Sjöblom, B., Kostan, J., Füreder, S. et al., Unexpected diversity of chlorite dismutases: a catalytically efficient dimeric enzyme from *Nitrobacter winogradskyi*. *J. Bacteriol.* 2011, *193*, 2408–2417.

[12] Kostan, J., Sjoeblom, B., Maixner, F., Mlynek, G. et al., Structural and functional analysis of the chlorite dismutase from the nitrite-oxidizing bacterium "*Candidatus* Nitrospira defluvii": identification of a catalytically important amino acid residue. *J. Struct. Biol.* 2010, *172*, 331–342.

[13] Eriksen, G. E., The Chilean nitrate deposits. *Am. Sci.* 1983, *71,* 366–374.

[14] Bardiya, N., Bae, J. H., Dissimilatory perchlorate reduction: a review. *Microbiol. Res.* 2011, *166*, 237–254.

[15] Goblirsch, B., Kurker, R. C., Streit, B. R., Wilmot, C. M., DuBois, J. L., Chlorite dismutases, DyPs and EfeB: 3 microbial heme enzyme families comprise the CDE structural superfamily. *J. Mol. Biol.* 2011, *408*, 379–398.

[16] Zámocký, M., Furtmüller, P. G., Obinger, C., Two distinct groups of fungal catalase/peroxidases. *Biochem. Soc. Trans.* 2009, *37*(Pt 4), 772–777.

[17] Zámocký, M., Furtmüller, P. G., Obinger, C., Evolution of structure and function of Class I peroxidases. *Arch. Biochem. Biophys.* 2010, *500*, 45–57.

[18] Kim, S. J., Shoda, M., Purification and characterization of a novel peroxidase from *Geotrichum candidum* Dec 1 involved in decolorization of dyes. *Appl. Environ. Microbiol.* 1999, *65*, 1029–1035.

[19] Roberts, J. N., Singh, R., Grigg, J. C., Murphy, M. E. et al., Molecular characterization of dye-decolorizing peroxidases from *Rhodococcus jostii* RHA1. *Biochemistry* 2011, *50*, 5108–5119.

[20] Liers, C., Pecyna, M. J., Kellner, H., Worrich, A. et al., Substrate oxidation by dye-decolorizing peroxidases (DyPs) from wood- and litter-degrading agaricomycetes compared to other fungal and plant heme-peroxidases. *Appl. Microbiol Biotechnol.* 2013, *97*, 5839–5849.

[21] Sezer, M., Santos, A., Kielb, P., Pinto, T. et al., Distinct structural and redox properties of the heme active site in bacterial dye decolorizing peroxidase-type peroxidases from two subfamilies: resonance Raman and electrochemical study. *Biochemistry* 2013, *52*, 3074–3084.

[22] van Bloois, E., Torres Pazmiño, D. E., Winter, R. T., Fraaije, M. W., A robust and extracellular heme-containing peroxidase from *Thermobifida fusca* as prototype of a bacterial peroxidase superfamily. *Appl. Microbiol. Biotechnol.* 2010, *86*, 1419–1430.

[23] Brown, M. E., Barros, T., Chang, M. C., Identification and characterization of a multifunctional dye peroxidase from a lignin-reactive bacterium. *ACS Chem. Biol.* 2012, *7*, 2074–2078.

[24] Scheibner, M., Hülsdau, B., Zelena, K., Nimtz, M. et.al., Novel peroxidases of *Marasmius scorodonius* degrade beta-carotene. *Appl. Microbiol. Biotechnol.* 2008, *77*, 1241–1250.

[25] Ogola, H. J. O., Kamiike, T., Hashimoto, N., Ashida, H.et al., Molecular Characterization of a Novel Peroxidase from the Cyanobacterium *Anabaena* sp. Strain PCC 7120. *Appl. Environ. Microbiol.* 2009, *75*, 7509–7518.

[26] Edgar, R. C., MUSCLE: multiple sequence alignment with high accuracy and high throughput. *Nucleic Acids Res.* 2004, *32*, 1792–1797.

[27] Tamura, K., Peterson, D., Peterson, N., Stecher, G., et al., MEGA5: Molecular Evolutionary Genetics Analysis using Maximum Likelihood, Evolutionary Distance, and Maximum Parsimony Methods. *Mol. Biol. Evol.* 2011, *28,* 2731–2739.

[28] Ahmad, M., Roberts, J. N., Hardiman, E. M., Singh, R., et al., Identification of DypB from *Rhodococcus jostii* RHA1 as a lignin peroxidase. *Biochemistry* 2011, *50*(23), 5096–5107.

[29] Dailey, T. A., Boynton, T. O., Albetel, A. N., Gerdes, S., et al., Discovery and Characterization of HemQ: an essential heme biosynthetic pathway component. *J. Biol. Chem.* 2010, *285*, 25978–25986.

[30] Mayfield, J. A., Hammer, N. D., Kurker, R. C., Chen, T. K. et al., Chlorite Dismutase (HemQ) from *Staphylococcus aureus* Has a Redox-Sensitive Heme and is Associated with the Small Colony Variant Phenotype. *J. Biol. Chem.* 2013, *288*, 23488–23504.

[31] Bab-Dinitz, E., Shmuely, H., Maupin-Furlow, J., Eichler, J., Shaanan, B., *Haloferax volcanii* PitA: an example of functional interaction between the Pfam chlorite dismutase and antibiotic biosynthesis monooxygenase families? *Bioinformatics* 2006, *22*, 671–675.

[32] de Geus, D. C., Thomassen, E. A. J., Hagedoorn, P.-L., Pannu, N. S. et al., Crystal structure of chlorite dismutase, a detoxifying enzyme producing molecular oxygen. *J. Mol. Biol.* 2009, *387*, 192–206.

[33] Goblirsch, B. R., Streit, B. R., DuBois, J. L., Wilmot, C. M., Structural features promoting dioxygen production by *Dechloromonas aromatica* chlorite dismutase. *J. Biol. Inorg. Chem.* 2010, *15*, 879–888.

[34] Ebihara, A., Okamoto, A., Kousumi, Y., Yamamoto, H. et al., Structure-based functional identification of a novel heme-binding protein from *Thermus thermophilis* HB8. *J. Struct. Func. Gen.* 2005, *6*, 21–32.

[35] Blanc, B., Rodgers, K. R., Lukat-Rodgers, G. S., DuBois, J. L., Understanding the roles of strictly conserved tryptophan residues in O2 producing chlorite dismutases. *Dalton Trans.* 2013, *42*, 3156–3169.

[36] Streit, B. R., Blanc, B., Lukat-Rodgers, B. S., Rodgers, K. R., DuBois, J. L., How active-site protonation state influences the reactivity and ligation of the heme in chlorite dismutase. *J. Am. Chem. Soc.* 2010, *132*, 5711–5724.

[37] Hofbauer, S., Bellei, M., Sündermann, A., Pirker, K. F. et al., Redox thermodynamics of high-spin and low-spin forms of chlorite dismutases with diverse subunit and oligomeric structures. *Biochemistry* 2012, *51*, 9501–9512.

[38] Blanc, B., Mayfield, J. A., McDonald C. A., Lukat-Rodgers, G. S. et al., Understanding how the distal environment directs reactivity in chlorite dismutase: spectroscopy and reactivity of Arg183 mutants. *Biochemistry* 2012, *51*, 1895–1910.

[39] Goblirsch, B. R., Streit, B. R., DuBois, J. L., Wilmot, C. M., Crystallization and preliminary X-ray diffraction of chlorite dismutase from *Dechloromonas aromatica* RCB. *Acta Crystallogr. Sect. F Struct. Biol. Cryst. Commun.* 2009, *65*, 818–821.

[40] Hofbauer, S., Gysel, K., Mlynek, G., Kostan, J. et al., Impact of subunit and oligomeric structure on the thermal and conformational stability of chlorite dismutases. *Biochim. Biophys. Acta* 2012, *1824*, 1031–1038.

[41] Kelly, S. M., Jess, T. J., Price, N. C., How to study proteins by circular dichroism. *Biochim. Biophys. Acta* 2005, *1751,* 119–139.

[42] Lee, A. Q., Streit, B. R., Zdilla, M. J., Abu-Omar, M. M., DuBois, J. L., Mechanism of and exquisite selectivity for O-O bond formation by the heme dependent chlorite dismutase. *Proc. Natl. Acad. Sci. USA* 2008, *105*, 15654–15659.

[43] Svistunenko, D. A., Worrall, J. A., Chugh, S. B., Haigh, S. C. et al., Ferric haem forms of *Mycobacterium tuberculosis* catalase-peroxidase probed by EPR spectroscopy: Their stability and interplay with pH. *Biochimie* 2012, *94*, 1274–1280.

[44] Dassama, L. M., Yosca, T. H., Conner, D. A., Lee, M. H. et al., O(2)-evolving chlorite dismutase as a tool for studying O_2-utilizing enzymes. *Biochemistry* 2012, *51*,1607–1616.

[45] Battistuzzi, G., Bellei, M., Bortolotti, C. A., Sola, M. Redox properties of heme peroxidases. *Arch. Biochem. Biophys.* 2010, *500*, 21–36.

[46] Farhangrazi, Z. S., Fossett, M. E., Powers, L. S., Ellis, W. R. Jr., Variable-temperature spectroelectrochemical study of horseradish peroxidase. *Biochemistry* 1995, *34*, 2866–2871.
[47] Dutton, P. L., Redox potentiometry: determination of midpoint potentials of oxidation-reduction components of biological electron-transfer systems. *Methods Enzymol.* 1978, *54,* 411–35.
[48] Pierik, A. J., Hagen, W. R., Redeker, J. S., Wolbert, R. B.et al., Redox properties of the iron-sulfur clusters in activated Fe-hydrogenase from *Desulfovibrio vulgaris* (Hildenborough). *Eur. J. Biochem.* 1992, *209*, 63–72.
[49] Massey, V., A simple method for the determination of redox potentials. In *Flavins and Flavoproteins* (Curti, B., Ronchi, S., and Zanetti, G., Eds.), Walter de Gruyter, Berlin. 1991, 66–69
[50] Singh R., Grigg J. C., Armstrong Z., Murphy M. E., Eltis L. D., Distal heme pocket residues of B-type dye-decolorizing peroxidase: arginine but not aspartate is essential for peroxidase activity. *J. Biol. Chem.* 2012 , *287*, 10623–10630.
[51] Thorell, H. D., Karlsson, J., Portelius, E., Nilsson, T., Cloning, characterisation, and expression of a novel gene encoding chlorite dismutase from *Ideonella dechloratans*. *Biochim. Biophys. Acta.* 2002, *1577*, 445–451.
[52] Danielsson Thorell, H., Beyer, N. H., Heegaard, N. H., Ohman, M., Nilsson, T.,Comparison of native and recombinant chlorite dismutase from *Ideonella dechloratans*. *Eur. J. Biochem.* 2004, *271*, 3539–3546

Biotechnology Journal

Supporting Information for DOI 10.1002/biot.201300210

Chlorite dismutases – a heme enzyme family for use in bioremediation and generation of molecular oxygen

Stefan Hofbauer, Irene Schaffner, Paul G. Furtmüller and Christian Obinger

Chlorite dismutases - a heme enzyme family for use in bioremediation and generation of molecular oxygen

Stefan Hofbauer, Irene Schaffner, Paul G. Furtmüller, and Christian Obinger*

Department of Chemistry, Division of Biochemistry, VIBT – Vienna Institute of BioTechnology, BOKU – University of Natural Resources and Life Sciences, A-1190 Vienna, Muthgasse 18, A-1190 Vienna, Austria

*Corresponding author. Phone: +43-1-47654-6073, fax: +43-1-47654-6050, email: christian.obinger@boku.ac.at

Supplemental Table 1. Overview of available crystal structures determined by X-ray diffraction (July 2013). a) No heme in crystal structure; b) no information about pH of crystallization condition; c) PDB-structure available, unpublished/Pubmed not available.

	pdb-code	organism	heme ligand	subunits	pH	resolution (Å)	reference
chlorite dismutases							
AoCld	2VXH	*Azospira oryzae* strain GR-1	SCN^-	6	5.5	2.10	[32]
DaCld	3Q08	*Dechloromonas aromatica*	NO_2^-	5	6.5	3.05	[33]
DaCld	3Q09	*Dechloromonas aromatica*	NO_2^-	5	9.0	3.00	[33]
NdCld	3NN1	"*Candidatus* Nitrospira defluvii"	Imidazole	5	7.5	1.85	[12]
NdCld	3NN2	"*Candidatus* Nitrospira defluvii"	CN^-	5	7.5	1.94	[12]
NdCld R173A	3NN3	*Candidatus* "Nitrospira defluvii"	H_2O	5	4.6	2.60	[12]
NdCld R173K	3NN4	"*Candidatus* Nitrospira defluvii"	H_2O	5	4.0	2.70	[12]
NwCld	3QPI	*Nitrobacter winogradskyi*	H_2O	2	8.2	2.10	[11]
putative chlorite dismutases							
GsCld	1T0T	*Geobacillus stearothermophilus*	a)	5	b)	1.81	Chang et al. c)
TaCld	3DTZ	*Thermoplasma acidophilum*	a)	5	b)	1.75	Gilski et al. c)
TtCld	1VDH	*Thermus thermophilus*	a)	5	4.4	2.00	[34]

Supplemental Table 2. Sequence identities of characterized functional chlorite dismutases (Clds) and chlorite dismutase-like enzymes, determined with the LALIGN server (http://embnet.vital-it.ch/software/LALIGN_form.html). Characterized Clds include AoCld, (chlorite dismutase from Azospira oryzae), DaCld (Cld from Dechloromonas aromatica), IdCld (Cld from Ideonella dechloratans), NdCld (Cld from "Candidatus Nitrospira defluvii"), NwCld (Cld from Nitrobacter winogradskyi) and PcCld (Cld from Pseudomonas chloritidismutans). Cld-like proteins include SaCld (Cld-like protein from Staphylococcus aureus) and TtCld (Cld-like protein from Thermus thermophilus).

%	AoCld	DaCld	IdCld	NdCld	NwCld	PcCld	SaCld	TtCld
AoCld	**100.0**	**94.3**	60.5	42.0	36.7	**95.4**	23.8	21.0
DaCld	**94.3**	**100.0**	63.5	42.0	36.7	**92.2**	23.8	21.0
IdCld	60.5	63.5	**100.0**	38.1	33.9	60.5	24.2	19.4
NdCld	42.0	42.0	38.1	**100.0**	31.5	42.3	23.8	22.1
NwCld	36.7	36.7	33.9	31.5	**100.0**	36.7	23.7	23.8
PcCld	**95.4**	**92.2**	60.5	42.3	36.7	**100.0**	24.8	22.6
SaCld	23.8	23.8	24.2	23.8	23.7	24.8	**100.0**	44.2
TtCld	21.0	21.0	19.4	22.1	23.8	22.6	44.2	**100.0**

Chapter 2

Aims of the thesis

Aims of the thesis

The thesis aimed at the elucidation of relationships between structure and function of two functional (i.e. chlorite degrading) chlorite dismutases (Clds) from nitrite-oxidizing bacteria, namely Cld from "*Candidatus* Nitrospira defluvii" (Maixner et al, 2008) and Cld from *Nitrobacter winogradskyi* (Mlynek et al, 2011). To understand the structural basis of catalysis and provide a mechanism of reaction as well as of the observed self-inactivation of Cld the following experiments were planned:

- ► Analysis of the phylogenetic relationship between functional Clds and non-functional Cld-like proteins as well as dye-decolorizing peroxidases

- ► Comparative study on biochemical and biophysical properties of pentameric NdCld and dimeric NwCld including (i) determination of kinetic parameters of chlorite degradation by spectrophotometric and polarographic means, (ii) redox thermodynamics by spectroelectrochemistry, (iii) ligand binding by stopped-flow spectroscopy as well as (iv) conformational and thermal stability by UV-vis, circular dichroism (CD) and fluorescence spectroscopy as well as differential scanning calorimetry. Select the more stable protein for design of mutants and further studies.

- ► Mutational analysis of conserved proximal and distal amino acids at the active site. Comparative study on biochemical and biophysical properties of the respective variants including (i) determination of kinetic parameters of chlorite degradation by spectrophotometric and polarographic means, (ii) redox thermodynamics by spectroelectrochemistry, (iii) cyanide binding by stopped-flow spectroscopy as well as (iv) UV-vis, CD- and electron paramagnetic resonance (EPR) spectroscopy and (v) X-ray crystallography.

- ► Analysis of modification of Cld during inactivation and probing the hypothesis that transiently formed hypochlorite is responsible for the observed irreversible inhibition during turnover by (i) investigation of the effect of specific traps of hypochlorite on catalysis, (ii) detailed analysis of the changes of the spectral properties of the prosthetic group during inactivation by UV-vis and EPR spectroscopy, (iii) mass spectrometric analysis of oxidative modifications of amino acids, and (iv) analysis of the role of the conserved distal arginine in this process.

References

Maixner, F., Wagner, M., Lücker, S., Pelletier, E., Schmitz-Esser, S., Hace, K., Spieck, E., Konrat, R., Le Paslier, D., and Daims, H. (2008) Environmenteal genomics reveals a functional chlorite dismutase in the nitrite-oxidizing bacterium *Candidatus* "Nitrospira defluvii". *Environ. Microbiol.*, *10*, 3043-3056

Mlynek, G., Sjöblom, B., Kostan, J., Füreder, S., Maixner, F., Gysel, K., Furtmüller, P. G., Obinger, C., Wagner, M., Daims, H., and Djinović-Carugo, K. (2011) Unexpected diversity of chlorite dismutases: a catalytically efficient dimeric enzyme from *Nitrobacter winogradskyi. J. Bacteriol*., *193*, 2408-2417

Chapter 3

Impact of subunit and oligomeric structure on the thermal and conformational stability of chlorite dismutases

Stefan Hofbauer, Kira Gysel, Georg Mlynek, Julius Kostan, Andreas Hagmüller, Holger Daims, Paul G. Furtmüller, Kristina Djinovic-Carugo, Christian Obinger

Research Article

Biochimica et Biophysica Acta - Proteins and Proteomics (2012), 1824, 1031-1038

Biochimica et Biophysica Acta 1824 (2012) 1031–1038

Contents lists available at SciVerse ScienceDirect

Biochimica et Biophysica Acta

journal homepage: www.elsevier.com/locate/bbapap

Impact of subunit and oligomeric structure on the thermal and conformational stability of chlorite dismutases

Stefan Hofbauer [a], Kira Gysel [b], Georg Mlynek [b,d], Julius Kostan [b], Andreas Hagmüller [b], Holger Daims [c], Paul G. Furtmüller [a], Kristina Djinović-Carugo [b,e], Christian Obinger [a,*]

[a] Department of Chemistry, Division of Biochemistry, VIBT, Vienna Institute of BioTechnology, BOKU, University of Natural Resources and Life Sciences, Muthgasse 18, A-1190 Vienna, Austria
[b] Department for Structural and Computational Biology, Max F. Perutz Laboratories, University of Vienna, Campus Biocenter 5, A-1030 Vienna, Austria
[c] Department of Microbial Ecology, University of Vienna, Althanstrasse 14, A-1090 Vienna, Austria
[d] Department of Food Sciences and Technology, VIBT, Vienna Institute of BioTechnology, BOKU, University of Natural Resources and Life Sciences, Muthgasse 18, A-1190 Vienna, Austria
[e] Department of Biochemistry, Faculty of Chemistry and Chemical Technology, University of Ljubljana, Aškerčeva 5, 1000 Ljubljana, Slovenia

ARTICLE INFO

Article history:
Received 20 April 2012
Received in revised form 25 May 2012
Accepted 26 May 2012
Available online 6 June 2012

Keywords:
Chlorite dismutase
Thermal stability
Conformational stability
Protein unfolding
Oligomeric structure
Bioremediation

ABSTRACT

Chlorite dismutases (Cld) are unique heme *b* containing oxidoreductases that convert chlorite to chloride and dioxygen. Recent phylogenetic and structural analyses demonstrated that these metalloproteins significantly differ in oligomeric and subunit structure. Here we have analyzed two representatives of two phylogenetically separated lineages, namely pentameric Cld from *Candidatus* "Nitrospira defluvii" and dimeric Cld from *Nitrobacter winogradskyi* having a similar enzymatic activity at room temperature. By application of a broad set of techniques including differential scanning calorimetry, electronic circular dichroism, UV–vis and fluorescence spectroscopy the temperature-mediated and chemical unfolding of both recombinant proteins were analyzed. Significant differences in thermal and conformational stability are reported. The pentameric enzyme is very stable between pH 3 and 10 (T_m = 92 °C at pH 7.0) and active at high temperatures thus being an interesting candidate for bioremediation of chlorite. By contrast the dimeric protein starts to unfold already at 53 °C. The observed unfolding pathways are discussed with respect to the known subunit structure and subunit interaction.

1. Introduction

Chlorite dismutases (Clds) are oligomeric heme *b*-containing oxidoreductases found in prokaryotic organisms. These oxidoreductases (EC 1.13.11.49) are able to catalyze the conversion of toxic chlorite (ClO_2^-) to chloride and dioxygen. In the last years several X-ray structures of multimeric (di-, penta-, hexa-) Clds and Cld-like proteins from archaea and bacteria have been published [1–5] that helped to critically analyze and complement mechanistic aspects of catalysis [6–10]. The proposed enzyme mechanism includes oxidation of the ferric heme protein to an oxoiron(IV) porphyryl radical intermediate (Compound I) by chlorite which is reduced to hypochlorite. The latter must be captured at the active site since it is rapidly oxidized by Compound I forming a new O—O bond, thereby releasing dioxygen (O_2), chloride (Cl^-) and the enzyme in its native ferric state [8–10]. Both atoms in the oxygen gas product originate entirely from the chlorite substrate [8–10]. The catalytic efficiency (k_{cat}/K_M) for this reaction varies from 6.0×10^5 $M^{-1}\,s^{-1}$ to 3.5×10^7 $M^{-1}\,s^{-1}$ [5].

The physiological role of Clds in prokaryotes is not fully understood, but it has been shown that some microorganisms can use perchlorate or chlorate as terminal electron acceptors for anaerobic respiration thereby producing chlorite that must be detoxified [11]. However, recent phylogenetic analyses showed that many other bacterial and archaeal genomes encode Cld-like proteins, although most of the respective organisms have never been observed to use (per)chlorate or convert chlorite [5,12]. Since the transformation of chlorite to harmless O_2 and Cl^- is mediated by Clds with high efficiency, there is increasing interest for using these catalysts for bioremediation [11,12]. Due to its oxidative nature, chlorite reacts with organic material and thus has toxic effects on living cells [13]. Perchlorate, chlorate and chlorite are brought to nature by anthropogenic activities (munition manufacturing, rocket fuel, fertilizer, bleaching agents, disinfectants, pesticides, etc.). They are a serious environmental concern since rising concentrations of these harmful compounds have been detected in groundwater, surface waters, and soils [11]. In order to use Clds for bioremediation it is important to know the conformational and thermal stability of these proteins as well as the temperature and pH-dependence of the enzymatic reaction. Since in addition to pentameric Clds [1–4] also active dimeric forms [5] are found, it is also important to know the correlation between the

Abbreviations: Cld, chlorite dismutase; NdCld, *Candidatus* "Nitrospira defluvii"; apo-NdCld, heme-free chlorite dismutase from *Candidatus* "Nitrospira defluvii"; NwCld, chlorite dismutase from *Nitrobacter winogradskyi*; DSC, differential scanning calorimetry; ECD, electronic circular dichroism; GdnHCl, guanidinium hydrochloride

* Corresponding author. Tel.: +43 1 47654 6073; fax: +43 1 47654 6050.
E-mail address: christian.obinger@boku.ac.at (C. Obinger).

1570-9639/$ – see front matter © 2012 Elsevier B.V. All rights reserved.
doi:10.1016/j.bbapap.2012.05.012

oligomeric structure and the stability of Clds in order to select the proper candidates for future application and molecular engineering.

In this work we have analyzed the conformational and thermal stability of recombinant dimeric Cld from *Nitrobacter winogradskyi* (NwCld) and of pentameric Cld from *Candidatus* "Nitrospira defluvii" (NdCld). Both enzymes have a comparable catalytic efficiency but differ significantly in oligomeric structure and subunit size and belong to different phylogenetic lineages (Fig. 1) [4,5]. The presented comprehensive biophysical analyses [differential scanning calorimetry (DSC), temperature-dependent electronic UV–vis and electronic circular dichroism spectrometry (ECD), denaturant-dependent fluorescence spectroscopy] show significant differences that are discussed with respect to the recently solved X-ray structures of both enzymes [4,5] and the temperature and pH-dependence of chlorite degradation.

2. Materials and methods

2.1. Cloning, heterologous expression and purification

Cloning, heterologous expression and purification of chlorite dismutase from *Nitrobacter winogradskyi* (accession no. YP_319047) was performed as described by Mlynek et al. using the expression vector pET-21b (+) (Merck/Novagen, Darmstadt, Germany) for subsequent production of a C-terminally His-tagged fusion protein [5]. Recombinant NwCld was expressed in *E. coli Tuner (DE3)* cells (Merck/Novagen) and purified using a HisTrap FF crude column (GE Healthcare) and a HiLoad 26/60 Superdex 200 pg column (GE Healthcare).

A DNA fragment containing the full length coding region of Cld from *Candidatus* "Nitrospira defluvii" (without the N-terminal signal peptide) was amplified by PCR using primers designed and described by Maixner et al. [14] and cloned into a modified pET-21b (+) vector for the production of a N-terminal TEV-cleavable Strep-II tagged fusion protein. Recombinant NdCld was expressed in *E. coli Tuner (DE3)* cells (Merck/Novagen, Darmstadt, Germany) and grown in hemin-enriched Luria–Bertani (LB) medium. The LB-Medium was supplemented with ampicillin (100 μg mL^{-1}) and was inoculated with a freshly prepared overnight culture (at a dilution 1:100). The culture was grown at 37 °C and 220 rpm agitation until the early stationary phase was reached (OD_{600} = 0.8). In order to induce NdCld expression, isopropyl-β-D-thiogalactopyranoside (IPTG) was added to a final concentration of 0.5 mM. Also hemin (50 μg mL^{-1}) was added to the culture. The temperature was lowered to 24 °C. After 4 h the culture was centrifuged (4000 rpm, 10 min, 4 °C) the resulting cell pellet was either processed immediately or stored at −80 °C until further use. When needed cell pellets were resuspended in 50 mM HEPES, pH 7.4, 5% glycerol, 0.5% Triton X-100, 0.5 mM EDTA, 1 mM phenylmethylsulfonylfluoride (PMSF). The cell suspension was lysed under sonication and clarified by centrifugation (18000 rpm. 25 min, 4 °C). Subsequently the supernatant was loaded to a StrepTrap HP 5 ml (GE Healthcare) column equilibrated with 20 mM HEPES, pH 7.4, 2% glycerol. The protein was eluted using 20 mM HEPES, pH 7.4, 2% glycerol, 2.5 mM desthiobiotin. Strep-II-tag was fully cleaved off using TEV-protease in 20 mM Hepes, pH 7.4, 2% glycerol, 0.5 mM DTT. Finally, 100 μM hemin was added to the cleaved protein and incubated for several hours at 4 °C. Precipitated hemin was removed by centrifugation (18000 rpm, 25 min, 4 °C). Resulting proteins were screened by SDS-PAGE and fractions containing NdCld were pooled and applied on a HiLoad 16/60 Superdex 200 pg (GE Healthcare) column equilibrated with 20 mM HEPES, pH 7.4, 2% glycerol. TEV protease

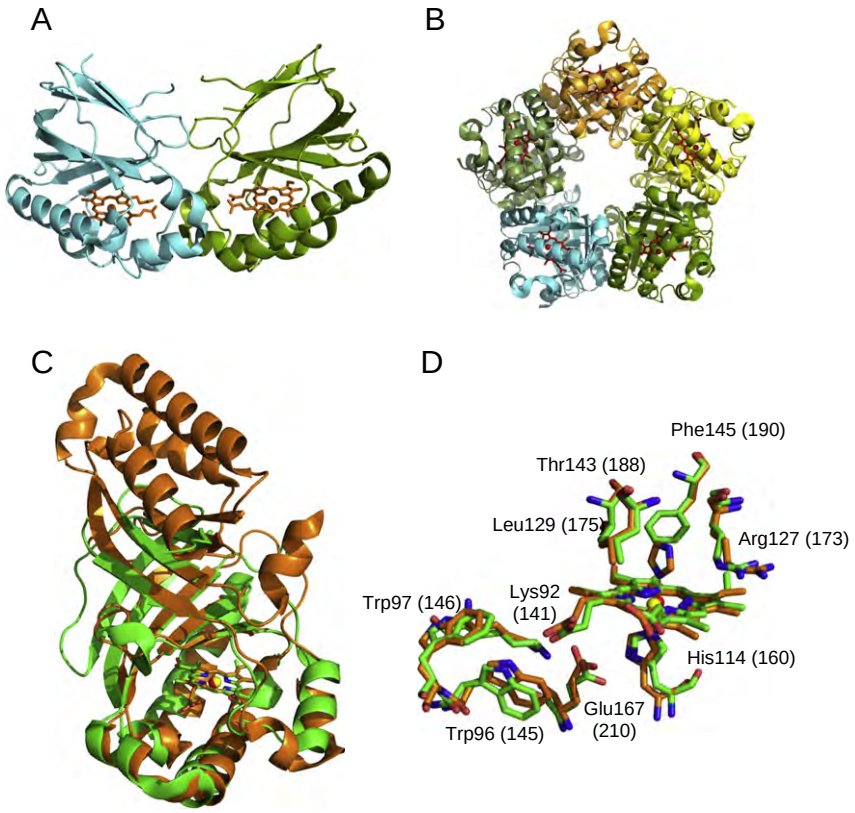

Fig. 1. Structures of dimeric chlorite dismutase from *Nitrobacter winogradskyi* (NwCld, PDB: 3QPI) [5] and pentameric chlorite dismutase from *Candidatus* "Nitrospira defluvii" (NdCld, PDB: 3NN1) [4]. (A) Ribbon representation of the NwCld dimer viewed perpendicular to the vertical 2-fold symmetry axis. Subunits are shown in different colors. Heme groups are depicted in orange. (B) Ribbon representation of the NdCld pentamer structure. Monomers are shown in different colors. (C) Ribbon representation of a superposition of subunits of NwCld (green) and NdCld (orange), respectively. (D) Superposition of heme cavity residues of NwCld (green) and NdCld (orange). Amino acid numbering according to NwCld and NdCld (brackets). NdCld shows an imidazole bound to the distal site of the heme. Figures were generated using PyMOL (http://www.pymol.org/).

(27 kDa) was separated from NdCld (130 kDa) in this step. Aliquots of purified protein were concentrated to 5 mg ml^{-1}, frozen in liquid nitrogen and stored until further use.

Expression and purification of the apo-form of NdCld were performed as described above with the exception that no hemin was added. The absence of any absorbance in the Soret region showed the presence of the pure apoform.

2.2. Steady-state kinetics

The temperature dependence of chlorite degradation was followed as absorbance decrease at 260 nm (Hitachi U-3900 UV–vis) using $\varepsilon_{260\ nm} = 155\ M^{-1}\ cm^{-1}$ [15]. The temperature was controlled with a water bath connected to the cuvette-holder. The enzymatic activity of NdCld and NwCld were measured between 30 °C–90 °C and 30 °C–55 °C, respectively. Reactions were carried out in 50 mM phosphate buffer, pH 7.0, and using a non-inhibiting $NaClO_2$ concentration of 40 μM (total reaction volume: 1 mL). Five measurements were performed and the corresponding arithmetic mean is presented. Reactions were started by addition of 32 nM NdCld or 24 nM NwCld. At room temperature the reactions were also followed polarographically using a Clark-type electrode (Oxygraph plus, Hansatech Instruments, UK) [4,5]. These data showed a stoichiometry of ClO_2^-:O_2 of 1:1 as was reported in the literature [7–10]. However, at temperatures >45 °C the Clark-type electrode could not be used according to the instructions of the manufacturer.

2.3. Differential scanning calorimetry

Differential calorimetric (DSC) measurements were performed using a VP-capillary DSC microcalorimeter from Microcal (cell volume: 137 μL), controlled by the VP-viewer program and equipped with an autosampler for 96 well plates. Samples were analyzed using a programmed heating scan rate of 60 °C h^{-1} over a temperature range of 20 °C to 110 °C and approximately 60 psi (4.136 bar) cell pressure. Maximum temperature inside the cuvette was 95 °C. Collected DSC data were corrected for buffer baseline and normalized for protein concentration. Conditions: 14.3 μM NdCld and 12.5 μM NwCld in 50 mM phosphate buffer, pH 7, as well as 12 μM apo-NdCld in 20 mM HEPES, pH 7.4, 2% glycerol. For data analysis and conversion the Microcal origin software was used. Heat capacity (C_p) was expressed in kcal $mol^{-1}\ K^{-1}$ (1 cal = 4.184 J). Data points were fitted to non-two-state equilibrium-unfolding models by the Lavenberg/Marquardt (LM) non-linear least square method.

For measurements of the pH dependence of thermal unfolding 50 mM acetate buffer (pH 3–6) and 50 mM phosphate buffer (pH 6–11) were used. Protein concentrations were 14.3 μM (NdCld) and 12.5 μM (NwCld), respectively.

2.4. Temperature-mediated unfolding followed by electronic circular dichroism spectroscopy

Besides DSC, thermal unfolding was followed by electronic circular dichroism (ECD) spectroscopy (Chirascan, Applied Photophysics, Leatherhead, UK). The instrument was flushed with nitrogen at a flow rate of 5 L min^{-1} and allowed simultaneous UV–vis and ECD monitoring. The instrument was equipped with a Peltier element for temperature control and temperature-mediated denaturation was monitored between 20 °C and 95 °C. Temperature was increased stepwise with 1.0 °C min^{-1}.

Single wavelength scans were performed with instrumental parameters set as follows. Visible ECD at Soret maximum was performed with 10 μM NdCld and 10 μM NwCld in 5 mM phosphate buffer, pH 7.0, containing 0.5 M GdnHCl (in order to avoid aggregation at higher temperatures). The pathlength was 10 mm, spectral bandwidth 1 nm and scan time per point was set at 10 s. Far-UV ECD at 208 nm was performed with 10 μM NdCld, NwCld or apo-NdCld in 5 mM phosphate buffer, pH 7.0, containing 0.5 M GdnHCl. The pathlength was at 1 mm, spectral bandwidth 3 nm and scan time per point was set at 10 s. At room temperature ECD spectra in the far-UV region were recorded for 5 μM NdCld and 5 μM NwCld in the presence and absence of 0.5 M GdnHCl in order to probe the effect of 0.5 M GdnHCl on the overall secondary structure.

The fraction α of unfolded protein was calculated according to $\alpha = (\theta_N - \theta)/(\theta_N - \theta_U)$ with θ_N being the ellipticity (in mdeg) at 208 or 417 nm/416 nm of the protein in the native folded state, θ the ellipticity at defined temperature (T), and θ_U being the ellipticity at 208 or 417 nm/416 nm of the completely unfolded state.

2.5. Chemical denaturation followed by fluorescence and UV–vis spectroscopy

Guanidinium hydrochloride (GdnHCl) was used to probe the chemical denaturation of both chlorite dismutases. Unfolding was monitored by following the changes in the emission of intrinsic tryptophan fluorescence as well as changes in the Soret region.

The fluorescence spectrophotometer (Hitachi F-7000 Fluorescence) was equipped with a thermostatic cell holder for quartz cuvettes of 10 mm path length. Instrumental parameters were set as follows. Excitation wavelength was at 295 nm, excitation and emission bandwidth at 5 nm and PMT voltage was set at 700 V for NwCld and 400 V for NdCld (scan speed: 60 nm min^{-1}). In detail, 500 nM NdCld or NwCld in 5 mM phosphate buffer, pH 7.0, were incubated with increasing concentrations of GdnHCl (0–8 M) over night at room temperature. For each GdnHCl concentration fraction α of unfolded protein was calculated according to $\alpha = (F_N - F)/(F_N - F_U)$, with F_N representing either the relative fluorescence intensity (F/F_0) at 350 nm or the fluorescence emission maximum of the native folded state, F being the relative fluorescence intensity (F/F_0) at 350 nm or the fluorescence emission maximum at defined GdnHCl concentrations and F_U the relative fluorescence intensity (F/F_0) at 350 nm or the fluorescence maximum of the completely unfolded state. The same samples were also measured for elucidation of changes in the Soret region. The UV–vis spectrophotometer (Hitachi U-3900) was equipped with a thermostatic cell holder for quartz cuvettes of 10 mm path length. Scan speed was 120 nm min^{-1}. For each GdnHCl concentration the fraction α of unfolded protein was calculated from the shift of the Soret maximum according to $\alpha = (A_N - A)/(A_N - A_U)$, with A representing the Soret band maximum at defined GdnHCl concentrations, A_N the Soret maximum of the native state and A_U the Soret maximum of the completely unfolded state.

3. Results

Recent progress in genome and metagenome sequencing has enormously increased the size and phylogenetic complexity of the Cld-like protein superfamily [12]. At the same time the practical relevance of Clds for the bioremediation of the anthropogenic pollutant chlorite increased. This prompted us to probe the conformational and thermal stability of two representatives of two major lineages that differ significantly in structure but have a comparable efficiency in chlorite degradation [4,5]. The two heme proteins were selected because we have been able to solve their X-ray structure recently and determine basic enzymatic parameters. Chlorite dismutase from *Candidatus* "Nitrospira defluvii" (NdCld) is a pentameric enzyme with each monomer consisting of two topologically equivalent four-stranded antiparallel β-sheets forming a β-barrel (ferredoxin-like fold) flanked on both sides by six α-helices (Fig. 1B and C) [4]. By contrast, Cld from *Nitrobacter winogradskyi* (NwCld) is a dimeric protein and each subunit lacks all helices in the N-terminal domain (Fig. 1A and C) [5]. These significant structural differences prompted us to probe the thermal stability of NdCld and NwCld (Fig. 2A–D) as well as the impact of temperature on the enzymatic activity (Fig. 2E).

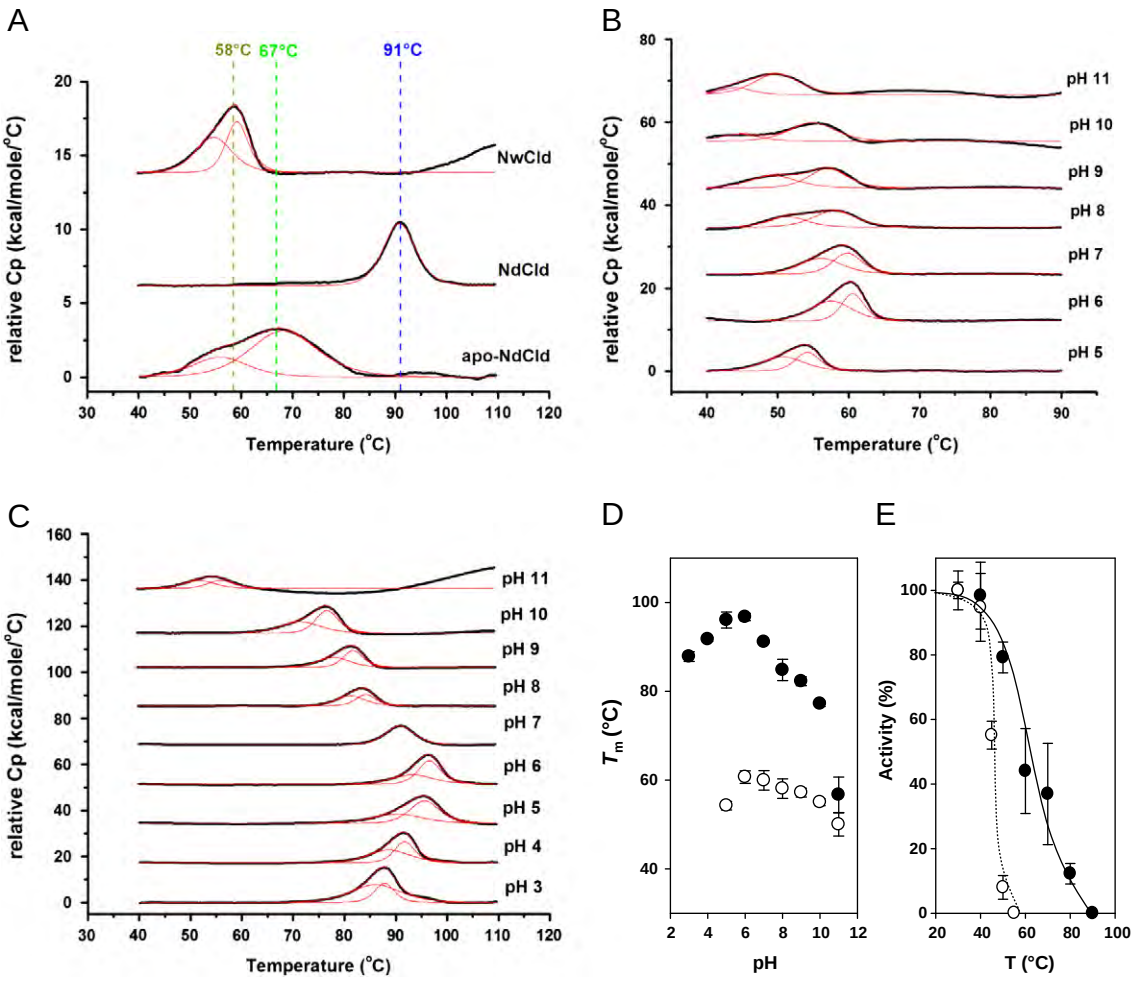

Fig. 2. Thermal stability of chlorite dismutases from *Nitrobacter winogradskyi* (NwCld) and *Candidatus* "Nitrospira defluvii" (NdCld) measured by differential scanning calorimetry. Black line: original data; red line: fit of endotherm to a non-two-state transition model. (A) Normalized thermograms of NwCld, NdCld and apo-NdCld in 50 mM phosphate buffer, pH 7. (B, C) pH-dependence of thermal stability of NwCld (B) and NdCld (C). Protein concentrations: 12.5 μM NwCld, pH 5 (bottom) to pH 11 (top); 14.3 μM NdCld, pH 3 (bottom) to pH 11 (top). (D) Plot of T_m *versus* pH. NwCld, empty circles; NdCld, filled circles. Note that for NwCld only the T_m values corresponding to the second transition are depicted. (E) Impact of temperature on chlorite degradation by chlorite dismutase from NdCld (filled circles) and NwCld (empty circles) measured spectrophotometrically at pH 7.0 as described in Material and methods. (For interpretation of the references to color in this figure legend, the reader is referred to the web version of this article.)

3.1. Enzymatic activity and the impact of temperature

The overall chlorite dismutase activities (polarographic measurement of the initial rate of O_2 release at 25 °C and pH 7.0) of NdCld and NwCld are similar. For NdCld K_M, k_{cat} and k_{cat}/K_M were determined to be 58 ± 9 μM, $35 \pm 5\ s^{-1}$ and $6.0 \times 10^5\ M^{-1}\ s^{-1}$, whereas for NwCld the corresponding values were 90 ± 12 μM, $190 \pm 14\ s^{-1}$ and $2.1 \times 10^6\ M^{-1}\ s^{-1}$, respectively. The pH optima for transformation of chlorite to chloride and dioxygen are 5.5 (NdCld) and 6.0 (NwCld). The similar enzymatic activity is well reflected by the almost identical active site architecture (see overlay of NdCld and NwCld in Fig. 1D).

However, the impact of temperature on the chlorite degradation reaction was significantly different. Since polarographic measurement of oxygen release could not be used at temperatures higher than 45 °C, chlorite degradation was followed photometrically at 260 nm (see Materials and methods). Up to 40 °C and pH 7.0 both heme proteins exhibited an almost unchanged enzymatic activity (Fig. 2E), but with NwCld the degradation rate of chlorite dramatically decreased with only 8% residual activity at 50 °C and complete inactivation at 55 °C. By contrast, chlorite dismutase from *Candidatus* "Nitrospira defluvii" showed still 80% and 36% of activity at 50 °C and 70 °C, respectively, and was completely inhibited at around 90 °C.

3.2. Thermal stability evaluated by differential scanning calorimetry and circular dichroism spectroscopy

In order to understand the impact of temperature on enzymatic inactivation we probed the thermal stability of both enzymes by differential scanning calorimetry (DSC). Fig. 2A compares the thermograms of NwCld, NdCld and heme-free NdCld (apo-NdCld) showing huge differences in the thermal stability of the two selected Clds. The pentameric enzyme exhibited a high thermal stability and the thermogram suggests a cooperative two-state transition at 92 °C (T_m) at pH 7.0. In the absence of the prosthetic group the enzyme was dramatically destabilized and followed a broad non-two-state transition with calculated T_m-values at 56 and 67 °C. In contrast to NdCld melting of the dimeric heme protein (NwCld) already occurred at around 58 °C. The asymmetric endotherm (Fig. 2A) suggested a non-two state transition and by fitting to a corresponding model T_m values were found to be at 53 and 58 °C.

Furthermore we probed the impact of pH of the thermal stability of both enzymes (Fig. 2B–C). With both enzymes the highest T_m values were obtained at pH 6 (97 °C and 61 °C for NdCld and NwCld, respectively). NdCld showed a broad range of stability within pH 3–10 (Fig. 2C and D), whereas NwCld precipitated below pH 5 upon heating and showed broad non-two-state transitions in the alkaline region (pH > 7) (Fig. 2B and D). In Fig. 2D the calculated T_m values are plotted *versus* pH.

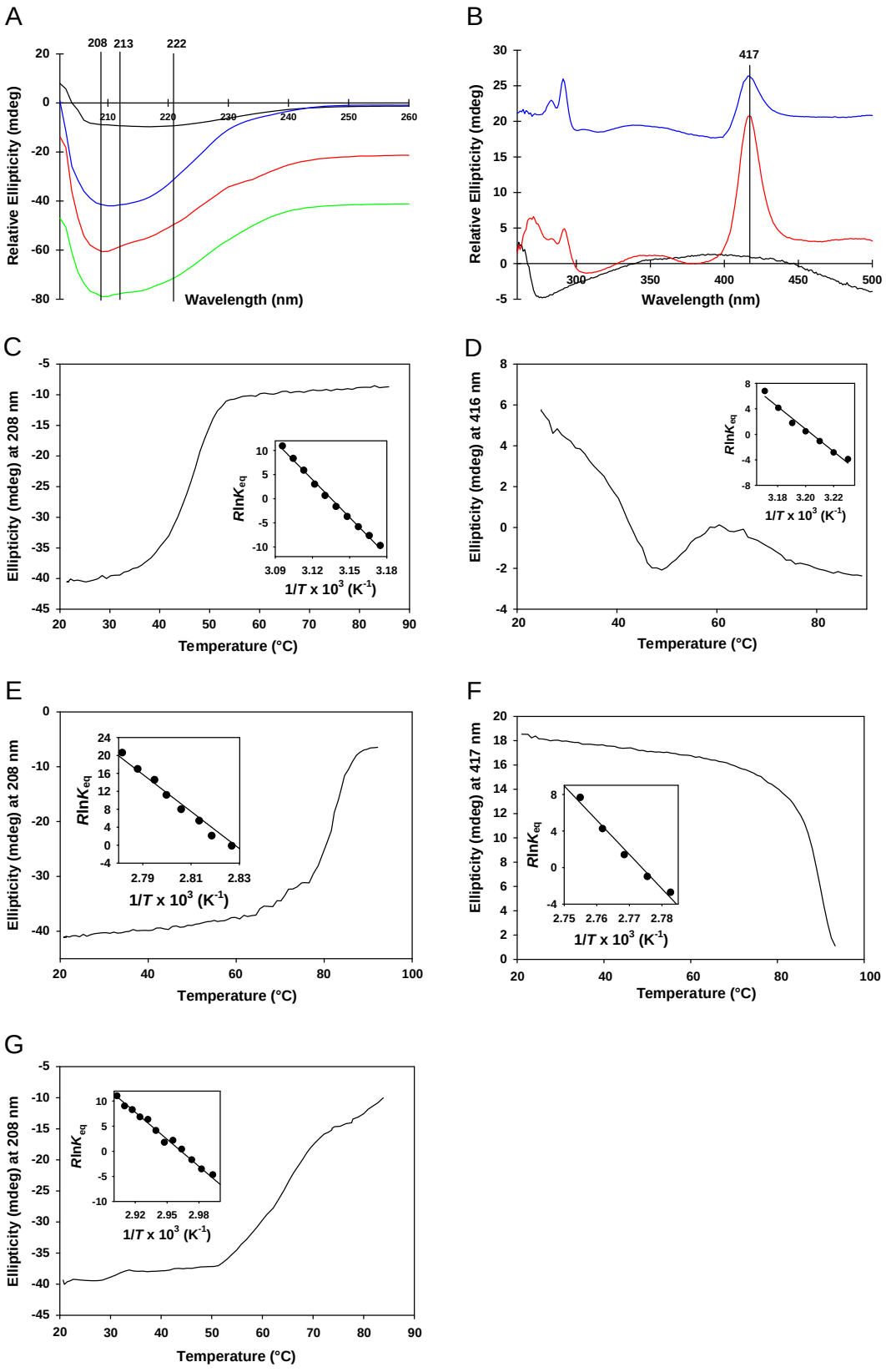

Fig. 3. Temperature-mediated unfolding of chlorite dismutases from *Nitrobacter winogradskyi* (NwCld) and *Candidatus* "Nitrospira defluvii" (NdCld) followed by electronic circular dichroism in the far-UV and visible region. Conditions: 5 mM phosphate buffer, pH 7.0. (A, B) Comparison of far-UV and visible ECD spectra of NdCld (red), apo-NdCld (green) and NwCld (blue) at 25 °C. For clarity spectra have been shifted. In addition the residual activity at 95 °C is shown (black), which is very similar for NwCld and NdCld. (C, D) Thermal unfolding of NwCld followed at 208 nm and 416 nm. (E, F) Thermal unfolding of NdCld followed at 208 nm and 417 nm. (G), Thermal unfolding of apo-NdCld. The insets show the corresponding van't Hoff plots. Note that the van't Hoff plot in (D) represents is calculated from equilibrium constants deriving only from the first transition. (For interpretation of the references to color in this figure legend, the reader is referred to the web version of this article.)

Next we followed thermal unfolding by electronic circular dichroism spectroscopy (ECD). Fig. 3A depicts the ECD spectra in the far-UV region for NdCld, apo-NdCld and NwCld. The spectra reflect the overall structure of chlorite dismutases that are composed of two similar domains with a ferredoxin-like fold (β-sheet flanked by varying content of α-helices). The ellipticity of α-helices typically shows two minima at 208 nm and 222 nm, whereas the contribution of β-sheets gives rise to negative ellipticity around 212–214 nm, but with Δε values that are 5-times smaller than those of α-helices [16]. The dimeric enzyme has been shown to miss all N-terminal α-helices present in NdCld [5] thus having a higher portion of β-strands. This is nicely reflected by the differences in the far-UV ECD spectra (Fig. 3A) of NwCld and NdCld. It is also demonstrated that in the absence of heme *b* the far-UV ECD spectrum was slightly different to that of the holoenzyme (Fig. 3A) suggesting an impact of the prosthetic group on the structural integrity of NdCld.

The near-UV and visible ECD spectra demonstrate a positive ellipticity in the Soret band region at 416 nm (NwCld) and 417 nm (NdCld) as well as differences in the circular dichroism of tyrosine and tryptophan residues. Upon completely unfolding of both proteins at $T = 95$ °C heme ECD signals were completely lost, whereas in the UV-region some residual ellipticity remained (Fig. 3A and B). Finally, based on these findings we followed temperature-mediated unfolding at 208 nm (reflecting melting of secondary structure, mainly α-helices) and 416 or 417 nm (reflecting release of the heme from the active site). The corresponding melting curves are depicted in Fig. 3C–G. In NwCld α-helices melted within 40 and 50 °C (calculated $T_m = 46$ °C) in a simple two-state transition. There was a clear linear relationship between the equilibrium constants and the reciprocal temperature allowing the calculation of the vant'Hoff enthalpy for this transition being (261 ± 7) kJ mol^{-1} (inset to Fig. 3C). The loss of ellipticity at 208 nm was accompanied by the loss of the prosthetic group with ΔH_m being (134 ± 7) kJ mol^{-1} (Fig. 3C and D). A further conformational change must occur between 50 and 60 °C as is evident by the change of ellipticity at 416 °C (Fig. 3D). This reflects the non-two-state transition of NwCld seen in the DSC experiments.

The higher thermostability of the pentameric protein could be confirmed by ECD measurements. In Fig. 3E and F the melting of the secondary structures and the release of the heme group followed a two-state transition and allowed the calculation of the van't Hoff enthalpy [(413 ± 8) kJ mol^{-1} and (372 ± 30) kJ mol^{-1}, respectively]. Furthermore, Fig. 3G support the finding that heme *b* is important in stabilizing the subunit structure of chlorite dismutase. In contrast to the holoform the apoform of Cld had a significantly decreased thermal stability. Loss of ellipticity at 208 nm occurred within a broad temperature range (50–70 °C) (Fig. 3G).

3.3. Conformational stability evaluated by UV–vis and fluorescence spectroscopy

Finally, we evaluated the conformational stability of both chlorite dismutases by chemical denaturation with guanidinium hydrochloride (GdnHCl). Firstly, we focused on the stability of the heme cavity by monitoring the release of the prosthetic group upon chemical denaturation. With increasing GdnHCl concentration the Soret absorbance was diminished (Fig. 4A and D) and the decrease of absorbance at the Soret maximum roughly followed a two-state transition (Fig. 4B and E) allowing the calculation of the conformational stability of the active site (Fig. 4C and F). The conformational stability (ΔG°_{H2O}) of NdCld and NwCld were determined to be $(12.7 \pm 1.7$ kJ mol^{-1}) and (4.3 ± 0.8) kJ mol^{-1}, respectively. This is reflected by calculated c_m values {corresponding to [GdnHCl] were $K = [D]/[N] = 1$} of 3.5 and 1.85 M, respectively. From the slope of the linear curves {$\Delta G^\circ_{[GdnHCl]} = \Delta G^\circ_{H2O} - (m \times [GdnHCl])$} m values were calculated to be 3.7 and

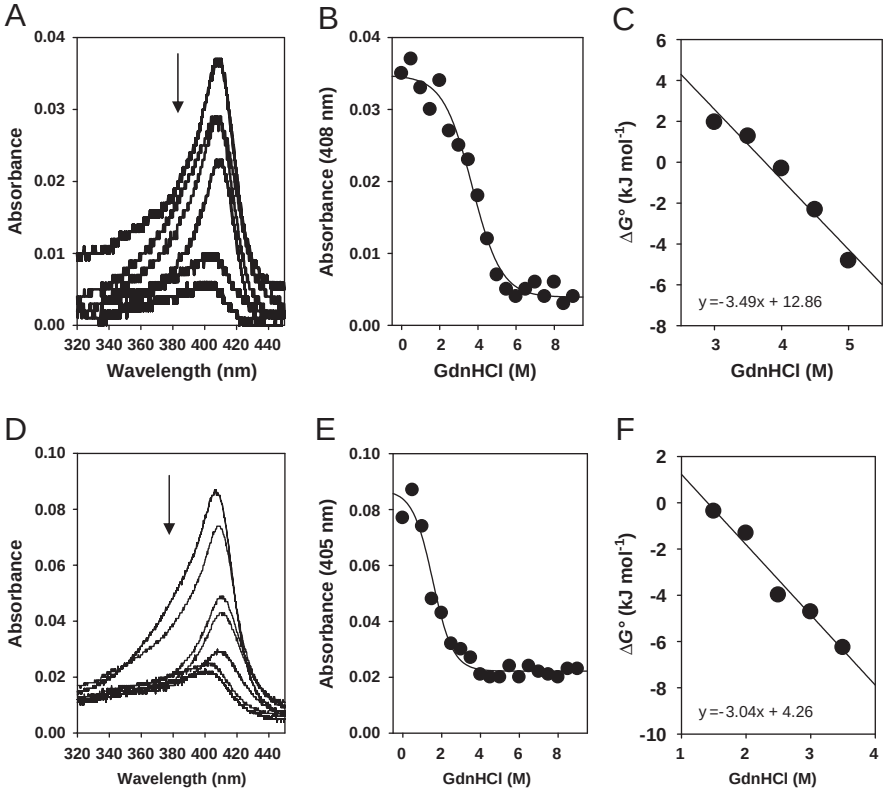

Fig. 4. Chemical denaturation of chlorite dismutases from *Candidatus* "Nitrospira defluvii" (NdCld, A–C) and *Nitrobacter winogradskyi* (NwCld, D–F) followed by UV–vis spectroscopy. NdCld (0.5 μM) and NwCld (0.5 μM) were incubated for 18 h with various concentrations of GdnHCl (5 mM phosphate buffer, pH 7.0). (A, D) Loss of Soret absorbance upon increasing the concentration of guanidinium hydrochloride. (B, E) Plots of change in Soret maximum absorbance *versus* guanidinium hydrochloride concentration. (C, F) Plot of change in free enthalphy at various guanidinium hydrochloride concentrations following the linear equation $\Delta G^\circ_{[GdnHCl]} = \Delta G^\circ_{H2O} - (m \times [GdnHCl])$. Arrows indicate changes in absorbance.

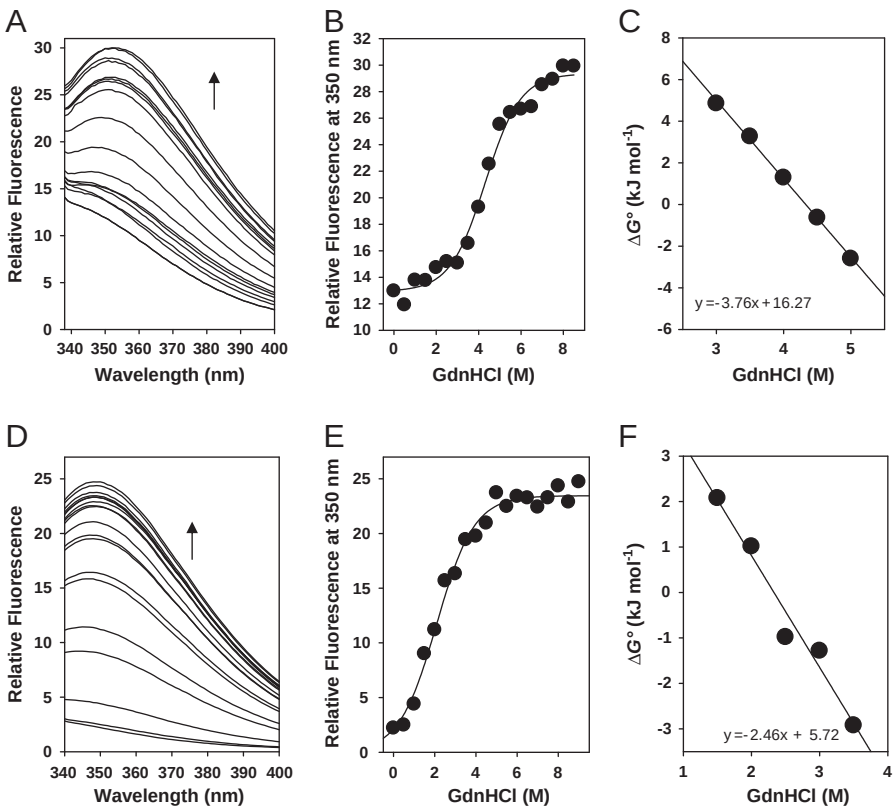

Fig. 5. Chemical denaturation of chlorite dismutases from *Candidatus* "Nitrospira defluvii" (NdCld, A–C) and *Nitrobacter winogradskyi* (NwCld, D–F) followed by fluorescence spectroscopy (excitation at 295 nm) . NdCld (0.5 μM) and NwCld (0.5 μM) were incubated for 18 h with various concentrations of GdnHCl (5 mM phosphate buffer, pH 7.0). (A, D) Change in intrinsic tryptophan emission upon increasing the concentration of guanidinium hydrochloride. (B, E) Plots of change in emission at 350 nm *versus* guanidinium hydrochloride concentration. (C, F) Plot of change in free enthalphy at various guanidinium hydrochloride concentrations following the linear equation $\Delta G^{\circ}_{[GdnHCl]} = \Delta G^{\circ}_{H2O} - (m \times [GdnHCl])$.

1.5 kJ mol^{-1} M^{-1}. The latter reflect the efficacy of the denaturant in unfolding and is proportional to the number of groups in the protein, i.e. large proteins are more sensitive to solvent denaturation than small ones [17].

Secondly, the overall unfolding was followed by monitoring the change in the intrinsic tryptophan fluorescence during unfolding. Fig. 5A and D show the increase of fluorescence intensity and red-shift of emission maxima of NdCld and NwCld mediated by increasing concentrations of GdnHCl. From the secondary plots (Fig. 5B and E) ΔG_{H2O} values of (16.3 ± 0.3) kJ mol^{-1} and (5.3 ± 0.7) kJ mol^{-1} kJ mol^{-1} were calculated (c_m-values: 3.8 and 2.5 M; m = 4.31 and 2.1 kJ mol^{-1} M^{-1}, respectively). These findings unequivocally underline the higher conformational stability of the pentameric enzyme compared to NwCld. The observed differences in the stability of the heme cavity compared with that of the overall protein indicate that the prosthetic group is released before complete unfolding of the protein is accomplished.

4. Discussion

So far chlorite dismutase-like proteins are found in 15 bacterial and archaeal phyla, suggesting ancient roots [4,14]. For several members of the Cld family it has been demonstrated that they are able to convert chlorite to chloride and dioxygen although the physiological relevance of this activity is not fully understood. Other (so far unknown) catalytic properties are possible and likely. Moreover, it has been demonstrated that the family of chlorite dismutases is also structurally related to other ancient and functionally mysterious protein families including dye-decolorizing peroxidases [12].

The pentameric protein from *Candidatus* "Nitrospira defluvii" is a representative of Lineage I of the Cld family that comprises the so-called canonical Clds that all have a very similar subunit structure and oligomerization [2–4]. All members of this subfamily have been shown to be able to degrade chlorite and occur in different subclasses of Proteobacteria but also some nonproteobacterial organisms (e.g. NdCld). Recently, the Cld from *Nitrobacter winigradskyi* was detected and found to belong to another Cld subfamily. Actually, it is the first representative of Lineage II of the chlorite dismutase family with known crystal structure [6] as well as known capacity to degrade chlorite. Sequence alignment has demonstrated that NwCld can be considered as a model for the respective subfamily [6,12].

Both heme enzymes exhibit a comparable activity regarding chlorite decomposition between 20 and 40 °C which is in agreement with the active site architecture of NdCld [4] and NwCld [5] showing the presence of identical and superimposable both proximal and distal residues (Fig. 1D). By contrast, significant differences in conformational and thermal stability of Lineage I and II Clds are evident from the presented findings.

The pentameric enzyme exhibits a very high thermal stability within a broad pH-range. Its unfolding pathway follows a simple two-state transition suggesting a cooperative process. At pH 7.0 unfolding starts around 80 °C and is completed at 95 °C. Subunit melting, release of the prosthetic group as well as separation of the subunits occur simultaneously as demonstrated by DSC and ECD measurements. This was also reflected by the fact that NdCld could degrade chlorite even at 80 °C. A closer inspection of the subunit structure and subunit interaction in NdCld [4] demonstrates that there is a pronounced interface between neighboring subunits (around 1400 Å^2). Since each subunit is in contact with two other molecules (Fig. 1B), the total area buried in the interface is about 23% of the total area of a subunit. Each monomer of NdCl has two topologically equivalent four-stranded antiparallel β-sheets forming a β-barrel (Fig. 1C) flanked on both sides by six α-helices (ferredoxin-like fold). Comparison with other Cld-like enzymes from the same Cld subfamily (PDB: 1TOT, 3DTZ, 1VDH, 2VXH) reveals high structural

conservation thus suggesting comparable stability and unfolding pathway. The interface between two subunits consists mainly of residues from the N-terminal helices α4 and strand β4 that interact with residues in the loop between strands β2 and β3. The compact pentameric structure is dictated by a combination of hydrophobic, ionic and hydrogen-bonding interactions [4] and it is reasonable to assume that unfolding of the individual subunits starts with simultaneous disruption of these close interactions. The heme *b* is buried in the C-terminal domain of a monomer and is embedded within a defined hydrophobic environment *via* many interactions. Among others two prominent examples are the fifth coordinating ligand (i.e. proximal His) which is part of the helix α3' and the heme propionates that form hydrogen bonds to helix α2' and to the β1' strand as well as to the loop between β4 and α1' [4]. This close interaction may explain (i) the simultaneous unfolding of the five subunits and release of the prosthetic groups as well as (ii) the stabilizing effect of the heme *b* group on the stability of chlorite dismutases. The latter was demonstrated by analysis of the apoform of NdCld.

The subunit structure and interaction of Lineage II Clds is completely different and allows explanation of the low thermal stability of the dimeric protein which has a T_m that is more that 35 °C below that of the pentameric protein. Firstly the primary sequence of NwCld is about 30% shorter than that of NdCld, with significant deletion in the N-terminal region (Fig. 1A). In particular, all terminal α-helices are missing, and the central β-barrel no longer consists of two similar four stranded β-sheets but of one three-stranded and one five-stranded β-sheet (Fig. 1A). But most importantly, the interface between the two monomers in NwCld is entirely different since it lacks all N-terminal helices and has longer loops between β-strands that adopt different conformations. In NwCld the dimer interface is formed from the loop between β4 and α1' that interacts with the loop between helix α2' and helix α3' from the other monomer [5]. The surface buried in this interface is 980 $Å^2$ which corresponds to 11.5% of the subunit surface (compared to 23% in NdCld). The interactions in NwCld dimer formation are mainly electrostatic and to a lesser extent hydrophobic compared to NdCld [5] which might explain the stronger impact of pH on its stability. In contrast to NdCld the thermograms of NwCld were asymmetric and could not be fitted by a simple two-state model. These phenomenon was more pronounced with increasing (basic) pH. A non-two-state unfolding pathway was also suggested by ECD measurements that focused on the loss of ellipticity from the heme.

Discrepancies in thermal stability between Lineage I and II Clds were also seen in unfolding experiments mediated by chemical denaturation. The conformational stability of both the overall structure as well as of the heme cavity of pentameric NdCld was calculated to be about 3 times higher than that of NwCld. The dimeric protein has a low conformational stability (5.3 kJ mol^{-1}) and already at a GdnHCl concentration of 1.85 M 50% of the molecules are in the denatured state.

Summing up, this is the first comprehensive biophysical investigation of the impact of temperature and chaotropic agents on the structural integrity of chlorite dismutases. Our observations clearly suggest that—from a biotechnological point of view—pentameric enzymes from Lineage I (e.g. NdCld) are the more interesting candidates for bioremediation, i.e. degradation of chlorite contaminations. Although *Candidatus* "Nitrospira defluvii" is a slow growing bacterium and extremely difficult to culture under laboratory conditions [18] large amount of active NdCld can easily be obtained by expression in *E. coli* as heterologous host [14]. Such recombinant chlorite dismutase from *Candidatus* "Nitrospira defluvii" can be applied between pH 3 and pH 10 and retains its integrity and chlorite degradation activity even at high temperatures up to 70 °C. Thus, NdCld provides an ideal starting scaffold for further stability engineering by both rational mutagenesis or directed evolution strategies.

Acknowledgments

This work was supported by the Austrian Science Foundation (FWF): Doctoral Program BioToP—Biomolecular Technology of Proteins (FWF W1224) and by the Research Focus "Symbiosis research and molecular principles of recognition" of the University of Vienna (project no. FS573001 "Molecular interactions between intracellular bacteria and their eukaryotic cells").

References

[1] A. Ebihara, A. Okamoto, Y. Kousumi, H. Yamamoto, R. Masui, N. Ueyama, S. Yokoyama, S. Kuramitsu, Structure-based functional identification of a novel heme-binding protein from *Thermus thermophilis* HB8, J. Struct. Func. Genom. 6 (2005) 21–32.
[2] D.C. de Geus, E.A.J. Thomassen, P.-L. Hagedoorn, N.S. Pannu, E. van Duijn, J.P. Abrahams, Crystal structure of chlorite dismutase, a detoxifying enzyme producing molecular oxygen, J. Mol. Biol. 387 (2009) 192–206.
[3] B.R. Goblirsch, B.R. Streit, J.L. DuBois, C.M. Wilmot, Structural features promoting dioxygen production by *Dechloromonas aromatica* chlorite dismutase, J. Biol. Inorg. Chem. 15 (2010) 879–888.
[4] J. Kostan, B. Sjoeblom, F. Maixner, G. Mlynek, P.G. Furtmüller, C. Obinger, M. Wagner, H. Daims, K. Djinovic-Carugo, Structural and functional analysis of the chlorite dismutase from the nitrite-oxidizing bacterium "*Candidatus Nitrospira defluvii*": identification of a catalytically important amino acid residue, J. Struct. Biol. 172 (2010) 331–342.
[5] G. Mlynek, B. Sjöblom, J. Kostan, S. Füreder, F. Maixner, K. Gysel, P.G. Furtmüller, C. Obinger, M. Wagner, H. Daims, K. Djinović-Carugo, Unexpected diversity of chlorite dismutases: a catalytically efficient dimeric enzyme from *Nitrobacter winogradskyi*, J. Bacteriol. 193 (2011) 2408–2417.
[6] C.G. van Ginkel, G.B. Rikken, A.G.M. Kroon, S.W.M. Kengen, Purification and characterization of chlorite dismutase: a novel oxygen-generating enzyme, Arch. Microbiol. 166 (1996) 321–326.
[7] P.L. Hagedoorn, D.C. de Geus, W.R. Hagen, Spectroscopic characterization and ligand-binding properties of chlorite dismutase from the chlorate respiring bacterial strain GR-1, Eur. J. Biochem. 269 (2002) 4905–4911.
[8] A.Q. Lee, B.R. Streit, M.J. Zdilla, M.M. Abu-Omar, J.L. DuBois, Mechanism of and exquisite selectivity for O—O bond formation by the heme dependent chlorite dismutase, PNAS 105 (2008) 15654–15659.
[9] B.R. Streit, J.L. DuBois, Chemical and steady-state analysis of a heterologously expressed heme dependent chlorite dismutase, Biochemistry 47 (2008) 5271–5280.
[10] B.R. Streit, B. Blanc, G.S. Lukat-Rodgers, K.R. Rodgers, J.L. DuBois, How active-site protonation state influences the reactivity and ligation of the heme in chlorite dismutase, J. Am. Chem. Soc. 132 (2010) 5711–5724.
[11] J.D. Coates, L.A. Achenbach, Microbial perchlorate reduction: rocket fueled metabolism, Nat. Rev. Microbiol. 2 (2004) 569–580.
[12] B. Goblirsch, R.C. Kurker, B.R. Streit, C.M. Wilmot, J.L. DuBois, Chlorite dismutases, DyPs and EfeB: 3 microbial heme enzyme families comprise the CDE structural superfamily, J. Mol. Biol. 408 (2011) 379–398.
[13] H. Ueno, K. Oishi, Y. Sayato, K. Nakamuro, Oxidative cell damage in Kat-sod assay of oxyhalides as inorganic disinfection by-products and their occurrence by ozonation, Arch. Environ. Contam. Toxicol. 38 (2000) 1–6.
[14] F. Maixner, M. Wagner, S. Lücker, E. Pelletier, S. Schmitz-Esser, K. Hace, E. Spieck, R. Konrat, D. Le Paslier, H. Daims, Environmenteal genomics reveals a functional chlorite dismutase in the nitrite-oxidizing bacterium "*Candidatus Nitrospira defluvii*", Environ. Microbiol. 10 (2008) 3043–3056.
[15] M. Philippi, H.S. dos Santos, A.O. Martins, C.M. Azevedo, M. Pires, Alternative spectrophotometric method for standardization of chlorite aqueous solutions, Anal. Chim. Acta 585 (2007) 361–365.
[16] S.M. Kelly, T.J. Jess, N.C. Price, How to study proteins by circular dichroism, Biochim. Biophys. Acta 1751 (2005) 119–139.
[17] A. Fersht, Structure and Mechanism in Protein Science, W. H Freeman and Company, New York, 1999, pp. 513–516.
[18] E. Spieck, C. Hartwig, I. McCormack, F. Maixner, M. Wagner, A. Lipski, H.E. Daims, Selective enrichment and molecular characterization of a previously uncultured Nitrospira-like bacterium from activated sludge, Environ. Microbiol. 8 (2006) 405–415.

Chapter 4

Redox thermodynamics of high-Spin and low-Spin forms of chlorite dismutases with diverse subunit and oligomeric structures

Stefan Hofbauer, Marzia Bellei, Axel Sündermann, Katharina F. Pirker, Andreas Hagmüller, Georg Mlynek, Julius Kostan, Holger Daims, Paul G. Furtmüller, Kristina Djinovic-Carugo, Chris Oostenbrink, Gianantonio Battistuzzi, Christian Obinger

Research Article

Biochemistry (2012), 51, 1031-1038

BIOCHEMISTRY
including biophysical chemistry & molecular biology

Article

pubs.acs.org/biochemistry

Redox Thermodynamics of High-Spin and Low-Spin Forms of Chlorite Dismutases with Diverse Subunit and Oligomeric Structures

Stefan Hofbauer,[†] Marzia Bellei,[‡] Axel Sündermann,[§] Katharina F. Pirker,[∥] Andreas Hagmüller,[⊥] Georg Mlynek,[⊥] Julius Kostan,[⊥] Holger Daims,[@] Paul G. Furtmüller,[†] Kristina Djinović-Carugo,[⊥,#] Chris Oostenbrink,[§] Gianantonio Battistuzzi,[▽] and Christian Obinger*[,†]

[†]Department of Chemistry, Division of Biochemistry, VIBT-Vienna Institute of BioTechnology, BOKU-University of Natural Resources and Life Sciences, A-1190 Vienna, Austria

[‡]Department of Life Sciences, University of Modena and Reggio Emilia, 41100 Modena, Italy

[§]Department of Material Sciences and Process Engineering, Institute of Molecular Modeling and Simulation, VIBT-Vienna Institute of BioTechnology, BOKU-University of Natural Resources and Life Sciences, A-1190 Vienna, Austria

[∥]Health and Environment Department, Environmental Resources and Technologies, AIT-Austrian Institute of Technology GmbH, A-3430 Tulln, Austria

[⊥]Department for Structural and Computational Biology, Max F. Perutz Laboratories, University of Vienna, Campus Biocenter 5, A-1030 Vienna, Austria

[@]Department of Microbial Ecology, University of Vienna, A-1090 Vienna, Austria

[#]Department of Biochemistry, Faculty of Chemistry and Chemical Technology, University of Ljubljana, Aškerčeva 5, 1000 Ljubljana, Slovenia

[▽]Department of Chemistry and Geology, University of Modena and Reggio Emilia, 41100 Modena, Italy

Supporting Information

ABSTRACT: Chlorite dismutases (Clds) are heme *b*-containing oxidoreductases that convert chlorite to chloride and dioxygen. In this work, the thermodynamics of the one-electron reduction of the ferric high-spin forms and of the six-coordinate low-spin cyanide adducts of the enzymes from *Nitrobacter winogradskyi* (NwCld) and *Candidatus* "Nitrospira defluvii" (NdCld) were determined through spectroelectrochemical experiments. These proteins belong to two phylogenetically separated lineages that differ in subunit (21.5 and 26 kDa, respectively) and oligomeric (dimeric and pentameric, respectively) structure but exhibit similar chlorite degradation activity. The $E^{\circ\prime}$ values for free and cyanide-bound proteins were determined to be −119 and −397 mV for NwCld and −113 and −404 mV for NdCld, respectively (pH 7.0, 25 °C). Variable-temperature spectroelectrochemical experiments revealed that the oxidized state of both proteins is enthalpically stabilized. Molecular dynamics simulations suggest that changes in the protein structure are negligible, whereas solvent reorganization is mainly responsible for the increase in entropy during the redox reaction. Obtained data are discussed with respect to the known structures of the two Clds and the proposed reaction mechanism.

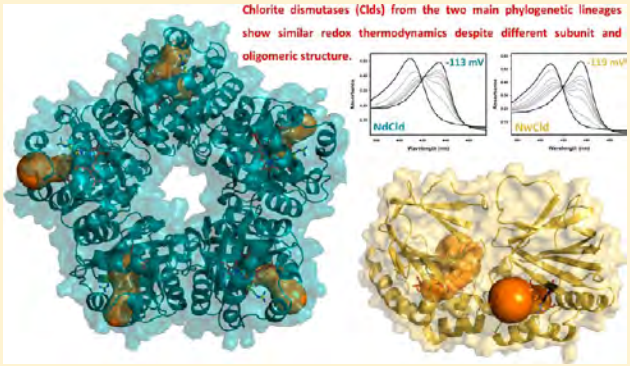

Heme proteins conduct a myriad of diverse biological functions such as O_2 transport, storage and reduction, electron transport, oxidation and oxygenation of manifold organic and inorganic compounds, hydrogen peroxide dismutation, O_2, NO, and CO sensing, etc.[1] The distinct reactivity of these oxidoreductases is determined by (i) the architecture of the active site and the substrate access channel(s), (ii) the conformation and modification of the prosthetic group, (iii) the nature of the proximal ligand of the heme iron and its mode of interaction with outer sphere ligands, (iv) the interaction of the two heme propionates with the protein, and (v) the nature and position of amino acids as well as the amount of space at the distal heme site where substrate binding and conversion take place.[1] All these factors determine the redox chemistry of the respective metalloproteins and as a consequence their (bioinorganic) reaction mechanism.[1]

Chlorite dismutases (Clds) are recently described heme *b* oxidoreductases (EC 1.13.11.49) found in prokaryotic organ-

Received: September 25, 2012
Revised: November 2, 2012
Published: November 5, 2012

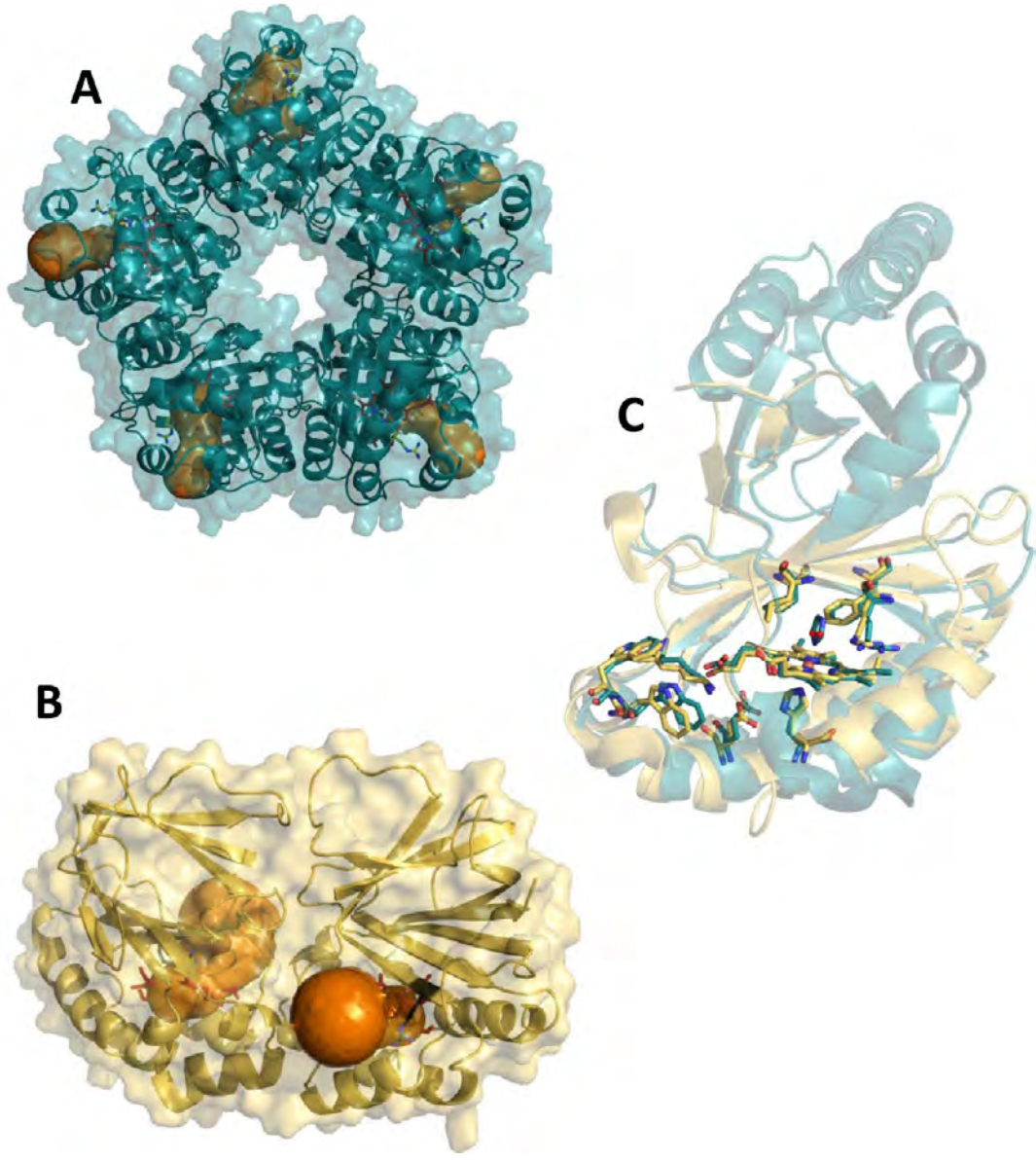

Figure 1. Overall and active site structures of chlorite dismutases from *Candidatus* "Nitrospira defluvii" (NdCld) and *N. winogradskyi* (NwCld). (A) Ribbon representation of pentameric NdCld (PDB entry 3NN1) after a 2 ns molecular dynamics (MD) simulation showing the secondary structure and semitransparent protein surface (cyan). Each subunit shows a heme *b* (red) as well as the catalytically important Arg173 of the distal heme side (yellow). Substrate channels leading to heme *b*, determined with CAVER, are colored orange. (B) Ribbon representation of dimeric NwCld (PDB entry 3QPI) after a 2 ns MD simulation showing the secondary structure and semitransparent protein surface (yellow), heme *b* (red), distal Arg127 (black), and substrate channels (orange). (C) Overlay of ribbon representations of the X-ray structures of NwCld (yellow) and NdCld (cyan). Heme cavity residues are shown as sticks. Figures were generated using PyMOL (http://www.pymol.org/).

isms. The given denomination "dismutase" is misleading because Cld converts chlorite (ClO_2^-) to chloride and dioxygen. In recent years, several X-ray structures of multimeric (di, penta, and hexa) Clds and Cld-like proteins from archaea and bacteria have been published.[2−6] Together with mechanistic studies,[7−12] these structures helped to postulate an enzymatic mechanism that includes oxidation of native ferric Cld by chlorite to an oxoiron(IV)porphyryl radical intermediate [$Por^{\bullet+}Fe(IV)=O$, Compound I] and hypochlorite, which is kept in the reaction sphere of active Clds by a fully conserved distal arginine (reaction 1).

$$PorFe(III) + [O-Cl-O]^- \rightarrow Por^{\bullet+}Fe(IV)=O\cdots[O-Cl]^- \quad (1)$$

The second redox half-reaction (reaction 2) is unique because it generates an O−O bond, a reaction found so far in biology mediated only by the water splitting manganese complex of photosystem II of oxygenic phototrophic organisms and by a yet-uncharacterized enzyme of an anaerobic methane-oxidizing bacterium.[13]

$$Por^{\bullet+}Fe(IV)=O\cdots[O-Cl]^- \rightarrow PorFe(III) + O=O + Cl^- \quad (2)$$

Reaction 1 resembles the heterolytic cleavage of hydrogen peroxide forming Compound I and water that occurs in heme peroxidases and catalases (Reaction 3).[14]

dx.doi.org/10.1021/bi3013033 | *Biochemistry* 2012, 51, 9501−9512

$$\text{PorFe(III)} + \text{H–O–O–H} \rightarrow \text{Por}^{\bullet+}\text{Fe(IV)=O} + \text{H–O–H} \quad (3)$$

Reaction 2 shows similarities with the action of some peroxidases (e.g., mammalian myeloperoxidase) that can oxidize chloride to hypochlorous acid using chloride as a two-electron donor of Compound I and releasing hypochlorite as the reaction product (Reaction 4).[15,16]

$$\text{Por}^{\bullet+}\text{Fe(IV)=O} + \text{Cl}^- \rightarrow \text{PorFe(III)} + [\text{O–Cl}]^- \quad (4)$$

Understanding differences in reaction mechanisms between related heme enzymes and the driving forces of individual redox reactions requires, besides knowledge of the structure and the catalytic amino acids in the heme cavity, information about the redox thermodynamics of the respective heme centers.[17] The reduction potential ($E^{\circ\prime}$) of the Fe(III)/Fe(II) couple not only determines the stable oxidation state of the heme proteins in their native state (i.e., the ferric state for Cld) but also reflects the hierarchy of redox properties of higher oxidation states (e.g., of the Compound I/ferric protein couple), which was demonstrated for many heme peroxidases.[17] Moreover, valuable information about the mechanism of $E^{\circ\prime}$ modulation in heme proteins can be obtained from the enthalpic ($\Delta H^{\circ\prime}_{rc}$) and entropic ($\Delta S^{\circ\prime}_{rc}$) changes of the reduction reaction, measured through variable-temperature spectroelectrochemical measurements.[17] It must be mentioned that single $E^{\circ\prime}$ values of the Fe(III)/Fe(II) couple of three Clds determined by different methods can be found in the literature (Cld from *Dechloromonas aromatica*, −23 mV;[12] Cld from *Ideonella dechloratans*, −21 mV;[18] and Cld from *Azospira oryzae*, −158 mV[3]), which differ significantly (as do the UV–vis spectra in comparison to those of NdCld and NwCld)[5,6,12,18,19] despite very similar structures of the respective heme cavities.[2−6]

This paper reports for the first time the thermodynamics of Fe(III)/Fe(II) reduction of chlorite dismutases determined spectroelectrochemically by using an OTTLE cell.[17] This allows direct comparison with related heme oxidoreductases that have been investigated by the same method. Two representatives of two phylogenetically separated lineages, namely, pentameric Cld from *Candidatus* "Nitrospira defluvii" [NdCld (Figure 1A)][5] and dimeric Cld from *Nitrobacter winogradskyi* [NwCld (Figure 1B)],[6] have been analyzed. Besides differences in oligomeric architecture, the two Clds exhibit differences in subunit structure (Figure 1C)[6] as well as in conformational and thermal stability.[19] Despite these significant disparities in overall structure and stability, the heme ligation and environment in NdCld and NwCld are almost identical to those of other published structures (Figure 1C)[2−4] of this protein family.[20,21] Moreover, NdCld and NwCld exhibit similar chlorite degradation kinetics.[5,6,19]

Here we report on (i) the $E^{\circ\prime}$ values of the Fe(III)/Fe(II) couple in the ferric high-spin native forms and of the six-coordinate low-spin cyanide adducts of NdCld and NwCld, (ii) the enthalpic and entropic contribution to the reduction reaction of the high-spin forms, (iii) the calculation of the contribution of the protein and the solvent to the reduction process, and (iv) the simulation of the molecular dynamics of the ferrous and ferric forms of NwCld and NdCld. Additionally, we have compared the substrate access channel dimensions and probed the kinetics of cyanide binding and dissociation by stopped-flow spectroscopy. The findings are discussed with respect to the known structures of NdCld[5] and NwCld[6] and the proposed reaction mechanism of Cld (reactions 1 and 2) in comparison with those of related heme enzymes.

MATERIALS AND METHODS

Cloning, expression, and purification of wild-type NdCld and NwCld were described previously.[5,6,19] All chemicals were reagent grade.

Spectroelectrochemistry. All experiments were conducted in a homemade OTTLE (optical transparent thin-layer spectroelectrochemical) cell.[22] The three-electrode configuration consisted of a gold minigrid working electrode (Buckbee-Mears, Chicago, IL), a homemade Ag/AgCl/KCl_{sat} microreference electrode, separated from the working solution by a Vycor set, and a platinum wire as the counter electrode.[22] The reference electrode was calibrated against a saturated calomel (HgCl) electrode before each set of measurements. All potentials are referenced to the SHE (standard hydrogen electrode, 242 mV).

Potentials were applied across the OTTLE cell with an Amel model 2053 potentiostat/galvanostat. A constant temperature was maintained by a circulating water bath, and the OTTLE cell temperature was monitored with a Cu-costan microthermocouple. UV–vis spectra were recorded using a Varian Cary C50 spectrophotometer. The OTTLE cell was flushed with argon gas to establish an oxygen-free environment in the cell.[22]

Variable-temperature experiments were performed using a nonisothermal cell configuration.[22] The temperature of the reference electrode and the counter electrode was kept constant, whereas that of the working electrode was varied.[22] Parametrization of enthalpic and entropic components was possible via calculation of $\Delta S'^{\circ}_{rc}$ from the slope of the plot of E'° versus temperature; $\Delta H^{\circ\prime}_{rc}$ could be obtained from the Gibbs–Helmholtz equation, thus from the slope of the plot $E^{\circ\prime}/T$ versus $1/T$.[22] Experiments with NwCld and NdCld were conducted over a temperature range from 15 to 35 °C using 650 μL samples containing 6 μM NdCld and 5 μM NwCld in 150 mM phosphate buffer (pH 7.0) and 100 mM NaCl, in the presence of various mediators: methyl viologen, lumiflavine 3-acetate, methylene blue, phenazine methosulfate, and indigo. The concentration of each mediator in the cell was 4.6 μM, except for that of methyl viologen (230 μM). Nernst plots consisted of at least five points and were invariably linear with a slope consistent with a one-electron reduction process.

The experiments for the determination of the $E^{\circ\prime}$ of the cyanide adducts of NdCld and NwCld were conducted at 25 °C using 650 μL samples containing 3 μM NdCld and 4 μM NwCld in 150 mM phosphate buffer (pH 7.0) with 100 mM NaCl and 50 mM cyanide, in the presence of the same mediator set as described above.

EPR Spectroscopy. For electron paramagnetic resonance (EPR) measurements, 200 μM NdCld and 240 μM wild-type NwCld were prepared in 50 mM phosphate buffer (pH 7.0). Solutions (100 μL) were transferred in Wilmad quartz tubes (3 mm inside diameter) under an inert nitrogen atmosphere in a glovebox.

Measurements were taken at 10 K on a Bruker EMXplus continuous wave (cw) spectrometer, operating at X-band (9 GHz) frequencies, equipped with a 4122SHQE resonator and an Oxford Instruments ESR900 cryostat. EPR spectra were recorded under nonsaturating conditions using a 0.2 mW microwave power, a 100 kHz modulation frequency, a 1 mT modulation amplitude, and a 21 ms conversion time and time constant. Saturation studies confirmed the presence of the

individual Fe(III) species. Simulations of high-spin and low-spin Fe(III) forms were conducted using EasySpin.[23]

Transient-State Kinetics. The experiments were conducted with a stopped-flow apparatus (model SX-18MV, Applied Photophysics) equipped for both conventional and sequential measurements. The optical quartz cell with a path length of 10 mm had a volume of 20 μL. The fastest time for mixing two solutions and recording the first data point was 1.3 ms. All measurements were performed at 25 °C. For the cyanide binding studies with ferric NwCld, the conventional stopped-flow mode was used and the increase in absorbance at 420 nm was monitored. In a typical experiment, one syringe contained 2 μM NwCld in 50 mM phosphate buffer (pH 7.0) and the second syringe contained an at least 5-fold excess of cyanide in the same buffer. A minimum of three measurements were performed for each ligand concentration. The apparent second-order rate constants, k_{on}, were obtained from the slope of a plot of k_{obs} versus cyanide concentration. Additionally, the binding of cyanide to NwCld was also investigated using the diode array detector (Applied Photophysics), which allowed the synthesis of artificial sets of time-dependent spectra as well as spectral analysis of enzyme intermediates.

Molecular Dynamics Simulations. Molecular dynamics simulations of NwCld (PDB entry 3QPI) and NdCld (PDB entry 3NN1) with a reduced and oxidized heme *b* were performed using the GROMOS11 molecular simulation package[24] and GROMOS force field 54A7.[25] The proteins were solvated in periodic rectangular simulation boxes containing the simple point charge water model[26] with a minimal solute−wall distance of 0.8 nm. Chloride and sodium counterions were added to create an overall neutral system at pH 7. The systems were gradually heated to 300 K with 60 K increases in temperature every 20 ps and equilibrated at a constant pressure for 100 ps.

Simulations were subsequently performed for 2 ns, using a step size of 2 fs. Coordinates were written out every 0.5 ps. The temperature and pressure were kept constant at 300 K and 1 atm, respectively. This was achieved through weak coupling with a relaxation time of 0.1 ps for the temperature and 0.5 ps for the pressure.[27] The isothermal compressibility was set to 4.575×10^{-4} (kJ mol^{-1} nm^{-3})$^{-1}$. Bond lengths were constrained to their optimal values with a relative geometric accuracy of 10^{-4} using the SHAKE algorithm.[28] The nonbonded interactions were calculated using a twin-range cutoff,[29] and a molecular pairlist, with a short-range cutoff of 0.8 nm and a long-range cutoff of 1.4 nm. A reaction-field contribution[30] was added to the electrostatic interactions and forces to account for a homogeneous medium outside the cutoff using a dielectric permittivity of 61.[31]

To analyze the amount and behavior of the water molecules in the binding pocket and substrate channels, the radial distribution function was calculated using GROMOS++ package for the analysis of biomolecular simulation trajectories.[32] The radial distribution function is defined here as the probability of finding a particle at a given distance relative to the same probability for a homogeneous distribution of the particles.

Substrate Channel Calculation. CAVER[33] was used to detect tunnels and therefore putative substrate channels of NwCld and NdCld (PDB entries 3QPI and 3NN1, respectively). For calculation of the length of the channels, the heme iron was set as the starting point.

RESULTS

Despite significant differences in oligomeric and subunit structure and stability,[5,6,19] the overall chlorite dismutase activities of NdCld and NwCld (polarographic measurement of the initial rate of O_2 release at 25 °C and pH 7.0) are similar. For NdCld, K_M, k_{cat}, and k_{cat}/K_M were determined to be 58 μM, 35 s^{-1}, and 6.0×10^5 M^{-1} s^{-1}, respectively, whereas for NwCld, the corresponding values were 90 μM, 190 s^{-1}, and 2.1×10^6 M^{-1} s^{-1}, respectively (Table 1).

Table 1. (A) Steady-State Kinetic Parameters for Chlorite Degradation Measured Polarographically as Dioxygen Evolution Mediated by NdCld[5] and NwCld[6] and (B) Pre-Steady-State Kinetic Parameters for the Binding of Cyanide to NdCld[5] and NwCld (this study)

	NdCld	NwCld
	(A)	
K_M (μM)	58 ± 9	90 ± 12
k_{cat} (s^{-1})	35 ± 5	190 ± 14
k_{cat}/K_M (M^{-1} s^{-1})	6.0×10^5	2.1×10^6
	(B)	
k_{on} (M^{-1} s^{-1})	2.6×10^6	1.0×10^6
k_{off} (s^{-1})	9.3	2.4
K_D (μM)	3.6	2.4

The spectroscopic properties of ferric wild-type NdCld and NwCld are indicative of predominant five-coordinate high-spin heme *b*. In detail, recombinant ferric high-spin NdCld ($S = {}^5/_2$) has its Soret maximum at 408 nm, a prominent Q-band at 533 nm (shoulder at 568 nm), and a charge-transfer (CT) band at 640 nm (Figure 2A). The corresponding maxima for recombinant ferric NwCld are at 405, 506, 543, and 640 nm, respectively (Figure 2A). It is important to note that so far published spectra of the ferric form of Clds from other sources show a rather broad Soret band at extraordinary peak maxima around 392 nm,[10,11,18] which is 12−15 nm blue-shifted compared to those of NdCld and NwCld (despite the high degree of similarity in heme cavity architecture).

The cw EPR spectrum of NdCld shows the presence of two rhombically distorted high-spin forms (Figure 2B), arising from the transition of $m_s = \pm{}^1/_2$ of an $S = {}^5/_2$ system. The rhombicity (determined by the zero-field interaction parameters *D* and *E*) of the two high-spin spectra differs slightly, leading to one broader and one narrower signal in the low-field part of the EPR spectrum (Table 1 of the Supporting Information). Additionally, spectral simulation (Table 1 of the Supporting Information) suggests the occurrence of two low-spin heme species. Comparable high-spin spectra were described previously for chlorite dismutases from other sources.[3,8,18] In contrast, the cw EPR spectrum of dimeric NwCld consists of only one dominant high-spin species with axial symmetry in addition to one minor low-spin Fe(III) form (Figure 2B). This indicates a higher symmetry around the heme cavity and two comparable coordination structures in the two subunits, whereas the different EPR spectra in the homopentamer NdCld lead to the assumption that the structural environment of the heme pocket within the subunits of the pentamer varies by distortion in the *x*−*y* plane.

Figure 3A depicts a representative family of spectra of ferric NdCld at different applied potentials in the OTTLE cell. The pentameric metalloprotein is directly reduced to its ferrous form with absorption maxima at 435 and 556 nm with a clear

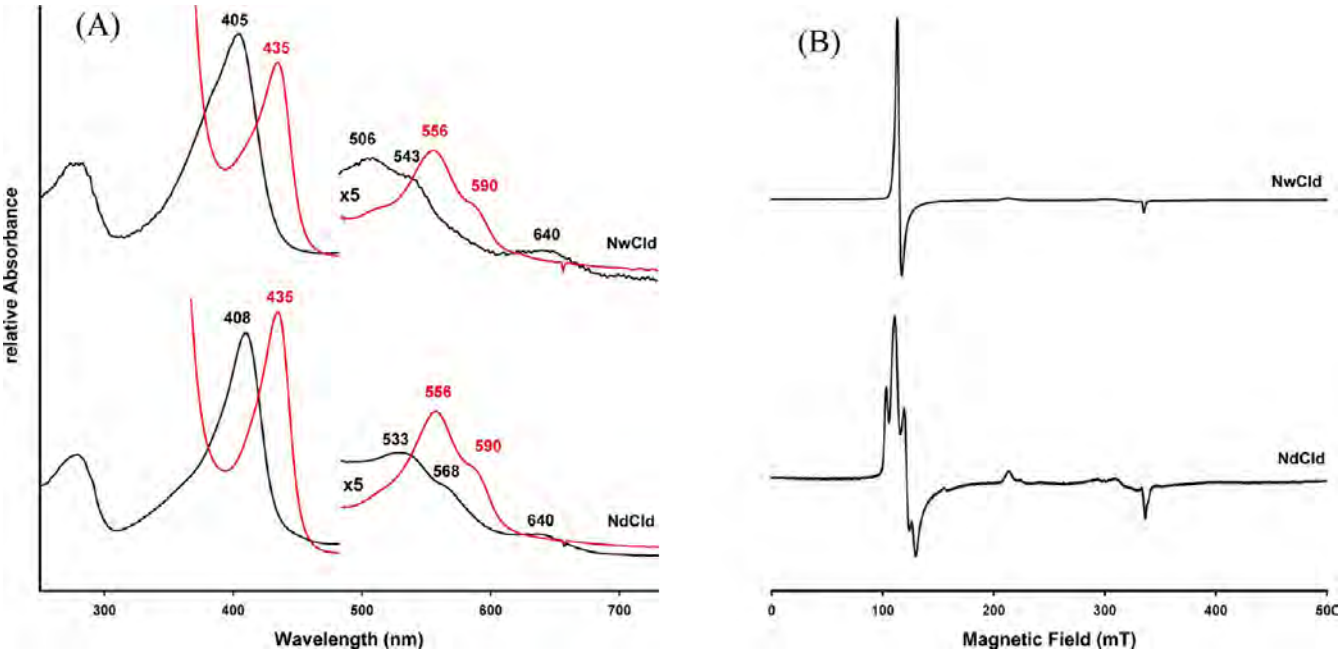

Figure 2. UV−vis and continuous wave electron paramagnetic resonance spectra of chlorite dismutases from *Candidatus* "Nitrospira defluvii" (NdCld) and *N. winogradskyi* (NwCld). (A) UV−vis spectra of NwCld and NdCld at pH 7.0. Spectra of the oxidized and reduced proteins are colored black and red, respectively. Enzymes were reduced with 10 mM sodium dithionite from a freshly prepared solution. (B) Continuous wave EPR spectra of NdCld and NwCld at pH 7.0 and 10 K.

isosbestic point at 420 nm. The calculated midpoint potential for the Fe(III)/Fe(II) couple, determined from the corresponding Nernst plot (inset of Figure 3A), was calculated to be −0.113 ± 0.001 V at 25 °C and pH 7.0. Similar experiments were performed with the dimeric chlorite dismutase from *N. winogradskyi*. Upon its direct conversion from Fe(III) to Fe(II), the identical ferrous spectrum was obtained (maxima at 435 and 556 nm, isosbestic point at 420 nm) and the standard reduction potential was very similar; i.e., $E^{\circ\prime}$ = −0.119 ± 0.002 V (25 °C, pH 7.0) (Figure 3B and Table 2).

To gain deeper insight into the mechanism of $E^{\circ\prime}$ modulation in chlorite dismutases from *Candidatus* "Nitrospira defluvii" and *N. winogradskyi*, the temperature dependence of the reduction potential of the high-spin forms was investigated (Figure 4). This allows parameterization of the corresponding enthalpic ($\Delta H^{\circ\prime}_{rc}$) and entropic ($\Delta S^{\circ\prime}_{rc}$) components of the Fe(III) to Fe(II) reduction reaction. For both metalloproteins, the oxidized state is enthalpically stabilized over the reduced state: NwCld (40 ± 4 kJ mol^{-1}) > NdCld (29 ± 6 kJ mol^{-1}) (Figure 4B and Table 3). Reduction of both species is entropically favored. The entropic components are positive for both chlorite dismutases: NwCld (95 ± 13 J mol^{-1} K^{-1}) > NdCld (63 ± 20 J mol^{-1} K^{-1}) (Figure 4A and Table 3). As a consequence, the resulting entropic contributions to $E^{\circ\prime}$ at 25 °C, i.e., 292 and 194 mV, respectively, partially compensate for the enthalpic stabilization of the ferric state, i.e., −413 and −305 mV, respectively (Table 3).

Upon addition of cyanide, both heme enzymes were converted to their low-spin complexes ($S = {}^1/_2$) exhibiting a red-shifted Soret maximum at 422 nm (isosbestic point at 413 nm) (Figure 5A). Ligand binding followed by stopped-flow spectroscopy at 420 nm was monophasic, and k_{obs} values could be obtained from single-exponential fits (Figure 5B). The apparent second-order rate constant for cyanide binding (k_{on}) was calculated from the slope of the linear plot of k_{obs} versus cyanide concentration (Figure 5C). The apparent dissociation rate constant, k_{off}, was determined from the intercept of the linear plots, allowing the calculation of the dissociation constant (K_D) of the cyanide complexes from k_{off}/k_{on} ratios. Both Clds exhibited similar kinetics and thermodynamics of cyanide binding with the following values: k_{on} = 2.57 × 10^6 M^{-1} s^{-1}, k_{off} = 9.3 s^{-1}, and K_D = 3.6 μM for NdCld,[4] and k_{on} = 1.0 × 10^6 M^{-1} s^{-1}, k_{off} = 2.4 s^{-1}, and K_D = 2.4 μM for NwCld (Table 1). These data clearly underline the fact that both access to and binding at the heme cavity of cyanide are very similar.

Next, we probed the effect of binding of the low-spin ligand cyanide on the redox properties of the Fe(III)/Fe(II) couple, performing redox titrations of cyanide complexes of both enzymes at different applied potentials (Figure 3C,D). The ferric cyanide complexes were directly reduced to the corresponding ferrous cyanide adducts (Soret band at 435 nm) with an isosbestic point at 430 nm. The calculated midpoint potentials determined from the corresponding Nernst plots are almost identical with values of −0.404 ± 0.005 V for NdCld and −0.397 ± 0.002 V for NwCld (25 °C, pH 7.0). The $E^{\circ\prime}$ values are similar to those of the six-coordinate low-spin cyanide adducts of other heme proteins (Table 2). However, the differences between the $E^{\circ\prime}$ values of high- and low-spin forms are sensibly higher in Clds (Table 2).

Because both the protein and the solvent contribute to enthalpic and entropic changes during the reduction of ferric Cld, it is important for the interpretation of data to know (i) the solvent accessibility of the heme center in the ferric and ferrous states and (ii) the extent of solvent reorganization and of conformational change of the protein during Fe(III) reduction. Thus, by using CAVER, we have identified and measured the dimensions of the substrate channels for each subunit of both proteins. Panels A and B of Figure 1 illustrate the substrate channels and their orientation within the oligomeric structures. Figure 1A shows that substrate channels

dx.doi.org/10.1021/bi3013033 | *Biochemistry* 2012, 51, 9501−9512

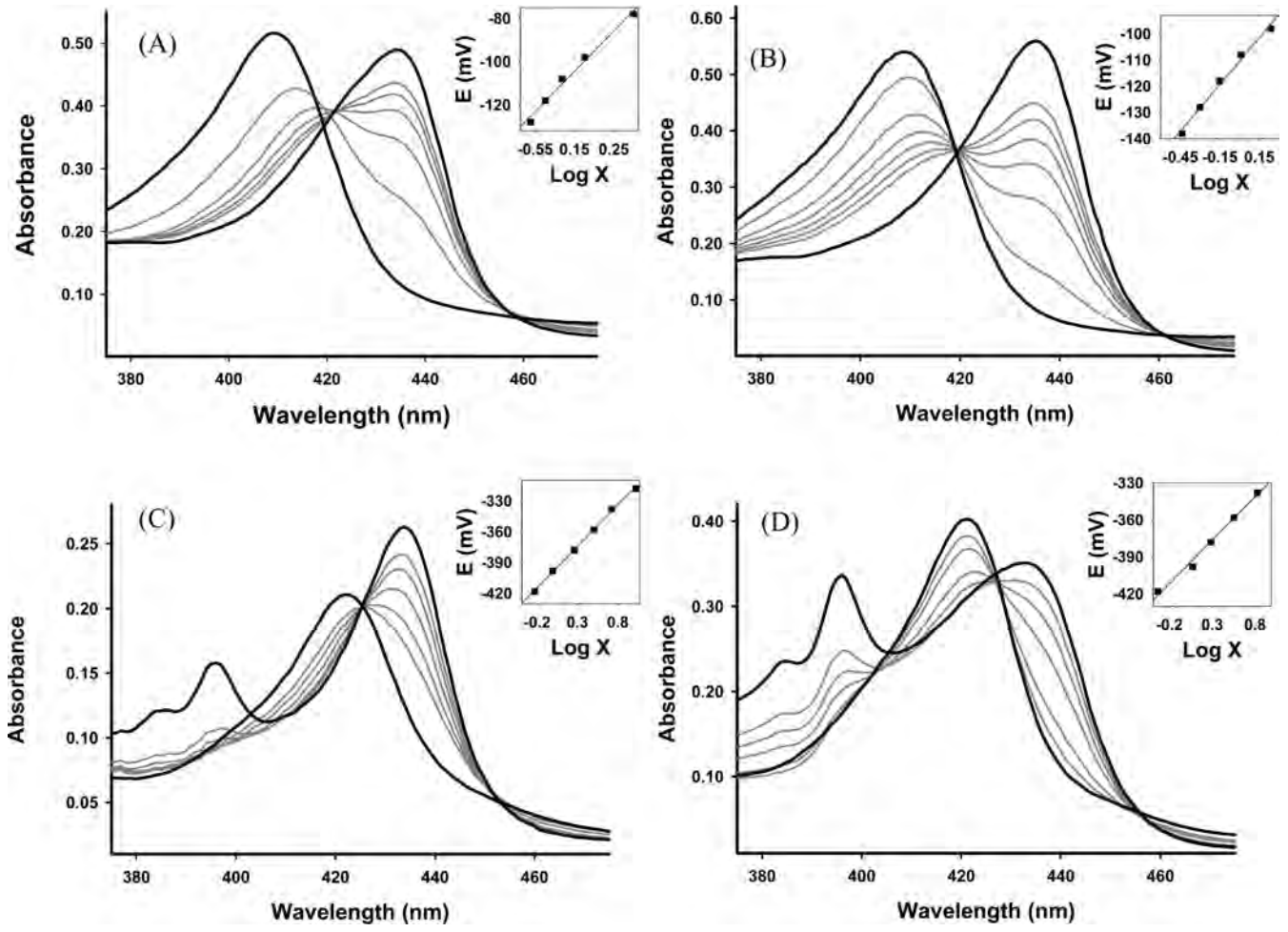

Figure 3. Spectroelectrochemical titrations of the Fe(III)/Fe(II) redox couple of the high-spin native form of chlorite dismutases from *Candidatus* "Nitrospira defluvii" (NdCld) and *N. winogradskyi* (NwCld) and their six-coordinate low-spin cyanide adducts. (A) Electronic spectra of high-spin native NdCld at various potentials at 25 °C in 150 mM phosphate buffer (pH 7.0) and 100 mM NaCl. (B) Electronic spectra of high-spin native NwCld at various potentials at 25 °C in 150 mM phosphate buffer (pH 7.0) and 100 mM NaCl. (C) Electronic spectra of the six-coordinate low-spin cyanide adduct (50 mM cyanide) of NdCld at various potentials at 25 °C in 150 mM phosphate buffer (pH 7.0) and 100 mM NaCl. (D) Electronic spectra of the six-coordinate low-spin cyanide adduct (50 mM cyanide) of NwCld at various potentials at 25 °C in 150 mM phosphate buffer (pH 7.0) and 100 mM NaCl. The insets depict the corresponding Nernst plots, where X represents $(A_{\lambda_{red}}{}^{Max} - A_{\lambda_{red}})/(A_{\lambda_{ox}}{}^{Max} - A_{\lambda_{ox}})$, where λ_{ox} = 409 nm and λ_{red} = 435 nm for high-spin NdCld, λ_{ox} = 422 nm and λ_{red} = 435 nm for the six-coordinate low-spin cyanide adduct of low-spin NdCld, λ_{ox} = 407 nm and λ_{red} = 435 nm for high-spin NwCld, and λ_{ox} = 422 nm and λ_{red} = 435 nm for the six-coordinate low-spin cyanide adduct of NwCld.

in the NdCld homopentamer are solvent-exposed on the outside of the protein and equidistant from each other. The substrate channels to heme *b* of both NwCld subunits (Figure 1B) have calculated averages for the bottleneck radius of 2.6 ± 0.05 Å, for the length of 15.7 ± 1.7 Å, and for the volume of 389 ± 27 Å^3. These values compare with the average values of the substrate channels for all five NdCld subunits (bottleneck radius of 2.8 ± 0.01 Å, length of 15.1 ± 0.9 Å, and volume of 518 ± 44 Å^3). Thus, despite the differences in overall and subunit structure, NdCld and NwCld have access channels of similar length and bottleneck radius. The observed discrepancy in volume might be explained by a more restricted channel entrance at the protein surface in NwCld (see the overlay in Figure 7A) and/or in some uncertainty in defining the position of the access channel entrance at the protein surface.

Finally, molecular dynamics simulations were performed to evaluate differences in protein structure and solvation between the ferric and ferrous state of the two Clds. Starting with the respective crystal structures,[5,6] we simulated both proteins for 2 ns in their oxidized and reduced heme states, demonstrating that the protein structures in both redox states are highly similar. For NdCld and NwCld, the backbone atom-positional root-mean-square deviations (rmsd) between the respective crystal structure and the ferric or ferrous state after a 2 ns simulation were 1.5 and 1.6 Å, and 1.3 and 1.4 Å, respectively. The calculated rmsd values for the backbone atom positions of active site residues were 1.4 and 1.4 Å, and 1.2 and 1.3 Å, respectively. It must be mentioned that both NdCld and NwCld structures as deposited in the PDB are most likely in the reduced state because of X-ray-induced radiation.[34] Additionally, no changes in the structure (including planarity) of the prosthetic group were observed (Figure 1 of the Supporting Information). These findings clearly suggest that during reduction of the ferric Clds to the ferrous state the overall protein structure and the active site are not altered.

To analyze the amount and behavior of water molecules in the binding pocket, we calculated the radial distribution function (rdf, defined here as the probability of finding a particle at a given distance relative to the same probability for a homogeneous distribution of particles). Figure 6 clearly depicts

Table 2. Reduction Potentials of the Fe(III)/Fe(II) Couple of High-Spin Native Forms and Six-Coordinate Low-Spin Cyanide Adducts of Chlorite Dismutases from *Candidatus* "Nitrospira defluvii" (NdCld) and *N. winogradskyi* (NwCld)[a]

	$E^{\circ\prime}$ (V)			
metalloprotein	high-spin	low-spin (cyanide adduct)	$\Delta E^{\circ\prime}$ (V)	ref
NdCld	−0.113 ± 0.001	−0.404 ± 0.005	0.291	this study
NwCld	−0.119 ± 0.002	−0.397 ± 0.002	0.278	this study
ARP	−0.183	−0.390	0.207	44
soybean peroxidase	−0.310	−0.443	0.133	45
HRP-C	−0.306	−0.430	0.124	22
cucumber basic peroxidase	−0.320	−0.412	0.092	46
MPO	0.005	−0.037	0.042	43

[a]For comparison, data from *Arthromyces ramosus* peroxidase (ARP), horseradish peroxidase isoform C (HRP-C), soybean peroxidase, cucumber basic peroxidase, and myeloperoxidase (MPO) are listed. $\Delta E^{\circ\prime}$ is the difference in the reduction potential of the Fe(III)/Fe(II) couple between high-spin and low-spin forms.

that the rdfs for the water molecules show a similar pattern for both NdCld and NwCld up to a distance of approximately 20 Å (thus including the full length of the substrate channel). In the Fe(III) state, the water dipoles are located closer to the metal ion compared to those in the Fe(II) state (see the spikes in Figure 6A,B). To investigate this further, the number of water molecules at a given distance was calculated from the rdf. In both proteins, the oxidized heme has one water molecule very close to it, and up to a distance of 7.0 Å, there are three more water molecules in the pocket than in ferrous Cld (Figure 6C). These findings reflect the solvent reorganization that occurs during the Fe(III) to Fe(II) reduction reaction (see below).

DISCUSSION

Chlorite dismutase-like proteins are found in 15 bacterial and archaeal phyla, suggesting ancient roots.[5,20] Recently, it has been demonstrated that Clds are structurally related to other protein families like dye-decolorizing heme peroxidases.[21] Indeed, when the active site of Clds and these novel peroxidases was examined, both the proximal and the distal amino acids (with the exception of the peroxidase-typical aspartate) are found at very similar positions,[21] suggesting also a comparable $E^{\circ\prime}$ value for the Fe(III)/Fe(II) couple. The two chlorite dismutases investigated in this study were selected because they belong to the two major lineages of the Cld family. Pentameric NdCld is a representative of lineage I that comprises the so-called canonical Clds all featuring very similar subunit structures and oligomerization,[2−5] whereas NwCld was the first representative of lineage II with a determined crystal structure and chlorite degradation activity (Table 1).[6] Moreover, because the two metalloproteins exhibit similar chlorite degradation kinetics and have their active site residues at very similar positions, we hypothesized that the reduction potentials might show similar values and thus could be representative for the whole Cld family.

In the native ferric state, both chlorite dismutases exhibit UV−vis and EPR spectra typical for heme *b* high-spin ($S = {}^5/_2$) enzymes. Although the subunit structure of NwCld as a typical representative of lineage II Clds is very different from that of NdCld (the primary sequence of the former is ∼30% shorter than that of the latter, with a significant deletion in the N-terminal region),[5,6] these findings clearly demonstrated that the heme ligation and environment as well as the dimension of the substrate access channel are very similar in the two enzymes (Figure 7B). Both NdCld and NwCld exhibit almost identical standard reduction potentials of the Fe(III)/Fe(II) couple of −113 and −119 mV at pH 7.0, respectively, underlining the fact that the native stable oxidation state of Cld is Fe(III).

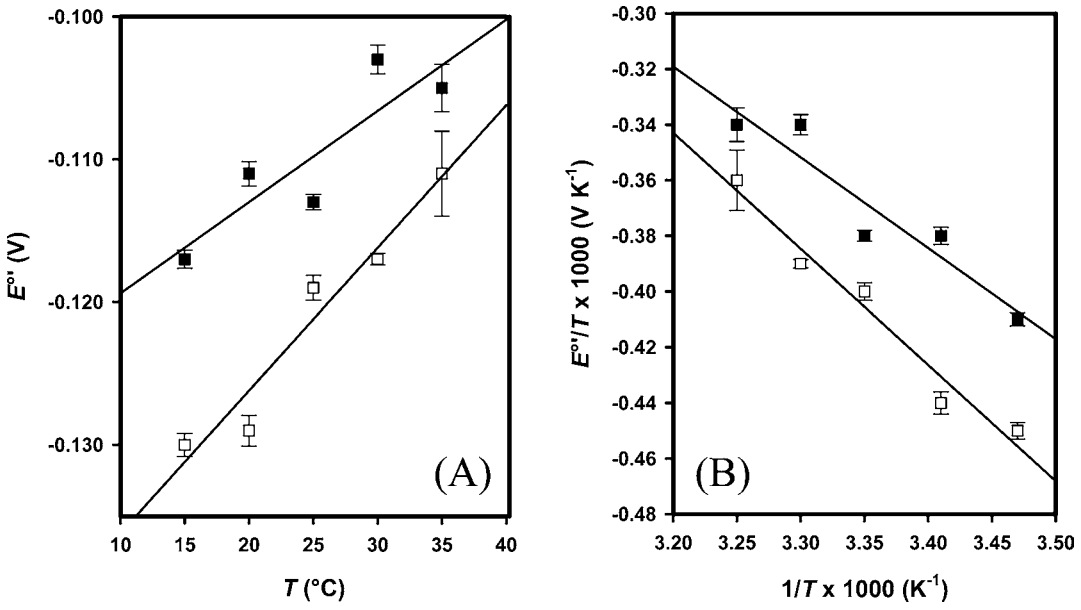

Figure 4. Redox thermodynamics of the high-spin native form of chlorite dismutases from *Candidatus* "Nitrospira defluvii" (NdCld) and *N. winogradskyi* (NwCld). (A) Temperature dependence of the reduction potential and (B) $E^{\circ\prime}/T$ vs $1/T$ plots for NdCld (■) and NwCld (□). The slopes of the plots yield the $\Delta S^{\circ\prime}_{rc}/F$ (A) and $-\Delta H^{\circ\prime}_{rc}/F$ (B) values. Solid lines are least-squares fits to the data points. All experiments were conducted in 150 mM phosphate buffer and 100 mM NaCl (pH 7.0).

dx.doi.org/10.1021/bi3013033 | *Biochemistry* 2012, 51, 9501−9512

Table 3. Thermodynamic Parameters for the Fe(III) → Fe(II) Reduction of High-Spin Native Chlorite Dismutases from *Candidatus* "Nitrospira defluvii" (NdCld) and *N. winogradskyi* (NwCld)[a]

protein	$E^{\circ\prime}$ (V)	$\Delta H^{\circ\prime}_{rc}$ (kJ mol^{-1})	$\Delta S^{\circ\prime}_{rc}$ (J mol^{-1} K^{-1})	$-\Delta H^{\circ\prime}_{rc}/F$ (V)	$T\Delta S^{\circ\prime}_{rc}/F$ (V)	$-FE^{\circ\prime}$ [$=\Delta H^{\circ\prime}_{rc(int)}$] (kJ mol^{-1})	ref
NwCld	−0.119 ± 0.005	40 ± 4	95 ± 13	−0.413 ± 0.040	0.292 ± 0.040	11.5 ± 0.1	this study
NdCld	−0.113 ± 0.005	29 ± 6	63 ± 20	−0.305 ± 0.060	0.194 ± 0.060	10.9 ± 0.1	this study
HRP-C	−0.306	91	210	−0.943	0.648	29	22
KatG	−0.226	17	−18	−0.176	−0.056	22	42
MPO	0.005	3	10	−0.031	0.031	0	43
IdCld	−0.021	–	–	–	–	–	18
AoCld	−0.023 ± 0.009	–	–	–	–	–	8
AoCld	−0.158 ± 0.009	–	–	–	–	–	3
DaCld	−0.023	–	–	–	–	–	12

[a]For comparison, the thermodynamic parameters of three heme peroxidases from different superfamilies are shown, namely, those of horseradish peroxidase isoform C (HRP-C), catalase-peroxidase (KatG) from *Synechocystis*, and myeloperoxidase (MPO). Furthermore, all available literature data about $E^{\circ\prime}$[Fe(III)/Fe(II)] values of chlorite dismutases are included: those from chlorite dismutases from *I. dechloratans* (IdCld), *D. aromatica* (DaCld), and *A. oryzae* (AoCld). Dashes indicate that no data are available.

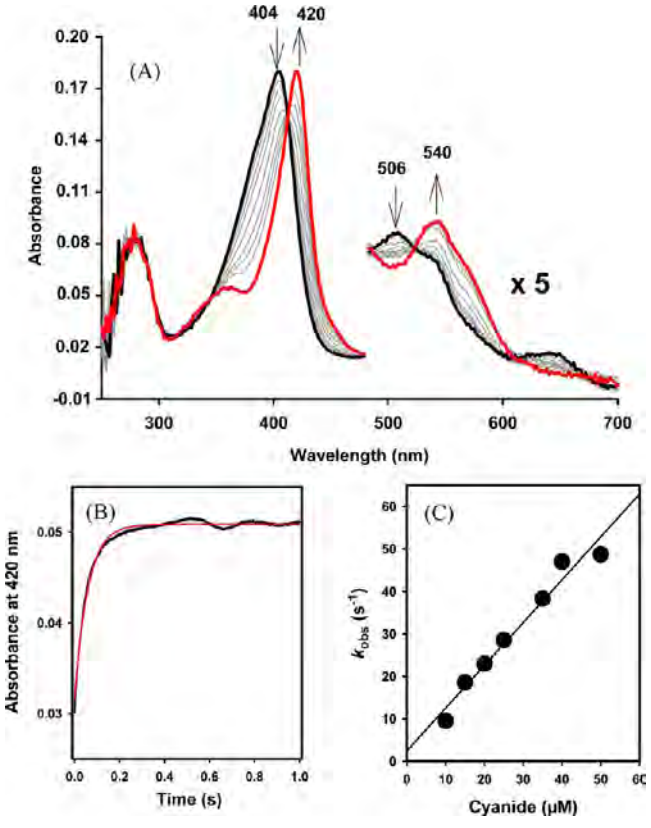

Figure 5. Transient-state kinetics of binding of cyanide to ferric chlorite dismutase from *N. winogradskyi* (NwCld). (A) Spectral changes upon reaction of 2 μM ferric NwCld with 10 μM cyanide measured in the conventional stopped-flow mode. The first spectrum is that of native NwCld; the second spectrum was recorded 1.3 ms after mixing, and subsequent spectra show the formation of the low-spin cyanide complex (absorbance maximum at 420 nm). Arrows indicate changes in absorbance with time. Conditions: 50 mM phosphate buffer, pH 7.0, and 25 °C. (B) Typical time trace at 420 nm with a single-exponential fit (1 μM NwCld and 15 μM cyanide). (C) Linear dependence of k_{obs} values from the cyanide concentration. The apparent association rate constant, k_{on}, was calculated from the slope and the apparent dissociation rate constant, k_{off}, from the intercept. The final concentration of NwCld was 1 μM in 50 mM phosphate buffer (pH 7.0).

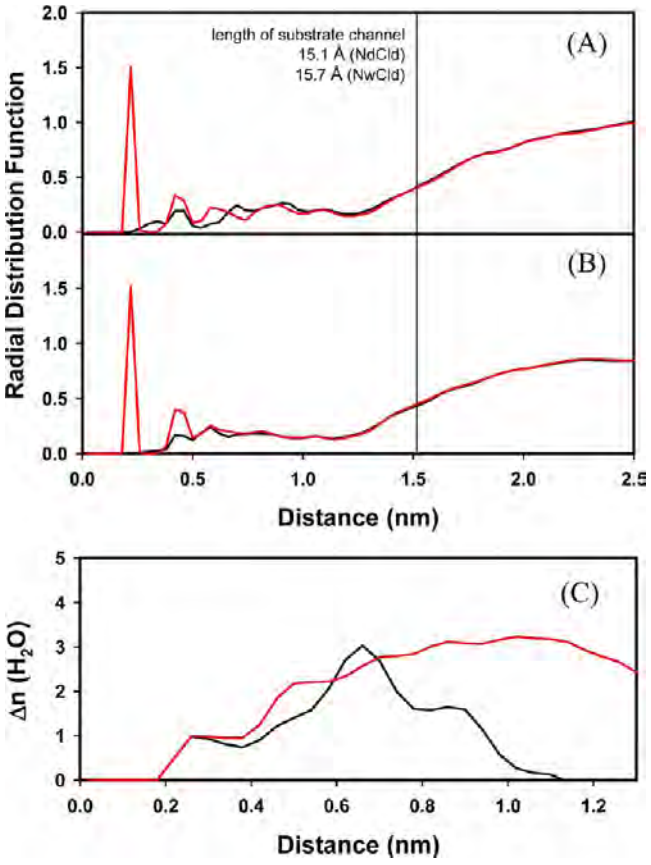

Figure 6. Radial distribution function of water molecules of high-spin ferric and ferrous chlorite dismutases from *Candidatus* "Nitrospira defluvii" (NdCld) and *N. winogradskyi* (NwCld). Radial distribution function with respect to the heme iron of NdCld (A) and NwCld (B) with oxidized states colored red and reduced states colored black. (C) Difference in the number of water molecules in the oxidized and reduced state, $\Delta n(H_2O)$, of NdCld (red) and NwCld (black).

It must be mentioned that $E^{\circ\prime}$ values of Clds from other sources reported so far (all available data are given in Table 3) range from −21 to −158 mV. Because the heme cavity architecture of all crystallized Clds[2−6] is almost superimposable (Figure 7B), this variability might result from different methods used in the determination of $E^{\circ\prime}$.[2,7,11,17] However, variability is also seen in the UV−vis spectra of those metalloproteins and in the kinetics of chlorite degradation. The ferric forms of chlorite dismutases from *I. dechloratans* (IdCld),[17] *D. aromatica* (DaCld),[11] and *A. oryzae* (AoCld)[2,7] (Table 3) were reported

dx.doi.org/10.1021/bi3013033 | *Biochemistry* 2012, 51, 9501−9512

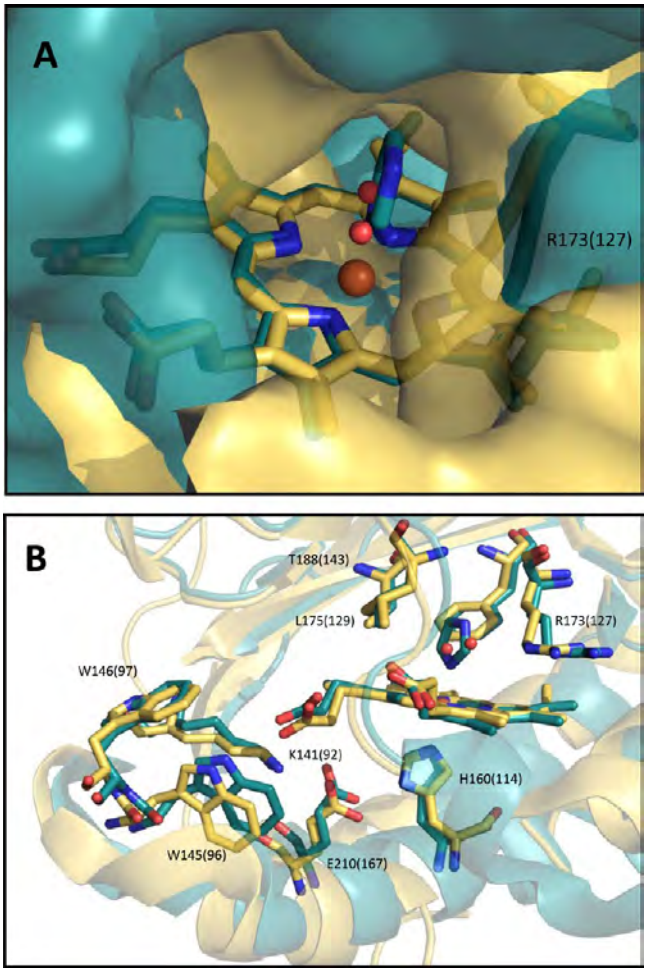

Figure 7. Structural analysis of the surface area at the substrate channel entrance and of the active site of chlorite dismutases from *Candidatus* "Nitrospira defluvii" (NdCld) and *N. winogradskyi* (NwCld). (A) Close-up of the surface area of substrate channels of NwCld (yellow, PDB entry 3QPI) and NdCld (cyan, PDB entry 3NN1). Catalytically active arginine 173(127) is highlighted. The crystal structure of NdCld shows an imidazole and that of NwCld two water molecules (red balls) bound to the distal heme side. (B) Superposition of active site residues of NwCld (yellow) and NdCld (cyan) and prosthetic groups. Amino acid numbering according to NdCld and NwCld (brackets). Figures were generated using PyMOL (http://www.pymol.org/).

to exhibit a rather broad Soret maximum around 392 nm, which is 13−16 nm blue-shifted compared to those of NwCld (405 nm) and NdCld (408 nm). At the same time, these enzymes show higher k_{cat} values of chlorite degradation compared to those of NdCld and NwCld, although comparison of kinetic parameters has been shown to be problematic because of the irreversible inhibition of the enzyme during chlorite degradation that starts to be relevant in different concentration regimes with different Clds.[5,10,11] On the other hand, chlorite dismutase from *Pseudomonas chloritidismutans* (PcCld)[35] exhibits a Soret absorbance of its resting state at 411 nm, similar to that of NdCld. Moreover, the related Dyp-type peroxidases, which together with chlorite dismutases constitute a distinct superfamily of heme enzymes because of similarities in overall fold and heme cavity architecture,[21] also exhibit Soret maxima in this range (404−409 nm).[36−41] Future comparative studies must be performed to elucidate the origin of the spectral differences among AoCld, DaCld, and IdCld on one hand as well as NdCld, NwCld, PcCld, and Dyp-type peroxidases on the other.

In addition to almost identical $E^{\circ\prime}$ values, the substrate access channels of NdCld and NwCld have similar lengths (15.1 and 15.7 Å, respectively) and bottleneck radii (2.8 and 2.6 Å, respectively). Moreover, the amount and distribution of water molecules in the ferric and ferrous state were shown to be very similar in the two metalloproteins (Figure 7A). This high degree of structural homology agrees with the overall chlorite degradation kinetics as well as the determined apparent bimolecular cyanide binding constants (2.6×10^6 and 1.0×10^6 M^{-1} s^{-1}, respectively) (Table 1).

When cyanide bound, the six-coordinate low-spin ($S = {}^1/_2$) forms of NdCld and NwCld were formed, inducing a significant decrease in the reduction potential of the Fe(III)/Fe(II) couple (−404 and −397 mV, respectively). The same phenomenon has been observed with other heme proteins.[17] Usually, in the ferrous high-spin form of heme proteins, the electrostatic interaction of the metal ion with the water molecules in the heme cavity is weakened compared to that in the ferric state.[22,42−45] This is also the case in Cld as has been demonstrated by the MD simulations of the ferric and ferrous forms of NdCld and NwCld (Figure 6). The electrostatic interaction described above is much smaller in the corresponding cyanide complexes, where the solvent accessibility to the heme is diminished.[22,42−45] As a consequence, the solvent-derived increase in entropy during the reduction reaction is significantly smaller in the six-coordinate low-spin cyanide adducts. In addition, the enthalpic stabilization of the ferric state is more pronounced and both phenomena lead to more negative $E^{\circ\prime}$ values (Table 2).[17,22,42−45]

To gain deeper insight into the mechanism of $E^{\circ\prime}$ modulation, the relative contributions of $\Delta H^{\circ\prime}_{rc}$ and $\Delta S^{\circ\prime}_{rc}$ were determined from $E^{\circ\prime}$ measurements at various temperatures (Table 3). The obtained values for both state functions (Table 3) were similar and demonstrated that the ferric state in native chlorite dismutases (NdCld and NwCld) is enthalpically stabilized (29 and 40 kJ mol^{-1}, respectively), whereas formation of the ferrous state is entropically favored (63 and 95 J mol^{-1} K^{-1}, respectively).

Reduction-induced changes in enthalpy and entropy contain contributions from both intrinsic protein-based factors ($\Delta H^{\circ\prime}_{rc,int}$ and $\Delta S^{\circ\prime}_{rc,int}$) and solvent-based factors ($\Delta H^{\circ\prime}_{rc,solv}$ and $\Delta S^{\circ\prime}_{rc,solv}$): $\Delta H^{\circ\prime}_{rc} = \Delta H^{\circ\prime}_{rc,int} + \Delta H^{\circ\prime}_{rc,solv}$, and $\Delta S^{\circ\prime}_{rc} = \Delta S^{\circ\prime}_{rc,int} + \Delta S^{\circ\prime}_{rc,solv}$.[17] It has been shown that $\Delta H^{\circ\prime}_{rc,int}$ is determined primarily by metal−ligand binding interactions and the electrostatics among the metal, the protein environment, and the solvent, whereas $\Delta S^{\circ\prime}_{rc}$ reflects the oxidation-state-dependent changes in conformational degrees of freedom of the polypeptide chain and solvent reorganization ($\Delta S^{\circ\prime}_{rc,solv}$) effects.[17] Our MD simulations have shown that the structures of both the protein and the prosthetic group in the Fe(III) and Fe(II) forms are very similar ($\Delta S^{\circ\prime}_{rc,int} \approx 0$), confirming that the change in entropy mainly reflects solvent reorganization ($\Delta S^{\circ\prime}_{rc} \approx \Delta S^{\circ\prime}_{rc,solv}$). This agrees with available data for the ferric and ferrous forms of other heme proteins that indicate that, in general, reduction-induced 3D structural changes are quite small in heme proteins.[17,42−45]

Because reduction-induced solvent reorganization effects usually induce compensatory enthalpy and entropy changes, the corresponding enthalpic contribution can be factored out from the measured enthalpy change,[17,44,46,47] finally allowing estimation of the protein-based contribution to $\Delta G^{\circ\prime}_{rc}$ =

$-nFE^{\circ\prime} = \Delta H^{\circ\prime}_{rc} - T\Delta S^{\circ\prime}_{rc} = \Delta H^{\circ\prime}_{rc,int} + \Delta H^{\circ\prime}_{rc,solv} - T\Delta S^{\circ\prime}_{rc,int} - T\Delta S^{\circ\prime}_{rc,solv}$. Because the solvent reorganization effects cancel exactly in the enthalpy and entropy, it follows that $\Delta G^{\circ\prime}_{rc} = -nFE^{\circ\prime} = \Delta H^{\circ\prime}_{rc,int} - T\Delta S^{\circ\prime}_{rc,int}$. Because the structures are very similar, the internal entropy change must be very small ($T\Delta S^{\circ\prime}_{rc,int} \approx 0$). Hence, to a first approximation, the measured $E^{\circ\prime}$ value coincides with $\Delta H^{\circ\prime}_{rc,int}$ and would ultimately be determined by the selective enthalpic stabilization of one of the two redox states by first coordination and electrostatic effects.[17,44,47] As a consequence, $\Delta H^{\circ\prime}_{rc,int} = -nFE^{\circ\prime}$ corresponds to 10.9 kJ/mol for NdCld and 11.5 kJ/mol for NwCld (Table 3). This approximation clearly suggests that in solution the heme iron environment in the two Clds is very similar.

In chlorite dismutases, the enthalpic stabilization of the ferric form could be attributed to the basic character of the proximal histidine (because of its hydrogen bond interaction with the nearby glutamate) (Figure 7B) and to the polarity of the distal heme site because of the presence of water molecules in the ferric state (Figure 6). In comparison with peroxidases that also have heme *b* as prosthetic group and a proximal histidine hydrogen-bonded to an acidic amino acid (i.e., aspartate) like HRP[39] or KatG[4] (Table 3), the polarity of the distal heme cavity is less pronounced because of the lack of the catalytic histidine. Recently, it has been reported that the imidazolate character of the proximal histidine in Cld is also less pronounced than in peroxidases because of weaker H-bonding interaction with the glutamate as suggested from recent resonance Raman spectroscopy measurements.[11,12] These differences could contribute to the more positive $E^{\circ\prime}$ values in Cld compared to those of most heme peroxidases, which (with the exception of MPO) have $E^{\circ\prime}$ values in the range from −180 to −320 mV (Tables 2 and 3).[17]

In summary, we could demonstrate that chlorite dismutases from both main lineages have, despite significantly different overall structures, a very similar active site and access channel architecture and as a consequence redox chemistry. Stabilization of the ferric high-spin state is important for efficient reaction with chlorite, thereby producing the enzyme intermediate Compound I and hypochlorite (reaction 1). Because within a defined heme enzyme the same molecular factors influence the redox properties of the heme iron at different oxidation states [e.g., in heme peroxidases, the hierarchy of $E^{\circ\prime}$ values of Fe(III)/Fe(II) couples reflects that of $E^{\circ\prime}$ values of the Compound I/ferric state couple],[17,47−51] it is reasonable to assume that the oxidation capacity of Cld Compound I is very high, possibly with $E^{\circ\prime}$ values of >1 V. This usually needs, to prevent unspecific oxidation of the protein matrix, stabilization of Compound I by (i) a partially (e.g., histidine H-bonded to Asp or Glu) or fully negatively charged (cysteinate or tyrosinate) proximal heme ligand and (ii) a short half-life of Compound I due to efficient reaction with the electron donor(s). In the case of Cld, both factors might contribute to partially prevent side reactions, although kinetic investigations have shown that with increasing chlorite concentrations the enzyme is progressively and irreversibly inactivated.[5−10]

■ ASSOCIATED CONTENT

Supporting Information

EPR simulation parameters of spectra from NdCld and NwCld (Table 1) and molecular dynamics simulations of NdCld and NwCld in the Fe(III) and Fe(II) states (Figure 1). This material is available free of charge via the Internet at http://pubs.acs.org.

■ AUTHOR INFORMATION

Corresponding Author

*Phone: +43-1-47654-6073. Fax: +43-1-47654-6050. E-mail: christian.obinger@boku.ac.at.

Funding

This project was supported by the Austrian Science Foundation, FWF [Doctoral program BioToP-Molecular Technology of Proteins (W1224) and FWF Project P25270-B22].

Notes

The authors declare no competing financial interest.

■ ACKNOWLEDGMENTS

We are grateful to Dr. Christopher W. M. Kay (University College London, London, U.K.), who provided the EPR spectrometer for low-temperature measurements.

■ ABBREVIATIONS

Cld, chlorite dismutase; NdCld, chlorite dismutase from *Candidatus* "Nitrospira defluvii"; NwCld, chlorite dismutase from *N. winogradskyi*; $E^{\circ\prime}$, standard reduction potential; $\Delta H^{\circ\prime}_{rc}$, enthalpy change for the reaction center upon reduction of the oxidized protein; $\Delta S^{\circ\prime}_{rc}$, entropy change for the reaction center upon reduction of the oxidized protein; SHE, standard hydrogen electrode; rdf, radial distribution function; rmsd, root-mean-square deviation; cw-EPR, continuous wave electron paramagnetic resonance; OTTLE, optical thin layer spectroelectrochemical; MD, molecular dynamics; PDB, Protein Data Bank.

■ REFERENCES

(1) Turano, P., and Lu, Y. (2001) Iron in heme and related proteins. In *Handbook of metalloproteins* (Bertini, I., Sigel, A., and Sigel, H., Eds.) pp 269−356, Marcel Dekker, Inc., New York.

(2) Ebihara, A., Okamoto, A., Kousumi, Y., Yamamoto, H., Masui, R., Ueyama, N., Yokoyama, S., and Kuramitsu, S. (2005) Structure-based functional identification of a novel heme-binding protein from *Thermus thermophilis* HB8. *J. Struct. Funct. Genomics 6*, 21−32.

(3) de Geus, D. C., Thomassen, E. A. J., Hagedoorn, P.-L., Pannu, N. S., van Duijn, E., and Abrahams, J. P. (2009) Crystal structure of chlorite dismutase, a detoxifying enzyme producing molecular oxygen. *J. Mol. Biol. 387*, 192−206.

(4) Goblirsch, B. R., Streit, B. R., DuBois, J. L., and Wilmot, C. M. (2010) Structural features promoting dioxygen production by *Dechloromonas aromatica* chlorite dismutase. *J. Biol. Inorg. Chem. 15*, 879−888.

(5) Kostan, J., Sjoeblom, B., Maixner, F., Mlynek, G., Furtmüller, P. G., Obinger, C., Wagner, M., Daims, H., and Djinovic-Carugo, K. (2010) Structural and functional analysis of the chlorite dismutase from the nitrite-oxidizing bacterium "*Candidatus* Nitrospira defluvii": Identification of a catalytically important amino acid residue. *J. Struct. Biol. 172*, 331−342.

(6) Mlynek, G., Sjöblom, B., Kostan, J., Füreder, S., Maixner, F., Gysel, K., Furtmüller, P. G., Obinger, C., Wagner, M., Daims, H., and Djinović-Carugo, K. (2011) Unexpected diversity of chlorite dismutases: A catalytically efficient dimeric enzyme from *Nitrobacter winogradskyi*. *J. Bacteriol. 193*, 2408−2417.

(7) van Ginkel, C. G., Rikken, G. B., Kroon, A. G. M., and Kengen, S. W. M. (1996) Purification and characterization of chlorite dismutase: A novel oxygen-generating enzyme. *Arch. Microbiol. 166*, 321−326.

(8) Hagedoorn, P. L., de Geus, D. C., and Hagen, W. R. (2002) Spectroscopic characterization and ligand-binding properties of

chlorite dismutase from the chlorate respiring bacterial strain GR-1. *Eur. J. Biochem. 269*, 4905−4911.
(9) Lee, A. Q., Streit, B. R., Zdilla, M. J., Abu-Omar, M. M., and DuBois, J. L. (2008) Mechanism of and exquisite selectivity for O-O bond formation by the heme dependent chlorite dismutase. *Proc. Natl. Acad. Sci. U.S.A. 105*, 15654−15659.
(10) Streit, B. R., and DuBois, J. L. (2008) Chemical and steady-state analysis of a heterologously expressed heme dependent chlorite dismutase. *Biochemistry 47*, 5271−5280.
(11) Streit, B. R., Blanc, B., Lukat-Rodgers, B. S., Rodgers, K. R., and DuBois, J. L. (2010) How active-site protonation state influences the reactivity and ligation of the heme in chlorite dismutase. *J. Am. Chem. Soc. 132*, 5711−5724.
(12) Blanc, B., Mayfield, J. A., McDonald, C. A., Lukat-Rodgers, G. S., Rodgers, K. R., and DuBois, J. L. (2012) Understanding how the distal environment directs reactivity in chlorite dismutase: Spectroscopy and reactivity of Arg183 mutants. *Biochemistry 51*, 1895−1910.
(13) Betley, T., Surendranath, Y., Childress, M., Alliger, G., and Fu, R. (2008) A ligand field chemistry of oxygen generation by the oxygen-evolving complex and synthetic active sites. *Philos. Trans. R. Soc. London, Ser. B 363*, 1293−1303.
(14) Poulos, T. L. (2010) Thirty years of heme peroxidase structural biology. *Arch. Biochem. Biophys. 500*, 3−12.
(15) Arnhold, J., Monzani, E., Furtmüller, P. G., Zederbauer, M., Casella, L., and Obinger, C. (2006) Kinetics and thermodynamics of halide and nitrite oxidation by heme peroxidases. *Eur. J. Inorg. Chem. 19*, 3801−3811.
(16) Furtmüller, P. G., Zederbauer, M., Jantschko, W., Helm, J., Bogner, M., Jakopitsch, C., and Obinger, C. (2006) Active site structure and catalytic mechanisms of human peroxidases. *Arch. Biochem. Biophys. 445*, 199−213.
(17) Battistuzzi, G., Bellei, M., Bortolotti, C. A., and Sola, M. (2010) Redox properties of heme peroxidases. *Arch. Biochem. Biophys. 500*, 21−36.
(18) Stenklo, K., Thorell, D., Bergius, H., Aasa, R., and Nilsson, T. (2001) Chlorite dismutase from *Ideonella dechloratans*. *J. Biol. Inorg. Chem. 6*, 601−607.
(19) Hofbauer, S., Gysel, K., Mlynek, G., Kostan, J., Hagmüller, A., Daims, A., Furtmüller, P. G., Djinovic-Carugo, K., and Obinger, C. (2012) Impact of subunit and oligomeric structure on the thermal and conformational stability of chlorite dismutases. *Biochim. Biophys. Acta 1824*, 1031−1038.
(20) Maixner, F., Wagner, M., Lücker, S., Pelletier, E., Schmitz-Esser, S., Hace, K., Spieck, E., Konrat, R., Le Paslier, D., and Daims, H. (2008) Environmenteal genomics reveals a functional chlorite dismutase in the nitrite-oxidizing bacterium "*Candidatus* Nitrospira defluvii". *Environ. Microbiol. 10*, 3043−3056.
(21) Goblirsch, B., Kurker, R. C., Streit, B. R., Wilmot, C. M., and DuBois, J. L. (2011) Chlorite dismutases, DyPs and EfeB: 3 microbial heme enzyme families comprise the CDE structural superfamily. *J. Mol. Biol. 408*, 379−398.
(22) Battistuzzi, G., Borsari, M., Ranieri, A., and Sola, M. (2002) Redox thermodynamics of the Fe(III)/Fe(II) couple in horseradish peroxidase and its cyanide complex. *J. Am. Chem. Soc. 124*, 26−27.
(23) Stoll, S., and Schweiger, A. (2006) EasySpin, a comprehensive software package for spectral simulation and analysis in EPR. *J. Magn. Reson. 178*, 42−55.
(24) Schmid, N., Christ, C. D., Christen, M., Eichenberger, A. P., and van Gunsteren, W. F. (2012) Architecture, implementation and parallelisation of the GROMOS software for biomolecular simulation. *Comput. Phys. Commun. 183*, 890−903.
(25) Schmid, N., Eichenberger, A. P., Choutko, A., Riniker, S., Winger, M., Mark, A. E., and van Gunsteren, W. F. (2011) Definition and testing of the GROMOS force-field versions 54A7 and 54B7. *Eur. Biophys. J. 40*, 843−856.
(26) Berendsen, H., Postma, J., Van Gunsteren, W., and Hermans, J. (1981) Interaction models for water in relation to protein hydration. In *Intermolecular Forces* (Pullman, B., Ed.) pp 331−342, D. Reidel Publishing Co., Dordrecht, The Netherlands.
(27) Berendsen, H., Postma, J., Van Gunsteren, W., DiNola, A., and Haak, J. (1984) Molecular dynamics with coupling to an external bath. *J. Chem. Phys. 81*, 3684−3690.
(28) Ryckaert, J., Ciccotti, G., and Berendsen, H. (1977) Numerical integration of the Cartesian equations of motion of a system with constraints: Molecular dynamics of n-alkanes. *J. Comput. Phys. 23*, 327−341.
(29) Berendsen, H., Gunsteren, W., Zwinderman, H., and Geurtsen, R. (1986) Simulations of Proteins in Water. *Ann. N.Y. Acad. Sci. 482*, 269−286.
(30) Tironi, I., Sperb, R., Smith, P., and van Gunsteren, W. (1995) A generalized reaction field method for molecular dynamics simulations. *J. Chem. Phys. 102*, 5451−5459.
(31) Heinz, T., van Gunsteren, W., and Hünenberger, P. (2001) Comparison of four methods to compute the dielectric permittivity of liquids from molecular dynamics simulations. *J. Chem. Phys. 115*, 1125−1136.
(32) Eichenberger, A. P., Allison, J. R., Dolenc, J., Geerke, D. P., Horta, B. A. C., Meier, K., Oostenbrink, C., Schmid, N., Steiner, D., Wang, D., and van Gunsteren, W. F. (2011) The GROMOS++ Software for the Analysis of Biomolecular Simulation Trajectories. *J. Chem. Theory Comput. 7*, 3379−3390.
(33) Petrek, M., Otyepka, M., Banás, P., Kosinová, P., Koca, J., and Damborský, J. (2006) CAVER: A new tool to explore routes from protein clefts, pockets and cavities. *BMC Bioinf. 7*, 316.
(34) Macedo, S., Pechlaner, M., Schmid, W., Weik, M., Sato, K., Dennison, C., and Djinović-Carugo, K. (2009) Can soaked-in scavengers protect metalloprotein active sites from reduction during data collection? *J. Synchrotron Radiat. 16*, 191−204.
(35) Mehboob, F., Wolterink, A. F., Vermeulen, A. J., Jiang, B., Hagedoorn, P. L., Stams, A. J., and Kengen, S. W. (2009) Purifcation and characterization of a chlorite dismutase from *Pseudomonas chloritidismutans*. *FEMS Microbiol. Lett. 293*, 115−121.
(36) Sugano, Y., Muramatsu, R., Ichiyanagi, A., Sato, T., and Shoda, M. (2007) DyP, a unique dye-decolorizing peroxidase, represents a novel heme peroxidase family: Asp171 replaces the distal histidine of classical peroxidases. *J. Biol. Chem. 282*, 36652−36658.
(37) Zubieta, C., Krishna, S. S., Kapoor, M., Kozbial, P., McMullan, D., Axelrod, H. L., Miller, M. D., Abdubek, P., Ambing, E., Astakhova, T., Carlton, D., Chiu, H. J., Clayton, T., Deller, M. C., Duan, L., Elsliger, M. A., Feuerhelm, J., Grzechnik, S. K., Hale, J., Hampton, E., Han, G. W., Jaroszewski, L., Jin, K. K., Klock, H. E., Knuth, M. W., Kumar, A., Marciano, D., Morse, A. T., Nigoghossian, E., Okach, L., Oommachen, S., Reyes, R., Rife, C. L., Schimmel, P., van den Bedem, H., Weekes, D., White, A., Xu, Q., Hodgson, K. O., Wooley, J., Deacon, A. M., Godzik, A., Lesley, S. A., and Wilson, I. A. (2007) Crystal structures of two novel dye-decolorizing peroxidases reveal a β-barrel fold with a conserved heme-binding motif. *Proteins 69*, 223−233.
(38) Ogola, H. J., Kamiike, T., Hashimoto, N., Ashida, H., Ishikawa, T., Shibata, H., and Sawa, Y. (2009) Molecular characterization of a novel peroxidase from the cyanobacterium *Anabaena sp.* strain PCC 7120. *Appl. Environ. Microbiol. 75*, 7509−7518.
(39) Roberts, J. N., Singh, R., Grigg, J. C., Murphy, M. E., Bugg, T. D., and Eltis, L. D. (2011) Molecular characterization of dye-decolorizing peroxidases from *Rhodococcus jostii* RHA1. *Biochemistry 50*, 5108−5119.
(40) van Bloois, E., Torres Pazmiño, D. E., Winter, R. T., and Fraaije, M. W. (2010) A robust and extracellular heme-containing peroxidase from *Thermobifida fusca* as prototype of a bacterial peroxidase superfamily. *Appl. Microbiol. Biotechnol. 86*, 1419−1430.
(41) Liers, C., Bobeth, C., Pecyna, M., Ullrich, R., and Hofrichter, M. (2010) DyP-like peroxidases of the jelly fungus *Auricularia auricula-judae* oxidize nonphenolic lignin model compounds and high-redox potential dyes. *Appl. Microbiol. Biotechnol. 85*, 1869−1879.
(42) Bellei, M., Jakopitsch, C., Battistuzzi, G., Sola, M., and Obinger, C. (2006) Redox thermodynamics of the ferric-ferrous couple of wild-type *Synechocystis* KatG and KatG(Y249F). *Biochemistry 45*, 4768−4774.

(43) Battistuzzi, G., Bellei, M., Zederbauer, M., Furtmüller, P. G., Sola, M., and Obinger, C. (2006) Redox thermodynamics of the Fe(III)/Fe(II) couple of human myeloperoxidase in its high-spin and low-spin forms. *Biochemistry 45*, 12750−12755.
(44) Battistuzzi, G., Bellei, M., De Rienzo, F., and Sola, M. (2006) Redox properties of the Fe^{3+}/Fe^{2+} couple in *Arthromyces ramosus* class II peroxidase and its cyanide adduct. *J. Biol. Inorg. Chem 11*, 586−592.
(45) Battistuzzi, G., Bellei, M., Borsari, M., Di Rocco, G., Ranieri, A., and Sola, M. (2005) Axial ligation and polypeptide matrix effects on the reduction potential of heme proteins probed on their cyanide adducts. *J. Biol. Inorg. Chem. 10*, 643−651.
(46) Battistuzzi, G., Bellei, M., Bortolotti, C. A., Rocco, G. D., Leonardi, A., and Sola, M. (2004) Characterization of the solution reactivity of a basic heme peroxidase from *Cucumis sativus*. *Arch. Biochem. Biophys. 423*, 317−331.
(47) Vlasits, J., Bellei, M., Jakopitsch, C., Furtmüller, P. G., Zamocky, M., Sola, M., Battistuzzi, G., and Obinger, C. (2010) Disruption of the H-bond network in the main access channel of catalase-peroxidase modulates enthalpy and entropy of Fe(III) reduction. *J. Inorg. Biochem. 104*, 648−656.
(48) Arnhold, J., Monzani, E., Furtmüller, P. G., Zederbauer, M., Casella, L., and Obinger, C. (2006) Kinetics and thermodynamics of halide and nitrite oxidation by heme peroxidases. *Eur. J. Inorg. Chem. 19*, 3801−3811.
(49) Jantschko, W., Furtmüller, P. G., Allegra, M., Livrea, M. A., Jakopitsch, C., Regelsberger, G., and Obinger, C. (2002) Redox intermediates of plant and mammalian peroxidases: A comparative transient-kinetic study of their reactivity toward indole derivatives. *Arch. Biochem. Biophys. 398*, 12−22.
(50) Furtmüller, P. G., Arnhold, J., Jantschko, W., Zederbauer, M., Jakopitsch, C., and Obinger, C. (2005) Standard reduction potentials of all couples of the peroxidase cycle of lactoperoxidase. *J. Inorg. Biochem. 99*, 1220−1229.
(51) Battistuzzi, G., Bellei, M., Vlasits, J., Banerjee, S., Furtmüller, P. G., Sola, M., and Obinger, C. (2010) Redox thermodynamics of lactoperoxidase and eosinophil peroxidase. *Arch. Biochem. Biophys. 494*, 72−77.

SUPPORTING INFORMATION

Redox thermodynamics of high-spin and low-spin forms of chlorite dismutases of diverse subunit and oligomeric structure

Stefan Hofbauer[1], Marzia Bellei[2], Axel Sündermann[3], Katharina F. Pirker[4], Andreas Hagmüller[5], Georg Mlynek[5], Julius Kostan[5], Holger Daims[6], Kristina Djinovic-Carugo[5], Chris Oostenbrink[3], Paul G. Furtmüller[1], Gianantonio Battistuzzi[7], Christian Obinger[1]

[1]Department of Chemistry, Division of Biochemistry, VIBT – Vienna Institute of BioTechnology, BOKU – University of Natural Resources and Life Sciences, A-1190 Vienna, Austria
[2]Department of Life Sciences, University of Modena and Reggio Emilia, 41100 Modena, Italy
[3]Department of Material Sciences and Process Engineering, Institute of Molecular Modeling and Simulation, VIBT – Vienna Institute of BioTechnology, BOKU – University of Natural Resources and Life Sciences, A-1190 Vienna, Austria
[4]Health and Environment Department, Environmental Resources and Technologies, AIT - Austrian Institute of Technology GmbH, A-3430 Tulln, Austria
[5]Department for Structural and Computational Biology, Max F. Perutz Laboratories, University of Vienna, Campus Biocenter 5, A-1030 Vienna, Austria
[6]Department of Microbial Ecology, University of Vienna, A-1090 Vienna, Austria
[7]Department of Chemistry and Geology, University of Modena and Reggio Emilia, 41100 Modena, Italy

Supplemental Table 1. EPR simulation parameters of spectra from chlorite dismutases from *Candidatus* "Nitrospira defluvii" (NdCld) and *Nitrobacter winogradskyi* (NwCld).

Fe(III) forms	g_x	g_y	g_z	E/D^*
NdCld				
HS narrow	6.05	5.52	1.99	0.012
HS broad	6.50	5.25	1.99	0.026
LS narrow	2.99	2.25	1.47	
LS broad	3.14	2.13	≤1.2	
NwCld				
HS	5.87	5.87	2	0
LS	3.15	2.12	≤1.2	

* E/D describes the rhombicity ($0 \leq E/D \leq 1/3$)

Supplemental Figure 1. **Molecular dynamics simulations (2 ns) of NdCld and NwCld in the Fe(III) and Fe(II) states.** (A) Calculated rmsd values of NwCld backbone (top left), NdCld backbone (top right), NwCld active site residues (bottom left) and NdCld active site residues (bottom right). Black: oxidized state, red: reduced state. (B) Planarity of the heme was assessed by the program tser, 1 equals planar and 0 not planar. Planarity over time for the heme in NwCld (left) and NdCld (right) in their reduced and oxidized states are depicted in red and in black, respectively; differences between oxidized and reduced heme are depicted in grey.

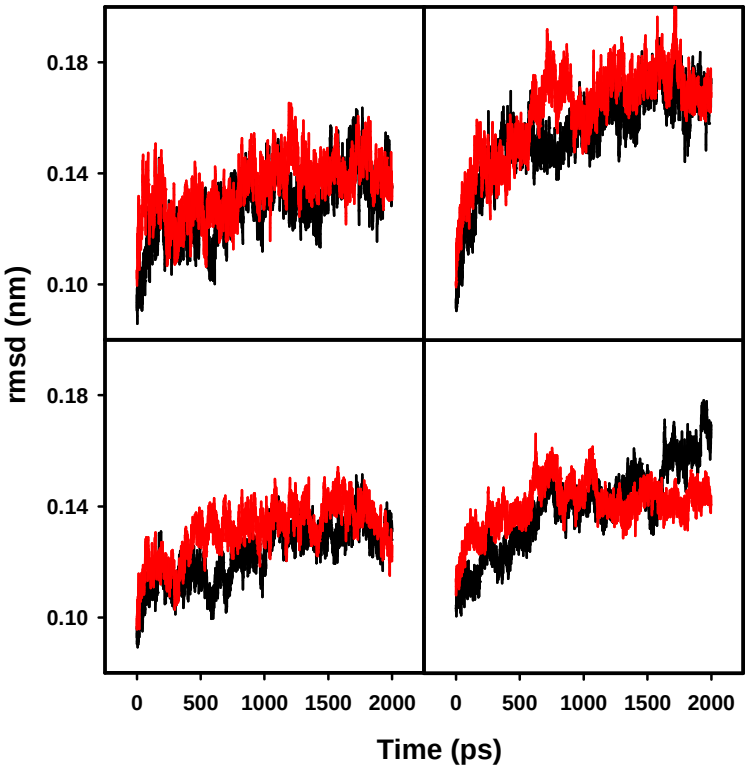

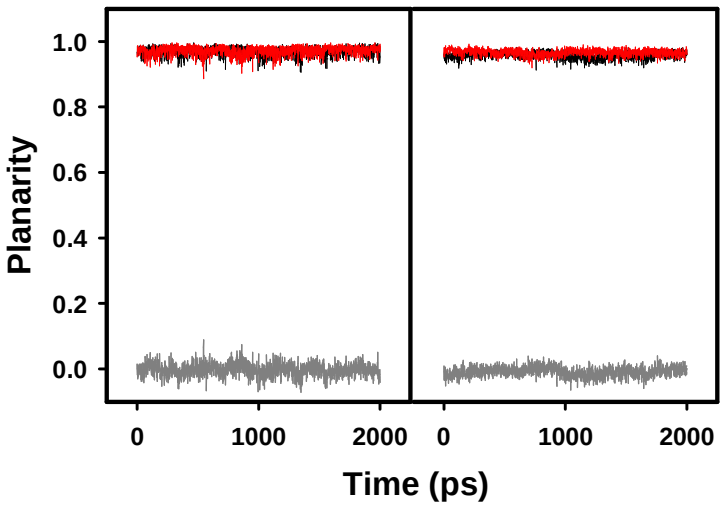

Chapter 5

Manipulating conserved heme cavity residues of chlorite dismutase: effect on structure, redox chemistry, and reactivity

Stefan Hofbauer, Kira Gysel, Marzia Bellei, Andreas Hagmüller, Irene Schaffner, Georg Mlynek, Julius Kostan, Katharina F. Pirker, Holger Daims, Paul G. Furtmüller, Gianantonio Battistuzzi, Kristina Djinovic-Carugo, Christian Obinger

Research Article

Biochemistry (2014), 53, 77-89

BIOCHEMISTRY
including biophysical chemistry & molecular biology

Article

pubs.acs.org/biochemistry

Manipulating Conserved Heme Cavity Residues of Chlorite Dismutase: Effect on Structure, Redox Chemistry, and Reactivity

Stefan Hofbauer,[†] Kira Gysel,[‡] Marzia Bellei,[⊥] Andreas Hagmüller,[‡] Irene Schaffner,[†] Georg Mlynek,[‡] Julius Kostan,[‡] Katharina F. Pirker,[†] Holger Daims,[∥] Paul G. Furtmüller,[†] Gianantonio Battistuzzi,[#] Kristina Djinović-Carugo,*[,‡,§] and Christian Obinger*[,†]

[†]Department of Chemistry, Division of Biochemistry, VIBT − Vienna Institute of BioTechnology, BOKU − University of Natural Resources and Life Sciences, A-1190 Vienna, Austria

[‡]Department for Structural and Computational Biology, Max F. Perutz Laboratories, University of Vienna, A-1030 Vienna, Austria

[§]Department of Biochemistry, Faculty of Chemistry and Chemical Technology, University of Ljubljana, 1000 Ljubljana, Slovenia

[⊥]Department of Life Sciences, University of Modena and Reggio Emilia, 41125 Modena, Italy

[∥]Department of Microbiology and Ecosystem Science, Division of Microbial Ecology, University of Vienna, A-1090 Vienna, Austria

[#]Department of Chemistry and Geology, University of Modena and Reggio Emilia, 41125 Modena, Italy

Supporting Information

ABSTRACT: Chlorite dismutases (Clds) are heme *b* containing oxidoreductases that convert chlorite to chloride and molecular oxygen. In order to elucidate the role of conserved heme cavity residues in the catalysis of this reaction comprehensive mutational and biochemical analyses of Cld from "*Candidatus* Nitrospira defluvii" (NdCld) were performed. Particularly, point mutations of the cavity-forming residues R173, K141, W145, W146, and E210 were performed. The effect of manipulation in 12 single and double mutants was probed by UV−vis spectroscopy, spectroelectrochemistry, pre-steady-state and steady-state kinetics, and X-ray crystallography. Resulting biochemical data are discussed with respect to the known crystal structure of wild-type NdCld and the variants R173A and R173K as well as the structures of R173E, W145V, W145F, and the R173Q/W146Y solved in this work. The findings allow a critical analysis of the role of these heme cavity residues in the reaction mechanism of chlorite degradation that is proposed to involve hypohalous acid as transient intermediate and formation of an O═O bond. The distal R173 is shown to be important (but not fully essential) for the reaction with chlorite, and, upon addition of cyanide, it acts as a proton acceptor in the formation of the resulting low-spin complex. The proximal H-bonding network including K141-E210-H160 keeps the enzyme in its ferric ($E^{\circ\prime}$ = −113 mV) and mainly five-coordinated high-spin state and is very susceptible to perturbation.

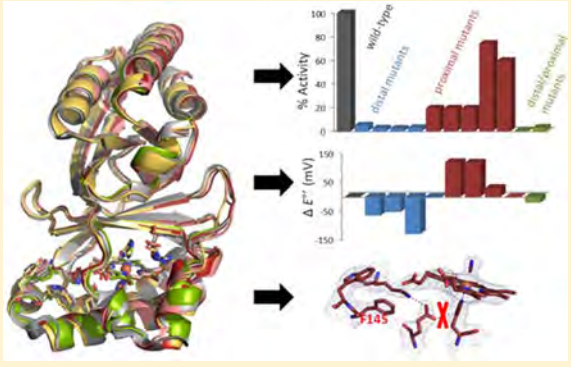

In 1996 a heme *b* containing and chlorite degrading oxidoreductase was discovered in chlorate- and perchlorate-reducing facultative anaerobic bacteria (PCRB).[1] The metalloprotein (EC 1.13.11.49) was found to degrade chlorite to chloride and molecular oxygen, and the misleading and chemically incorrect name chlorite dismutase (Cld) was assigned to it.[1] As it was initially found in PCRBs, it was attributed a role of protecting PCRBs from accumulation of harmful chlorite. In recent years, homologous proteins were found in many other bacterial and archaeal phyla. Reconstruction of the phylogeny of chlorite dismutases as well as elucidation of X-ray structures revealed the presence of two main clades of active enzymes as well as similarities in overall fold and heme cavity architecture with another relatively new family of so-called dye-decolorizing peroxidases.[2−8]

X-ray structures are available for representatives of both phylogenetically separated main Cld lineages. Three-dimensional structures of Clade 1 comprise homopentameric Clds from *Dechloromonas aromatica* (PDB codes 3QO8, 3QO9: 3.05 and 3.0 Å resolution, respectively)[5] and "*Candidatus* Nitrospira defluvii" (3NN1, 3NN2: 1.85 and 1.94 Å resolution, respectively)[6] and homohexameric Cld from *Azospira oryzae* (2VXH: 2.1 Å),[7] whereas Clade 2 Clds seem to be homodimeric proteins [Cld from *Nitrobacter winogradskyi* (3QPI: 2.1 Å)[8]]. Besides differences in oligomeric architecture, Clds of Clades 1 and 2 exhibit differences in subunit structure[5−8] as well as in conformational and thermal stability.[9] Despite these disparities in overall structure and stability, the heme binding cavity provides an almost identical environment

Received: August 1, 2013
Revised: December 23, 2013
Published: December 23, 2013

   dx.doi.org/10.1021/bi401042z | *Biochemistry* 2014, 53, 77−89

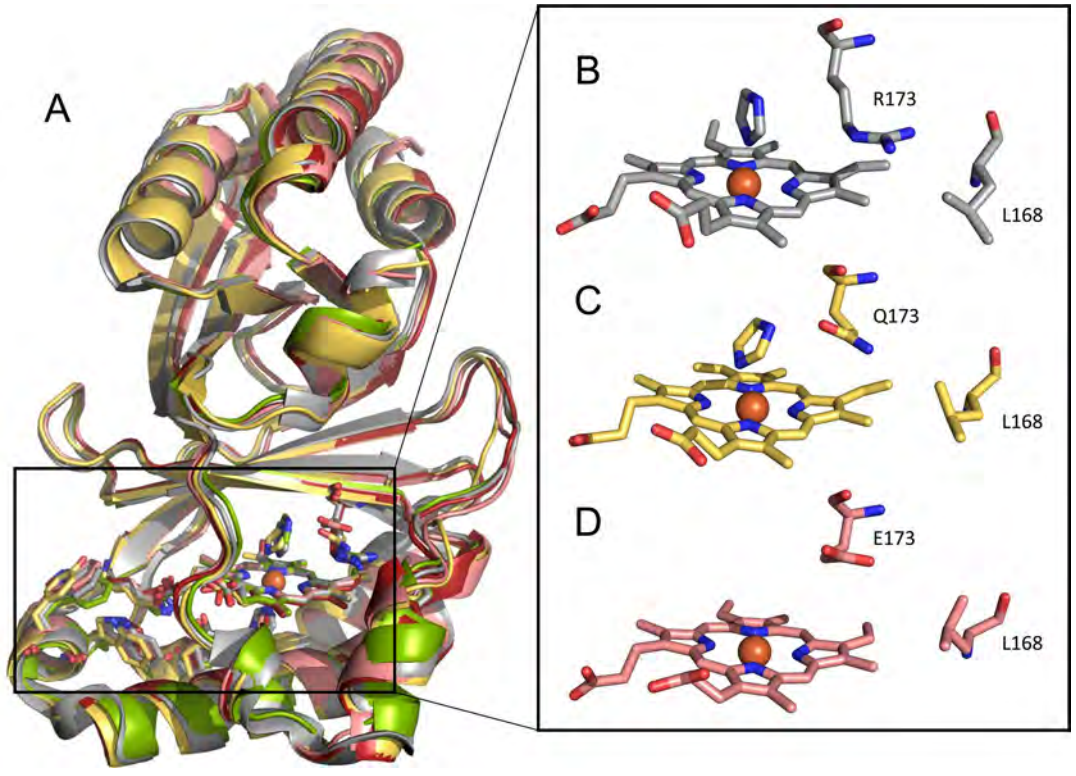

Figure 1. Overlay of subunit and distal heme architecture of NdCld wild-type and variants. (A) Cartoon representation of NdCld wild-type and the variants R173E, R173QW146Y, W145V, and W145F with the respective heme and active site residues represented as sticks. (B–D) Enlargement of the distal heme side of NdCld wild-type (B), and variants R173QW146Y (C) and R173E (D). Figures were generated using PyMOL (http://www.pymol.org/).

in Clds from both clades.[5−8] This is supported by the fact that both the high-spin and low-spin forms of Clds from *Candidatus Nitrospira defluvii* (NdCld) and *Nitrobacter winogradskyi* (NwCld) exhibit similar standard reduction potentials of the Fe(III)/Fe(II) couple[10] as well as similar chlorite degradation activity (NdCld: $k_{cat}/K_M = 6.2 \times 10^5\ M^{-1}\ s^{-1}$; NwCld: $k_{cat}/K_M = 2.1 \times 10^6\ M^{-1}\ s^{-1}$) .[6,8]

The prosthetic group in chlorite dismutases is heme *b*, which is proximally coordinated by a histidine (His160, NdCld numbering) that is hydrogen-bonded to a glutamate residue (E210). This couple of amino acids, together with neighboring lysine (K141) and two tryptophan residues (W145, W146), are found in all structures of functional Clds solved so far (Figure 1).[5−8] The most prominent and fully conserved amino acid residue on the distal side of functional Clds is an arginine (R173). Its side chain is flexible and is found in diverse conformations in crystal structures of Clds: either pointing away from the heme *b* iron toward the putative substrate entrance[6,8] or oriented toward the active site.[5,7] The latter conformation seems to be stabilized by anionic ligands.[6] Being the only charged residue in the distal side, R173 was proposed to participate in the chlorite degradation mechanism. Namely, R173 was suggested to be involved in substrate binding and reduction as well as in stabilization of the transient intermediate hypochlorous acid (reaction 1).[6,11]

The following redox pathway has been proposed based on a few studies.[11−14] The native ferric heme enzyme is oxidized to a transient intermediate (compound I) state, which — in analogy to conventional heme peroxidases — was suggested to be an oxoiron(IV)porphyryl radical [$Por^{\bullet+}Fe(IV)$=O] (reaction 1).[12] The reaction product hypochlorous acid must be kept close to the oxoferryl-oxygen since it serves as two-electron donor, thereby restoring the Fe(III)-state and releasing chloride and dioxygen (reaction 2). In the second half-reaction, an O–O bond is formed, a reaction so far only described in the water-splitting manganese complex of photosystem II of oxygenic phototrophic organisms[15] and in a yet uncharacterized enzyme of an anaerobic methane-oxidizing bacterium.[16]

$$PorFe(III) + [O\text{-}Cl\text{-}O]^- \rightarrow Por^{\bullet+}Fe(IV) = O\cdots[O\text{-}Cl^-] \quad (1)$$

$$Por^{\bullet+}Fe(IV) = O\cdots[O\text{-}Cl^-] \rightarrow PorFe(III) + O = O + Cl^- \quad (2)$$

Proof of reactions 1 and 2 requires the characterization of the electronic and spectral properties of the involved (transient) redox states and reaction products, the kinetics of interconversion and the role(s) of the conserved heme cavity residues in these reactions. Two Clds have been used for those studies so far, namely, chlorite dismutases from *Dechloromonas aromatica* (DaCld)[11,17] and NdCld,[6] suggesting a catalytic role for the distal arginine[6,11] and the formation of protein radical(s).[17] Notably, DaCld and NdCld show tremendous spectral differences [e.g., the Soret maximum at pH 7.0 has been reported to be at 393 nm (DaCld)[17] and 408 nm (NdCld)[10]]. Diverse spectral properties could be related to significant differences in the conformational and thermal stability of enzymes in solution,[9] since the crystal structures[5,6] show an almost identical heme cavity architecture. Six crystal structures of NdCld variants were solved successfully [see ref 6 and this work], whereas no structures of DaCld mutants are reported.[11,17]

dx.doi.org/10.1021/bi401042z | *Biochemistry* 2014, 53, 77−89

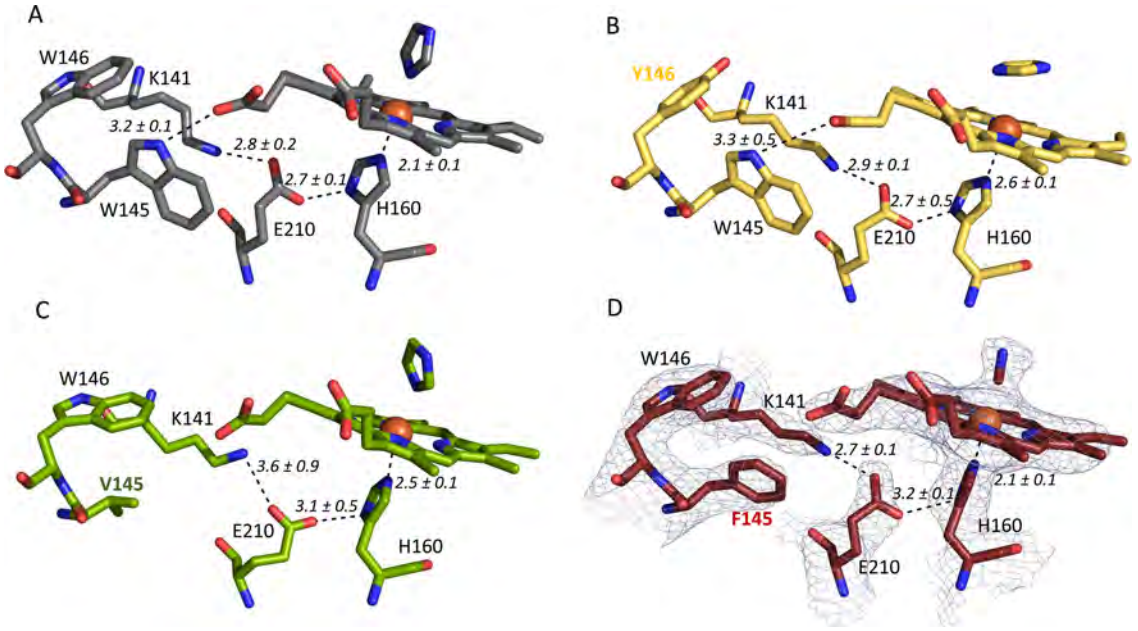

Figure 2. Architecture of the proximal heme side of wild-type NdCld (A) and the variants W146Y (B), W145V (C) and W145F together with its 2|F_o| − |F_c| electron density map countered at 1σ level (D). Figures were generated using PyMOL (http://www.pymol.org/). Putative H-bonds are shown as dotted black lines.

In this study we have analyzed the role of residues suggested to be important for the catalysis of chlorite degradation (R173, E210, K141, W145, and W146) (Figures 1 and 2), with special emphasis on the role of conserved residues on the proximal side and further evaluation of the distal arginine. The single mutants R173E, R173Q, E210A, K141E, W145F, W145V, W146Y and the double mutants W145V/W146Y, R173Q/E210A, and R173Q/W146Y were recombinantly produced in *Escherichia coli* and thoroughly biochemically characterized. Recombinant production and first characterization of distal mutants R173A and R173K were reported previously[6] and are studied more extensively in this work. In detail, the effect of mutation(s) on the UV−vis spectra, the redox properties of the Fe(III)/Fe(II) couple, the enzymatic parameters of chlorite degradation (K_M, k_{cat}, and k_{cat}/K_M) as well as the kinetics of cyanide binding were analyzed. Moreover, mutants R173E, W145V, W145F as well as R173Q/W146Y were structurally characterized using X-ray crystallography. The structures of these mutants together with already available structures of wild-type NdCld and the variants R173A and R173K[6] and the obtained biochemical/physical data allow a comprehensive structure−function analysis of this new enzyme family. The importance of R173 in the chlorite degradation reaction and formation of the Cld-cyanide complex is demonstrated and discussed as is the role of the K141-E210-H160 triad in maintenance of the heme cavity architecture and redox properties.

MATERIALS AND METHODS

Site-Directed Mutagenesis, Expression, and Purification. To obtain plasmids for expressing the NdCld variants R173A, R173K, R173E, R173Q, E210A, K141E, W145F, W145V, W146Y mutagenesis was carried out using Phusion-Flash polymerase (Finnzymes) with primers and their reverse complements listed in Supplemental Table 1, Supporting Information. The plasmid encoding the N-terminal TEV-cleavable Strep-II tagged fusion protein wild-type NdCld (without the N-terminal signal peptide) was used as template. Cloning of the wild-type NdCld plasmid was described previously.[6] To obtain plasmids for expressing the double mutated NdCld proteins R173Q/W146Y and R173Q/E210A, the plasmid of R173Q was used as a template. Similarly, for the double mutant W145V/W146Y the plasmid of W146Y was used as template (Supplemental Table 1). Total volume of mutagenesis PCR was 20 μL and a two-step thermocycle was followed (98 °C for denaturation, 72 °C for annealing and elongation). Original templates were digested with *DpnI* (Fermentas) and PCR product was transformed into *E. coli* DH5α cells (Invitrogen). Plasmid DNA was extracted using GeneJET Plasmid Miniprep Kit (Fermentas), and sequencing was performed from T7prom and T7term by LGC Genomics to confirm successful site-directed mutagenesis.

Recombinant wild-type NdCld was expressed in *E. coli* Tuner (DE3) cells (Merck/Novagen, Darmstadt, Germany) and purified via a StrepTrap HP 5 mL (GE Healthcare) column as it was described previously.[9] All mutants were expressed and purified using the same protocol as for the wild-type protein.

Crystallization, Data Collection, and Processing. The NdCld variants W145V, R173Q/W146Y were concentrated to 10 mg/mL and stored in buffer (20 mM HEPES, pH 7.4, 2% glycerol) and crystallized in conditions containing high ammonium sulfate and low pH ranges from 3.5 to 4.5 (derived from condition 13 of JCSG+ commercial screen, Qiagen), which is similar to crystallization conditions of the wild-type NdCld.[6] For cryoprotection, the crystal was soaked stepwise in the mother liquor containing increasing concentrations (10%) of ethylene glycol up to final 50% (v/v). The mutant R173E was crystallized in 0.1 M sodium acetate, pH 4, and 40% (v/v) ethylene glycol (condition 2 from the Cryol+II screen, Emerald Biosciences), which already served as a cryoprotectant. W145F with and without cyanide was crystallized in 0.7−0.8 M ammonium citrate dibasic in 100 mM sodium acetate buffers pH 4.4−4.5 and 30% (v/v) ethylene glycol.

Diffraction data were collected either in-house on a Bruker Microstar (Bruker AXS Inc.) rotating anode at 1.54 Å

dx.doi.org/10.1021/bi401042z | *Biochemistry* 2014, 53, 77−89

Table 1. Data Collection and Refinement Statistics[a]

	NdCld R173E	NdCld W146Y R173Q	NdCld W145F +CN	NdCld W145F	NdCld W145V
PDB code	4m05	4m09	4m06	4m07	4m08
wavelength (Å)	0.976	0.872	0.872	0.872	1.54
resolution range (Å)	44.22−2.28 (2.36−2.28)	44.38−2.45 (2.54−2.45)	43.45−2.6 (2.69−2.60)	43.55−2.5 (2.59−2.50)	63.15−2.80 (2.90−2.80)
space group	*C* 1 2 1	*C* 1 2 1	*C* 1 2 1	*C* 1 2 1	*P* 32 2 1
unit cell	136.47 112.39 119.25 90 117.8 90	138.1 114.98 118.87 90 118.1 90	136.21 113.42 118.84 90 117.9 90	138.29 112.61 120.32 90 118.5 90	145.83 145.83 137.225 90 90 120
total reflections	707036 (40837)	190696 (17024)	340749 (17213)	148231 (5141)	1490427 (89611)
unique reflections	72249 (6981)	59228 (5551)	47172 (3833)	48975 (2676)	41940 (4097)
multiplicity	9.8 (5.8)	3.2 (3.1)	7.2 (4.5)	3.0 (1.9)	35.5 (21.9)
completeness (%)	99.60 (96.78)	98.29 (92.58)	96.00 (78.55)	87.29 (48.08)	99.92 (99.39)
mean $I\sigma(I)$	5.30 (0.23)	5.69 (0.39)	10.01 (0.38)	12.64 (0.23)	23.34 (2.08)
Wilson *B*-factor	30.0	33.7	59.8	52.9	49.8
R-merge	0.371 (6.865)	0.1964 (3.48)	0.1423 (3.495)	0.06243 (3.033)	0.1957 (1.657)
R-meas	0.3915	0.2366	0.1532	0.07519	0.1984
$CC_{1/2}$	0.993 (0.129)	0.99 (0.231)	0.998 (0.149)	0.999 (0.148)	0.998 (0.817)
CC*	0.998 (0.478)	0.998 (0.613)	0.999 (0.509)	1 (0.508)	0.999 (0.948)
R-work	0.2680 (0.4283)	0.2774 (0.4470)	0.2111 (0.4901)	0.2050 (0.4511)	0.2205 (0.2922)
R-free	0.3201 (0.4562)	0.3325 (0.4377)	0.2584 (0.4906)	0.2535 (0.4491)	0.2798 (0.4065)
resolution $I/\sigma(I) > 2$	2.93	2.99	2.93	2.93	2.80
R-free @ $I/\sigma(I) > 2$	0.2710	0.2894	0.2310	0.2293	0.2798
number of atoms	19584	10015	19422	19567	10082
macromolecules	9588	9544	9543	9524	9560
ligands	227	306	239	291	390
water	133	165	5	47	114
protein residues	1190	1190	1190	1188	1190
RMS (bonds)	0.009	0.003	0.005	0.008	0.004
RMS (angles)	1.160	0.751	0.944	1.101	0.783
Ramachandran favored (%)	97	96	97	95	98
Ramachandran outliers (%)	0	0.26	0	0.26	0
clash-score	4.52	6.83	3.50	3.48	5.82
average *B*-factor	73.4	68.1	92.0	94.3	62.0
macromolecules	74.1	68.9	92.5	94.8	62.4
ligands	56.5	56.0	74.9	83.1	60.6
solvent	48.4	45.5	65.8	68.7	37.1

[a]Statistics for highest-resolution shell are shown in parentheses.

wavelength or at several ESRF beamlines (ID23-1, BM14-U). Integration and scaling was done with XDS and XSCALE[18] for data collected at ESRF beamlines, while diffraction data in-house was integrated and scaled with the software package Proteum2 (Bruker AXS Inc.). Data collection statistics are summarized in Table 1.

Phasing, Model Building, Refinement, and Validation of the Structures. All structures were solved by molecular replacement using the program MOLREP.[19] Chain A from the wild-type NdCld structure (3NN1)[6] was used as search template.

Model building and refinement steps were performed with PHENIX suite[20] and COOT.[21] The overall structure quality was judged with the web server MOLPROBITY.[22] Refinement statistics are summarized in Table 1.

In assessing the data quality and establishing the resolution cutoff we relied on novel, recently published criteria based on correlation coefficient $CC_{1/2}$.[23] We then performed a controlled paired-refinement,[23,24] where the starting model was refined using the same refinement protocol against both a full data set and a truncated version (to 2.85−2.95 Å) of the full data set. The resulting two models were then compared in terms of *R* values (R_{work}, R_{free}) to judge which model was better (Supplemental Table 2, Supporting Information). In all cases apart from W145F CN, the paired-refinement showed superior model quality and lower R factors when high-resolution diffraction cutoff was used. In case of W145F CN we opted for the high-resolution cutoff as well, despite slightly higher *R*-factor because of good model quality and lower overall B-factors.

Structure factors and coordinates are deposited in the Protein Data Bank: R173E (entry code 4M05), W145V (4M08), W145F (4M07), cyanide complex of W145F (4M06), and R173QW146Y (4M09), respectively.

UV−vis Spectroscopy. Spectra of wild-type NdCld and mutants were recorded between 250 and 800 nm with an Agilent 8453 diode array spectrophotometer (Hewlett-Packard). Protein concentration varied between 10 and 25 μM in 50 mM phosphate buffer, pH 7.0 . The enzymes were reduced with 10 mM sodium dithionite from a freshly prepared stock solution.

Steady-State Kinetics. Chlorite dismutase mediated degradation of chlorite was monitored by measuring the release of O_2 using a Clark-type oxygen electrode (Oxygraph Plus; Hansatech Instruments, Norfolk, United Kingdom) inserted into a stirred water bath kept at 30 °C. The electrode was

dx.doi.org/10.1021/bi401042z | *Biochemistry* 2014, 53, 77−89

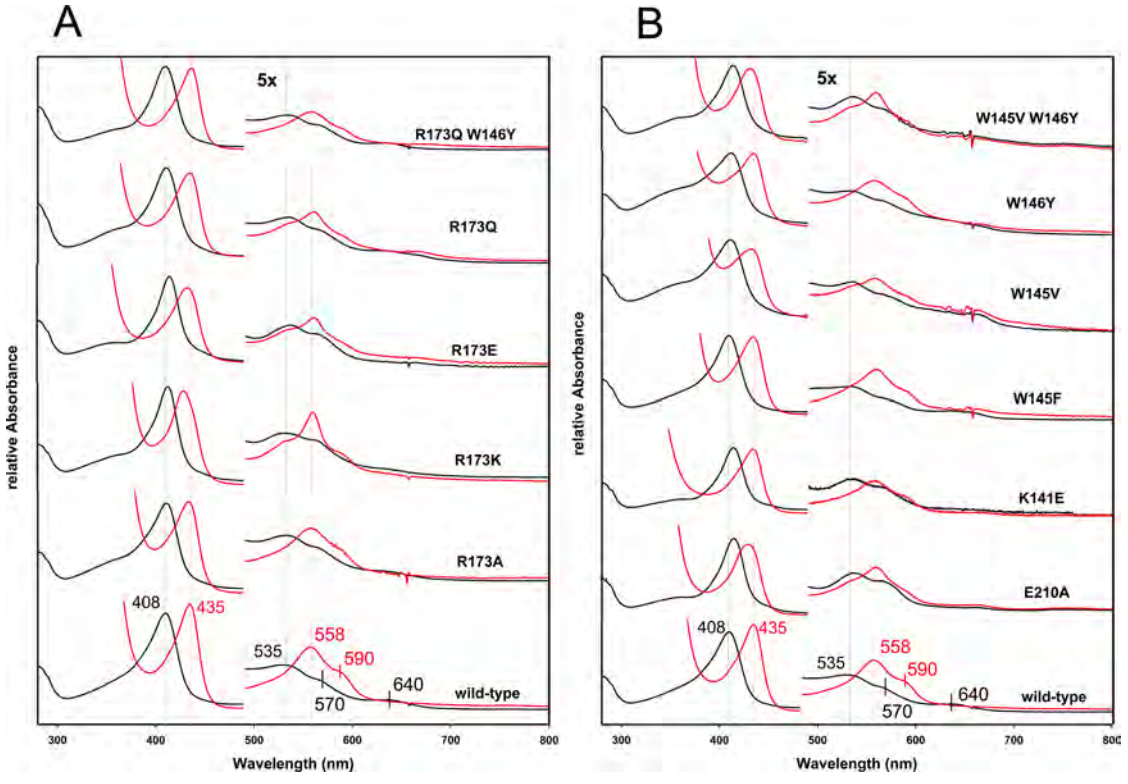

Figure 3. UV−vis spectra of NdCld wild-type and mutant proteins in oxidized (ferric) and reduced (ferrous) states at pH 7.0. (A) UV−vis spectra of distal side variants including the double mutant R173Q/W146Y. (B) UV−vis spectra of proximal side variants. Spectra of ferric proteins are depicted in black, and those of ferrous forms are in red.

equilibrated to 100% O_2 saturation by bubbling O_2 to the reaction mixture for at least 10 min and for 0% saturation by bubbling with N_2 for at least 15 min to derive an offset and calibration factor. Reactions were carried out in O_2-free 50 mM phosphate buffer, pH 7.0, with 10 μM to 2 mM $NaClO_2$ added from a stock made in the same buffer. Reactions were started by addition of 20 nM of wild-type NdCld or 200−400 nM of mutants. With increasing chlorite concentrations, irreversible inactivation of the enzyme occurred, as was evident with inspection of individual time traces. Therefore it was important to use only the initial linear phase for rate computation of the Michaelis−Menten parameters. Molecular oxygen production rates (μM O_2 s^{-1}) were obtained from initial linear time traces (<10% substrate consumed) and plotted against chlorite concentrations.

Transient-State Kinetics. The experiments were carried out with a stopped-flow apparatus (model SX-18MV, Applied Photophysics) equipped for both conventional and sequential measurements. The optical quartz cell with a path length of 10 mm had a volume of 20 μL. The fastest time for mixing two solutions and recording the first data point was 1.3 ms. All measurements were performed at 25 °C. For studies on cyanide binding to ferric wild-type NdCld and the mutants, the conventional stopped-flow mode was used, and the decrease of the absorbance at the respective Soret maximum was monitored. In a typical experiment, one syringe contained 0.5 μM enzyme in 50 mM phosphate buffer, pH 7.0, and the second syringe contained at least a 5-fold excess of cyanide in the same buffer; in detail cyanide concentrations ranged from 2.5 μM to 5000 μM. A minimum of four measurements were performed for each ligand concentration. The apparent second-order rate constants, k_{on}, were obtained from the slope of a plot of k_{obs} versus cyanide concentration. Routinely, cyanide binding was also monitored by using the diode array detector (Applied Photophysics), which allowed the synthesis of artificial sets of time-dependent spectra as well as spectral analysis of enzyme intermediates.

Spectroelectrochemistry. All experiments were carried out in a homemade optical transparent thin-layer spectroelectrochemical (OTTLE) cell.[10,25,26] The three-electrode configuration consisted of a gold minigrid working electrode (Buckbee-Mears, Chicago, IL), a homemade Ag/AgCl/KCl_{sat} microreference electrode, separated from the working solution by a Vycor set, and a platinum wire as the counter electrode.[10,24] The reference electrode was calibrated against a saturated calomel (Hg_2Cl_2) electrode before each set of measurements. All potentials are referenced to the standard hydrogen electrode (SHE, +242 mV).

Potentials were applied across the OTTLE cell with an Amel model 2053 potentiostat/galvanostat. Constant temperature was maintained by a circulating water bath, and the OTTLE cell temperature was monitored with a Cu-costan microthermocouple. UV−vis spectra were recorded using a Varian Cary C50 spectrophotometer. The OTTLE cell was flushed with Argon gas to establish an oxygen-free environment in the cell.

Spectroelectrochemical experiments were performed using 650 μL samples containing 4−6 μM of wild-type or mutant NdCld in 150 mM phosphate buffer, pH 7.0, plus 100 mM NaCl, in the presence of various mediators: methyl viologen, lumiflavine-3-acetate, methylene blue, phenazine methosulfate, and indigo carmine. The concentration of each mediator in the cell was 4.6 μM, except for methyl viologen (230 μM). Nernst plots consisted of at least five points and were invariably linear with a slope consistent with a one-electron reduction process

dx.doi.org/10.1021/bi401042z | *Biochemistry* 2014, 53, 77−89

(n-values of wild-type and mutant NdClds varied between between 1.0 and 1.4).

Variable temperature experiments for NdCld as well as for selected mutants were carried out using a nonisothermal cell configuration over a temperature range from 10 to 35 °C.[24] The temperature of the reference electrode and the counter electrode was kept constant, whereas that of the working electrode was varied. Parametrization of enthalpic and entropic components was possible by calculating $\Delta S_{rc}^{\circ\prime}$ from the slope of the plot $E^{\circ\prime}$ versus temperature; $\Delta H_{rc}^{\circ\prime}$ could be obtained from the Gibbs–Helmholtz equation, thus from the slope of the plot $E^{\circ\prime}/T$ versus $1/T$.[25,26]

RESULTS

Recombinant Production and Spectral Characterization of NdCld Variants. Native and mutated NdClds were expressed in *E. coli*. With the exception of the double mutant R173Q/E210A, the heme occupancy in all variants was higher than 85% meaning that the purity numbers (Reinheitszahlen) $A_{Soret,max}/A_{280\ nm}$ varied between 1.7 and 2.2 (Supplemental Table 3, Supporting Information).

Figure 3 shows the UV–vis spectra of oxidized (ferric) and reduced (ferrous) states of wild-type NdCld and all mutants investigated in this work. The spectroscopic properties of ferric wild-type NdCld are indicative of a dominating high-spin (HS) heme b[10] with a Soret maximum at 408 nm, Q bands at 535 and 570 nm, and a charge-transfer (CT) band at 640 nm (Figure 3 and Supplemental Table 3). Charge-transfer bands are typical for high-spin heme proteins and are located within the range 610–650 nm, with five-coordinated (5c) HS being typically ≥640 nm and six-coordinated (6c) HS around 630 nm.

With the exception of the double mutant R173Q/E210A, the Soret maxima of all variants were red-shifted (408–414 nm) compared to the native protein. The distal mutants R173K and R173E as well as the proximal variants E210A and K141E had their Soret maximum at 414 nm and did not show any absorbance in the CT region, indicating that the heme group had pronounced low-spin character.

Upon addition of cyanide to these ferric proteins, the corresponding low-spin variants were formed having the Soret maxima around 420 nm (see below), that is, red-shifted by 9–12 nm compared to the corresponding high-spin state. Concomitantly, the CT absorbance disappeared. Upon reduction by dithionite, most of the variants showed similar high-spin ferrous spectra with Soret maxima between 432 and 435 nm and Q bands at 558–560 and 590 nm (Figure 3 and Supplemental Table 3). Spectra of ferrous R173K, E210A, and the double mutant R173Q/E210A exhibited blue-shifted Soret maxima at 428, 430, and 424 nm respectively indicating the presence of ferrous low-spin species.

X-ray structures of NdCld R173E, W145V, W145F, and R173Q/W146Y. The X-ray structures of wild-type chlorite dismutase from "*Candidatus* Nitrospira defluvii" as well as the two variants R173A and R173K have been published recently.[6] In order to enable a comprehensive analysis of the structural and functional role of conserved active site residues in Clds the X-ray structures of additional variants (R173E, W145V, W145F, R173QW146Y) were determined (Figure 1). Data were collected and crystal structures were refined for R173E, W145V, and R173QW146Y. In both W145V and R173QW146Y, an imidazole served as the sixth ligand of the heme b. The mutant W145F was crystallized without and with cyanide bound to the heme iron.

W145V crystallized in the hexagonal space group $P3_221$, whereas W145F, R173E, and R173QW146Y crystallized in the monoclinic space group $C2$ (Table 1). Each subunit of wild-type NdCld and its mutants is composed of two topologically equivalent ferredoxin-like domains, as was described in detail by Kostan et al.[6] The overall structure of the subunits of the mutants does not change compared to the wild-type protein, with r.m.s.d. deviations between equivalent C_α atoms ranging from 0.310 Å for mutant W145F+CN to 0.518 Å for the R173Q/W146Y double mutant (Figure 1A).

The five subunits in the wild-type and mutant proteins are arranged in a ring-like fashion around a central channel. The active site of NdCld is located in a cavity of the C-terminal ferredoxin-like domain with heme b embedded in a defined hydrophobic environment. On the distal heme side, the only residue able to provide a positive charge, or to shift toward the active site in the presence of an anionic ligand, is Arg173. In wild-type NdCld arginine 173 was shown to be oriented away from the heme iron and points toward the putative substrate entrance (Figure 1B).[6] In the structure of the mutant R173K, the lysine side chain points into the heme cavity and forms a hydrogen bond with a trapped sulfate anion.[6] Figure 1C,D depicts the structures of R173Q and R173E with imidazole and acetate (present in crystallization solution) bound at the distal site of the heme iron. The side chain of the negatively charged glutamic residue in R173E is oriented away from the heme iron, similar to what is observed for R173 in wild-type NdCld. In the mutant protein, the side chain of L168 shifts toward E173, filling in this way the cavity occupied in the wild-type NdCld by the guanidinium group of R173 (Figure 1).

Figure 2A depicts the proximal H-bonding network of wild-type NdCld including H160-E210-K141. The H-bond between the proximal histidine and E210 (2.7 Å) keeps the heme ligand in the imidazolate state. Only small changes were observed when W146 was exchanged by tyrosine except an increase in the bond length between H160 and the heme iron (Figure 2B). The proximal NdCld variants W145V and W145F were designed with the rationale to probe the role of this fully conserved aromatic residue in redox catalysis. One of the heme propionate carboxylate groups interacts with the NE1 atom of Trp145 which might indicate the possibility of forming a radical site at this position during enzyme turnover.[5] Upon its replacement by a smaller valine, a cavity is formed (Figure 2C), and the neighboring W146 (oriented orthogonally to W145 in the wild-type Clds) is tilted by about 20° compared to the wild-type structure. Additionally, the H-bonding network within the conserved amino acid triad K141, E210, and H160 on the proximal side is weakened in the absence of W145 (Figure 2), with both K141 and E210 forming alternative H-bonds with solvent molecules. Additionally, in the mutant W145V the H-bond between E210 and H160 appears 0.6 Å longer compared to the wild-type protein (2.7 Å) (Figure 2C).

As expected, upon replacement of the W145 residue by a bulky phenylalanine, the architecture of the heme cavity is similar to wild-type NdCld, with one important difference. In the mutant W145F the H-bond between E210 and H160 is broken (length: 3.2 Å) (Figure 2D). We did not succeed in obtaining the crystal structures of NdCld K141E and E210A.

The double mutant R173Q/W146Y was designed to mimic chlorite dismutase-like proteins that differ in their active site composition from the canonical Clds, such as the Cld-like protein from *Listeria monocytogenes*. In this variant, only minor structural effects were observed (Figure 1), for example, a

dx.doi.org/10.1021/bi401042z | *Biochemistry* 2014, 53, 77–89

Table 2. Kinetics of Chlorite Degradation and Cyanide Binding of Wild-Type "*Candidatus* Nitrospira defluvii" and a Series of Distal and Proximal Heme Cavity Mutants: (A) Steady-State Kinetic Parameters of Chlorite Degradation Following the Release of O_2 Polarographically and (B) Pre-Steady-State Kinetic Parameters for Cyanide Binding (k_{on}) and Dissociation (k_{off}). The Dissociation Constant K_D Was Calculated from the Ratio k_{off}/k_{on}

	(A)			(B)			
	K_M (μM)	k_{cat} (s^{-1})	k_{cat}/K_M (M^{-1} s^{-1})	k_{on} (M^{-1} s^{-1})	k_{off} (s^{-1})	K_D (μM)	
wild-type	69 ± 6	43.0	6.2×10^5	2.6×10^6	9.3	3.6	(6)
Arg173Ala	90 ± 9	2.8	3.1×10^4	3.4×10^3	0.5	145.8	(6)
Arg173Lys	898 ± 138	14.0	1.5×10^4	1.6×10^3	0.3	185.2	(6)
Arg173Glu	195 ± 27	2.7	1.4×10^4	73	0.3	3,874	this study
Arg173Gln	130 ± 7	2.3	1.8×10^4	2.3×10^3	0.5	216.4	this study
Glu210Ala	382 ± 15	46.7	1.2×10^5	40	0.7	17,300	this study
Lys141Glu	70 ± 19	32.5	4.6×10^5	50	1.9	38,800	this study
Trp145Phe	172 ± 10	20.0	1.2×10^5	1.9×10^6	2.9	1.5	this study
Trp145Val	103 ± 11	12.0	1.2×10^5	2.7×10^5	3.9	14.6	this study
Trp146Tyr	87 ± 8	32.0	3.7×10^5	1.1×10^6	9.7	9.2	this study
Trp145Val Trp146Tyr	106 ± 23	22.0	2.9×10^5	5.3×10^5	4.6	8.7	this study
Arg173Gln Glu210Ala	184 ± 36	0.9	4.6×10^3	no binding			this study
Arg173Gln Trp146Tyr	205 ± 18	4.0	1.9×10^4	1.5×10^3	0.1	84.4	this study

change in the orientation of L168 (as in R173E, see above), while Y146 is found in the same position as W146 in wild-type NdCld.

Enzymatic Activity of NdCld Mutants with Chlorite. In order to probe the effect of exchange of active site residues of "*Candidatus* Nitrospira defluvii" on the degradation of chlorite, the release of O_2 at pH 7.0 was followed polarographically (Table 2). As long as the substrate concentration was below 1 mM (in order to avoid Cld inactivation), a typical Michaelis–Menten behavior was seen, and data could be fitted best with a single rectangular hyperbola function (Supplemental Figure 1, Supporting Information). Wild-type NdCld has a catalytic efficiency k_{cat}/K_M of 6.2×10^5 M^{-1} s^{-1} and a K_M of 69 μM. Exchange of Arg173 decreased the catalytic efficiency [wild-type (100%) > R173A (5%) > R173Q (2.9%) > R173K (2.4%) > R173E (2.3%)] and increased the Michaelis constant [wild-type (100%) < R173A (130%) < R173Q (188%) < R173E (283%) < R173K (1301%)]. It was interesting to see that (i) R173E is still able to degrade ClO_2^- to some extent (its k_{cat} is still ~6.3% of the wild-type value) and that (ii) substitution of a R173 by another basic amino acid (lysine) increased the K_M by a factor of 13 (Table 2).

From the proximal variants, W146Y exhibited an enzymatic activity very similar to the wild-type protein. Tryptophan 146 is not directly involved in the proximal H-bonding network that stabilizes heme ligation by H160. By contrast, exchange of the direct H-bonding partner (E210) of the proximal histidine by alanine leads to a decrease of the catalytic efficiency by 87% compared to the wild-type protein. The significant increase in the K_M value of the variant E210A (382 μM) compared to the wild-type enzyme reflects a more than 5-fold decrease in chlorite binding at the distal heme cavity. By comparison, the effect of disruption of the hydrogen bond between lysine 141 and glutamate 210 in the mutant K141E was relatively small (Table 2). The two variants having the fully conserved proximal tryptophan 145 exchanged (W145F and W145V) exhibit k_{cat}/K_M values of about 20% of the wild-type enzyme.

The effects of mutations in the three double variants on the enzymatic activity seemed to be additive. The double mutant R173Q/E210A has the lowest catalytic efficiency and a turnover number smaller than 1 s^{-1}. The double mutant of NdCld R173Q/W146Y, which mimics the heme cavity of the chlorite dismutase-like protein from *Listeria monocytogenes*, still has a catalytic efficiency of 1.9×10^4 M^{-1} s^{-1}.

Kinetics of Formation of the Low-Spin Cyanide Complex of Cld Variants. Cyanide is a low-spin ligand that is often used to probe the accessibility of the active site of heme proteins. Manipulation of the (distal) heme cavity architecture is often reflected by changes in both binding rates as well as in the strength of binding of cyanide to the ferric heme iron. Figure 4A shows a representative spectral conversion when ferric mutant W145F was mixed with cyanide monitored with the stopped-flow apparatus. The corresponding time trace followed at 408 nm is depicted in the inset. Cyanide converts the high-spin ($S = 5/2$) ferric iron state to the low-spin ($S = 1/2$) ferric state, thereby shifting the Soret maximum from 408 to 420 nm with a clear isosbestic point at 414 nm. The time traces could be fitted best by a double-exponential equation [obtaining pseudo-first-order rate constants $k_{obs(1)}$ and $k_{obs(2)}$; Figure 4A] with $k_{obs(1)}$ being responsible for more than 90% of the decrease in absorbance and $k_{obs(2)}$ showing no dependence on concentration of cyanide (Figure 4B, inset) as was reported for wild-type NdCld.[6] As a consequence, the apparent second-order rate (k_{on}) constant for cyanide binding was calculated from the slope of the linear plot of $k_{obs(1)}$ versus cyanide concentration (Figure 4B). In contrast, cyanide binding to distal arginine mutants R173Q, R173Q/W146Y, and R173E was monophasic, and k_{obs} was obtained by single exponential fits, which is in agreement with cyanide binding studies of R173A and R173K.[6]

Obtained data suggest that manipulation of proximal W145 and W146 only slightly affected cyanide binding at the distal side (Table 2). By contrast, in both E210A and K141E mutants cyanide binding was extremely slow, and the dissociation constant increased by 4 orders of magnitude (Table 2). Since in (i) all four variants the H-bond between E210 and H160 is extended or broken, and (ii) cyanide binding of W145F (with broken H-bond) is similar to wild-type NdCld, these

dx.doi.org/10.1021/bi401042z | *Biochemistry* 2014, 53, 77–89

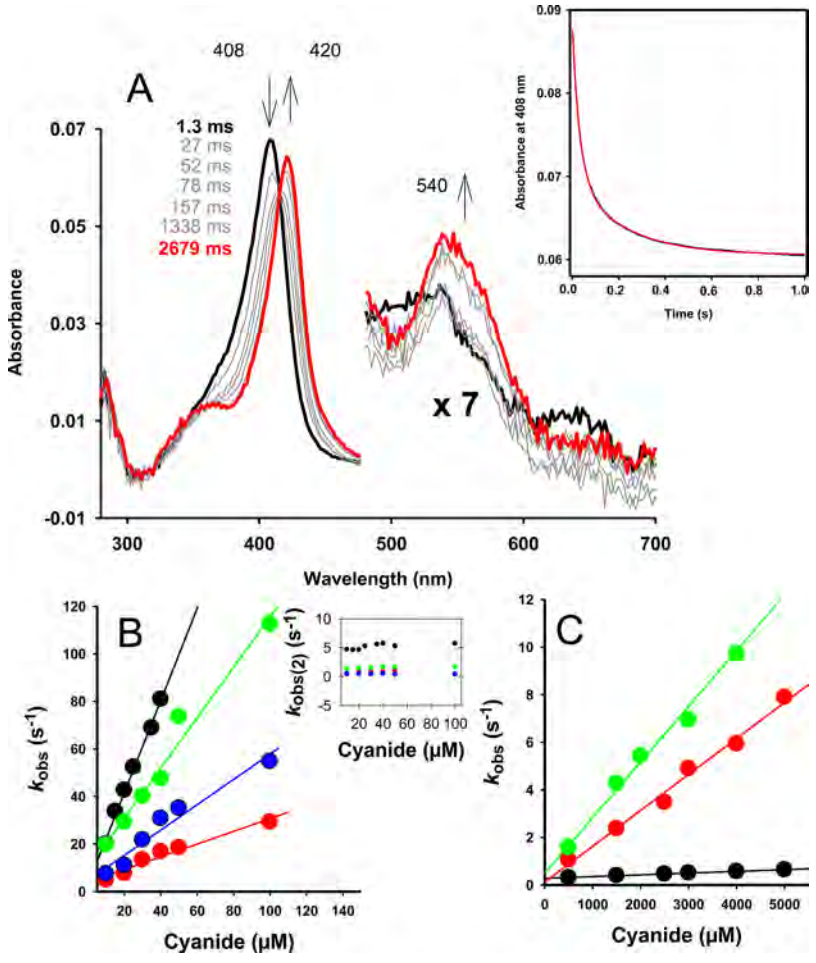

Figure 4. Kinetics of cyanide binding to ferric high-spin NdCld Trp145Phe followed by stopped-flow spectroscopy. (A) Spectral changes upon reaction of 0.5 μM NdCld W145F with 10 μM cyanide measured in the conventional stopped-flow mode. The first spectrum shows native high-spin NdCld W145F (Soret band at 408 nm), the second spectrum was recorded 1.3 ms after mixing. Subsequent spectra show the formation of the low-spin cyanide complex (absorbance maximum 420 nm). Arrows indicate changes of absorbance with time. Conditions: 50 mM phosphate buffer, pH 7.0, and 25 °C. The inset shows a typical time trace at 408 nm with double exponential fit (0.7 μM NdCld W145F and 15 μM cyanide). Linear dependence of $k_{obs(1)}$ and $k_{obs(2)}$ (inset) from the cyanide concentration is shown in (B) for NdCld W145F (black), NdCld W145V (red), NdCld W146Y (green), NdCld W145V/W146Y (blue), as well as in (C) for NdCld R173E (black), NdCld R173Q (red), and NdCld R173Q/W146Y (green).

differences in cyanide complex formation cannot be related with the imidazolate character of the proximal histidine. It is reasonable to assume that the performed mutations at E210 and K141 led to significant changes of both the proximal and distal heme cavity architecture, which is also reflected by the high low-spin character of these variants that hinders cyanide binding.

As already previously reported,[6] cyanide binding to wild-type NdCld and the variants R173A and R173K were monophasic, and exchange of R173 showed a significantly decreased bimolecular rate constant as well as increased K_D values [= k_{off}/k_{on}, with k_{off} representing the intercepts of the linear plots in Figure 4B,C]. Upon exchanging the positively charged arginine 173 with the negatively charged glutamate, cyanide binding is even more impeded, whereas the binding kinetics of NdCld R173Q and R173Q/W146Y is comparable with R173A and R173K (Figure 3C and Table 2). In any case, Table 2 demonstrates that the impact of exchange of arginine 173 on the catalytic efficiency of chlorite degradation is significantly smaller than on the binding of the low-spin ligand cyanide.

Spectroelectrochemical Analyses. Figure 5 depicts a representative family of spectra of ferric wild-type NdCld (Figure 5A) and variants R173E (Figure 5B), R173K (Figure 4C), and W145F (Figure 5D) at different applied potentials in the OTTLE cell. The pentameric wild-type metalloprotein is directly reduced to its ferrous form with absorption maxima at 435 and 560 nm with a clear isosbestic point at 420 nm. The calculated reduction potential for the Fe(III)/Fe(II) couple, determined from the corresponding Nernst plot (inset to Figure 5A), was calculated to be at −0.113 ± 0.001 V at 25 °C and pH 7.0.[10] The slope of the Nernst plot indicates that a single electron is exchanged.

Table 3 summarizes the $E^{\circ\prime}$ values obtained for the various Cld variants. The mutant R173Q exhibited a wild-type-like reduction potential, whereas exchange of arginine 173 by negatively charged glutamate shifted the reduction potential by about 120 mV to more negative values. Additionally, mutation of arginine 173 to small and uncharged alanine lowered $E^{\circ\prime}$ by 66 mV. In both R173E and R173A variants, the ferric state has been stabilized due to deletion of the positively charged guanidinium group. In all these distal mutant proteins, the

dx.doi.org/10.1021/bi401042z | *Biochemistry* 2014, 53, 77−89

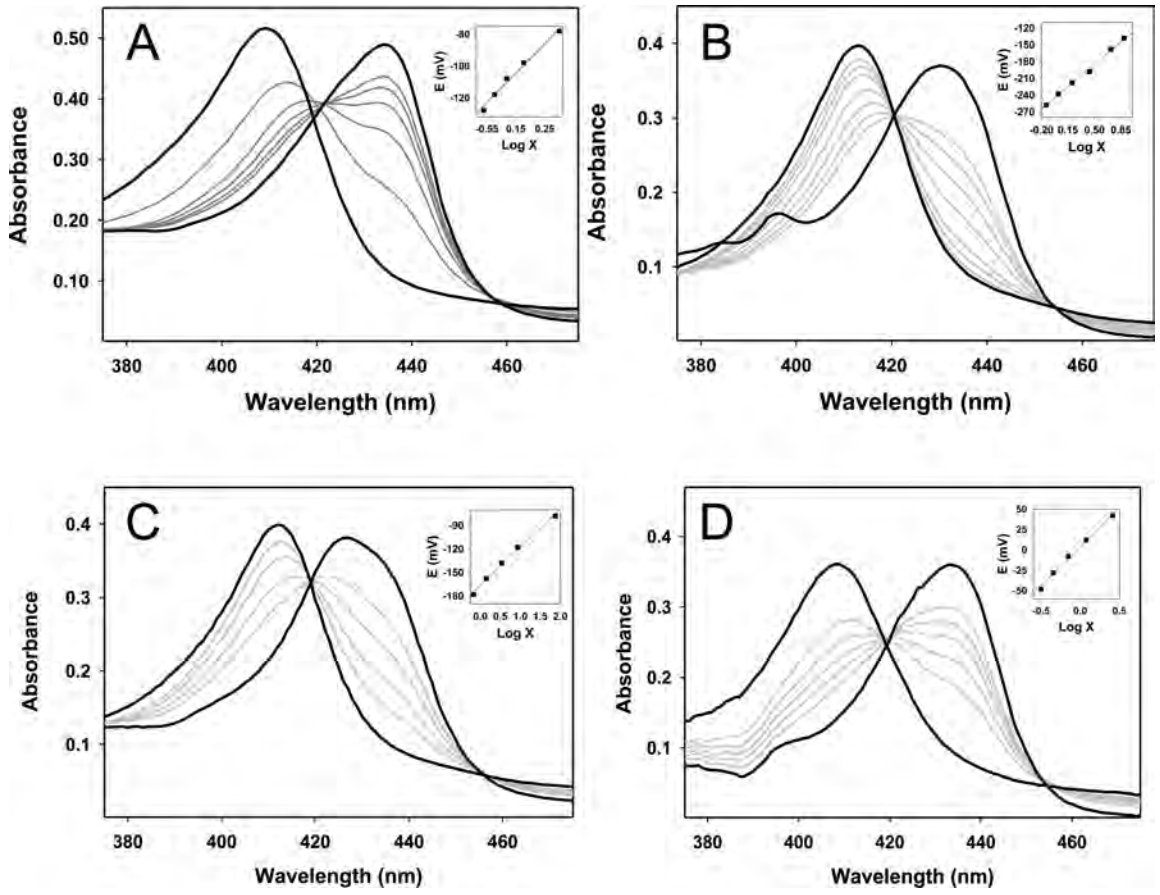

Figure 5. Spectroelectrochemistry of NdCld variants. Representative electronic spectra of (A) wild-type chlorite dismutase from "*Candidatus* Nitrospira defluvii", (B) NdCld R173E, (C) NdCld R173K, and (D) NdCld W145F at various potentials at 25 °C and pH 7.0. The insets depict the corresponding Nernst plots, were X represents the ratio $(A_{\lambda red}{}^{max} - A_{\lambda red})/(A_{\lambda ox}{}^{max} - A_{\lambda ox})$. For wild-type NdCld: λ_{ox} = 410 nm and λ_{red} = 435 nm. For the variants, the corresponding Soret maxima of the ferric and ferrous states are summarized in Table 3.

Table 3. Standard Reduction Potentials of Wild-Type Chlorite Dismutase from "*Candidatus* Nitrospira defluvii" and Distal and Proximal Heme Cavity Variants Obtained from Spectroelectrochemical Measurements[a]

	$E^{\circ\prime}$ (mV)	$\Delta H^{\circ\prime}_{rc}$ (kJ mol^{-1})	$\Delta S^{\circ\prime}_{rc}$ (J mol^{-1} K^{-1})	$-\Delta H^{\circ\prime}_{rc}/F$ (mV)	$T\Delta S^{\circ\prime}_{rc}/F$ (mV)	$-FE^{\circ\prime}$ ($=\Delta H^{\circ\prime}{}_{rc(int)}$) (kJ mol^{-1})
wild-type	−113 ± 1.0	+29 ± 6	+63 ± 20	−305 ± 60	+194 ± 60	+10.9 ± 0.1
Arg173Ala	−179 ± 1.5	ND[c]	ND	ND	ND	
Arg173Lys	−166 ± 2.0	+2 ± 32	+6 ± 31	−16 ± 304	+19 ± 114	+16.0 ± 0.2
Arg173Glu	−243 ± 1.7	ND	ND	ND	ND	ND
Arg173Gln	−117 ± 1.0	ND	ND	ND	ND	ND
Glu210Ala	*b*					
Lys141Glu	+6 ± 2.0	ND	ND	ND	ND	ND
Trp145Phe	+4 ± 1.4	+17 ± 14	+65 ± 47	−181 ± 142	+201 ± 147	−0.4 ± 0.1
Trp145Val	−84 ± 2.1	ND	ND	ND	ND	ND
Trp146Tyr	−115 ± 1.7	ND	ND	ND	ND	ND
Trp145Val	*b*					
Trp146Tyr						
Arg173Gln	*b*					
Glu210Ala						
Arg173Gln	−133 ± 0.4	ND	ND	ND	ND	ND
Trp146Tyr						

[a]In addition, for wild-type Cld and the variants R173K and W145F the enthalpic and entropic contribution to the reduction reaction has been calculated. [b]Obtained data are not reliable due to formation of the Fe−O_2 adduct. [c]ND, not determined.

maximum of the Soret band of the ferrous form was at 435 nm and no clear shoulder at 424 nm was observed, indicating no O_2 binding to the ferrous state.

At first sight, it was surprising that exchange of arginine 173 by positively charged lysine also shifts the standard reduction potential to a more negative value compared to wild-type

dx.doi.org/10.1021/bi401042z | *Biochemistry* 2014, 53, 77−89

NdCld. However, this nicely reflects the pronounced low-spin character of this variant (see Discussion).

The proximal heme cavity variants W146Y showed a wild-type like redox behavior suggesting very limiting reorganization of H160 and E210. The $E^{\circ\prime}$ value of the mutant W145V was slightly more positive ($\Delta E^{\circ\prime}$ = +29 mV) compared to wild-type NdCld. Compared to the reorganization of the proximal H-bonding pattern observed in the X-ray structure of W145V (see above), this effect is small. Exchange of tryptophan 145 by valine disrupts the H-bond between the heme propionate and the NE1 of the mutated tryptophan residue (which should lower $E^{\circ\prime}$, since the negative charge of the propionate group increases upon the disappearance of the H-bond, in which it acts as H-bond acceptor). Additionally, this mutation promotes a reorientation of the side chains of K141 and E210, resulting in a weakening of the H-bond between H160 and E210 (which should decrease the anionic character of the proximal His and increase $E^{\circ\prime}$) as seen in the X-ray structure. Most probably both effects partly compensate in W145V.

Although the overall X-ray structure of W145F was wild-type-like, one significant difference concerns the breaking of the H-bond between the proximal histidine and E210. This was nicely reflected by the measured reduction potential for the Fe(III)/Fe(II) couple, which was much more positive ($\Delta E^{\circ\prime}$ = +117 mV) compared to the wild-type enzyme. In the X-ray structure additionally a limited rearrangement of K141 is seen. Similarly, exchange of lysine 141 by glutamate increased the reduction potential by 119 mV. The effect cannot be of electrostatic origin, since in this variant K141 was replaced by a negative residue. More likely also this mutation has disrupted the interaction between E210 and H160. Thus, weakening of the H-bonding network within the triad K141-E210-H160 and especially breaking of the H-bond between E210 and H160 leads to complete loss of the imidazolate character of H160 and significantly increases the reduction potential of the Fe(III)/Fe(II) couple.

It was not possible to obtain reliable $E^{\circ\prime}$ values for the E210A as well as the double mutants W145V/W146Y and R173Q/E210A, since the corresponding ferrous states easily bound dioxygen thus not allowing exact determination of concentrations of pure ferrous forms in the equilibria. Interestingly, $E^{\circ\prime}$ of the double mutant R173Q/W146Y of NdCld (−133 mV) is slightly more negative than $E^{\circ\prime}$ the wild-type protein and of the corresponding single mutants, indicating that the effect of the two point mutations on $E^{\circ\prime}$ is not additive. This variant resembles the residues of the heme cavity of a chlorite dismutase-like protein from *Listeria monocytogenes* (Table 3).

To gain a deeper insight into the mechanism of $E^{\circ\prime}$ modulation of wild-type NdCld and the variants R173K and W145F, the temperature dependence of the reduction potential was investigated (Figure 6). This allows parametrization of the corresponding enthalpic ($\Delta H^{\circ\prime}{}_{rc}$) and entropic ($\Delta S^{\circ\prime}{}_{rc}$) components of the reduction reaction.[25,26] Fe(III) reduction enthalpy and entropy for wild-type NdCld and for its R173K and W145F mutants are invariantly positive (Table 3). Therefore, in all proteins the reduction potential is the result of two opposing contributions: an enthalpic term, which disfavors Fe(III) reduction, and an entropic contribution, which instead favors Fe(III) reduction. Thus, the enthalpy and entropy changes partially compensate. The negative $E^{\circ\prime}$ of native Cld is due to the large enthalpic term (+29 kJ mol^{-1}), which overcomes the smaller, yet relevant, entropic contribution (+63 J K^{-1} mol^{-1}). The significant enthalpic stabilization

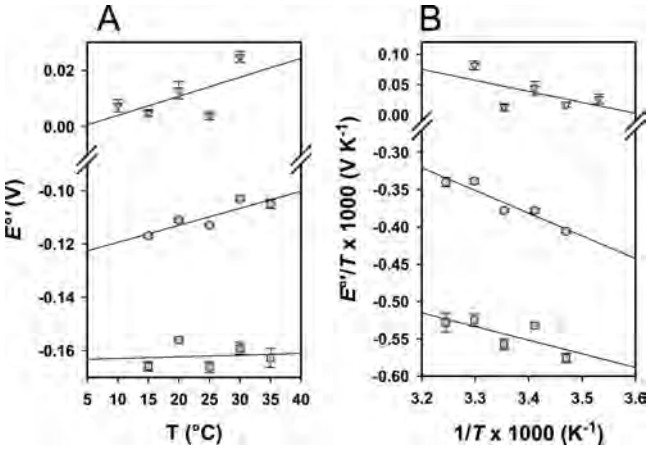

Figure 6. Reduction thermodynamics of wild-type NdCld and the variants R173K and W145F. (A) Temperature dependence of the reduction potential and (B) $E^{\circ\prime}/T$ versus $1/T$ plots for wild-type NdCld (circles), NdCld R173K (squares) and NdCld W145F (diamonds). The slope of the plot yields the $\Delta S^{\circ\prime}_{rc}/F$ (A) and $-\Delta H^{\circ\prime}_{rc}/F$ (B) values, respectively. Solid lines are least-squares fits to the data points. All experiments were carried out in 150 mM phosphate buffer, pH 7.0, containing 100 mM NaCl.

of the ferric enzyme is consistent with the anionic character conferred to the proximal histidine by the H-bond network formed with the E210 and K141. Compared to plant heme peroxidases, this effect seems to be partially offset by mutation-induced deletion of the hydrogen bond connecting one of the heme propionates with the ring of the native tryptophan and by the increased hydrophobicity of heme pocket.[25] The positive reduction entropy of native Cld is consistent with reduction-induced solvent reorganization effects in the catalytic site, since the decreased electrostatic interaction of the metal ion in its reduced form with the water molecules in the cavity should lead to a decrease in ordering.[25,26] Further contributions to the positive $\Delta S^{\circ\prime}{}_{rc}$ value could arise from a reduction-induced increase of the flexibility of the side chain of R173.

The relevant increase in the reduction potential of the Fe(III)/Fe(II) couple induced by the W145F mutation [$\Delta E^{\circ\prime}$ (mutant − wild-type) = +117 mV] has a fully enthalpic origin. In fact, replacement of the native tryptophan residue with a phenylalanine significantly reduces $\Delta H^{\circ\prime}_{rc}$, but does not modify $\Delta S^{\circ\prime}_{rc}$. This is consistent with the structural effects of the present mutation, which are limited to the proximal heme site and cause the breaking of the H-bond between H160 and E210, thereby decreasing the anionic character of the latter.

Surprisingly, replacement of R173 with a lysine deeply alters the reduction thermodynamics of the Fe(III)/Fe(II) couple. In fact the $E^{\circ\prime}$ of the R173K mutant does not show any pronounced temperature dependence (please note in Table 3 the big errors, which are a consequence of the very small impact of temperature on $E^{\circ\prime}$). This behavior again reflects the pronounced low-spin character of the mutant R173K (see above), which diminishes the reduction induced reorganization within the heme site.[25,26]

DISCUSSION

Chlorite dismutases constitute a novel heme enzyme family with a structurally unique active site and peculiar enzymatic properties. Being first described in perchlorate-respiring bacteria[1] that actually produce chlorite as metabolic inter-

dx.doi.org/10.1021/bi401042z | *Biochemistry* 2014, 53, 77−89

mediate, it has been found that other bacterial groups such as nitrite-oxidizing bacteria and cyanobacteria also encode this enzyme, and the chlorite-degrading activity of Clds from nitrite oxidizers was demonstrated.[6,8−10] As these organisms are not known PCRB, and it appears to be rather unlikely that chlorite is the main *in vivo* substrate of their Clds. This raises the question about the physiological role of functional Clds in these organisms and the nature of the oxidant and electron donor that catalyzes reactions 1 and 2 in these organisms. In order to address these challenging questions and identify candidate substrates other than chlorite, it is important to first understand the impact of active site residues on the well-established chlorite degradation activity. This was the aim of this study.

Three papers that report on mutational analyses of Cld functionality have been published so far using DaCld (chlorite dismutase from perchlorate-respiring *Dechloromonas aromatica*[11,17]) and NdCld (Cld from nitrite-oxidizing "*Candidatus* Nitrospira defluvii"[6]) as model proteins. It was interesting to see that DaCld and NdCld, although having the active site residues at almost identical positions, exhibit significant differences in spectral properties and conformational stability.[6,9−11,17] As the conformational and thermal stability of NdCld is high[9] and its mutants can readily be structurally elucidated by X-ray diffraction,[6] we focused on the *Nitrospira* protein as model chlorite dismutase in this work.

In all known functional and highly efficient Clds arginine 173 is fully conserved and represents the only charged amino acid in the distal heme cavity and a role in the ClO_2^- degradation activity has been postulated.[7] It has been proposed to bind the anionic oxidant chlorite [pK_a (chlorous acid, $HClO_2$) = 1.97[27]] (reaction 1) as well as to keep the proposed anionic intermediate hypochlorite [pK_a (hypochlorous acid, HClO) = 7.53[28]] in the reaction sphere. In the presence of the guanidinium group the anionic conjugate base, that is, hypochlorite, dominates (reaction 2). Conformational flexibility of R173 as suggested by inspection of the available X-ray structures[5−8] would be compatible with this role. It was interesting to see that despite exchange of R173 by small hydrophobic alanine (R173A), neutral glutamine (R173Q), positively charged lysine (R173K), and negatively charged glutamate (R173E) the respective mutants still exhibited chlorite degradation activity with relatively similar catalytic efficiencies between 2.2 and 5% of the wild-type activity at pH 7.0. More insightful is the inspection of the steady-state turnover number, k_{cat}, and the Michaelis constant, K_M. With 14 s^{-1} R173K had still 32.5% of the wild-type turnover, followed by R173A (6.5%), R173E (6.3%), and R173Q (5.4%). By contrast, the K_M value of R173K was the highest (898 μM) followed by R173E (195 μM), R173Q (130 μM), R173A (90 μM), and the wild-type protein (69 μM). If the conserved arginine residue is critical for binding and stabilizing anionic substrates and intermediates, it seems peculiar that the positively charged lysine in the mutant R173K had an even lower affinity for chlorite than R173E. However, the spectral properties of both ferric and ferrous R173K mutant (Table 1) as well as the redox data (Table 3) suggest the existence of mainly low-spin ferric heme in R173K. A low-spin heme was also detected in the R183K mutant of DaCld.[11] The X-ray structure shows that the lysine side chain points into the heme cavity to a water molecule that coordinates the Fe(III).[6] Additionally, the lysine forms a hydrogen bond with a trapped sulfate ion from the cryo-solution.[6] The low-spin character of R173K could derive from the deprotonation of the coordinating water in close proximity to two positively charged species, that is, Fe(III) and the positively charged lysine side chain. This would be consistent with the lower reduction potential of the Fe(III)/Fe(II) couple compared to the native enzyme ($\Delta E^{\circ\prime}$ = −53 mV), as well as its nearly independence from temperature ($\Delta S^{\circ\prime}_{rc}$ close to 0 J K^{-1} mol^{-1}). Existence of a low-spin complex in R173K is also reflected by a cyanide binding rate that is 3 orders of magnitude lower and a cyanide complex dissociation constant that is 50-times higher than in wild-type NdCld (Table 2).

In the crystal structure of R173E (Figure 1), the side chain points away from the heme iron. The ferric and ferrous UV−vis spectra suggest a noticeable low-spin portion in R173E. Despite the presence of the carboxylate group, the mutant was still active and its K_M value for chlorite was only increased by a factor of 2.8. By contrast, it dramatically decreased the rate of cyanide binding as well as the stability of the resulting low-spin complex (Table 2). If R173 is exchanged by a neutral side chain, k_{cat} is decreased by a factor of about 20 (R173A, R173Q), but K_M is increased only by a factor of 1.3 (R173A) and 1.9 (R173Q). Again, this decrease in chlorite degradation activity and affinity for the anionic substrate is modest compared to the decrease in the rate of cyanide binding as well as the stability of the resulting cyanide complex.

These data suggest that the distal arginine is important for chlorite binding and reduction but not fully essential for reaction 1. Even in its absence chlorite can bind and react with the ferric enzyme. The impact of exchange of Arg173 was significantly more pronounced when the binding of cyanide was studied. At pH 7 cyanide is protonated (pK_a of HCN is 9.2) and R173 is unprotonated (pK_a of 6.5) as was demonstrated recently.[29] Arginine 173 must therefore act as proton acceptor before cyanide can bind to the Lewis acid Fe(III). Thus, R173 promotes the deprotonation reaction as well as stabilization of the resulting cyanide complex (Table 2). Binding to and oxidation of the enzyme by chlorite (pK_a = 1.97) does not need the presence of a proton acceptor, but the arginine may support the attraction of the anionic substrate to the heme cavity as well as contribute to the stabilization of the initial Fe(III)-ClO_2^- complex. It is not as essential as is the distal histidine in heme peroxidases that must deprotonate hydrogen peroxide before Compound 0 formation (i.e., Fe(III)-O-O-H complex) can occur. Most probably R173 is more important in reaction 2 for keeping hypochlorite in the reaction sphere for redox reaction with compound I. Chlorite dismutases are inactivated during degradation of chlorite, but the mechanism is unknown. It will be interesting to answer this question in the near future using the R173 mutants designed in this work.

The proximal heme cavity of functional chlorite dismutases is characterized by a conserved H-bonding network including H160-E210-K141. Its disruption significantly alters the redox properties of the heme iron as well as the ligand binding behavior at the distal side. In both E210A and K141E, cyanide binding was almost completely impaired, and in the latter variant the reduction potential was more positive than in the native enzyme. Pronounced binding to molecular oxygen of the ferrous form of E210A in the spectroelectrochemical experiments also suggests some reorganization at the distal heme cavity. In wild-type NdCld, the proximal histidine has some imidazolate character due to its H-bond to E210. Upon exchange of E210 or neighboring K141, this noncovalent bond is disrupted, H160 becomes neutral, and the electron density at the heme iron is decreased. Simultaneously, the low-spin

dx.doi.org/10.1021/bi401042z | *Biochemistry* 2014, 53, 77−89

character of the respective proteins increases (Figure 3 and Supplemental Table 3). Again, as was already observed with the R173 variants, the impact of these structural changes on the chlorite degradation capacity was much smaller compared to the impact on the formation of the Cld-cyanide complex.

Generally, the proximal H-bonding network in Clds seems to be very labile and can easily be disrupted. While the mutant W146Y showed wild-type-like biochemical and physical properties, exchange of tryptophan 145 by phenylalanine significantly increased the $E^{\circ\prime}$ value of the Fe(III)/Fe(II) couple. This can be explained by the X-ray structure of W145F that shows a complete break of the H-bond between E210 and H160 thereby decreasing the electron density at the heme iron. Thus, the proximal heme cavity architecture in chlorite dismutases is very susceptible to perturbances. This could also be the reason for the observed differences between NdCld[10] and DaCld.[17] Whereas the crystal structures[5,6] show almost identical active sites, the biophysical properties are very different. The reported Soret maximum of ferric DaCld at 393 nm might reflect disruption of the interaction between the heme iron and the proximal histidine. This assumption is also supported by recent findings with proximal mutants of DaCld[17] where the variant W155F (corresponding to W145F in NdCld) showed dramatic differences compared to wild-type DaCld including loss of the characteristic pentameric oligomerization state, secondary structure as well as of the prosthetic group. The fact that also proximal mutants of NdCld could be crystallized (whereas crystallization of DaCld variants failed[17]) suggests that recombinant NdCld is the more suitable model Cld for future mechanistic studies.

■ ASSOCIATED CONTENT

Supporting Information

Supplemental Table 1 (primers used for site-directed mutagenesis of NdCld), Supplemental Table 2 (Controlled paired-refinement statistics), Supplemental Table 3 (UV−vis spectral signatures of wild-type and mutated chlorite dismutases), and Supplemental Figure 1 (Monitoring of dioxygen release by wild-type and mutated chlorite dismutase mediated chlorite degradation). This material is available free of charge via the Internet at http://pubs.acs.org.

Accession Codes

Atomic coordinates and structure factors have been deposited in the RSCB Protein Data Bank: 4M05, 4M06, 4M07, 4M08, 4M09.

■ AUTHOR INFORMATION

Corresponding Authors

*(C.O.) Phone: +43-1-47654-6073, fax: +43-1-47654-6050, e-mail: christian.obinger@boku.ac.at.

*(K.D.-C.) Phone: +43-1-4277-52203, e-mail: kristina.djinovic@univie.ac.at.

Funding

This project was supported by the Austrian Science Foundation, FWF [Doctoral program BioToP − Molecular Technology of Proteins (W1224) and the Projects P25270 and P22276]. G.M. and J.K. were supported by the Federal Ministry of Economy, Family and Youth through initiative "Laura Bassi Centres of Expertise", funding Center of Optimized Structural Studies (Project Number 253275).

Notes

The authors declare no competing financial interest.

■ ABBREVIATIONS

Cld, chlorite dismutase; NdCld, chlorite dismutase from "*Candidatus* Nitrospira defluvii"; NwCld, chlorite dismutase from *Nitrobacter winigradskyi*; DaCld, chlorite dismutase from *Dechloromonas aromatica*; $E^{\circ\prime}$, standard reduction potential; $\Delta H^{\circ\prime}_{rc}$, enthalpy change for the reaction center upon reduction of the ferric protein; $\Delta S^{\circ\prime}_{rc}$, entropy change for the reaction center upon reduction of the ferric protein; SHE, standard hydrogen electrode

■ REFERENCES

(1) van Ginkel, C. G., Rikken, G. B., Kroon, A. G. M., and Kengen, S. W. M. (1996) Purification and characterization of chlorite dismutase: a novel oxygen-generating enzyme. *Arch. Microbiol. 166*, 321−326.

(2) Maixner, F., Wagner, M., Lucker, S., Pelletier, E., Schmitz-Esser, S., Hace, K., Spieck, E., Konrat, R., Le Paslier, D., and Daims, H. (2008) Environmental genomics reveals functional chlorite dismutase in the nitrite-oxidizing bacterium Candidatus "Nitrospira defluvii". *Environ. Microbiol. 10*, 3043−3053.

(3) Sugano, Y. (2009) DyP-type peroxidases comprise a novel heme peroxidase family. *Cell. Mol. Life Sci. 66*, 1387−1403.

(4) Goblirsch, B., Kurker, R. C., Streit, B. R., Wilmot, C. M., and DuBois, J. L. (2011) Chlorite dismutases, DyPs and EfeB: 3 microbial heme enzyme families comprise the CDE structural superfamily. *J. Mol. Biol. 408*, 379−398.

(5) Goblirsch, B. R., Streit, B. R., DuBois, J. L., and Wilmot, C. M. (2010) Structural features promoting dioxygen production by *Dechloromonas aromatica* chlorite dismutase. *J. Biol. Inorg. Chem. 15*, 879−888.

(6) Kostan, J., Sjoeblom, B., Maixner, F., Mlynek, G., Furtmüller, P. G., Obinger, C., Wagner, M., Daims, H., and Djinovic-Carugo, K. (2010) Structural and functional analysis of the chlorite dismutase from the nitrite-oxidizing bacterium *Candidatus* "Nitrospira defluvii": identification of a catalytically important amino acid residue. *J. Struct. Biol. 172*, 331−342.

(7) de Geus, D. C., Thomassen, E. A. J., Hagedoorn, P.-L., Pannu, N. S., van Duijn, E., and Abrahams, J. P. (2009) Crystal structure of chlorite dismutase, a detoxifying enzyme producing molecular oxygen. *J. Mol. Biol. 387*, 192−206.

(8) Mlynek, G., Sjöblom, B., Kostan, J., Füreder, S., Maixner, F., Gysel, K., Furtmüller, P. G., Obinger, C., Wagner, M., Daims, H., and Djinović-Carugo, K. (2011) Unexpected diversity of chlorite dismutases: a catalytically efficient dimeric enzyme from *Nitrobacter winogradskyi*. *J. Bacteriol. 193*, 2408−2417.

(9) Hofbauer, S., Gysel, K., Mlynek, G., Kostan, J., Hagmüller, A., Daims, H., Furtmüller, P. G., Djinovic-Carugo, K., and Obinger, C. (2012) Impact of subunit and oligomeric structure on the thermal and conformational stability of chlorite dismutases. *Biochim. Biophys. Acta 1824*, 1031−1038.

(10) Hofbauer, S., Bellei, M., Sündermann, A., Pirker, K. F., Hagmüller, A., Mlynek, G., Kostan, J., Daims, H., Furtmüller, P. G., Djinovic-Carugo, K., Oostenbrink, C., Battistuzzi, G., and Obinger, C. (2012) Redox thermodynamics of high-spin and low-spin forms of chlorite dismutases with diverse subunit and oligomeric structures. *Biochemistry 51*, 9501−9512.

(11) Blanc, B., Mayfield, J. A., McDonald, C. A., Lukat-Rodgers, G. S., Rodgers, K. R., and Dubois, J. L. (2012) Understanding how the distal environment directs reactivity in chlorite dismutase: spectroscopy and reactivity of Arg183 mutants. *Biochemistry 51*, 1895−1910.

(12) Hagedoorn, P. L., de Geus, D. C., and Hagen, W. R. (2002) Spectroscopic characterization and ligand-binding properties of chlorite dismutase from the chlorate respiring bacterial strain GR-1. *Eur. J. Biochem. 269*, 4905−4911.

(13) Lee, A. Q., Streit, B. R., Zdilla, M. J., Abu-Omar, M. M., and Dubois, J. L. (2008) Mechanism of and exquisite selectivity for O-O bond formation by the heme dependent chlorite dismutase. *Proc. Natl. Acad. U.S.A. 105*, 15654−15659.

(14) Streit, B. R., and DuBois, J. L. (2008) Chemical and steady-state analysis of a heterologously expressed heme dependent chlorite dismutase. *Biochemistry 47*, 5271−5280.
(15) Vinyard, D. J., Ananyev, G. M., and Dismukes, G. C. (2013) Photosystem II: The Reaction Center of Oxygenic Photosynthesis. *Annu. Rev. Biochem. 82*, 577−606.
(16) Ettwig, K. F., Butler, M. K., Le Paslier, D., Pelletier, E., Mangenot, S., Kuypers, M. M. M., Schreiber, F., Dutilh, B. E., Zedelius, J., de Beer, D., Gloerich, J., Wessels, H. J. C. T., van Alen, T., Luesken, F., Wu, M. L., van de Pas-Schoonen, K. T., Op den Camp, H. J. M., Janssen-Megens, E. M., Francoijs, K.-J., Stunnenberg, H., Weissenbach, J., Jetten, M. S. M., and Strous, M. (2010) Nitrite-driven anaerobic methane oxidation by oxygenic bacteria. *Nature 464*, 543−548.
(17) Blanc, B., Rodgers, K. R., Lukat-Rodgers, G. S., and DuBois, J. L. (2013) Understanding the roles of strictly conserved tryptophan residues in O_2 producing chlorite dismutases. *Dalton Trans. 42*, 3156−31.
(18) Kabsch, W. (2010) XDS. *Acta Crystallogr., Sect. D: Biol. Crystallogr. 66*, 125−132.
(19) Vagin, A., and Teplyakov, A. (1997) MOLREP: an Automated Program for Molecular Replacement. *Appl. Cryst. 30*, 1022−1025.
(20) Adams, P. D., Afonine, P. V., Bunkóczi, G., Chen, V. B., Davis, I. W., Echols, N., Headd, J. J., Hung, L. W., Kapral, G. J., Grosse-Kunstleve, R. W., McCoy, A. J., Moriarty, N. W., Oeffner, R., Read, R. J., Richardson, D. C., Richardson, J. S., Terwilliger, T. C., and Zwart, P. H. (2010) PHENIX: a comprehensive Python-based system for macromolecular structure solution. *Acta Crystallogr., Sect. D: Biol. Crystallogr. 66*, 213−221.
(21) Emsley, P., and Cowtan, K. (2004) Coot: model-building tools for molecular graphics. *Acta Crystallogr., Sect. D: Biol. Crystallogr. 60*, 2126−2133.
(22) Davis, I. W., Murray, L. W., Richardson, J. S., and Richardson, D. C. (2004) MOLPROBITY: structure validation and all-atom contact analysis for nucleic acids and their complexes. *Nucleic Acids Res. 32*, 615−619.
(23) Karplus, P. A., and Diederichs, K. (2012) Linking crystallographic model and data quality. *Science 336*, 1030−1033.
(24) Diederichs, K., and Karplus, P. A. (2013) Better models by discarding data? *Acta Crystallogr., Sect. D: Biol. Crystallogr. 69*, 1215−1222.
(25) Battistuzzi, G., Bellei, M., Bortolotti, C. A., and Sola, M. (2010) Redox properties of heme peroxidases. *Arch. Biochem. Biophys. 500*, 21−36.
(26) Battistuzzi, G., Borsari, M., Ranieri, A., and Sola, M. (2002) Redox thermodynamics of the Fe(III/Fe(II) couple in horseradish peroxidase and its cyanide complex. *J. Am. Chem. Soc. 124*, 26−27.
(27) Holleman, A. F., and Wiberg, N. (2007) *Lehrbuch der Anorganischen Chemie*, Vol. *102*, Berlin.
(28) Harris, D. C. (2009) *Exploring Chemical Analysis*, 4th ed., p 538.
(29) Streit, B. R., Blanc, B., Lukat-Rodgers, G. S., Rodgers, K. R., and DuBois, J. L. (2010) How active-site protonation state influences the reactivity and ligation of the heme in chlorite dismutase. *J. Am. Chem. Soc. 132*, 5711−5724.

SUPPORTING INFORMATION

Manipulating Conserved Heme Cavity Residues of Chlorite Dismutase: Effect on Structure, Redox Chemistry and Reactivity

Stefan Hofbauer[1], Kira Gysel[2], Marzia Bellei[4], Andreas Hagmüller[2], Irene Schaffner[1], Georg Mlynek[2], Julius Kostan[2], Katharina F. Pirker[1], Holger Daims[5], Paul G. Furtmüller[1], Gianantonio Battistuzzi[6], Kristina Djinović-Carugo[2,3*], Christian Obinger[1]*

[1]Department of Chemistry, Division of Biochemistry, VIBT – Vienna Institute of BioTechnology, BOKU – University of Natural Resources and Life Sciences, A-1190 Vienna, Austria,

[2]Department for Structural and Computational Biology, Max F. Perutz Laboratories, University of Vienna, A-1030 Vienna, Austria

[3]Department of Biochemistry, Faculty of Chemistry and Chemical Technology, University of Ljubljana, 1000 Ljubljana, Slovenia

[4]Department of Life Sciences, University of Modena and Reggio Emilia, 41125 Modena, Italy

[5]Department of Microbiology and Ecosystem Science, Division of Microbial Ecology, University of Vienna, A-1090 Vienna, Austria

[6]Department of Chemistry and Geology, University of Modena and Reggio Emilia, 41125 Modena, Italy

Supplemental Table 1. Primers used for site-directed-mutagenesis of NdCld.

Mutation	Primer
Arg173Ala	5′-TATCTGAAGACGGTGAAAGCAAAACTGTATCATTCGAC G-3′
Arg173Lys	5′-CTGAAGACGGTGAAAAAGAAACTGTATCATTCG-3′
Arg173Glu	5′-CCTAACTGAAGACGGTGAAAGAAAAACTGTATCATTCGACGGG-3′
Arg173Gln	5′-CTGAAGACGGTGAAACAAAAACTGTATCATTCG-3′
Glu210Ala	5′-CTGCAGCAGGTGAAGGCATTCCGCCACAATCGAC-3'
Lys141Glu	5'- GTGATCCCTATCAAGGAAGACGCGGAATGGTGG -3'
Trp145Phe	5'- GAAGGACGCGGAATTTTGGGCACTGGACCAGG -3'
Trp145Val	5'- TCCCTATCAAGAAGGACGCGGAAGTGTGGGCACTG -3'
Trp146Tyr	5'- GAAGGACGCGGAATGGTACGCACTGGAACCAGG-3'
T7prom	5′-TAATACGACTCACTATAGGG-3′
T7term	5′-CTAGTTATTGCTCAGCGGTGG-3′

Supplemental Table 2. Controlled paired-refinement statistics.A random shift of 0.3 Å was applied to coordinates, and the models refined using two different refinement protocols (with or without simulated annealing).

Protocol 1

Random shifts of 0.3 Å, remove H2O

Refinement strategy: update H2O, TLS, NCS, optimize stereochemistry, simulated annealing

W146Y R173Q

	Refined at 2.45 Å validated at 2.9 Å	Refined at 2.9 Å validated at 2.9 Å
R free	0.3069	0.3079
R work	0.2324	0.2347
Diff free-work	0.0745	0.0732
B	67.2	75.00
rama	0.3%	0.5%
rotamers	1.8%	1.0%

R173e

	Refined at 2.28 validated at 2.85 Å	Refined at 2.85 validated at 2.85 Å
R free	0.2740	0.2808
R work	0.2209	0.2248
Diff free-work	0.0531	0.0560
B	58.5	115.8
rama	0.2%	0.8
rotamers	1.1%	1.4

W145F

	Refined at 2.5 validated at 2.95 Å	Refined at 2.95 validated at 2.95 Å
R free	0.2353	0.2356
R work	0.1869	0.1855
Diff free-work	0.0484	0.0501
B	81.30	86.50
rama	0.3	0.2
rotamers	1.1	1.2

W145F CN

	Refined at 2.6 validated at 2.95 Å	Ref 2.95 validated at 2.95 Å
R free	0.2395	0.2360
R work	0.1861	0.1829
Diff free-work	0.0534	0.0531
B	84.7	92.6
rama	0	0.1
rotamers	2.2	1.7

Protocol 2

Random shifts of 0.3 Å, remove H2O

Refinement strategy: update H2O, TLS, NCS, optimize stereochemistry

W146Y R173Q

	Refined at 2.45 Å validated at 2.9 Å	Refined at 2.9 Å validated at 2.9 Å
R free	0.3064	0.3071
R work	0.2405	0.2393
Diff free-work	0.0659	0.0678
B	68.90	74.6
rama	0.5	0.7
rotamers	1.5	1.2

R173E

	Refined at 2.28 validated at 2.85 Å	Ref 2.85 validated at 2.85 Å
R free	0.2741	0.2805
R work	0.2194	0.2259
Diff free-work	0.0547	0.0546
B	71.2	77.9
rama	0.1	0.6
rotamers	1.5	1.8

W145F

	Refined at 2.5 validated at 2.95 Å	Ref 2.95 validated at 2.95 Å
R free	0.2368	0.2401
R work	0.1899	0.1943
Diff free-work	0.0469	0.0458
B	82.2	88.4
rama	0.4	0.4
rotamers	1.5	1.1

W145f CN

	Refined at 2.6 validated at 2.95 Å	Ref 2.95 validated at 2.95 Å
R free	0.2392	0.2365
R work	0.1862	0.1890
Diff free-work	0.0530	0.0475
B	85.4	92.4
rama	0.3	0.3
rotamers	1.7	1.9

Supplemental Table 3. UV-vis spectral signatures of wild-type NdCld and a series of distal and proximal heme cavity variants in their oxidized (A) and reduced (B) states. Additionally, the Reinheitszahl (purity number) of the various recombinant proteins is given.

	(A)				(B)				
	Soret (nm)	β (nm)	α (nm)	CT (nm)	Soret (nm)	Q-bands (nm)			*Reinheitszahl*
						shoulder		shoulder	
wild-type	408	535	570	640	435		558	590	2.1
Arg173Ala	410	535	570	640	435		558	590	2.0
Arg173Lys	412	535	565		428	530	560	590	2.2
Arg173Glu	413	537	570		432	530	560	590	1.9
Arg173Gln	411	537	570	640	435	530	560	590	1.7
Glu210Ala	414	536	570		430	530	560	590	1.9
Lys141Glu	414	535	570		434		558	590	2.1
Trp145Phe	409	535	575	640	434	530	560	590	2.2
Trp145Val	411	537	575	645	433	530	558	590	1.7
Trp146Tyr	411	535	569	640	434		558	590	2.1
Trp145Val/ Trp146Tyr	413	537	569	640	432	530	560	590	1.6
Arg173Gln/ Glu210Ala	406	540		625	424		560		0.9
Arg173Gln/ Trp146Tyr	408	535	570	635	435		558	590	1.8

Supplemental Figure 1. Monitoring of dioxygen release by wild-type and mutated chlorite dismutase mediated chlorite degradation. Plots of initial rates (v_0) of O_2 evolution as a function of chlorite concentration. Points (black circles) represent averages of three measurements, additionally single-rectangular hyperbola fits are shown (red lines). Conditions: 50 mM phosphate buffer, pH 7.0. (A) 25 nM wild-type NdCld; (B) 296 nM NdCld R173A; (C) 355 nM NdCld R173K; (D) 220 nM NdCld R173Q; (E) 284 nM NdCld R173E; (F) 418 nM NdCld R173Q/W146Y; (G) 260 nM NdCld W145F; (H) 130 nM NdCld W146Y; (J) 363 nM W145V/W146Y; (K) 175 nM NdCld E210A; (L) 488 nM NdCld K141E; (M) 246 nM NdCld R173Q/E210A.

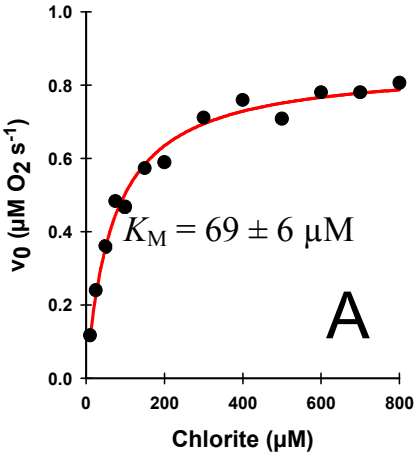
v0 (μM O2 s-1)
Chlorite (μM)
KM = 69 ± 6 μM
A

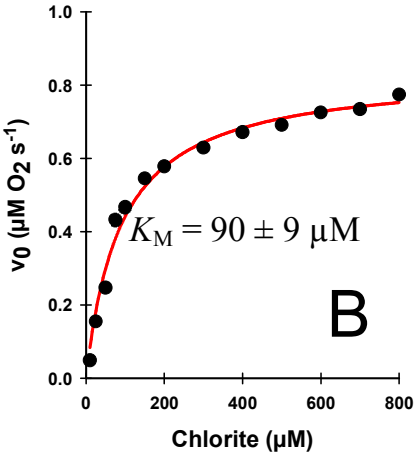
v0 (μM O2 s-1)
Chlorite (μM)
KM = 90 ± 9 μM
B

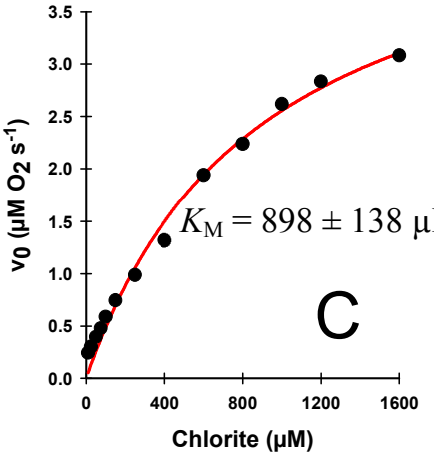
v0 (μM O2 s-1)
Chlorite (μM)
KM = 898 ± 138 μM
C

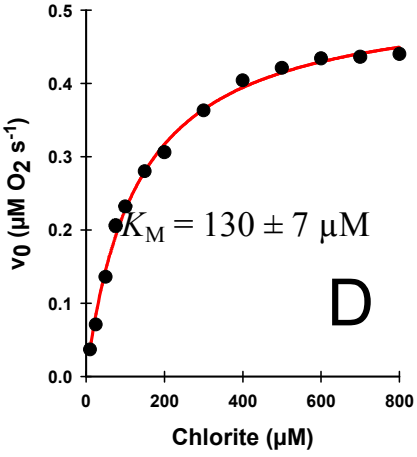
v0 (μM O2 s-1)
Chlorite (μM)
KM = 130 ± 7 μM
D

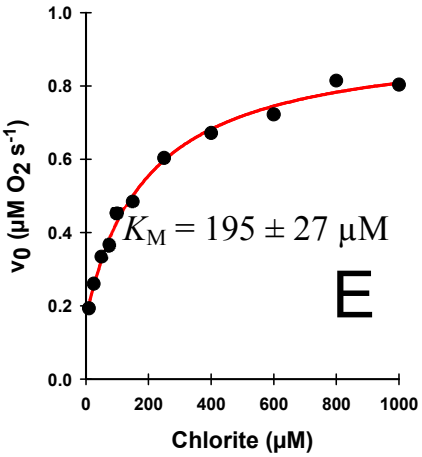
v0 (μM O2 s-1)
Chlorite (μM)
KM = 195 ± 27 μM
E

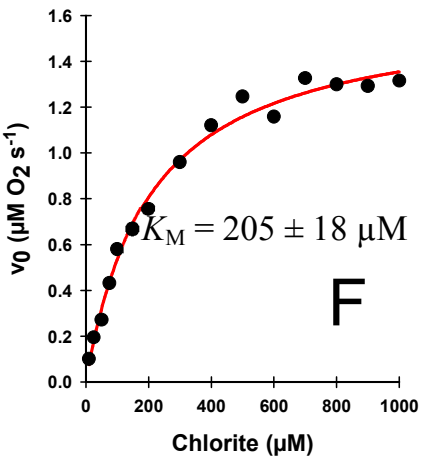
v0 (μM O2 s-1)
Chlorite (μM)
KM = 205 ± 18 μM
F

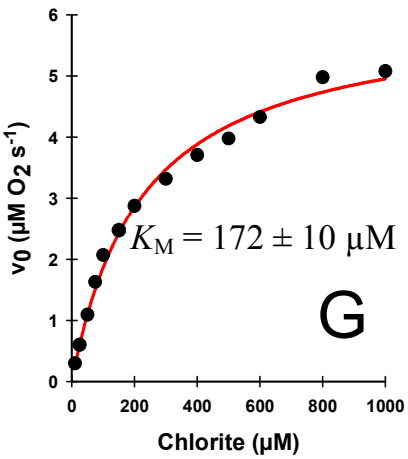
v0 (μM O2 s-1)
Chlorite (μM)
KM = 172 ± 10 μM
G

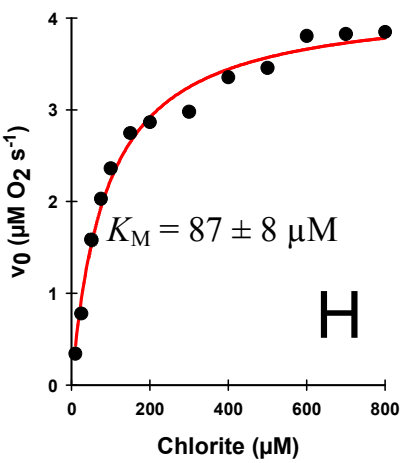
v0 (μM O2 s-1)
Chlorite (μM)
KM = 87 ± 8 μM
H

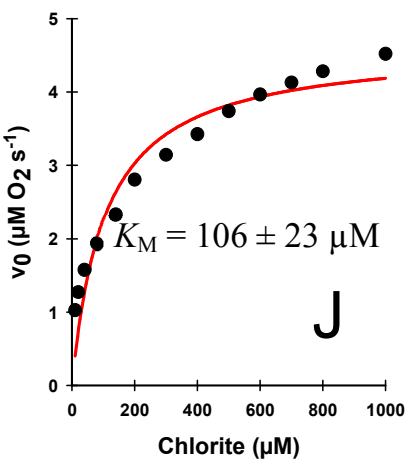
v0 (μM O2 s-1)
Chlorite (μM)
KM = 106 ± 23 μM
J

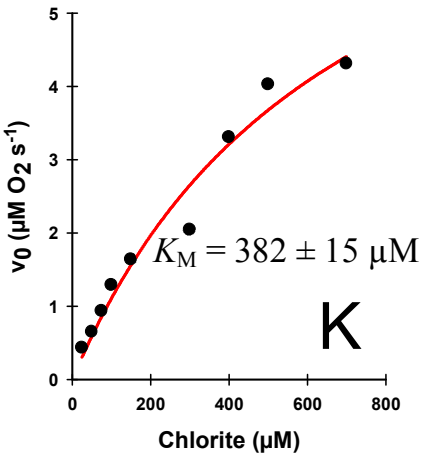
v0 (μM O2 s-1)
Chlorite (μM)
KM = 382 ± 15 μM
K

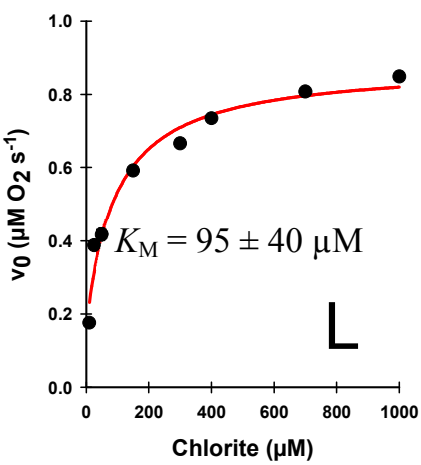
v0 (μM O2 s-1)
Chlorite (μM)
KM = 95 ± 40 μM
L

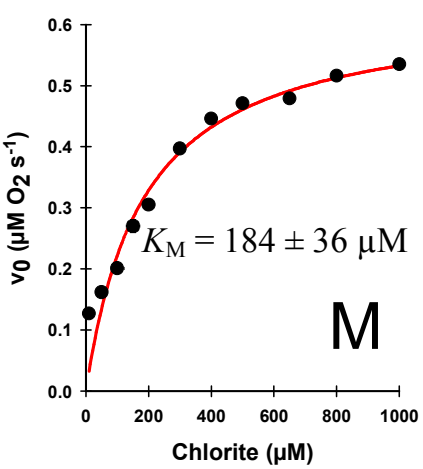
v0 (μM O2 s-1)
Chlorite (μM)
KM = 184 ± 36 μM
M

Chapter 6

Transiently produced hypochlorite is responsible for the irreversible inhibition of chlorite dismutase

Stefan Hofbauer, Clemens Gruber, Katharina F. Pirker, Axel Sündermann, Irene Schaffner, Christa Jakopitsch, Chris Oostenbrink, Paul G. Furtmüller, Christian Obinger

Research Article

Submitted to *Biochemistry*

Transiently produced hypochlorite is responsible for the irreversible inhibition of chlorite dismutase

Stefan Hofbauer[1], Clemens Gruber[1], Katharina F. Pirker[1], Axel Sündermann[2], Irene Schaffner[1], Christa Jakopitsch[1], Chris Oostenbrink[2], Paul G. Furtmüller[1], Christian Obinger[1]*

[1]*Department of Chemistry, Division of Biochemistry, VIBT – Vienna Institute of BioTechnology, BOKU – University of Natural Resources and Life Sciences, A-1190 Vienna, Austria*

[2]*Department of Material Sciences and Process Engineering, Institute of Molecular Modeling and Simulation, BOKU – University of Natural Resources and Life Sciences, A-1190 Vienna, Austria*

KEYWORDS: Chlorite dismutase, "Candidatus Nitrospira defluvii", heme cavity, enzyme kinetics, inhibition

ABSTRACT: Chlorite dismutases (Clds) are heme *b* containing prokaryotic oxidoreductases that catalyze the reduction of chlorite to chloride with concomitant release of molecular oxygen. Thereby they are irreversibly inactivated with time. In order to elucidate the mechanism of inactivation and investigate the role of the postulated intermediate hypochlorite, the pentameric chlorite dismutase of "*Candidatus* Nitrospira defluvii" (NdCld) as well as two variants (having the conserved distal arginine 173 exchanged by alanine and lysine) were recombinantly produced in *Escherichia coli*. Exchange of the distal arginine boosts the irreversible inactivation. In the presence of the hypochlorite traps methionine, monochlorodimedone and 2-[6-(4-aminophenoxy)-3-oxo3H-xanthen-9-yl]-benzoic acid, the extent of chlorite degradation and release of molecular oxygen is significantly increased, whereas heme bleaching and oxidative modifications of the protein are suppressed. Among other modifications hypochlorite-mediated formation of chlorinated tyrosines is demonstrated by mass spectrometry. Obtained data are analyzed with respect to the proposed reaction mechanism for chlorite degradation and its dependence on pH. We discuss the role of distal Arg173 by keeping hypochlorite in the reaction sphere for O-O bond formation.

INTRODUCTION

Chlorite dismutases (Clds) (EC 1.13.11.49) are heme *b* dependent oxidoreductases that can convert chlorite into chloride and dioxygen. First biochemical characterizations of Clds demonstrated that Cld does not catalyze a dismutation or disproportionation.[1] Thus the denomination chlorite "dismutase" is misleading. The reduction of chlorite to chloride has been proposed to occur in three steps starting with the addition of ClO_2^- to the heme iron [PorFe(III)] to form a Fe(III)-ClO_2^- adduct (Reaction 1), immediately followed by the oxidation of the ferric enzyme by chlorite to form Compound I [oxoiron(IV) porphyryl radical, i.e. $Por^{\bullet+}Fe(IV)=O$] and HOCl/OCl^- (Reaction 2). Finally, hypochlorite rebinds to the ferryl oxygen of Compound I and chloride and dioxygen are released (Reaction 3).[2] However, a classical Compound I spectrum typical for a heme *b* enzyme that shows hypochromicity at the Soret maximum could not be trapped so far upon mixing ferric Cld with chlorite.

$$PorFe(III) + [O\text{-}Cl\text{-}O]^- \rightarrow PorFe(III)\text{-}O\text{-}Cl\text{-}O^- \quad \text{Reaction 1}$$

$$PorFe(III)\text{-}O\text{-}Cl\text{-}O^- \rightarrow Por^{\bullet+}Fe(IV)=O...[O\text{-}Cl^-] \quad \text{Reaction 2}$$

$$Por^{\bullet+}Fe(IV)=O...[O\text{-}Cl^-] \rightarrow PorFe(III) + O=O + Cl^- \quad \text{Reaction 3}$$

Besides this mechanism that involves heterolytic cleavage of chlorite and Compound I formation (Reactions 1 and 2), density functional theory (DFT) calculations of water-soluble model iron porphyrins[3,4] suggest formation of Compound II [oxoiron(IV), i.e. Fe(IV)=O] and chlorine monoxide ($O\text{-}Cl^{\bullet}$) through homolytic cleavage of chlorite (Reaction 4). Chlorine monoxide then recombines with Compound II forming Cl^- and O_2 to complete the cycle (Reaction 5).

$$PorFe(III)\text{-}O\text{-}Cl\text{-}O^{-} \rightarrow PorFe(IV)=O...[O\text{-}Cl^{\bullet}] \quad \text{Reaction 4}$$

$$PorFe(IV)=O...[O\text{-}Cl^{\bullet}] \rightarrow PorFe(III) + O=O + Cl^{-} \quad \text{Reaction 5}$$

Crystal structures of functional (i.e. chlorite degrading) Clds[5-8] demonstrated that a fully conserved arginine [i.e. Arg173 in chlorite dismutase from "*Candidatus* Nitrospira defluvii" (NdCld)] is the only charged amino acid at the distal heme side. Extensive characterization of Arg mutants demonstrated that the basic amino acid is catalytically important but not essential for chlorite degradation.[7,9,10] Crystal structures suggest that the distal arginine is flexible and may adopt two main conformations either pointing to the entry of the main access channel into the heme cavity or directly to the heme iron. Principally, the guanidinium group could participate in all five reactions depicted above and could support substrate binding as well as potentially keep the postulated reaction intermediate hypochlorite (or O-Cl$^{\bullet}$) in the vicinity of the ferryl oxygen for the recombination step and O_2 formation. Recent mutational analysis indicated that Arg173 might be more important in stabilizing the Compound I-hypochlorite complex (Reaction 2) (or the Compound II-chlorine monoxide complex, Reaction 5) rather than supporting the binding of chlorite to the heme center.[10]

Additionally, kinetic studies on Clds from different organisms[1,2,5-8,11-15] also demonstrated that these oxidoreductases are irreversibly inhibited with time at higher chlorite concentrations. Their ability to convert chlorite to chloride and dioxygen is limited and an off-pathway was postulated based on the formation of tryptophanyl radicals on the proximal heme side of Clds[6]. Later, mutational studies on chlorite dismutases from *Dechloromonas aromatica* (DaCld)[16] and "*Candidatus* Nitrospira defluvii"[10] showed that the exchange of those conserved tryptophan residues on the proximal side did not prevent deactivation of Clds. In the corresponding DaCld mutants the heme binding properties and the oligomerization state were impaired, whereas in the corresponding NdCld mutants the reduction potential of the Fe(III)/Fe(II) couple was altered.[10]

In the present work we aimed to elucidate the mechanism of irreversible inhibition of chlorite degrading Clds. We demonstrate that chlorite to chloride degradation follows Reactions 1, 2 and 3 and that hypochlorite (and not chlorite) is responsible for heme bleaching as well as oxidation and chlorination reactions at amino acids of the protein moiety. Traps of hypochlorite like methionine, monochlorodimedon (MCD) and aminophenyl fluorescein (APF) are shown to allow complete degradation of even millimolar chlorite by NdCld and significantly increase the amount of released chloride and O_2 without affecting the catalytic efficiency. We compare the pH dependence of the enzymatic activity and the inhibitory effect and analyze the kinetics of heme bleaching by time-resolved UV-vis and electron paramagnetic resonance (EPR) spectroscopy. Hypochlorite-mediated modifications of the protein moiety are demonstrated by mass spectrometry. Mutational analysis demonstrates the important role of the conserved distal arginine in keeping the transiently produced hypochlorite in the reaction sphere for O-O bond formation according to Reaction 3. The obtained data are discussed with respect to the available biochemical/physical properties of Cld and its known high-resolution structure.

MATERIALS AND METHODS

Expression and purification. Expression and purification of StrepII-tagged TEV-cleavable NdCld wild-type and variants was reported recently[10,17].

Polarographic oxygen measurement. Chlorite dismutase-mediated degradation of chlorite was monitored by measuring the release of O_2 using a Clark-type oxygen electrode (Oxygraph Plus; Hansatech Instruments, Norfolk, United Kingdom) inserted into a stirred water bath kept at 30 °C. The electrode was equilibrated to 100 % O_2 saturation by bubbling O_2 to the reaction mixture and for 0 % saturation by bubbling with N_2 until plateaus where reached to derive an offset and calibration factor. Reactions for testing the influence of methionine were carried out in O_2-free 50 mM phosphate buffer solutions at pH 5.5 and pH 7.0, with 25 µM to 800 µM $NaClO_2$ added from a stock made in the same buffer and eventually with 5.0 mM methionine. Reactions were started by addition of 25 nM wild-type NdCld, 200 nM NdCld R173A, and 200 nM NdCld R173K, respectively. It was important to only use the initial linear phase (v_0) for calculation of rates and Michaelis-Menten parameters, because with increasing chlorite concentrations, irreversible inactivation of the enzyme occurred. This was immediately evident by inspection of the respective time traces. Molecular oxygen production rates (µM O_2 s^{-1}) were obtained from initial linear time traces (<10% substrate consumed) and plotted against chlorite concentrations for determination of catalytic parameters. Reactions were monitored for approximately 2 minutes to determine the final amount of produced oxygen. The influence of enzyme concentration was tested by starting the reaction with 5 to 500 nM wild-type NdCld, the chlorite concentration was 340 µM, eventually with 5.0 mM methionine. Reactions for the pH dependence of NdCld was carried out in O_2-free 50 mM buffer solutions from pH 4.3 (citrate-phosphate) to pH 8.3 (phosphate), with 10 µM to 1000 µM $NaClO_2$ added from a stock made in the same buffer. Reactions were started by addition of 50 nM wild-type NdCld.

Spectrophotometric monitoring of chlorite degradation. The conversion of chlorite (ClO_2^-) into chloride and dioxygen was monitored photometrically by following the decrease in absorbance at 260 nm ($\varepsilon_{260\ nm}$ = 155 M^{-1} s^{-1})[18] on a Hitachi U-3900 spectrophotometer. Reactions were carried out in 50 mM buffer solutions (pH 5.5, 7.0). Chlorite concentration was 340 µM and reactions were started by the addition of the enzyme.

Stopped-flow UV-visible spectroscopy. The experiments were carried out with a stopped-flow apparatus (model SX-18MV, Applied Photophysics) equipped for both conventional and sequential measurements. The optical quartz cell with a pathlength of 10 mm had a volume of 20 µL. The fastest time for mixing two solutions and recording the first data point was 1 or 3 ms. All measurements were performed at 25 °C. To study the impact of hypochlorite traps like methionine[19,20] or monochlorodimedone (MCD)[21] on chlorite degradation by Cld, the conventional stopped-flow mode was used following the decrease of the absorbance of MCD at 290 nm ($\varepsilon_{290\ nm}$ = 19,000 M^{-1} s^{-1}).[22] Simultaneously, the spectral changes in the Soret region of NdCld were monitored. In a typical experiment, one syringe contained 2 µM enzyme in 50 mM buffer, the second syringe contained 0 - 1 mM chlorite and eventually a hypochlorite-trap (100 µM MCD or 5 mM methionine) in the same buffer. A minimum of three measurements were performed for each substrate concentration and spectra were recorded for 20 s. To determine the amount of chlorinated MCD by transiently produced HOCl, the difference between the starting concentration and the end-concentration of MCD of each measurement was plotted against chlorite concentration. The effect of HOCl-traps on chlorite degradation was also monitored by using the diode array detector (Applied Photophysics), which allowed the synthesis of artificial sets of time-dependent spectra as well as spectral analysis of enzyme intermediates.

Trapping of hypochlorous acid with Aminophenylflurescein. As a further method to detect hypochlorous acid as intermediate in Cld catalysis we used aminophenyl fluorescein (APF) which specifically detects hypohalous acids but does not react with chlorite.[23,24] Here the HOCl-derived oxidation of APF was followed at 25 °C by measuring the fluorescence intensity at 522 nm (excitation at 488 nm). The fluorescence spectrophotometer (Hitachi F-7000) was equipped with a thermostatic cell holder for quartz cuvettes of 10 mm path length. Instrumental parameters were set as follows. Excitation wavelength was set to 488 nm, excitation and emission bandwidth at 5 nm and PMT voltage was set at 700 V, wavelength scans were recorded from 495 nm to 600 nm (scan speed: 60 nm min^{-1}). In detail, 100 nM NdCld were incubated with 0 µM to 750 µM chlorite in 50 mM phosphate buffer pH 7.0, eventually in presence of 5 mM methionine. 10 µM APF were added to the reaction mixture and incubated in the dark at room temperature for 30 minutes before measurement.

Mass spectrometry. Mass spectrometry (MS) was used to detect modifications on NdCld after treatment with either chlorite (in absence and in presence of methionine) or hypochlorite. In typical experiments 100 µM wild-type NdCld in 50 mM phosphate buffer, pH 7.0, were mixed with 500 mM chlorite (in absence or presence of 25 mM methionine). For protein analysis, 3 µg of treated and untreated wild-type NdCld and for peptide analysis, 5 µg of trypsin-digested treated or untreated NdCld were directly injected to the LC-MS system (LC: Dionex Ultimate 3000 LC, MS: Bruker, Maxis 4G, equipped with the standard ESI source). The protein was eluted by developing a linear gradient from 15 % to 70 % acetonitrile of 42 minutes (Supelco Discovery Bio Wide Pore C5 column, 50 × 0.32 mm, 3 µm packing). Data were processed using Data Analysis 4.0 (Bruker) and spectra were deconvoluted by MaxEnt.

Electron paramagnetic resonance spectroscopy. Electron paramagnetic resonance (EPR) spectroscopy was used to determine the effect of chlorite (in the presence or absence of methionine) as well as of HOCl on the electronic structure of the heme-iron. Typically, 100 µl samples were prepared in 125 mM MES buffer, pH 5.5 (final concentration), containing 30 µM wild-type NdCld, 0 - 400 mM chlorite (with eventual 17.5 mM methionine) or 0 - 23 mM HOCl. After waiting for at least 3 minutes (until reaction was completed), samples were transferred into Wilmad quartz tubes (3 mm inner diameter) and flash frozen in liquid N_2. Frozen samples were kept frozen on dry ice whilst the headspace above the sample was flushed with argon. Oxygen-free samples were frozen back to 77 K and transferred into the resonator for 10 K measurements. Spectra were recorded on a Bruker EMX continuous wave (cw) EPR spectrometer, operating at X-band (9 GHz) frequencies, equipped with a high-sensitivity resonator and an Oxford Instruments ESR900 cryostat. EPR spectra were recorded under non-saturating conditions using 2 mW microwave power, 100 kHz modulation frequency, 1 mT modulation amplitude, 41 ms conversion time, 41 ms time constant and 2048 points. Simulations of high-spin and low-spin Fe(III) forms were carried out using the software EasySpin[25] and consist of a weighted sum of simulations of the individual high-spin and low-spin compounds. The rhombicity was obtained from g_x^{eff} and g_y^{eff} [26] and the relative intensities were calculated on the basis of the simulations.

Molecular Dynamics Simulations. Molecular dynamics simulations were performed with the chlorite dismutase crystal structure from "*Candidatus* Nitrospira defluvii" (PDB: 3NN1).[7] The GROMOS molecular dynamics simulation package[27] was used in conjunction with the GROMOS 54A7 forcefield.[28] Detailed simulation settings and force-field parameters for Compound I and hypochlorite were taken from *Sündermann et al.*[29].

RESULTS

pH-dependence of chlorite degradation and the effect of methionine. Chlorite dismutases efficiently degrade chlorite to chloride and molecular dioxygen with reported K_M values at pH 7.0 varying from 69 to 260 µM, k_{cat} values from 43 to 7500 s^{-1} and k_{cat}/K_M values from 6.2 × 10^5 M^{-1} s^{-1} to 3.5 × 10^7 M^{-1} s^{-1} [30]. Figure 1 shows the pH-dependence of these enzymatic parameters for NdCld obtained from polarographic measurements of the release of O_2. In contrast to K_M (138 ± 20 µM at pH 7.0), k_{cat} (83 ± 4 s^{-1} at pH 7.0) as well as the catalytic efficiency (5.9 × 10^5

M^{-1} s^{-1} at pH 7.0) showed a clear pH-dependence with an optimum at pH 5.5. Figure 1D clearly depicts that at the pH-optimum both the initial rate of O_2 release as well as the total yield of produced dioxygen is highest. Upon increasing the pH, both the initial reaction velocity (v_o) and the yield of O_2 (which corresponds to the amount of degraded chlorite) were significantly decreased. The more chlorite was added to 50 nM NdCld the more pronounced was this effect (Figure 1D). During the reaction NdCld was irreversibly inhibited. Desalting and buffer exchange did not result in any recovery of enzymatic activity (not shown). The pH-optima of the NdCld variants R173A and R173K are also in the acidic region around pH 4.5 (Supplemental Figure 1).

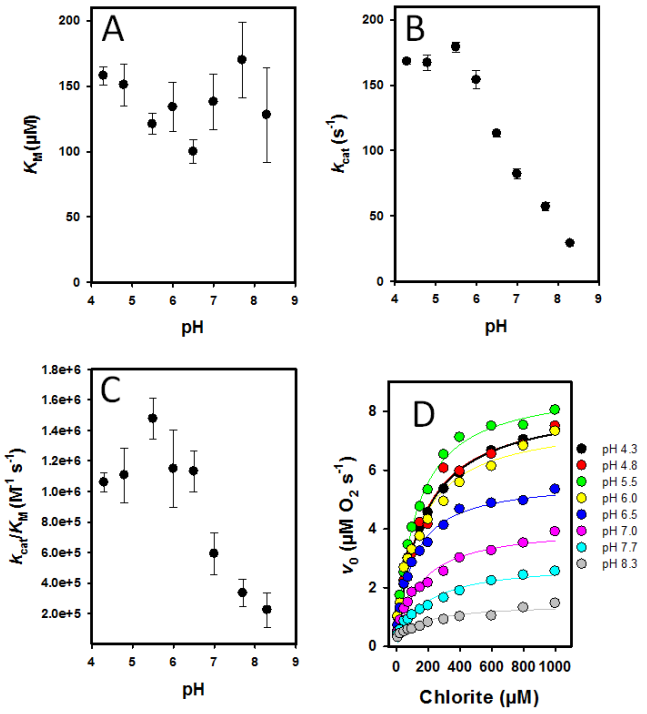

Figure 1. pH-dependence of enzymatic parameters of wild-type NdCld. Influence of pH on (A) K_M - values, (B) turnover number (k_{cat}), and (C) catalytic efficiency (k_{cat}/K_M). (D) Plot of the initial rate (vo) of release of molecular oxygen as a function of chlorite concentration at pH 4.3-8.3.

As postulated in Reactions 2 and 3 HOCl/$^-$OCl is formed during turnover. In order to test whether hypochlorite is involved in the irreversible inactivation of NdCld, the polarographic measurements were also performed in the presence of 5 mM methionine. The latter is known to react with HOCl very fast (8.7×10^8 M^{-1} s^{-1}) and efficiently,[19] whereas chlorite does not react with methionine.[24] Figures 2A and 2B compare the effect of methionine on the chlorite degradation by wild-type NdCld (20 nM) measured as the amount of O_2 released after 120 s at the pH optimum (i.e. pH 5.5) and pH 7.0. At low chlorite concentrations (<50 μM) the effect of methionine was small. However, at higher chlorite concentration in the presence of methionine the yield of O_2 increased and this effect was more pronounced at pH 7.0. These data clearly demonstrate that (i) methionine is able to partially protect NdCld from irreversible inhibition and (ii) that the inhibition reaction is boosted apart from the pH optimum.

Next, we wanted to analyze the role of arginine 173 in the inhibition reaction at pH 5.5 and pH 7.0. Compared to wild-type NdCld (K_M = 69 μM, k_{cat} = 43 s^{-1}, k_{cat}/K_M = 6.2×10^5 M^{-1} s^{-1}) the two variants R173A and R173K exhibited K_M values of 90 μM and 898 μM, k_{cat} values of 2.8 s^{-1} and 14.0 s^{-1} and k_{cat}/K_M values of 3.1×10^4 M^{-1} s^{-1} and 1.5×10^4 M^{-1} s^{-1} (pH 7.0), respectively.[30] In Figures 2C and 2D (200 nM NdCld R173A) and Figures 2E and 2F (200 nM NdCld R173K) the amount of produced O_2 after 2 min at various chlorite concentrations in the absence and presence (5 mM) of methionine at pH 5.5 and 7.0 is plotted. The data clearly demonstrate that in the absence of the distal arginine 173 NdCld is much more prone to inactivation (despite a 10-times higher enzyme concentration in the assays) both at pH 5.5 and pH 7.0 {$[O_2]/[chlorite]$ ratio of wild-type NdCld >> R173K > R173A} and that methionine can rescue also the variants at least to some extent.

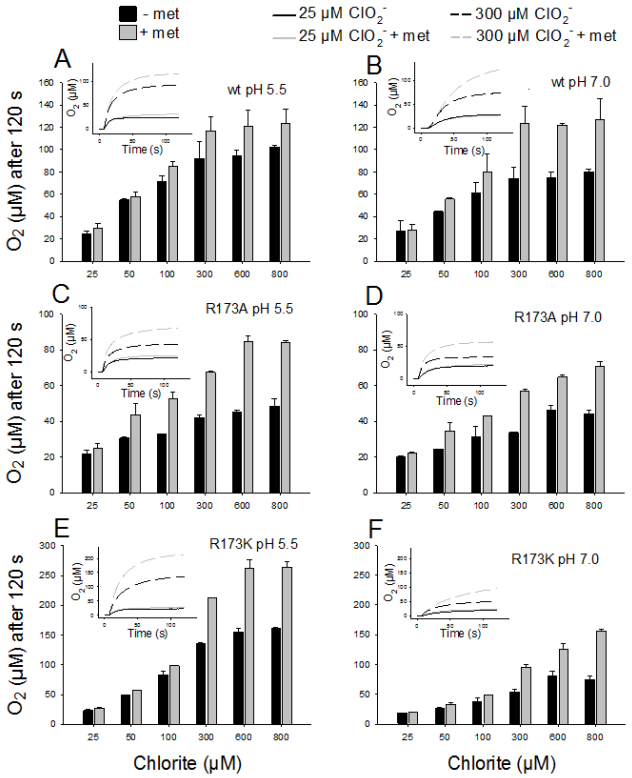

Figure 2. Influence of methionine on the generation of O_2 during chlorite degradation mediated by wild-type (A,B) and mutant (C-F) NdCld at pH 5.5 (A, C, E) and pH 7.0 (B, D, F). Insets depict typical time traces of oxygen generation.

Besides the amount of produced O_2, methionine also increased the turnover number of wild-type NdCld, R173K and R173A, respectively (Figure 3A), simply because it kept the number of active enzyme molecules at higher levels. This is evident upon degrading a defined amount of chlorite (340 μM) by increasing enzyme concentrations. Figure 3B depicts two representative time traces following the O_2 release during degradation of 340 μM chlorite by 25 nM {[chlorite]/[NdCld] = 13600} and 100 nM

NdCld {[chlorite]/[NdCld] = 3400} in the absence and presence of methionine (5 mM). In the presence of methionine and with 100 nM enzyme all chlorite was degraded and the theoretical yield of O_2 (340 µM) was achieved, whereas at lower enzyme concentrations or in the absence of methionine the yield of produced dioxygen was significantly lower. This is summarized in Figure 3C. In order to produce the 340 µM O_2 from 340 µM chlorite in the absence of methionine an enzyme concentration of about 400 nM was necessary {[chlorite]/[NdCl] = 850}, whereas in the presence of 5 mM methionine complete degradation of chlorite was already achieved by about 100 nM enzyme {[chlorite]/[NdCl] = 3400}.

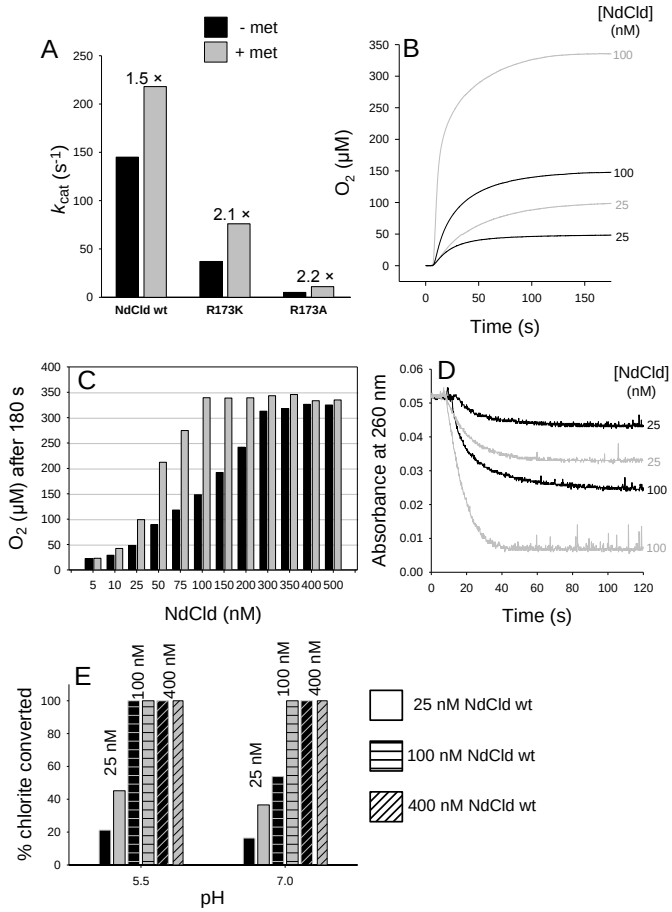

Figure 3. Effect of methionine on the kinetics (A) and extent of O2 release (B, C) and chlorite degradation (D, E), varying the enzyme concentration (B-E) and the pH (E).

Very similar results were obtained when the degradation of chlorite was monitored photometrically at 260 nm under identical conditions. Figure 3D depicts two representative time traces from photometric experiments following the decrease of absorbance at 260 nm during degradation of 340 µM chlorite by 25 nM and 100 nM NdCld in the absence and presence of methionine (5 mM) at pH 7.0. Figure 3E compares the extent of degradation of 340 µM chlorite by 25, 100 and 400 nM NdCld at pH 5.5, and pH 7.0, respectively, in the absence and presence of 5 mM methionine. It demonstrates that 25 nM NdCld {[chlorite]/[NdCld] = 13600} are able to convert about 21% of the initial amount of chlorite in absence and approximately 45% of chlorite in presence (5 mM) of methionine at pH 5.5. At pH 7.0 those numbers decrease to about 16% and 36%, respectively. When 100 nM NdCld {[chlorite]/[NdCl] = 3400} was used all chlorite independent of the addition of methionine could be converted at pH 5.5, in contrast to pH 7.0 where only in presence of 5 mM methionine the entire initial amount of chlorite was converted and only about 54 % in absence of methionine. At an enzyme concentration of 400 nM NdCld {[chlorite]/[NdCl] = 850} the entire amount of chlorite was converted independent from pH and the presence of methionine.

These data clearly demonstrate that (i) Cld is irreversibly inhibited during chlorite degradation, (ii) inhibition is smallest at pH optimum of enzymatic activity, (iii) methionine can rescue the enzyme from inhibition to some extent (depending on the [chlorite]/[NdCl] ratio) and, finally, (iv) that exchange of the distal arginine amplifies the inhibitory effect.

Quantification of hypochlorous acid released during catalysis. Next, we aimed to trap hypochlorite by two molecules, namely monochlorodimedone (MCD) and 2-[6-(4-aminophenoxy)-3-oxo3H-xanthen-9-yl]-benzoic acid (APF) that allow to roughly calculate the amount of released hypochlorite by UV-vis[21] and fluorescence[31] spec-

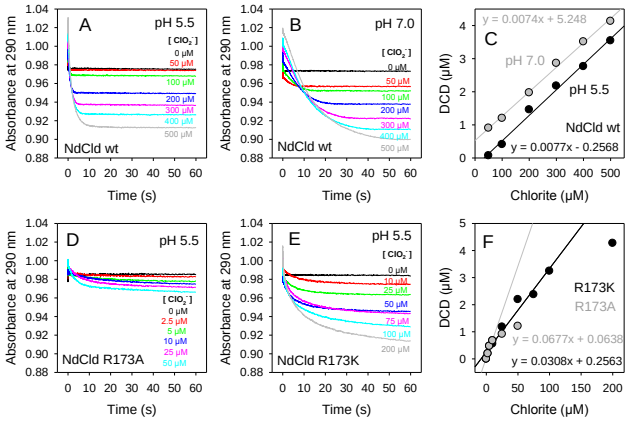

Figure 4. Trapping hypochlorite by monochlorodimedone in wild-type NdCld (A-C) at different pH-values and mutant NdClds (D-F).

In Figure 4A the kinetics of MCD (55 µM) chlorination during NdCld (100 nM) mediated chlorite degradation is depicted at various substrate concentrations at pH 5.5 (Figure 4A) and pH 7.0 (Figure 4B). During chlorination of MCD to DCD (dichlorodimedone) absorbance at 290 nm is lost. Chlorite does not react with MCD.[24] Upon plotting the decrease of absorbance of MCD *versus* chlorite concentration a linear dependence was observed at chlorite concentrations of > 50 µM at pH 5.5 and > 0 µM at pH 7.0 (Figure 4C). Based on the assumption that all released hypochlorite reacted with MCD it can be calculated from the slope of the linear curves that at least ~7.5 µM hypochlorite per mM chlorite escaped from the reaction sphere at pH 5.5 and pH 7.0.

Similar reactions were performed with 200 nM NdCld R173A (Figure 4D) and 200 nM R173K (Figure 4E) at pH 5.5. In contrast to the wild-type enzyme a linear dependence of formed DCD from the chlorite concentration was only observed in a small concentration range [0-10 µM for R173A and 0-100 µM for R173K (Figure 4F)]. Based on the assumption that all released hypochlorite reacted with MCD, it can be estimated that at least ~68 µM and ~31 µM hypochlorite per mM chlorite escaped from the reaction sphere in R173A and R173K at pH 5.5, respectively. These findings clearly suggest that in the absence of R173 the amount of hypochlorous acid released from the reaction sphere is increased significantly.

A further hypochlorite trapping molecule is aminophenyl fluorescein (APF). Upon reaction of $^{-}$OCl with APF the fluorescence intensity at 522 nm (excitation at 488 nm) is increased. Supplemental Figure 2 depicts the reaction of 100 nM NdCld at various chlorite concentrations at pH 7.0 followed by fluorescence spectroscopy (10 µM APF). Based on a calibration curve (Supplemental Figures 2A and 2B) the amount of hypochlorite trapped by APF was estimated from its linear dependence of the concentration of chlorite concentration (< 500 µM) at pH 7.0 (Supplemental Figure 2D). Based on the assumption that all released hypochlorite reacted with APF it can be calculated that at least ~4 µM hypochlorite per mM chlorite escaped from the reaction sphere at pH 7.0.

Heme bleaching during chlorite degradation monitored by EPR and UV-vis spectroscopy. Both time-resolved UV-vis spectroscopy as well as EPR spectroscopy revealed irreversible heme bleaching in NdCld during degradation of chlorite or upon addition of hypochlorite. EPR spectroscopy gives valuable information about the electronic architecture of the paramagnetic ferric heme *b* center of NdCld. Wild-type NdCld has spectral features that are composed of two high-spin species at pH 5.5 (Figure 5A, Supplemental Table 1) and two high-spin and two low-spin species at pH 7.0 (Figure 5B, Supplemental Table 1). Simulation and spin quantification parameters of the experimental spectra are given in Supplemental Table 1. The overall high-spin spectrum resembles that of previously published NdCld spectra.[1] It is worth pointing out that differences in buffer- and cryoconditions effect the rhombicity in NdCld samples.[15]

The intensity of the high-spin signal of wild-type NdCld decreases in the presence of chlorite (Figure 5 and Supplemental Figure 3). With 100 mM chlorite the rhombic signal disappears almost completely but part of the axial signal remains (Supplemental Figure 3A). This decrease in intensity of the high-spin signal with no concomitant formation of a low spin signal indicates a change of the paramagnetic oxidation state of Fe(III) NdCld and hence an inactivation of the protein. At high excess of chlorite (~ 2500 ×) the formation of protein radicals at a *g*-value of ~2 appear. As already observed in the steady-state kinetic assays, methionine is able to protect NdCld (Supplemental Figure 3B). It acts as a weak ligand of NdCld [indicated by slight changes of the rhombicity in spectra ii) in Figure 5A and 5B, Supplemental Table 1] suggesting that it can enter the heme cavity and trap hypochlorite at the site of its production. In the presence of methionine (17.5 mM) the remaining high-spin signal of NdCld (40 µM) incubated with 100 mM chlorite still has a significant amount of rhombic high-spin signal. The protective effect of methionine is more pronounced at pH 7 compared to pH 5.5 (see also the difference spectra depicted in Figure 5).

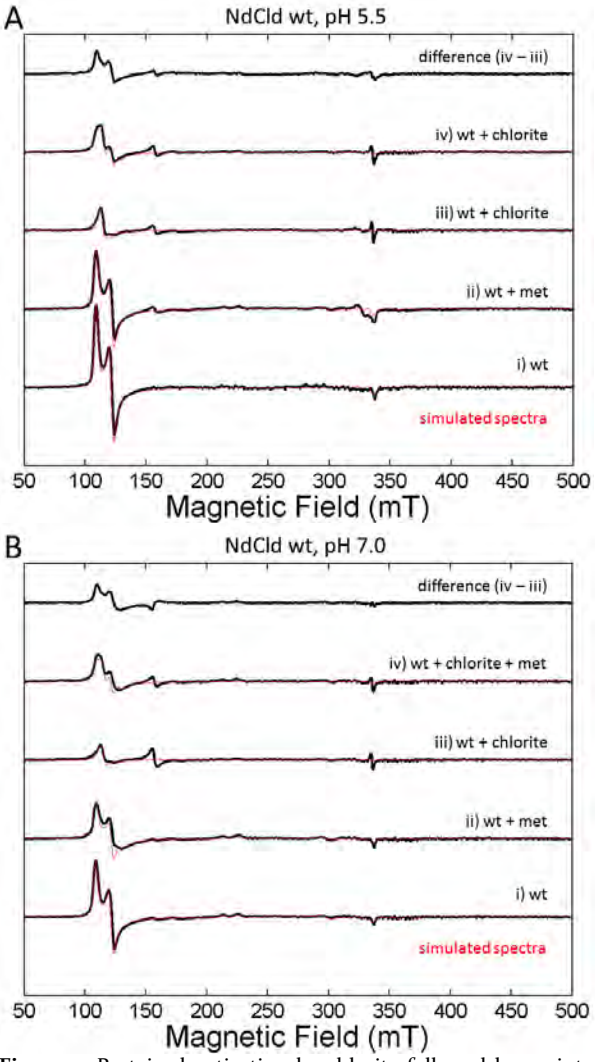

Figure 5. Protein deactivation by chlorite followed by an intensity change of the cw electron paramagnetic resonance high-spin spectra at (A) pH 5.5 and (B) 7.0, detected at 10 K (black – experimental spectrum, red – simulated spectrum).

Finally, NdCld was incubated directly with hypochlorous acid (Supplemental Figure 4). With increasing amount of hypochlorous acid the rhombic high-spin compound disappears and a non-heme Fe(III) high-spin signal (g = 4.3) representative of degraded protein, grows significantly in intensity. A small protein radical species is also observed. The effect of HOCl on the deactivation and degradation of NdCld is much more pronounced in this experiment compared to the one where HOCl is generated during

chlorite turnover due to a much higher HOCl conce tion at the heme site.

Besides EPR, we investigated the modification of the tral signatures of the prosthetic group during ch degradation by UV-vis stopped-flow spectroscopy (F 6). Figure 6A depicts the spectral changes, when 1 μ wild-type NdCld is mixed with 1 mM of chlorite at p in the conventional stopped-flow modus. The ferric ing state with its Soret maximum at 406 nm (green trum) is rapidly converted within 1 ms to an interme with a Soret maximum of 414 nm and a prominent pe 535 nm (black spectrum). During chlorite degrad this species dominated and was converted to the re state within 10 s. The resulting heme spectrum si cantly lost Soret absorbance (maxima at 408 and 54 suggesting heme bleaching (red spectrum in Figure At pH 7.0 the loss of absorbance at Soret maximun more pronounced and the rate and extent of chlorite radation was smaller (Supplemental Figure 5). Perfor the same reactions in the presence of 5 mM methi reveals a different outcome. The reaction rate i hanced, chlorite degradation is complete and bleaching is less pronounced (Figure 6B and Su mental Figure 5D).

Mixing 1 μM NdCld R173A with 1 mM of chlorite (condition as wild-type protein) led to complete lo heme absorbance within 2 seconds. Thus, the varian mixed with only 50 μM chlorite in the absence (F 6C) and presence (Figure 6D) of 5 mM methionir contrast to the wild-type protein the Soret maximu mained at 406 nm during chlorite degradation and the effect of methionine on heme bleaching was small. The mutant R173K was more robust and could be mixed with 1 mM chlorite (Figure 6E). The Soret maximum of ferric R173K is at 410 nm and was described as low-spin species recently.[10] Upon mixing of R173K with chlorite no spectral shift occurs and more than 60% of heme absorbance disappears (Figure 6F).

Mass spectrometric analyses of heme and protein modification. Furthermore, we analyzed the modifications of the protein moiety of NdCld incubated with chlorite in the presence and absence of methionine by mass spectrometry. StrepII-tagged NdCld has a theoretical mass of 29751.8 Da without the heme *b* cofactor (which is lost during sample preparation for MS). Analysis of recombinant NdCld revealed the presence of some heterogeneity at the N-terminus in the region of the StrepII-tag and the TEV-cleavage site.

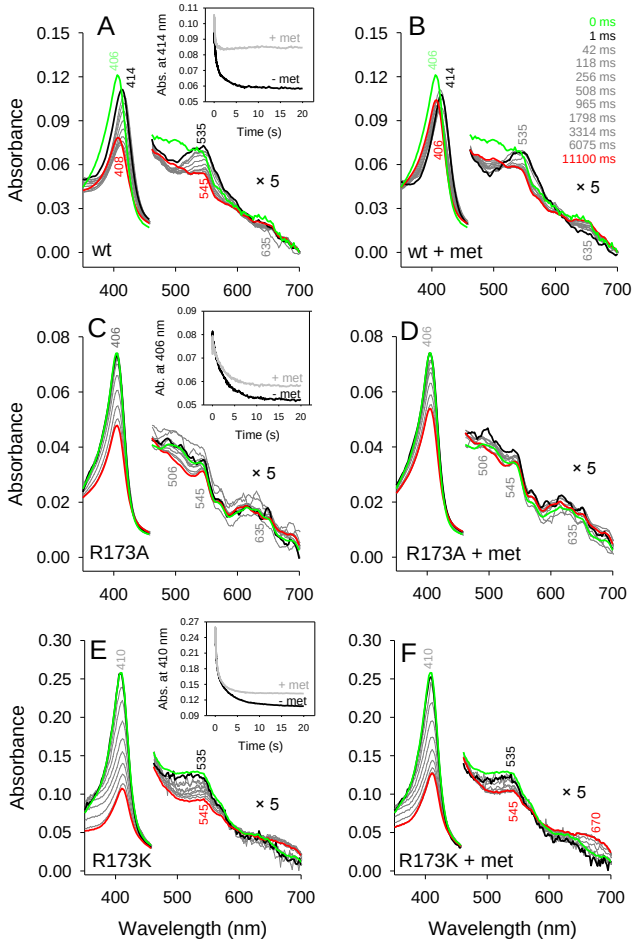

Figure 6. Effect of methionine on the interconversion of redox intermediates and heme bleaching in wild-type NdCld (A, B) and NdCld variants (C-F). Insets depict representative time traces at Soret maximum.

Six different variants were detected with the full length protein having the highest intensity (peak maximum at 29751.3 Da and two minor peaks at higher m/z values, reflecting possibly methylation and acetylation) (Figure 7A).

Truncated versions start at Met-22, Phe-14, Phe-5, Gly-3, Met-1, Ala1 (data not shown). Upon treatment with a 5000-fold stoichiometric excess of chlorite, the resulting spectrum (Figure 7B) shows two dominating species representing two- and three-times oxidized NdCld in addition to other forms having been oxidized up to approximately 10 times. A peak of low intensity at the original mass is still detected, suggesting the presence of some unmodified NdCld after reaction with chlorite. In the presence of methionine, the mass peak of the unmodified enzyme is still the most prominent one (Figure 7C). Modified (1- to 5-times oxidized) NdCld was also detected in this sample (Figure 7C) but to a much smaller extent compared to the sample where methionine was absent.

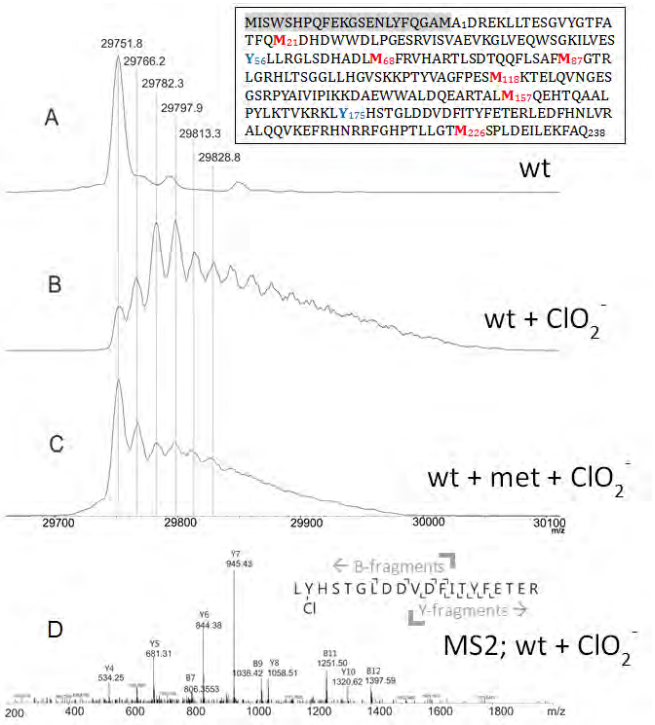

Figure 7. Modification of protein during NdCld mediated degradation of chlorite. Wild-type NdCld (A) was treated with chlorite (B) and with chlorite and also in presence of methionine (C). MS2 spectrum of peptide 175-194 of wild-type NdCld upon treatment with chlorite. Inset shows amino acid sequence of NdCld including N-terminal StrepII-tag and TEV-cleavage site (underplayed in gray).

Finally, in order to identify modified (oxidized) residues, peptide analysis of NdCld incubated with chlorite was performed. All methionines in the protein are oxidized to a large degree. By contrast tryptophan- and tyrosine (Y189) residues are marginally oxidized (Table 1). Interestingly, two out of seven tyrosines (Tyr56 and Tyr176) were found to be chlorinated, as was proven by MS/MS analysis (Figure 7D). 3-Chlorotyrosines are specific fingerprints for the action of hypochlorite.[32-34] Both modified tyrosine residues are in the core of the protein on the distal side of the heme, where the hypochlorite is produced during turnover (Figure 8). They are located at rather remote sites with respect to the cofactor but are connected with the heme center by tunnel as calculated with CAVER[35] (Figure 8A).

The addition of free methionine to the reaction mixture significantly reduced the percentage of modifications of methionine, tyrosine and tryptophan residues of NdCld (Table 1). The fact that methionine both at the surface and the protein interior are oxidized (Figures 8B and 8C) demonstrates that hypochlorite escapes the active site during degradation of chlorite.

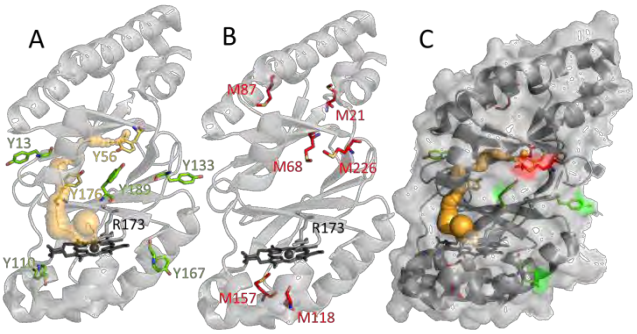

Figure 8. Amino acids modified during NdCld mediated chlorite degradation. (A) Ribbon representation of a single NdCld subunit. A possible pathway of hypochlorite within the subunit towards modified tyrosine residues is depicted as orange spheres and an orange ribbon. (B) All oxidized methionines are depicted in red. (C) NdCld with semitransparent surface. Figures were generated using PyMOL (http://www.pymol.org/).

Molecular dynamics simulation of movement of hypochlorite. MD simulations support the finding that transiently produced hypochlorite migrates away from the reaction sphere. In this setup hypochlorite is placed *in silico* to the distal side of the heme in its Compound I state with Arg173 in an "in"-conformation (pointing to the heme iron not towards the substrate channel).

In MD simulations hypochlorite cannot further react to form chloride and dioxygen. It leaves the active site rapidly in all five monomers of NdCld. This is illustrated in Figure 9, where the positions of one hypochlorite molecule over time are shown (every 5 ps) over a 20 ns simulation. Positions early in the simulation are depicted in green gradually changing to blue, yellow, orange and red (final position after 20 ns of simulation).

Table 1. Digestion of 100 µM NdCld, treated with 500 mM chlorite in absence and presence of 25 mM methionine, by gluC/trypsin and analysis by LC-MS; 50 mM phosphate buffer, pH 7.0.

		NdCld + chlorite		NdCld + chlorite + methionine		
amino acid	peptide sequence	% Tyr-Cl	% total modification	% Tyr-Cl	% total modification	Δ %
6-33	LLTESGVYGTFATFQMDHDWWDLPGESR		57.27		5.86	51.41
34-41	VISVAEVK		no modification		no modification	
42-50	GLVEQWSGK		22.22		2.57	19.65
51-59	ILVESYLLR	2.53	2.53	0.04	0.04	2.50
60-70	GLSDHADLMFR		98.49		6.54	91.95
75-90	TLSDTQQFLSAFMGTR		99.76		24.92	74.84
94-106	HLTSGGLLHGVSK		no modification		no modification	
107-119	KPTYVAGFPESMK		96.75		18.86	77.90
120-140	TELQVNGESGSRPYAIVIPIK		no modification		no modification	
142-153	DAEWWALDQEAR		20.79		1.78	19.01
154-169	TALMQEHTQAALPYLK		85.43		16.74	68.69
175-194	LYHSTGLDDVDFITYFETER	8.53	13.56	0.67	2.46	11.10
195-203	LEDFHNLVR		no modification		no modification	
204-209	ALQQVK		no modification		no modification	
217-235	FGHPTLLGTMSPLDEILEK		99.88		14.34	85.54

DISCUSSION

Understanding the inhibition mechanism of chlorite dismutase (Cld) is fundamental for future enzymatic application of Cld in bioremediation and biotechnology.[30] The enzyme from "*Candidatus* Nitrospira defluvii" (NdCld) was chosen as a model protein for inhibition studies because it has a high thermal and conformational stability[17] and thus is the most promising candidate for biotechnological application.[30]

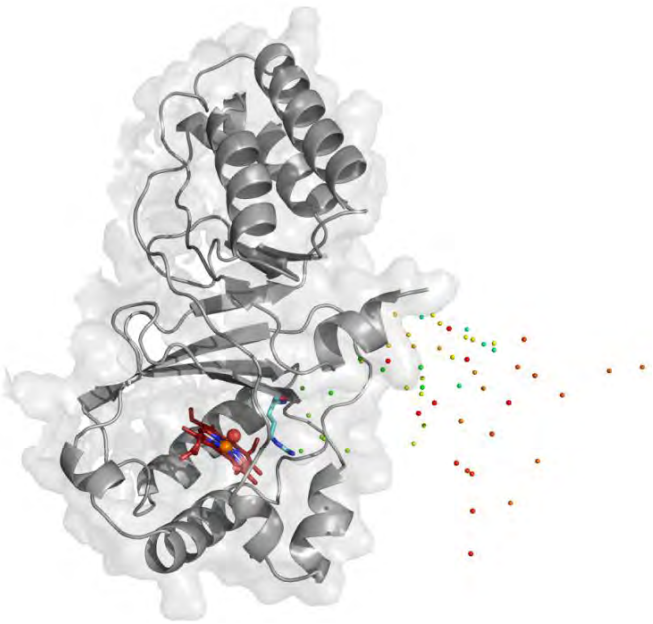

Figure 9. Molecular dynamics simulation of movement of hypochlorite. A single NdCld monomer is shown, along with the position of one hypochlorite molecule at different time points (0 - 20 ns, green - blue - yellow - orange - red spheres). Hypochlorite escapes the active site rapidly. Compound I oxygen is depicted as red sphere and Compound I heme iron as orange sphere. Catalytically important R173 is depicted in cyan and pointing away from the active site, being unable to keep the transiently produced hypochlorite in the reaction sphere. Figure was generated using PyMOL (http://www.pymol.org/).

Chlorite reacts with a variety of different heme containing enzymes, including methemoglobin[36] or cytochrome P450.[37] Among heme peroxidases, chlorite was shown to be utilized by cytochrome *c* peroxidase, chloroperoxidase and horseradish peroxidase (HRP).[38] With HRP it was demonstrated that chlorite mediates the two-electron oxidation of ferric HRP to Compound I (similar to postulated Reaction 2 for Cld) but also serves as one-electron reductant of both Compound I and Compound II.[37] Thereby, HRP is inactivated with time. Importantly, upon mixing with chlorite HRP produces a halogenating agent that reacts with MCD and which was postulated to be hypochlorite.[38] By contrast, chlorite rapidly and irreversibly inactivates human peroxidases, like myeloperoxidase (MPO) or lactoperoxidase[24], which belong to a different heme peroxidase superfamily.[39] However, the first heme enzyme that was described to utilize chlorite as a natural substrate and degrade it efficiently was Cld from perchlorate-respiring bacteria that actually produces chlorite as a metabolic intermediate.[40]

Both the overall fold and the heme cavity architecture of heme peroxidases like HRP or MPO are completely different compared to Cld. In heme peroxidases hydrogen peroxide is the natural oxidant that mediates the two-electron oxidation of the ferric enzyme to Compound I. A basic amino acid, typically histidine is essential for acting as proton acceptor forming the anionic peroxide that binds to Fe(III). The following heterolytic cleavage of H_2O_2 is supported by a conserved arginine. Thus, Compound I formation in a peroxidase typically depends on the pK_a of the distal histidine.

In functional Cld the only charged amino acid in the distal heme cavity is an arginine (Arg173 in NdCld). The natural oxidant [$E°'(ClO_2/ClO^-)$ = 1175 mV] is chlorite (at least most probably in those Clds found in perchlorate-respiring bacteria), which is deprotonated (pK_a = 1.97) in the biological pH range. Thus a proton acceptor is not necessary for binding to Fe(III) according to Reaction 1. This is reflected by the fact that the calculated K_M value is independent of pH (Figure 1A). One might speculate about the role of Arg173 in Reaction 1. Exchange of R173 by either alanine or glutamine has only a small effect on the K_M value (i.e. increase by factor of 1.3 in R173A and 1.9 in R173Q compared to the wild-type protein)[10] suggesting that its role in substrate binding is negligible.

In contrast to K_M, k_{cat} of NdCld shows a clear dependence on pH. Above the pH optimum of chlorite degradation (i.e. pH 5.5) the turnover number decreases with increasing pH (Figure 1B). This behavior could be related with a role of Arg173 in (i) the heterolytic cleavage of chlorite (Reaction 2) and/or (ii) the recombination reaction between the (postulated) transiently produced intermediate hypochlorite and Compound I (Reaction 3). The turnover number (k_{cat}) for chlorite degradation is ~6.5% (R173A) and 33% (R173Q) compared to the wild-type enzyme. Thus, arginine is not fully essential for catalysis. In its presence the turnover number is increased and, as demonstrated in this work, inactivation is significantly retarded (see below).

It has been postulated that the pH-dependence of chlorite degradation by Cld reflects the protonation state of the distal arginine, which was reported to have its pK_a at ~pH 6.5 in *Dechloromonas aromatica* Cld (DaCld).[14] The high similarity of (i) the hydrophobic distal site architecture of NdCld[7] and DaCld[5] and (ii) the pH-dependence of chlorite degradation determined in this work (Figure 1B) suggests a similar pK_a for Arg173 in NdCld. At pH 5.5 the positively charged guanidinium group of Arg173 is perfectly suited to keep the transiently produced hypochlorite in place for the postulated rebound mechanism of Reaction 3. In close vicinity to the guanidinium group the $HOCl/^-OCl$ equilibrium (pK_a = 7.54) will be shifted to the anionic conjugated base (i.e. hypochlorite). With increasing pH the interaction between hypochlorite and Arg173 will gradually be weakened. However, as demonstrated in this work, this behavior is emphasized by the fact that Cld is irreversibly inactivated during catalysis. This is the main reason why the published catalytic properties are problematic to compare, since the various enzymes were probed at different chlorite concentration regimes and are differently susceptible to inactivation.[29]

The present work shows that the extent of degraded chlorite (which corresponds to the yield of produced O_2) is significantly smaller at alkaline pH (Figure 1D) and that

the presence of millimolar methionine is able to increase both the extent of chlorite degradation as well as the reaction rate. This was demonstrated both polarographically and spectrophotometrically. The protecting effect of methionine clearly suggests a role of hypochlorite in the inactivation reaction, since it is able to trap the transiently formed intermediate but not the substrate chlorite. Methionine easily can enter the relatively large substrate channel as well as the active site of Cld.[7,15] EPR demonstrated that methionine forms a six-coordinated complex with Cld (Figure 5). It does not inhibit the reaction, quite the contrary, its presence increases the life time of active Cld molecules. The favourable impact of methionine on catalysis is more pronounced at increasing alkaline conditions.

The fact that transiently formed hypochlorite is able to react with methionine suggests that Reaction 3 is slower than Reaction 2 and that not all hypochlorite generated in Reaction 2 reacts with Compound I. A small fraction escapes the active site. The species formed within 1 ms by mixing of Cld with chloride in the stopped-flow apparatus with absorbance maxima at 414 nm and 535 nm most probably represents {Por$^{\bullet+}$Fe(IV)=O...[O-Cl$^-$]}. As long as chlorite is available and Cld is active its spectral signatures dominate. Note that a Compound I spectrum [i.e. Por$^{\bullet+}$Fe(IV)=O, produced by mixing Cld with peracetic acid] exhibits a blue-shifted and hypochromic Soret band at 395 nm and further bands at 525, 550, 600, and 645 nm.[41]

To further confirm production and release of hypochlorite two additional traps (MCD[21] and APF[23,31]) were used. They allowed to roughly calculate the amount of released hypochlorite by spectroscopic means. At pH optimum (k_{cat} ~180 s^{-1}) and a stoichiometric excess of chlorite of 500-1000-fold ~7.7 µM hypochlorite per mM chlorite could be trapped by MCD. This is a minimum number since it is based on the assumption that all released HOCl molecules reacted with MCD. In the absence of the distal arginine the amount of released hypochlorite is significantly higher, i.e. 31 µM (R173K) and 68 µM (R173A) per mM chlorite. With increasing pH the turnover of Cld gradually decreased in contrast to the amount of trapped HOCl. These findings strongly indicate that (i) hypochlorite is formed during catalysis, (ii) Arg173 helps to keep it in the reaction sphere for the recombination reaction, and (iii) that the decrease in the amount of degraded chlorite (or released O_2) is related to the promoted inhibition of Cld by escaped HOCl under more alkaline conditions.

Remains the question about the target(s) and the inhibitory effect of hypochlorite. Both UV-vis and EPR spectroscopy demonstrated that the heme of Cld is severely modified during catalysis. Loss of heme absorbance and intensity of the high-spin signal together with the release of free iron occurs. In the absence of Arg173 and at higher pH these reactions are more pronounced, whereas in the presence of HOCl-traps they are partially suppressed. Additionally, the protein moiety is modified. Protein radicals are formed and amino acids, mostly methionine and a few tyrosine and tryptophans, were oxidatively modified. Most importantly, 3-chlorotyrosine is produced, which is a typical fingerprint for the action of hypochlorite.[32-34] Solvent exposed tyrosines and tyrosines in the interface of pentameric NdCld subunits did not show this modification whereas two chlorinated tyrosines in the core of the protein were found. Their molecular surface accessibility is zero Å^2 (according to the WHATIF webserver, http://swift.cmbi.ru.nl/servers/html/index.html) but they may be reached by HOCl by a small tunnel. On this way Tyr176 is the first target (8.5% chlorination) and Tyr56 the second one (2.5% chlorination). Importantly, all these modifications could be significantly suppressed in the presence of methionine (Table 1).

Summing up, the data presented in this work support the postulation that chlorite degradation by Cld follows Reactions 1-3. Upon reduction of chlorite hypochlorite is formed and kept in the reaction sphere for recombination with the oxoiron(IV) group of Compound I. The guanidinium group of a fully conserved arginine with a pK_a around 6.5 supports this reaction. However, about 1 molecule of HOCl per 100 full cycles escapes and reacts with both the prosthetic group and the protein moiety. As a consequence irreversible inactivation of Cld is observed and this reaction is more pronounced with increasing pH. Importantly, HOCl traps like methionine can rescue the enzyme from inactivation.

ASSOCIATED CONTENT

Supporting Information. pH-dependence of reaction with chlorite of NdCld variants, hypochlorite trapping with APF, additional EPR spectra of chlorite titrations, effect of methionine to heme bleaching and chlorite degradation at pH 7.0.This material is available free of charge via the Internet at http://pubs.acs.org.

AUTHOR INFORMATION

Corresponding Author

christian.obinger@boku.ac.at

Funding Sources

This project was supported by the Austrian Science Foundation, FWF [Doctoral Program BioToP - Molecular Technology of Proteins (W1224) and the projects P25270 and P22276]

Notes

The authors declare no competing financial interest.

REFERENCES

(1) Hagedoorn, P. L., de Geus, D. C., and Hagen, W. R. (2002) Spectroscopic characterization and ligand-binding properties of chlorite dismutase from the chlorate respiring bacterial strain GR-1. *Eur. J. Biochem. 269*, 4905-4911

(2) Lee, A. Q., Streit, B. R., Zdilla, M. J., Abu-Omar, M. M., and Dubois, J. L. (2008) Mechanism of and exquisite selectivity for O-O bond formation by the heme dependent chlorite dismutase. *Proc. Natl. Acad. U.S.A. 105*, 15654-15659

(3) Keith, J. M., Abu-Omar, M. M., and Hall, M. B. (2011) Computational investigation of the concerted dismutation of chlorite ion by water-soluble iron porphyrins. *Inorg. Chem. 50,* 7928-7930

(4) Sun, S., Li, Z. S., and Chen, S. L. (2014) A dominant homolytic O-Cl bond cleavage with low-spin triplet-state Fe(IV)=O formed is revealed in the mechanism of heme-dependent chlorite dismutase. *Dalton Trans. 43,* 973-981

(5) de Geus, D. C., Thomassen, E. A. J., Hagedoorn, P.-L., Pannu, N. S., van Duijn, E., and Abrahams, J. P. (2009) Crystal structure of chlorite dismutase, a detoxifying enzyme producing molecular oxygen. *J. Mol. Biol. 387*, 192-206

(6) Goblirsch, B. R., Streit, B. R., DuBois, J. L., and Wilmot, C. M. (2010) Structural features promoting dioxygen production by *Dechloromonas aromatica* chlorite dismutase. *J. Biol. Inorg. Chem. 15*, 879-888

(7) Kostan, J., Sjoeblom, B., Maixner, F., Mlynek, G., Furtmüller, P. G., Obinger, C., Wagner, M., Daims, H., and Djinovic-Carugo, K. (2010) Structural and functional analysis of the chlorite dismutase from the nitrite-oxidizing bacterium *Candidatus* "Nitrospira defluvii": identification of a catalytically important amino acid residue, *J. Struct. Biol. 172*, 331-342

(8) Mlynek, G., Sjöblom, B., Kostan, J., Füreder, S., Maixner, F., Gysel, K., Furtmüller, P. G., Obinger, C., Wagner, M., Daims, H., and Djinović-Carugo, K. (2011) Unexpected diversity of chlorite dismutases: a catalytically efficient dimeric enzyme from *Nitrobacter winogradskyi*. *J. Bacteriol. 193*, 2408-2417

(9) Blanc, B., Mayfield, J. A., McDonald, C. A., Lukat-Rodgers, G. S., Rodgers, K. R., and Dubois, J. L. (2012) Understanding how the distal environment directs reactivity in chlorite dismutase: spectroscopy and reactivity of Arg183 mutants. *Biochemistry 51*, 1895-1910

(10) Hofbauer, S., Gysel, K., Bellei, M., Hagmüller, A., Schaffner, I., Mlynek, G., Kostan, J., Pirker, K. F., Daims, H., Furtmüller, P. G., Battistuzzi, G., Djinovic-Carugo, K., and Obinger, C. (2014) Manipulating conserved heme cavity residues of Chlorite dismutase: Effect on structure, redox chemistry and reactivity. *Biochemistry 53,* 77-89

(11) Stenklo, K., Thorell, D., Bergius, H., Aasa, R., and Nilsson, T. (2001) Chlorite dismutase from *Ideonella dechloratans*. *J. Biol. Inorg. Chem. 6*, 601-607

(12) Mehboob, F., Wolterink, A. F., Vermeulen, A. J., Jiang B., Hagedoorn P. L., Stams, A. J., and Kengen, S. W. (2009) Purifcation and characterization of a chlorite dismutase from *Pseudomonas chloritidismutans. FEMS Microbiol. Lett*. *293*, 115-121

(13) Streit, B. R., and DuBois, J. L. (2008) Chemical and steady-state analysis of a heterologously expressed heme dependent chlorite dismutase. *Biochemistry 47,* 5271-5280

(14) Streit, B. R., Blanc, B., Lukat-Rodgers, B. S., Rodgers, K. R., and DuBois, J. L. (2010) How active-site protonation state influences the reactivity and ligation of the heme in chlorite dismutase. *J. Am. Chem. Soc*. *132*, 5711-5724

(15) Hofbauer, S., Bellei, M., Sündermann, A., Pirker, K. F., Hagmüller, A., Mlynek, G., Kostan, J., Daims, H., Furtmüller, P. G., Djinovic-Carugo, K., Oostenbrink, C., Battistuzzi, G., and Obinger, C. (2012) Redox thermodynamics of high-spin and low-spin forms of chlorite dismutases with diverse subunit and oligomeric structures. *Biochemistry 51*, 9501-9512

(16) Blanc, B., Rodgers, K. R., Lukat-Rodgers, G. S., and DuBois, J. L. (2013) Understanding the roles of strictly conserved tryptophan residues in O_2 producing chlorite dismutases. *Dalton Trans. 42*, 3156-31

(17) Hofbauer, S., Gysel, K., Mlynek, G., Kostan, J., Hagmüller, A., Daims, H., Furtmüller, P. G., Djinovic-Carugo, K., and Obinger, C. (2012) Impact of subunit and oligomeric structure on the thermal and conformational stability of chlorite dismutases. *Biochim. Biophys. Acta 1824*, 1031-1038

(18) Philippi, M., dos Santos, H. S., Martins, A. O., Azevedo, C. M., and Pires, M. (2007) Alternative spectrophotometric method for standardization of chlorite aqueous solutions. *Anal Chim Acta 585*, 361-365

(19) Armesto, X. L., Canle, M. L., Fernandez, M. I., Garcia, M. V.,and Santaballa, J. A. (2000) First steps in the oxidation of sulfur-containing amino acids by hypohalogenation: Very fast generation of intermediate sulfenyl halides and halosulfonium cations. *Tetrahedon 56,* 1103-1109

(20) Peskin, A. V., Turner, R., Maghzal, G. J., Winterbourn, C. C., and Kettle, A. J. (2009) Oxidation of methionine to dehydromethionine by reactive halogen species generated by neutrophils. *Biochemistry 48*, 10175-10182

(21) Tachikawa, M., Sayama, C., Saita, K., Tezuka, M., and Sawamura, R. (2002) Effects of isocyanuric acid on the monochlorodimedone chlorinating rates with free chlorine and ammonia chloramine in water. *Water Res.* 10, 2547-2554

(22) Kettle, A. J., and Winterbourn, C. C. (1988) The mechanism of myeloperoxidase-dependent chlorination of monochlorodimedon. *Biochim Biophys Acta. 957*, 185-191

(23) Flemmig, J., Zschaler, J., Remmler, J., and Arnhold, J. (2012) The fluorescein-derived dye aminophenyl fluorescein is a suitable tool to detect hypobromous acid (HOBr)-producing activity in eosinophils. *J. Biol. Chem. 287,* 27913-27923

(24) Jakopitsch, C., Pirker, K. F., Flemmig, J., Hofbauer, S., Schlorke, D., Furtmüller, P. G., Arnhold, J., Obinger, C. (2014) Mechanism of reaction of chlorite with mammalian heme peroxidases. *J. Inorg. Biochem., 135*, 10-19

(25) Stoll, S., and Schweiger, A. (2006) EasySpin, a comprehensive software package for spectral simulation and analysis in EPR. *J. Magn. Reson. 178,* 42-55

(26) Peisach, J., Blumberg, W. E., Ogawa, S., Rachmilewitz, E. A., and Oltzik R. (1971) The effects of protein conformation on the heme symmetry in high spin and ferric heme proteins as studied by electron paramagnetic resonance. *J. Biol. Chem. 246*, 3342-3355

(27) Schmid, N., Christ, C. D., Christen, M., Eichenberger, A. P., and van Gunsteren, W. F. (2012) Architecture, implementation and parallelisation of the GROMOS software for biomolecular simulation. *Comp. Phys. Comm. 183*, 890-903

(28) Schmid, N., Eichenberger, A. P., Choutko, A., Riniker, S., Winger, M., Mark, A. E., and van Gunsteren W. F. (2011) Definition and testing of the GROMOS force-field versions 54A7 and 54B7. *Eur. Biophys. J. 40,* 846-856

(29) Sündermann, A., Reif, M., Hofbauer, S., Obinger C., and Oostenbrink, C (2014) Investigation of ion binding in chlorite dismutases by means of molecular dynamics simulations. *To be submitted to J. Am. Chem. Soc.*

(30) Hofbauer, S., Schaffner, I., Furtmüller, P. G., and Obinger C. (2014) Chlorite dismutases - a heme enzyme family for use in bioremediation and generation of molecular oxygen. *Biotechn. J. 9*, 461-473

(31) Setsukinai, K., Urano, Y., Kakinuma, K., Majima, H. J., and Nagano, T. (2003) Development of novel fluorescence probes that can reliably detect reactive oxygen species and distinguish specific species. *J. Biol. Chem. 278,* 3170-3175

(32) Delporte, C., Zouaoui Boudjeltia, K., Noyon, C., Furtmüller, P. G., Slomianny, M.-C., Dufour, D., Vanhamme, L., Reyé, F., Rousseau, A., Vanhaeverbeek, M., Ducobu, J., Michalski, J.-C.,

Nève, J., Obinger, C., Malle, E., Van Antwerpen, P. 2013. Impact of interaction between low-density lipoproteins and myeloperoxidase on specific enzymatic activity and post-translational oxidative modifications of apoB100. *J. Lipid Res.,* in press

(33) Hazen, S. L., and Heinecke, J. W. (1997) 3-Chlorotyrosine, a specific marker of myeloperoxidase-catalyzed oxidation, is markedly elevated in low density lipoprotein isolated from human artherosclerotic intima. *J. Clin. Invest. 99*, 2075-2081

(34) Hazen, S. L., Crowley, J. R., Mueller, M. D., and Heinecke, J. W. (1997) Mass spectrometric quantification of 3-chlorotyrosine in human tissues with attomole sensitivity: a sensitive and specific marker for myeloperoxidase-catalyzed chlorination at sites of inflammation. *Free Radic. Biol. Med. 23*, 909-916

(35) Petrek, M., Otyepka, M., Banás, P., Kosinová, P., Koca, J., and Damborský, J. (2006) CAVER: A new tool to explore routes from protein clefts, pockets and cavities. *BMC Bioinf. 7*, 316

(36) French, C. L., Yaun, S. S., Baldwin, L. A., Leonhard, D. A., Zhao, X. Q., Calabrese, E. J. (1995) Potency ranking of methemoglobin-forming agents. *J. Appl. Toxicol. 15*, 167-174

(37) Hrycay, E. G., Gustafsson, J. A., Ingelman-Sundberg, M., Ernster, L. (1975) Sodium periodate, sodium chloride, and organic hydroperoxides as hydroxylating agents in hepatic microsomal steroid hydroxylation reactions catalyzed by cytochrome P450. *FEBS Lett. 56*, 161-165

(38) Jakopitsch, C., Spalteholz, H., Furtmüller P. G., Arnhold, J., Obinger, C. (2008) Mechanism of reaction of horseradish peroxidase with chlorite and chlorine dioxide. *J. Inorg. Biochem. 102*, 293-302

(39) Zamocky, M., Jakopitsch, C., Furtmüller, P. G., Dunand, C., Obinger, C. (2008) The peroxidase-cyclooxygenase superfamily. Reconstructed evolution of critical enzymes of the innate immune system. *Proteins 71*, 589-605

(40) van Ginkel, C. G., Rikken, G. B., Kroon, A. G. M., and Kengen, S. W. M. (1996) Purification and characterization of chlorite dismutase: a novel oxygen-generating enzyme. *Arch. Microbiol. 166*, 321-326

(41) Mayfield, J. A., Blanc, B., Rodgers, K. R., Lukat-Rodgers, G. S., and DuBois, J. L. (2013) Peroxidase-type reactions suggest a heterolytic/nucleophilic O-O joining mechanism in the heme-dependent chlorite dismutase. *Biochemistry 52*, 6982-94

--TOC graphics--

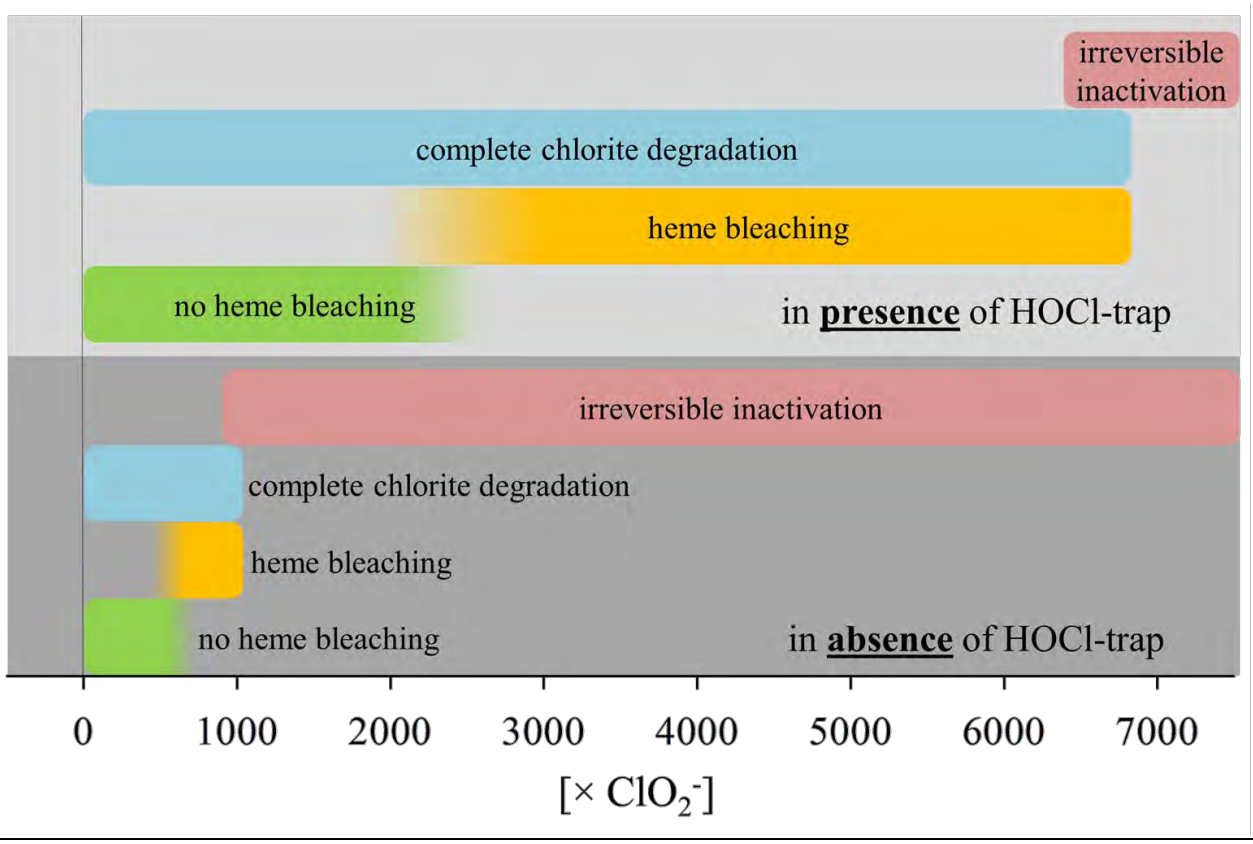

SUPPORTING INFORMATION

Transiently produced hypochlorite is responsible for the irreversible inhibition of chlorite dismutase

Stefan Hofbauer[1], Clemens Gruber[1], Katharina F. Pirker[1], Axel Sündermann[2], Irene Schaffner[1], Christa Jakopitsch[1], Chris Oostenbrink[2], Paul G. Furtmüller[1], Christian Obinger[1]*

[1]Department of Chemistry, Division of Biochemistry, VIBT – Vienna Institute of BioTechnology, BOKU – University of Natural Resources and Life Sciences, A-1190 Vienna, Austria

[2]Department of Material Sciences and Process Engineering, Institute of Molecular Modeling and Simulation, BOKU – University of Natural Resources and Life Sciences, A-1190 Vienna, Austria

Supplemental Figure 1. pH-dependence of chlorite conversion by NdCld mutants. (A) Initial rates of production of dioxygen from 40 µM chlorite mediated by 200 nM NdCld mutant R173A at different pH-values (50 mM citrate phosphate buffer pH 4 - 7; 50 mM phosphate buffer pH 7 - 8; 50 mM Tris/HCl buffer, pH 8 - 9). (B) Total amount of produced dioxygen in the range of pH 4 - 9. Conditions in (C), where 200 nM NdCld mutant R173K was used resembled conditions from (A); and conditions in (D) were equal to conditions in (B) using 200 nM NdCld mutant R173K.

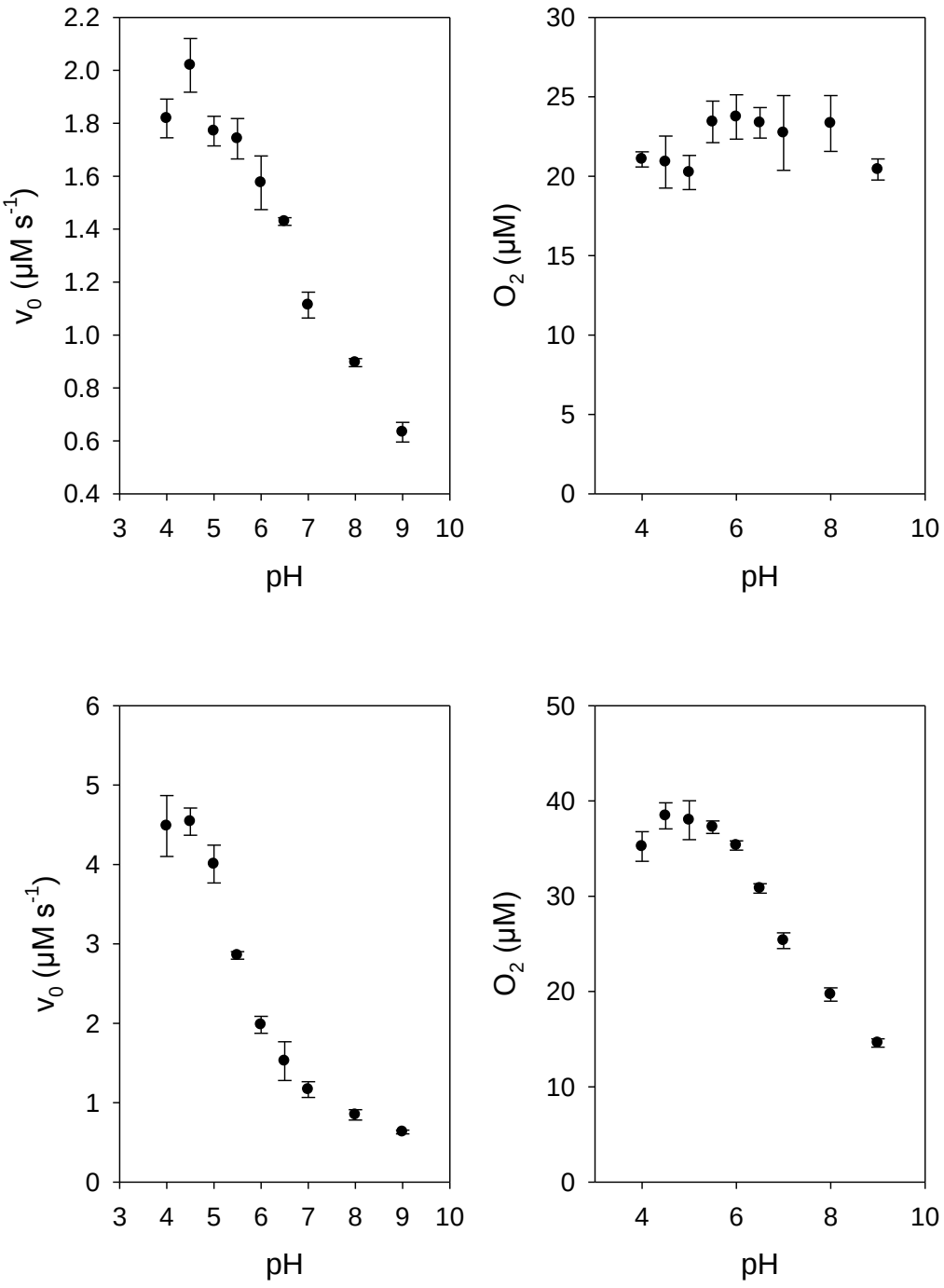

Supplemental Figure 2. Calibration curve of APF fluorescence for hypochlorite. (A) fluorescence spectra of 10 µM APF between 495 and 600 nm ($\lambda_{excitation}$ = 488 nm) after reactions with with 0 µM to 20 µM hypochlorite; 50 mM phosphate buffer pH 7.0. (B) Plot of fluorescence intensity *versus* hypochlorite concentration, showing a sigmoidal fit (logistic, 4 parameter). (C) Fluorescence spectra of 10 µM APF between 495 and 600 nm ($\lambda_{excitation}$ = 488 nm) after reactions with 100 nM NdCld wild-type with 0 µM (black), 100 µM (red), 200 µM (green), 300 µM (yellow), 400 µM (blue), 500 µM (magenta), and 750 µM (cyan) chlorite; 50 mM phosphate buffer pH 7.0. (D) Plot of trapped HOCl concentration versus chlorite concentration, showing a linear fit between 100 and 500 µM chlorite.

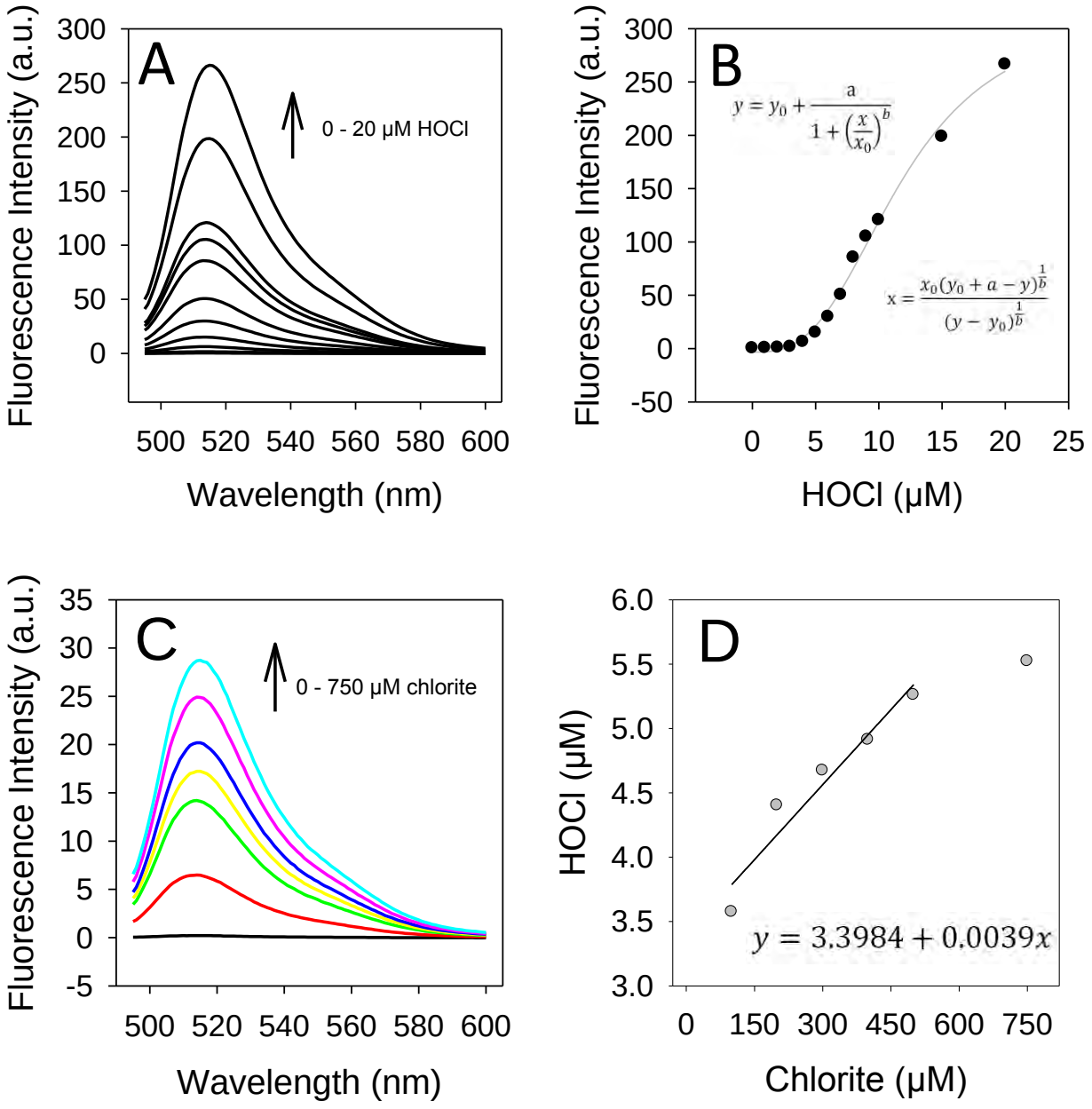

Supplemental Figure 3. (A) Electron Paramagnetic Resonance spectra of 30 µM NdCld in 50 mM MES buffer, pH 5.5., in absence (black lines) and presence (red lines) of 17.5 mM methionine, after reaction with 0 mM (bottom) to 100 mM (top) chlorite. (B) Ferric high spin signal intensity of chlorite treated samples in absence (black bars) and in presence (red bars) of methionine.

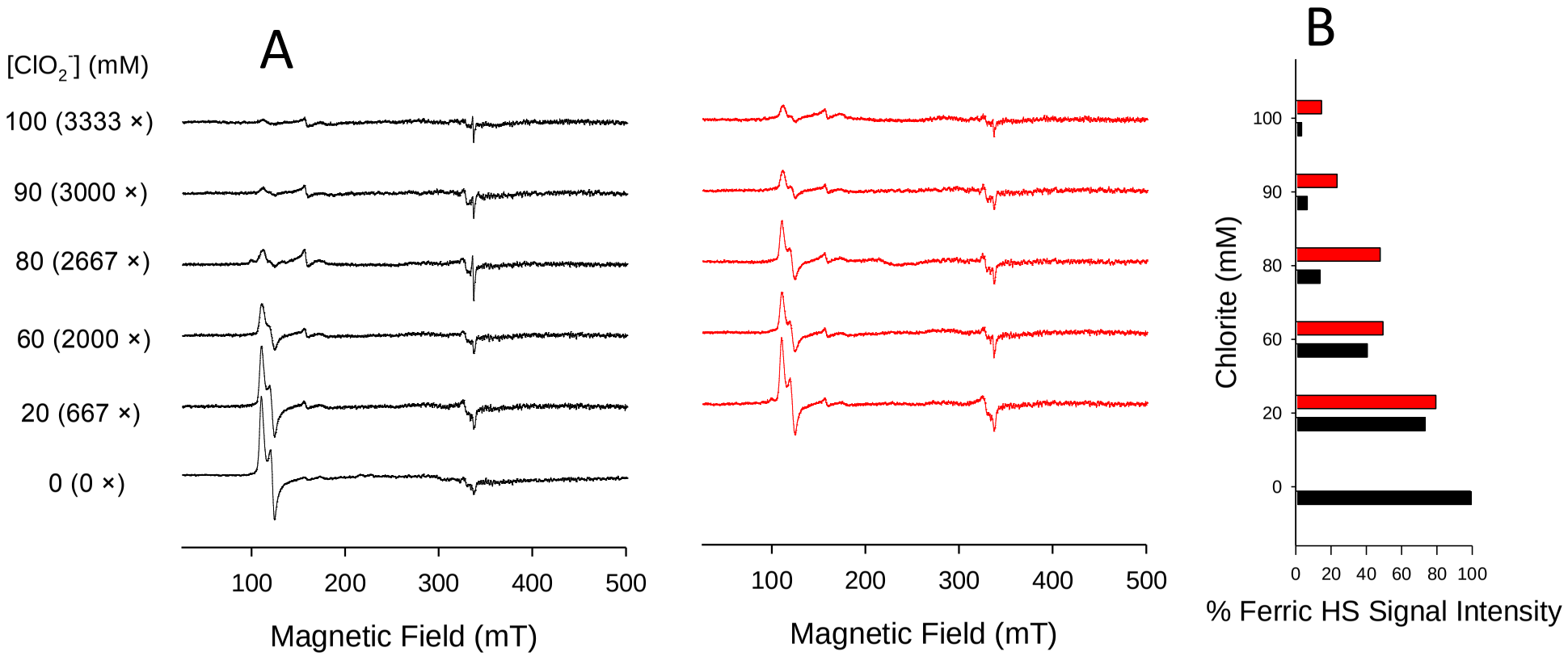

Supplemental Figure 4. Influence of hypochlorite to the architecture of the heme-iron of chlorite dismutase from "*Candidatus* Nitrospira defluvii". EPR spectra of 30 µM wild-type NdCld treated with (bottom to top) 0 mM, 1 mM, 16 mM, and 23 mM of hypochlorite

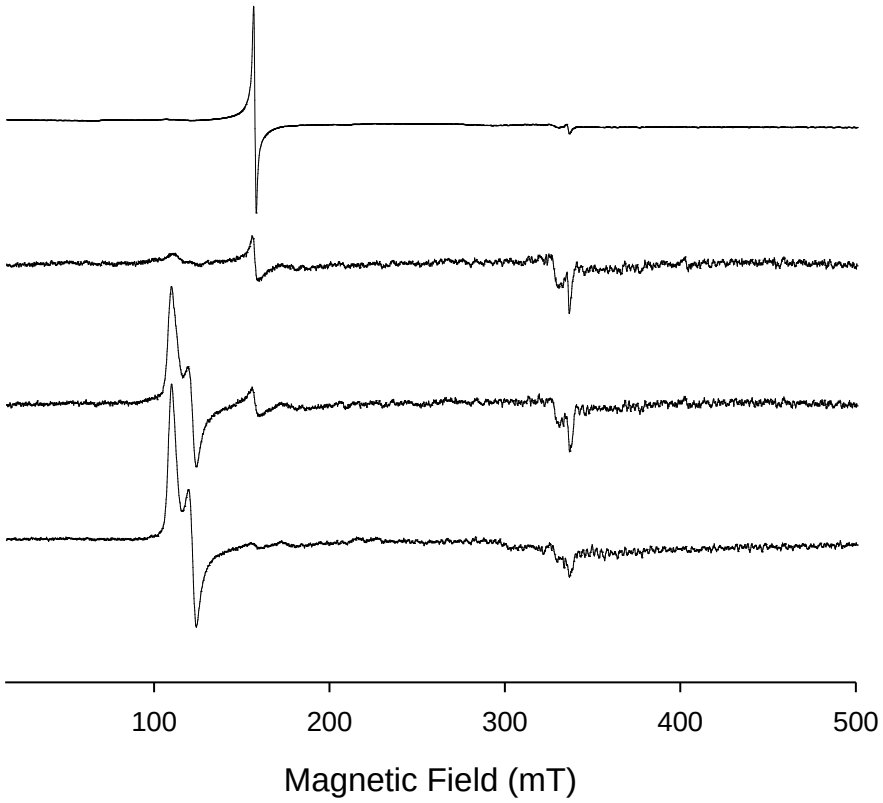

Supplemental Figure 5. The effect of methionine on the interconversion of redox intermediates and heme bleaching. (A) Spectral changes, when 1 µM of wild-type NdCld was mixed with 1 mM of chlorite at pH 5.5 (50 mM citrate-phosphate buffer) in the conventional stopped-flow modus. Spectra were taken at 3 ms (black spectrum), 74 ms, 403 ms, 755 ms, 1352 ms, 2367 ms, 4090 ms, 7018 ms, and 11990 ms, respectively. The final spectrum (20000 ms) is depicted in red. Inset shows enlargement of Soret region. (B) Same reaction as in (A) but in the presence of 5 mM methionine. (C) Same reaction as in (A) but at pH 7.0 (50 mM phosphate buffer), (D) same reaction as (C) but in presence of 5 mM methionine.

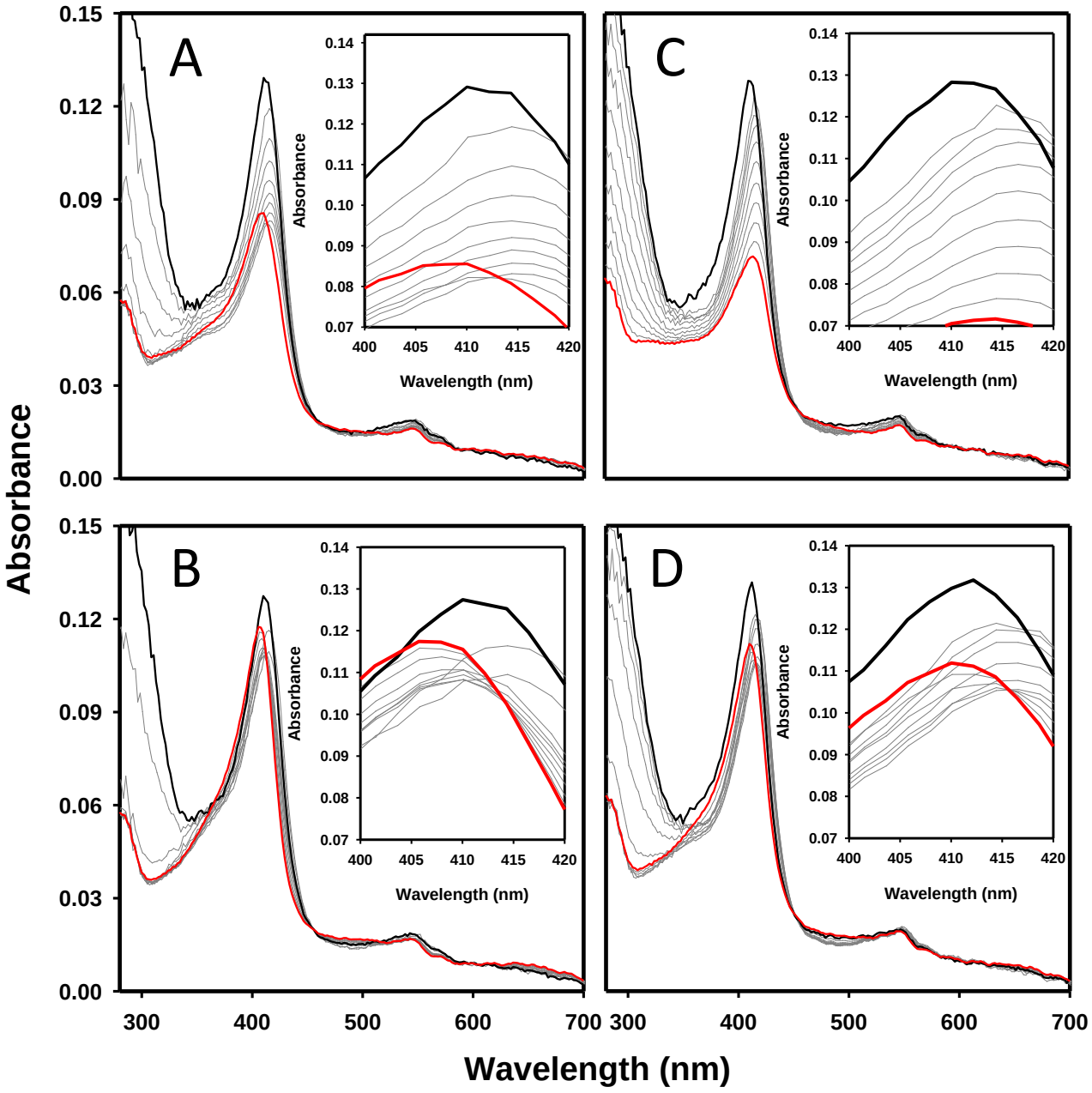

Supplemental Table 1. EPR simulation parameters from individual high spin and low spin forms of NdCld at pH 5.5 and pH 7.0, eventually with chlorite and methionine (HS – high spin, LS – low spin, R – rhombicity, I – relative intensity, E/D – rhombic to axial contribution, TI – total intensity with respect to untreated protein).

	HS LS compounds*	g_x^{eff} g_x	g_y^{eff} g_y	g_z^{eff} g_z	E/D	R (%)	I (%)	TI (%)
NdCld pH 5.5	HS1	5.500	6.175	1.990	0.014	4.2	80	100
	HS2	5.950	5.950	1.995			20	
	HS1	5.500	6.175	1.990	0.014	4.2	49	104
NdCld pH 5.5	HS2	5.950	5.950	1.995			26	
+ 17.5 mM methionine	LS1	2.980	2.250	1.875			13	
	LS2	3.150	2.250	1.800			13	
NdCld pH 5.5	HS1	5.625	6.225	1.990	0.013	3.7	43	14
+ 100 mM chlorite	HS2	5.950	5.950	1.995			57	
NdCld pH 5.5	HS1	5.500	6.175	1.990	0.014	4.2	50	36
+ 100 mM chlorite	HS2	5.950	5.950	1.995			28	
+ 17.5 mM methionine	HS3	5.250	6.375	1.975	0.025	7.0	22	
	HS1	5.500	6.175	1.990	0.014	4.2	49	100
NdCld pH 7.0	HS2	5.950	5.950	1.995			19	
	LS1	2.980	2.250	1.875			15	
	LS2	3.150	2.250	1.800			16	
	HS1	5.500	6.175	1.990	0.014	4.2	32	83
NdCld pH 7.0	HS2	5.950	5.950	1.995			28	
+ 17.5 mM methionine	HS3	5.250	6.375	1.975	0.025	7.0	14	
	LS1	2.980	2.250	1.875			13	
	LS2	3.150	2.250	1.800			14	
NdCld pH 7.0	HS1	5.500	6.175	1.990	0.014	4.2	18	11
+ 100 mM chlorite	HS2	5.950	5.950	1.995			64	
	HS3	5.450	6.225	1.990	0.017	4.8	18	
NdCld pH 7.0	HS1	5.500	6.175	1.990	0.014	4.2	41	42
+ 100 mM chlorite	HS2	5.950	5.950	1.995			23	
+ 17.5 mM methionine	HS3	5.250	6.375	1.975	0.025	7.0	36	

*minimum number of high-spin and low-spin compounds used for simulation

Chapter 7

Investigation of the structural implications of ion binding in chlorite dismutases by means of molecular dynamics simulations

Axel Sündermann, Maria Reif, Stefan Hofbauer, Christian Obinger, Chris Oostenbrink

Research Article

Submitted to *Biochemistry*

Structural implications of anion binding to chlorite dismutase in ferrous, ferric and Compound I state - a molecular dynamics simulations study

Axel Sündermann[1], Maria Reif[1], Stefan Hofbauer[2], Christian Obinger[2], Chris Oostenbrink[1]*

[1] *Department of Material Sciences and Process Engineering, Institute of Molecular Modeling and Simulation, BOKU – University of Natural Resources and Life Sciences, A-1190 Vienna, Austria*

[2] *Department of Chemistry, Division of Biochemistry, VIBT – Vienna Institute of BioTechnology, BOKU – University of Natural Resources and Life Sciences, A-1190 Vienna, Austria*

KEYWORDS: Chlorite dismutase, molecular dynamics simulation, chlorite, hypochlorite, Compound I

ABSTRACT: Chlorite dismutases are prokaryotic heme *b* oxidoreductases which convert chlorite to chloride and dioxygen. It has been postulated that during turnover hypochlorite is formed transiently, which might be responsible for the observed irreversible inactivation of these iron proteins. The only distal residue in the heme cavity is a conserved and mobile arginine, but its role in catalysis and inactivation is not fully understood. In the present study, the pentameric chlorite dismutase (Cld) from the bacterium "*Candidatus* Nitrospira defluvii" was probed for binding of the low spin ligand cyanide, the substrate chlorite and the intermediate hypochlorite. Simulations were performed with the enzyme in the ferrous, ferric and Compound I state. Additionally, the variant R173A was studied. We report the parametrization for the GROMOS forcefield of the anions ClO^-, ClO_2^-, ClO_3^- and ClO_4^- and describe spontaneous binding, unbinding and rebinding events of cyanide, chlorite and hypochlorite as well as the dynamics of the conformations of Arg173 during simulations. The findings suggest that (i) chlorite binding to ferric NdCld occurs spontaneously and (ii) that Arg173 is important to impair hypochlorite leakage from the reaction sphere. This is discussed in comparison with experimental data on catalysis and inhibition of chlorite dismutase.

INTRODUCTION

Chlorite dismutases (Clds) are prokaryotic heme *b* containing oxidoreductases (EC 1.13.11.49) that convert chlorite to dioxygen and chloride. Based on subunit architecture and oligomerization two main clades are distinguished.[1-5] Clade 1 contains pentameric proteins including Cld from the bacterium "*Candidatus* Nitrospira defluvii" (NdCld), which was investigated in this work. In Clade 2 dimeric representatives with smaller subunit size are found. Chlorite dismutases are suggested to have ancient roots as similar proteins where found in many different bacterial and archaeal phyla.[5,6]

Several crystal structures of Clds have been published in recent years[3–5,7] which demonstrated that the only charged residue in the distal heme cavity is a conserved arginine residue, which was shown to be catalytically important but not essential for the degradation of chlorite.[5,8,9]

In the resting state the heme iron of Cld is in the ferric state which is stabilized by the imidazolate character of the proximal histidine.[7,10] It was shown by Hofbauer et al.[10] that the structural changes upon reduction of Cld to the ferrous form are very small, which is in agreement with other heme enzymes.[11-15] In NdCld the chlorite access channel has a length of 1.5 nm with a bottle neck radius of 0.28 nm.[10] Chlorite (ClO_2^-) enters the channel and binds to ferric heme forming the Fe(III)-ClO_2 adduct. This induces the redox reaction which includes the heterolytic cleavage of chlorite to hypochlorite (ClO^-) with concomitant oxidation of ferric NdCld to the Compound I state (which most probably is an oxoiron(IV) porphyrin radical). In the final reaction hypochlorite recombines with the ferryl oxygen of Compound I thereby releasing O_2 and chloride.[16]

In this postulated mechanism several issues still need clarification including the question about the catalytic role of the distal arginine (i.e. Arg173 in NdCld). Crystal structures have shown that this basic amino acid can

adopt two distinct conformations, either pointing towards the heme iron ('in') or towards the substrate channel entry ('out').[9] Mutational analyses suggested that the distal arginine is important to keep the transiently produced hypochlorite close to the ferryl oxygen for the rebound mechanism.[9,17] On the other hand chlorite degradation can also occur in its absence, however significantly slower and with increased susceptibility for irreversible inactivation.[3–5,7,16,18–22] Hofbauer et. al.[17] demonstrated that inactivation includes heme bleaching as well as oxidation and chlorination of amino acids of the protein moiety. The authors concluded that hypochlorite released from the active site during turnover is responsible for these modifications.[17]

In this work we aimed at studying the binding of the low-spin ligand cyanide, the substrate chlorite and the postulated intermediate hypochlorite to wild-type NdCld and the mutant R173A by means of molecular dynamics simulations in order to get more information about the role of the flexible Arg173. Simulations were performed with the heme iron in its ferrous, ferric as well as Compound I state (Table I). Prior to the simulations, the ions ClO^-, ClO_2^-, ClO_3^- and ClO_4^- were parametrized for the GROMOS forcefield.[23,24] Our findings suggest that chlorite is attracted by the ferric state and that the role of Arg173 in formation of the Fe(III)-ClO_2 complex is negligible. By contrast, the conserved basic amino acid seems to support the rebound mechanism by diminishing the escape of transiently form hypochlorite. The findings are discussed with respect to experimental data on catalysis and inhibition of chlorite dismutase.

Table 1. Overview of performed simulations with the pentameric chlorite dismutase from "Candidatus Nitrospira defluvii". First column: label of simulation; second column: anion; third column: starting position of the conserved arginine 173 being either 'in' (pointing towards the heme iron) or 'out' (pointing towards the substrate entry channel); fourth column: oxidation state of heme iron. The last 4 columns show simulation details including amount of counter ions and water molecules, box size and length of simulation.

Simulation	Arginine 173 [%]		Substrate ion [%]	
	In	Out	In	Out
OC	39	61	100	0
ON	85	15	100	0
OX	0	100	-	-
RC	30	70	16	84
RN	11	89	4	96
RX	38	62	-	-
CC	1	99	7	93
CI	1	99	8	92
MO	-	-	100	0
MC	-	-	2	98
OF	0	100	1	99
RF	4	96	0	100

MATERIALS AND METHODS

Parametrization. Experimental absolute intrinsic hydration free energies for the series of Cl^-, ClO^-, ClO_2^-, ClO_3^- and ClO_4^- ions were derived from available experimental data. This involved the formation enthalpy and entropy of the gas-phase ion, the conventional formation free energy of the aqueous ion and an assumed absolute intrinsic proton hydration free energy of -1100 kJ.mol^{-1}.[24,25] The resulting absolute intrinsic hydration free energies are given in Table II and the detailed derivation outlined in the supplementary material (Table SI). ΔG_{cor} was calculated according to the correction scheme for oligoatomic ion hydration[26] for the case of lattice-sum electrostatic interactions, as outlined in the supplementary material.

Table 2. Comparison between $\Delta_s G$ from experimental data and simulations. Detailed information about derivation of the experimental values is found in the supplementary material.[25]

Ion	Experimental $\Delta_s G^{\ominus}$ [kJ·mol^{-1}]	Simulation $\Delta_s G^{\ominus}$ [kJ·mol^{-1}]
Cl^-	-309.4	-310.2[a]
ClO^-	-335.0	-337.2
ClO_2^-	-310.6	-311.0
ClO_3^-	-240.7	-228.8
ClO_4^-	-227.1	-216.9

Molecular dynamics simulations. The molecular dynamics simulations of the pentameric protein were performed using the GROMOS11 molecular simulation package.[27] Parameters from the GROMOS forcefield 54A7 were used. The parameters for the ferric and ferrous heme group were taken from Zou et. al.[28] For Compound I an oxygen atom with GROMOS integer atom code 2 and a partial charge of -0.38 was covalently bound to the iron ion with a bond length of 0.161 nm and O-Fe-N angles kept at 90° with a force constant of 380 kJ.mol^{-1}. The iron ion maintained a partial charge of 0.48, with the remaining charge distribution spread over the atoms of the porphyrin system. Building blocks for all heme species are available in the supplementary material.

The protein was solvated in simple point charge (SPC) water molecules[29] in a periodic rectangular simulation box to which chloride and sodium ions were added to obtain an overall neutral system at pH 7. The temperature of the systems was slowly increased to 300 K by 60 K every 20 ps and further equilibrated for 100 ps. A step size of 2 fs was used and the coordinates were read out every 0.5 ps. A weak coupling with a relaxation time of 0.1 ps for the temperature and 0.5 ps for the pressure was used to keep the temperature and pressure constant at 300 K and 1 atm, respectively.[30] The isothermal compressibility was set to $4.575.10^{-4}$ (kJ.mol^{-1}.nm^{-3})$^{-1}$. The SHAKE algorithm[31] was used to constrain the bond lengths to their optimal values with a relative geometric accuracy of 10^{-4}. A molecular pairlist was generated using a triple-range cutoff.[32]

Nonbonded interactions up to a short range of 0.8 nm were calculated at every timestep from a pairlist that was updated every 5 steps. Interactions up to a long-range cutoff of 1.4 nm were calculated at pairlist updates and kept constant in between. A reaction-field contribution[33] was added to the electrostatic interactions and forces to account for a homogeneous medium with a dielectric permittivity of 61[34] outside the cutoff. A summary of all performed simulations is given in Table I.

Analysis. The GROMOS++ software package[35] was used to analyze the simulations. The atom-positional root-mean-square deviations from the initial model structures and the secondary structure according to the DSSP rules defined by Kabsch and Sander[36] were calculated to assess the stability of the protein. Hydrogen bonds were monitored based on the criterion that a hydrogen atom connected to a donor atom has an acceptor atom within 0.25 nm and the donor-hydrogen-acceptor angle is least 135°.

RESULTS

Parametrization. The derivation of experimental reference values for the free energy of solvation is summarized in Table SI (supplementary material). Table II compares these data with the results from the simulations. The simulation data is calculated as the sum of a free energy of cavitation, a raw charging free energy as well as various corrections to account for artefacts in the treatment of electrostatic interactions as well as a standard state correction (see Table SII). When comparing $\Delta_s G^o$ values of the parametrization with those calculated from the experimental values (Table II), $\Delta_s G^o$ from the parametrization is within an acceptable range of the experimental value, and should render the ions compatible with the 54A7 and 54A8 GROMOS parameter sets.[23,24] The final interaction parameters are presented in Table III.

Table 3. Nonbonded and bonded parameters for the ion series. IAC refers to the integer atom code according to the GROMOS 54A7 forcefield.[23]

Nonbonded parameters			
Ion	**Atom**	**IAC**	**q[e]**
Cl^-	Cl^-	38	-1
ClO^-	Cl	33	-0.17
	O	2	-0.83
ClO_2^-	Cl	33	0.55
	O	2	-0.775
ClO_3^-	Cl	33	-0.1
	O	2	-0.3
ClO_4^-	Cl	33	-0.2
	O	2	-0.2
Bonded parameters			
Ion	**Property**	**Minimum energy value**	**force constant**
ClO^-	Cl-O bond	0.1758 nm	$8.12 \cdot 10^6$ kJ·mol^{-1}·nm^{-4}
ClO_2^-	Cl-O bond	0.161 nm	$4.84 \cdot 10^6$ kJ·mol^{-1}·nm^{-4}
	O-Cl-O Angle	120.0°	780 kJ·mol^{-1}
ClO_3^-	Cl-O bond	0.153 nm	$7.15 \cdot 10^6$ kJ·mol^{-1}·nm^{-4}
	O-Cl-O Angle	108.0°	465 kJ·mol^{-1}
	Improper dihedral	35.26439°	0.102 kJ·mol^{-1}·degree^{-2}
ClO_4^-	Cl-O bond	0.150 nm	$8.37 \cdot 10^6$ kJ·mol^{-1}·nm^{-4}
	O-Cl-O Angle	109.5°	450 kJ·mol^{-1}

Overall protein structure. After parametrization of the ions, a total of twelve simulations were performed with pentameric chlorite dismutase from "Candidatus *Nitrospira defluvii*" (NdCld, PDB id: 3nn1)[5] and its R173A mutant (PDB id: 3nn3)[5] (Table I). In order to assess the stability of the protein during the simulations and investigate possible structural changes, several analyses were performed. The average values of various properties over the simulation for the five monomers are presented in Table IV.

Table 4. Overview of the structural parameters of the simulations. First column: label of simulation; second column: root mean square deviation (RMSD) with respect to the crystal structure; third column: amount of α-helices and β-sheets over the course of the simulations. The values for the crystal structures are 43.9 % α-helices and 25.5 % β-sheets for the wild-type structure and 44.3 % α-helices and 24.7 % β-sheets for the R173A mutant structure. Fourth column: hydrogen bonds between the monomers; fifth column: interface area between the monomers. All values are averages over the last 10 ns of the simulation and over the five monomers with statistical uncertainties obtained from block averaging.[37]

Simulation	RMSD [nm]	Secondary structure [%]		Number of hydrogen bonds
		Helix	Sheet	
OC	0.16 ± 0.01	42.8 ± 1.0	22.7 ± 0.5	11.0 ± 1.7
ON	0.16 ± 0.01	43.0 ± 0.5	23.5 ± 0.9	10.5 ± 0.7
OX	0.17 ± 0.01	42.4 ± 1.1	23.1 ± 0.9	10.4 ± 1.6
RC	0.16 ± 0.01	43.0 ± 1.1	22.9 ± 1.2	10.3 ± 2.5
RN	0.16 ± 0.01	42.9 ± 0.8	22.4 ± 1.5	11.4 ± 1.4
RX	0.18 ± 0.01	43.1 ± 1.0	23.8 ± 1.0	11.0 ± 1.4
CC	0.17 ± 0.01	42.9 ± 1.2	22.2 ± 2.8	11.6 ± 1.5
CI	0.16 ± 0.01	42.0 ± 1.5	22.6 ± 0.7	11.5 ± 3.0
MO	0.19 ± 0.02	42.6 ± 0.8	23.6 ± 1.3	10.9 ± 2.1
MC	0.19 ± 0.01	43.5 ± 1.5	22.8 ± 1.6	9.4 ± 1.9
OF	0.17 ± 0.02	42.7 ± 0.6	22.6 ± 0.8	10.7 ± 0.9
RF	0.18 ± 0.03	42.4 ± 1.1	23.1 ± 1.0	12.2 ± 0.8

The atom-positional root-mean-square deviation (rmsd) with respect to the crystal structures (i.e. 3nn1 and 3nn3, respectively) was in the range 0.16 nm to 0.19 nm with a statistical uncertainty of 0.01 nm to 0.03 nm. This indicates that the pentameric protein is very stable during all simulations. No significant deviation from the crystal structure were observed. Moreover, the rmsd of the mutant is comparable to wild-type NdCld. Secondary structural elements over time were analyzed using the DSSP algorithm. As Figure 1 depicts, the dominating α-helical structures did not change significantly during the simulations. The percentage of amino acids that are part of a helix over 20 ns of simulations over all five monomers ranges from 42.0 % to 43.5 % with a statistical uncertainty from 0.5 % to 1.5 %. In the crystal structures of wild-type NdCld and the variant R173A 43.9 % and 44.3 % of the amino acids are part of α-helical structures. The major helices did not unfold during the various simulations. Furthermore, the β-sheet structures at the center of each monomer were analyzed. The percentage of amino acids which are part of a β-sheet structure over the simulation time for all five monomers was found to range from 22.4 % to 23.8 % with a statistical uncertainty of 0.5 % to 2.8 %. This compares with 25.5 % and 24.7 % found in the crystal structures of the wild-type and mutant proteins. The absence of significant changes of secondary structure

elements clearly suggests that the monomers of NdCld are very stable during the simulations.

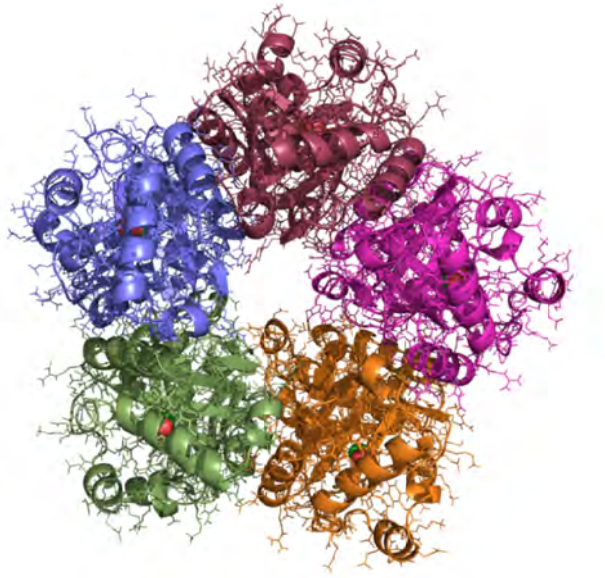

Figure 1. Structure of pentameric chlorite dismutase from "*Candidatus* Nitrospira defluvii". The five different monomers are colored differently and the secondary structure elements are shown in a cartoon representation while the side chains are depicted as sticks. The heme is also shown with a stick representation and the anions in the active sites are represented with a bubble representation.

Next we assessed the stability of the quaternary structure of NdCld by monitoring the number of hydrogen bonds between the monomers over time. The average number of hydrogen bonds over 20 ns of simulation at the five interfaces ranges from 9.4 to 12.2 with a statistical uncertainty of 0.7 to 3.0 hydrogen bonds. This indicates that the monomers interact stably and the pentamer does not lose its quaternary structure over the time course of the simulations.

Cyanide and chlorite binding to ferrous and ferric NdCld. The stability assessments described above clearly suggest that the overall structure of NdCld does not change during the twelve 20 ns simulations. This concurs with the literature that heme enzymes do not undergo big structural changes during redox catalysis in general[11–15] thus allowing us to study the impact of the oxidation state of NdCld and/or the presence of various anions on the behaviour of the fully conserved Arg173. The latter was shown to participate in the chlorite degradation mechanism[5,8,9] and to adopt two distinct conformations, one pointing towards the heme iron (here referred to as 'in') and one pointing towards the entry of the active site substrate access channel (here referred to as 'out'). This prompted us to study the change in distance between the C_ζ atom of Arg173 and the heme iron over the course of the simulations in all five monomers (Figure 2 and Table V).

In the resting ferric state R173 stayed in the 'out' conformation as long as anions were absent in the initial protein structure (Figure 2G) or anions (e.g. chlorite) were free in solution (Figure 2I). By contrast, in ferrous NdCld R173 can adopt both positions (Figure 2H) with 38 % in the 'in' position and 62 % in the 'out' position (Table V). As the simulation was started with the arginine in the 'out' position, transitions between the two conformations occurred during the 20 ns simulation. This indicates that the ferrous heme attracts the positively charged arginine at a distance within the cutoff chosen for the simulations (1.4 nm). In the presence of chlorite in the solution (Figure 2J) R173 mainly adopted the 'out' position (i.e. 4 % 'in' and 96 % 'out') most probably due to chlorite ions that came close to the active site.

Table 5. Positions of arginine 173 and anions. First column: label of simulation; second column: percentage of the simulation time the arginine 173 was either in the 'in' position, (pointing towards the heme iron with iron to arginine C_ζ distance being 0.64 nm or less) or 'out' position (pointing towards the substrate channel entry). Third column: percentage of simulation time the substrate ion was inside or outside of the active sites of the pentamer. The ion was considered to be in the active site when the heme iron to anion distance was 0.8 nm or less.

Simulation	Arginine 173 [%]		Substrate ion [%]	
	In	Out	In	Out
OC	39	61	100	0
ON	85	15	100	0
OX	0	100	-	-
RC	30	70	16	84
RN	11	89	4	96
RX	38	62	-	-
CC	1	99	7	93
CI	1	99	8	92
MO	-	-	100	0
MC	-	-	2	98
OF	0	100	1	99
RF	4	96	0	100

With ferric NdCld and a cyanide ion (i.e. a low-spin ligand in heme proteins) in the active site and starting with R173 in the 'out' position, during 85 % of the simulation time the arginine was in the 'in' position. Apparently, the negatively charged cyanide ion represents a strong attractive force. With ferrous NdCld and CN^- in the heme cavity the 'in" conformation was adopted only during 11 % of the simulation time, most probably because the anion left the active site after a short period of time.

Next we placed the substrate chlorite in the heme cavity of either ferric or ferrous NdCld (Figures 2C and 2D). In both cases the amount of time of Arg173 spent in each position was similar (39 % and 30% 'in' *versus* 61 % and 70 % 'out', respectively). However, the distance distribution with ferric NdCld showed two distinct peaks, whereas in the reduced protein three smaller and wider peaks were found, which might reflect substrate leaving the active site. The fact that with cyanide (in contrast to chlorite)

the arginine conformation is more balanced towards the 'in' position could be due to the partial charges assigned to the chlorite ion. In the cyanide ion the negative charge is more concentrated, while in the chlorite ion it is delocalized over the atoms (Table III).

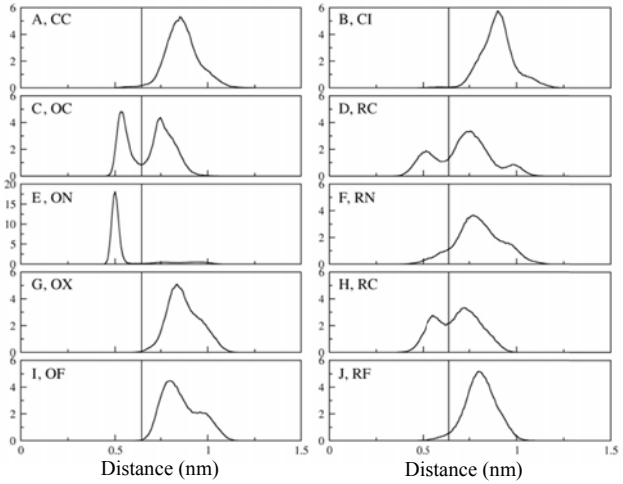

Figure 2. Distribution of the distance between the heme iron and the atom C_ζ of R173. The position of R173 is either 'in' (pointing towards the heme iron) or 'out' (pointing towards the substrate channel entry). The arginine was considered as 'in' when the heme iron to arginine distance was 0.64 nm or less. This threshold is represented by a vertical black line in all graphs. (A) Simulation with Compound I, hypochlorite and the argininie starting from an 'out' position (CC). (B) Simulation with Compound I, hypochlorite and the arginine starting from an 'in' position (CI). (C, E, G) Simulations with ferric NdCld and chlorite, cyanide and no anion, respectively (OC, ON, OX). (D, F., H) Simulations with ferrous NdCld and chlorite, cyanide and no anion, respectively (RC, RN, RX). (I, J) Simulations with 20 chlorite ions free in solution with the ferric and ferrous NdCld (OF, RF).

Figure 3 depicts the distribution of the distance between the heme iron and the anions, whereas Table V summarizes the respective fraction being either in the heme cavity or outside. With ferric NdCld both cyanide and chlorite remained close to the heme iron for 100 % of the simulation time. In comparison, in the ferrous state cyanide spent only 11 % and chlorite 30 % of the time in the active site. Figures 3F and 3H show that some ions moved as far as into the bulk water.

In two simulations twenty chlorite ions were added to the water box. As can be seen in Figure 3I, some ions moved into the active site of the ferric protein, whereas this did not occur in ferrous NdCld (Figure 3J). With ferrous NdCld several chlorite ions came close to an active site but never entered it. By contrast, in ferric pentameric NdCld four of the five active sites had chlorite close to the heme cavity during large part of the simulation time (Figures 4A & 4D). Two active sites even bound a chlorite ion which stayed in the active site for the rest of the simulation. Figure 5 demonstrates that the position of bound chlorite in this simulation was similar to the simulation, in which the substrate was in the active site from the beginning. Only the orientation of chlorite was different. In any case, spontaneous binding of the anionic substrate occurred during the 20 ns simulations. These findings clearly suggest that chlorite is attracted by the ferric heme state and that the role of Arg173 in substrate binding is negligible.

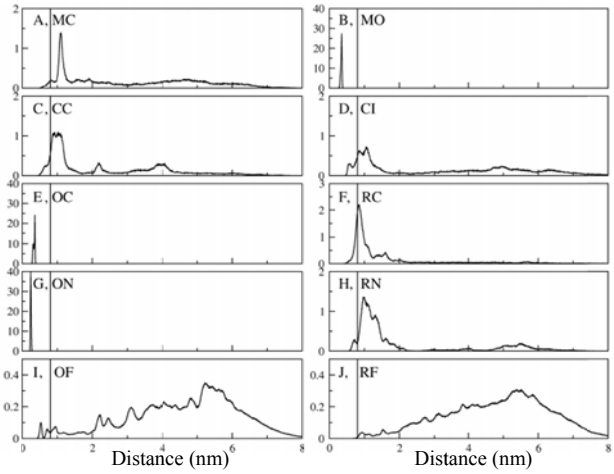

Figure 3. Distribution of the position of the anion. The anion was considered inside the active site when the distance between the anion and the heme iron was 0.8 nm or less. This threshold is shown as a vertical black line in all graphs. (A, B) Simulations with the R173A mutant structure in Compound I state and hypochlorite (MC) and ferric state and chlorite (MO) respectively. (C, D) Simulations with Compound I and hypochlorite with the conserved arginine 173 pointing towards the substrate channel entry (CC) or towards the heme iron (CI), respectively. (E, G) Simulations with an Fe(III) state and chlorite (OC) and cyanide (ON), respectively. (F, H) Simulations with Fe(II) state and chlorite (RC) and cyanide (RN), respectively. (I, J) Simulations with chlorite ions free in solution and ferric (OF) and ferrous NdCld (RF), respectively.

Hypochlorite binding to Compound I. Hypochlorite has been postulated to be a transiently formed intermediate during the degradation of chlorite that reacts with Compound I to form chloride and O_2. Simulating Compound I and hypochlorite in the free solution showed that Arg173 adopts the 'out' position almost exclusively (Figure 2A) regardless of its starting position. During the simulations no evidence was found that arginine mediates the shuttling of the ion to the active site. By contrast, Arg173 follows an anion that occupies the active site and adopts the 'in' position.

Next we evaluated the distribution of the distance between the heme iron in the Compound I state and hypochlorite with R173 either in the 'in' or in the 'out' conformation. In both simulations, most of the anions left the active site during the simulation (Figures 3C & 3D, Table V). Only 7 % or 8 % of the simulation time ClO^- was found in the heme cavity. This suggests that this transiently formed intermediate (in contrast to the substrate chlorite) easily escapes from the heme cavity.

Simulation of the mutant structure (R173A) with hypochlorite in the active site gave a similar picture. In contrast to the wild-type enzyme ClO^- spent only 2 % of the simulation time in the heme cavity. The difference between wild-type and mutant protein is relatively small. It

was previously suggested[17] that Arg173 helps to keep hypochlorite in the reaction sphere for the rebound mechanism. It has to be mentioned that in MD simulations using a classical force field description no reaction can take place and a small difference in the residence time of hypochlorite may be sufficient to explain differences in the leaking behaviour. Moreover, as a reaction could take place relatively quickly, it is impossible to quantitatively compare experimentally observed leaking rates to the ones observed in our simulations.

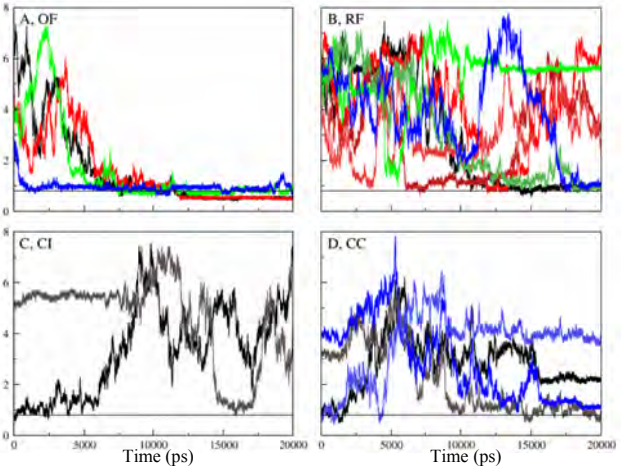

Figure 4. Distance between the anions and the heme iron over the course of the simulations. The horizontal black line at 0.8 nm represents the threshold for considering an ion as being inside the active site or not. (A) Simulation with 20 chlorites free in solution and ferric NdCld (OF). (B) Simulation with 20 chlorites free in solution and ferrous NdCld (RF). (C, D) Simulations with Compound I and hypochlorite and the conserved arginine 173 pointing towards the heme iron (CI) or towards the substrate channel entry (CC), respectively. For clarity, only curves for ions that show spontaneous binding are drawn. When two curves with matching colors are given, these are representative of a single ion interacting with multiple active sites.

During the simulation of the Compound I with hypochlorite, most of the ions left the active site. But it was also observed that in some cases a hypochlorite ion returned to positions close to the active site independent whether Arg173 was initially in the 'in' or 'out' position (Figures 4C & 4D). Analysis revealed that it was not the same hypochlorite that had left the active site previously.

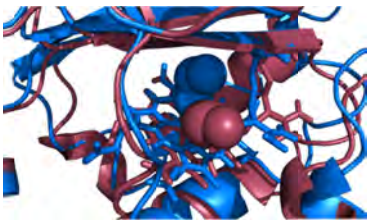

Figure 5. Overlay of one active site of the pentameric chlorite dismutase from "*Candidatus* Nitrospira defluvii" (NdCld) in the crystal structure with a chlorite bound (in blue) and after spontaneous binding during the simulation with 20 chlorite ions free in solution and ferric NdCld (in red). The R173 is pointing towards substrate channel entry in both cases.

DISCUSSION

The pentameric chlorite dismutase from "*Candidatus* Nitrospira defluvii" in its ferrous, ferric and Compound I state was simulated in the presence of its substrate chlorite, the postulated intermediate hypochlorite and the low-spin ligand cyanide in order to evaluate the role of the conserved distal arginine in these events. In functional Clds Arg173 (NdCld numbering) represents the only charged amino acid in heme cavity.

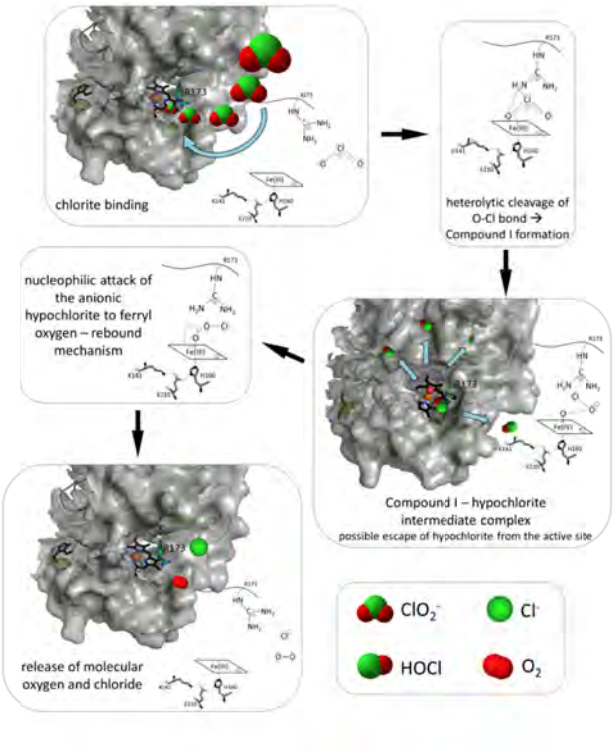

Figure 6. Proposed reaction mechanism for chlorite dismutases. First (I) the substrate ClO_2^- binds to ferric NdCld forming the Fe(III)-ClO_2 adduct. This reaction is followed by oxidation (II) of the heme to Compound I with concomitant reduction of chlorite to hypochlorite, ClO^-. Subsequently, (III) the ferryl oxygen of Compound I is rebound by hypochlorite and (IV) chloride and dioxygen are released.[16]

In Figure 6 we summarize the MD simulation data from this work and present a reaction mechanism that also incorporates the so far published experimental data. The initial reaction includes binding of the anionic substrate chlorite to the ferric resting state of NdCls forming the respective complex. Experimental data have shown that the role of Arg173 in this reaction is marginal. Exchange of R173 by either alanine or glutamine had only a small effect on the K_M value (i.e. increase by factor of 1.3 in R173A compared to the wild-type protein).[9] This is supported by the MD data, which showed that Arg173 plays neither a role in complex formation nor in shuttling the anion into the active site. It rather followed the charged molecules and changed its orientation ('in' *versus* 'out') accordingly. This might suggest that role of Arg173 in this initial reac-

tion step is substrate recognition, since no spontaneous binding events were observed with the structure of the mutant Arg173Ala. By contrast, with both ferrous and ferric wild-type NdCld some chlorite or hypochlorite ions came close to the active site. But real binding was only observed with the ferric protein, which represents the resting state of chlorite dismutase. The Fe(II) state does not participate in catalysis.

Binding of cyanide to the active site of heme proteins typically occurs with the respective ferric forms. The low-spin cyanide complexes of the corresponding Fe(II) forms are week. Recent experimental data have demonstrated[9] that both the binding rate of cyanide to ferric NdCld as well as the stability of the low-spin complex was extremely low in NdCld mutants that lacked Arg173. The present MD study shows that cyanide remained in the heme cavity of wild-type ferric NdCld during simulation and promoted 'in' conformation of Arg173. With ferrous NdCld cyanide easily escaped from the active site and the 'out' conformation of Arg173 dominated.

Immediately after binding of the substrate chlorite to ferric NdCld the heterolytic cleavage of chlorite occurs thereby oxidizing the enzyme to the Compound I state and reducing chlorite to hypochlorite (Figure 6). This transiently intermediate must stay in the reaction sphere for the subsequent recombination step. The turnover number (k_{cat}) for chlorite degradation is ~6.5% (R173A)[9] compared to the wild-type enzyme. This underlines the importance of Arg173 in these reaction steps but also demonstrates that it is not fully essential for catalysis. Besides the decreased turnover number the variant Arg173Als was shown to be also more prone to inactivation than the wild-type enzyme.

The MD simulations of Compound I with hypochlorite indicate that the conserved arginine 173 might play a role as already suggested[9,17] and that it is important to keep the transiently formed hypochlorite in the active site. Recent experimental data suggest that some hypochlorite nevertheless escapes from the active site in a pH-dependent manner. As a consequence the enzyme becomes irreversibly inactivated by oxidative modifications of both the protein matrix as well as the prosthetic group.[17] Escape of hypochlorite is more pronounced at high chlorite concentrations as well as with mutant enzymes that lack Arg173. The present MD study clearly demonstrates that a large portion of hypochlorite escapes from the heme cavity and enters the bulk phase. This fits with the experimental data that reported oxidative modifications of amino acids on the surface of NdCld that derive from hypochlorite.[17] The present findings also show that leakage of hypochlorite in the mutant R173A is higher than in the wild-type protein although the MD simulations do not allow a correlation with experimental data since no recombination reaction can take place.

Chlorite dismutase is a promising biocatalyst that can be used for the degradation of anthropogenic chlorite contamination in the environment. For this purpose it is necessary to select robust representatives and/or engineer the metalloenzymes and decrease their susceptibility for inactivation. The present study allowed new insights into the dynamics and the role of the conserved arginine in this process. It will be interesting to perform comparative studies of Clade II dimeric chlorite dismutases, which are less prone to inactivation (unpublished data) but have a very similar heme cavity architecture.[7]

ASSOCIATED CONTENT

Supporting Information. Supporting information is available about (i) detailed derivation of experimental and calculated absolute intrinsic hydration free energies of the ions, (ii) molecular topology building blocks of the ions for the GROMOS force field, and (iii) molecular topology building blocks of the different heme species for the GROMOS force field.This material is available free of charge via the Internet at http://pubs.acs.org.

AUTHOR INFORMATION

Corresponding Author

chris.oostenbrink@boku.ac.at

Funding Sources

Financial support of the Vienna Science and Technology Fund (WWTF; grant number LS08-QM03), the European Research Council (ERC; starting grant number 260408) and the Austrian Science Fund (doctoral program BioToP W1224) is gratefully acknowledged.

Acknowledgments

Prof. Lars Olsen, University of Copenhagen is gratefully acknowledged for providing us with a charge distribution for Compound I.

Notes

The authors declare no competing financial interest.

REFERENCES

(1) Turano, P. and Lu, Y. (2001) Handbook of Metalloproteins, Marcel Dekker, Inc., New York., 2001, pp 269 – 356.

(2) Ebihara, A., Okamoto, A., Kousumi, Y., Yamamoto, H., Masui, R., Ueyama, N., Yokoyama, S., Kuramitsu, S. (2005) *J. Struct. Funct. Genomics* 6, 21–32.

(3) de Geus, D. C., Thomassen, E. A., Hagedoorn, P.-L., Pannu, N. S., van Duijn, E., Abrahams, J. P. (2009) *J. Mol. Biol*. 387, 192–206.

(4) Goblirsch, B. R., Streit, B. R., DuBois, J. L.,Wilmot, C. M. (2010) *J. Biol. Inorg. Chem*. **15**, 879–888.

(5) Kostan, J., Sjöblom, B., Maixner, F., Mlynek, G., Furtmüller, P. G., Obinger, C.,Wagner, M., Daims, H., Djinovic-Carugo, K. (2010) *J. Struct. Biol*. **172**, 331–42.

(6) Maixner, F.,Wagner, M., Lücker, S., Pelletier, E., Schmitz-Esser, S., Hace, K., Spieck, E., Konrat, R., Le Paslier, D., Daims, H. (2008) *Environ. Microbiol*. **10**, 3043–3056.

(7) Mlynek, G., Sjöblom, B., Kostan, J., Füreder, S., Maixner, F., Gysel, K., Furtmüller, P. G., Obinger, C., Wagner, M., Daims, H., Djinovic-Carugo, K. (2011) *J. Bacteriol*. **193**, 2408–17.

(8) Blanc, B., Mayfield, J. A., McDonald, C. A., Lukat-Rodgers, G. S., Rodgers, K. R., DuBois, J. L. (2012) *Biochemistry* **51**, 1895–1910.

(9) Hofbauer, S., Gysel, K., Bellei, M., Hagmüller, A., Schaffner, I., Mlynek, G., Kostan, J., Pirker, K. F., Daims, H., Furtmüller, P. G., Battistuzzi, G., Djinovic-Carugo, K., Obinger, C. (2014) *Biochemistry* **53**, 77–89.

(10) Hofbauer, S., Bellei, M., Sündermann, A., Pirker, K. F., Hagmüller, A., Mlynek, G., Kostan, J., Daims, H., Furtmüller, P. G., Djinovic-Carugo, K., Oostenbrink, C., Battistuzzi, G., Obinger, C. (2012) *Biochemistry* **51**, 9501–9512.

(11) Battistuzzi, G., Bellei, M., Bortolotti, C. A., Sola, M. (2010) *Arch. Biochem. Biophys*. **500**, 21–36.

(12) Bellei, M., Jakopitsch, C., Battistuzzi, G., Sola, M., Obinger, C. (2006) *Biochemistry* **45**, 4768–74.

(13) Battistuzzi, G., Bellei, M., Zederbauer, M., Furtmüller, P. G., Sola, M., Obinger, C. (2006) *Biochemistry* **45**, 12750–5.

(14) Battistuzzi, G., Bellei, M., De Rienzo, F., Sola, M. (2006) *J. Biol. Inorg. Chem*. **11**, 586–92.

(15) Battistuzzi, G., Bellei, M., Borsari, M., Di Rocco, G., Ranieri, A., Sola, M. (2005) *J. Biol. Inorg. Chem.* **10**, 643–51.

(16) Lee, A. Q., Streit, B. R., Zdilla, M. J., Abu-Omar, M. M., DuBois, J. L. (2008) *Proc. Natl. Acad, Sci.* **105**, 15654–15659.

(17) Hofbauer, S., Gruber, C., Pirker, K. F., Schaffner, I., Jakopitsch, C., Sündermann, A., Oostenbrink, C., Furtmüller, P. G., Obinger, C. (2014) *J. Am. Chem. Soc*., submitted.

(18) Hagedoorn, P. L., de Geus, D. C., Hagen,W. R. (2002) *Eur. J. Biochem*. **269**, 4905–4911.

(19) Stenklo, K., Danielsson Thorell, H., Bergius, H., Aasa, R., Nilsson, T. (2001) *J. Biol. Inorg. Chem.* **6**, 601–607.

(20) Mehboob, F.,Wolterink, A. F. M., Vermeulen, A. J., Jiang, B., Hagedoorn, P.-L., Stams, A. J. M., Kengen, S. W. M. (2009) *FEMS Microbiol. Lett*. **293**, 115–21.

(21) Streit, B. R., DuBois, J. L. (2008) *Biochemistry* **47**, 5271–80.

(22) Streit, B. R., Blanc, B., Lukat-Rodgers, G. S., Rodgers, K. R., DuBois, J. L. (2010) *J. Am. Chem. Soc.* **132**, 5711–24.

(23) Schmid, N., Eichenberger, A. P., Choutko, A., Riniker, S., Winger, M., Mark, A. E., van Gunsteren, W. F. (2011) *Eur. Biophys. J.* **40**, 843–56.

(24) Hunenberger, P., Reif, M. (2011) Single-Ion Solvation, RSC Theoretical and Computational Chemistry Series, Royal Society of Chemistry: Cambridge.

(25) Reif, M. M., Hünenberger, P. H. (2011) *J. Chem. Phys*. **134**, 144104.

(26) Reif, M. M., H¨ unenberger, P. H., Oostenbrink, C. (2012) *J. Chem. Theory Comp*. **8**, 3705–3723.

(27) Schmid, N., Christ, C. D., Christen, M., Eichenberger, A. P., van Gunsteren, W. F. (2012) *Comp. Phys. Commun*. **183**, 890–903.

(28) Zou, C., Larisika, M., Nagy, G., Srajer, J., Oostenbrink, C., Chen, X., Knoll,W., Liedberg, B., Nowak, C. (2013) *J. Phys. Chem*. **117**, 9606–14.

Berendsen, H., Postma, J., Van Gunsteren, W., and Hermans, J. (1981) In: Intermolecular Forces, Pullman, B., Ed., pp 331–342.

(30) Berendsen, H. J. C., Postma, J. P. M., van Gunsteren, W. F., DiNola, A., Haak, J. R. (1984) *J. Chem. Phys*. **81**, 3684.

(31) Ryckaert, J.-P., Ciccotti, G., Berendsen, H. J. (1977) *J. Comp. Phys.* **23**, 327–341.

(32) Berendsen, H. J. C., van Gunsteren, W. F., Zwinderman, H. R. J., Geurtsen, R. G. (1986) *Ann. N. Y. Acad. Sci*. **482**, 269–286.

(33) Tironi, I. G., Sperb, R., Smith, P. E., van Gunsteren, W. F. (1995) *J. Chem. Phys*. **102**, 5451.

(34) Heinz, T. N., van Gunsteren, W. F., Hunenberger, P. H. (2001) *J. Chem. Phys*. **115**, 1125.

(35) Eichenberger, A. P., Allison, J. R., Dolenc, J., Geerke, D. P., Horta, B. A. C., Meier, K., Oostenbrink, C., Schmid, N., Steiner, D., Wang, D., van Gunsteren, W. F. (2011) *J. Chem. Theory Comp*. **7**, 3379–3390.

(36) Kabsch,W., Sander, C. (1983) *Biopolymers* **22**, 2577–637.

(37) Allen, M., Tildesley, D. (1989) Computer Simulation of Liquids, Oxford University Press, USA.

Supplementary material

Detailed derivation of experimental and calculated absolute intrinsic hydration free energies of the ions

Experimental absolute intrinsic hydration free energies for the series of Cl^-,ClO^-,ClO_2^-,ClO_3^- and ClO_4^- ions, were derived based on available experimental data and an assumed absolute intrinsic proton hydration free energy of -1100 kJ·mol^{-1}.[1,2] This involved considering the protonated gas-phase molecular species HX_g, where "X" denotes the ion species in question and "g" or "aq" indicates whether the ion is in the gas phase (standard pressure 1 bar) or in aqueous solution (standard molality 1 molal) respectively. The experimental data is also derived for the Cl^- ion to validate the procedure against other available experimental data for that ion. The formation enthalpy of the gas-phase ion X_g^- is

$$\Delta_f H^\ominus(X_g^-) = -\Delta_r H^\ominus_{ac}(X_g^-) + \Delta_f H^\ominus(HX_g) - \Delta_f H^\ominus(H_g^+) \quad , \tag{1}$$

where $\Delta_r H^\ominus_{ac}(X_g^-)$ is the enthalpy of the gas-phase protonation reaction $X_g^- + H_g^+ \rightarrow HX_g$, with the standard formation enthalpy of the gas-phase proton $\Delta_f H^\ominus(H_g^+)$ = 1533.1 kJ·mol^{-1}.[1] The formation entropy of the gas-phase ion X_g^- is given by the corresponding formation reaction,

$$\Delta_f S^\ominus(X_g^-) = s^\ominus(X_g^-) - (n/2)s^\ominus(O_{2,g}) - (1/2)s^\ominus(Cl_{2,g}) - s^\ominus(e_g^-) \quad , \tag{2}$$

with the molar entropy of the electron $s^\ominus(e_g^-)$ = 22.734 J·mol^{-1}·K^{-1}. The conventional hydration free energy of the gas-phase ion X_g^- can be expressed in terms of the above quantities and the conventional formation free energy for the aqueous ion X_{aq}^-, $\Delta_f G^{\bullet}(X_{aq}^-)$, as

$$\Delta_s G^{\bullet}(X_g^-) = \Delta_f G^{\bullet}(X_{aq}^-) - \Delta_f H^\ominus(X_g^-) + T^- \Delta_f S^\ominus(X_g^-) - \Delta_f G^\ominus(H_g^+) \quad , \tag{3}$$

where $\Delta_f H^\ominus(X_g^-)$ and $\Delta_f S^\ominus(X_g^-)$ are given by Eqs. 1 and 2, respectively and $\Delta_f G^\ominus(H_g^+)$ = 1513.3 kJ·mol^{-1}.[1] The absolute intrinsic hydration free energy of the gas-phase ion X_g^-

follows from the conventional hydration free energy in combination with the absolute intrinsic proton hydration free energy

$$\Delta_s G^{\ominus}(X_g^-) = \Delta_s G^{\bullet}(X_g^-) - \Delta_s G^{\ominus}(H_g^+) \quad , \tag{4}$$

where $\Delta_s G^{\bullet}(X_g^-)$ is given by Eq. 3 and $\Delta_s G^{\ominus}(H_g^+) = -1100$ kJ·mol^{-1}.[1] The experimental data used is summarized in Table SI. Hydration free energies from MD simulation are given by

$$\Delta_s G^{\ominus} = \Delta G_{chg}^{raw} + \Delta G_{cav} + \Delta G_{cor} + \Delta G_{std}^{\ominus} \quad , \tag{5}$$

where ΔG_{chg}^{raw} is the raw free energy of reversibly growing the partial charges of the atoms, ΔG_{cav} is the free energy of reversibly growing the van der Waals envelope of the neutral ion and $\Delta G_{std}^{\ominus} = 7.95$ kJ·mol^{-1} is the standard-state correction[1,2] from equal concentrations in the gas and aqueous phase (simulated situation) to concentrations corresponding to a pressure of 1 bar in the gas phase and 1 m in the aqueous phase. ΔG_{chg}^{raw} was calculated using a modified version of the GROMOS96 program.[3] Thermodynamic integration (TI)[4] calculations were performed along a scaling parameter $\lambda = 0.0, 0.1, ...0.9, 1.0$ controlling the growth of partial charges q_i at atom site i from $q_i = 0$ to the full charges $q_i = Q_i$ via linear scaling. The simulations were performed in systems containing one ion and 877, 876, 874 or 875 water molecules in the case the ClO^-, ClO_2^-, ClO_3^- and ClO_4^- ions, respectively. Pressure and temperature were kept constant at 1 bar and 298.15 K, respectively using the weak coupling barostat (coupling time 0.5 ps) and thermostat (coupling time 0.1 ps).[5] A pairlist with an atom-based cutoff of 1.0 nm, updated at each time step of the simulation, was used. Interactions were also updated at each time step. Van der Waals interactions were modeled with the Lennard-Jones potential, truncated based on atoms at a distance of 1.0 nm, and electrostatic interactions were handled with the particle-particle particle-mesh algorithm,[6] using a spherical hat charge-shaping function of width 1.0 nm, a triangular shaped cloud assignment function, a finite-difference scheme of order two and a grid-spacing of about 0.09 nm. The self-energy term[7–10] was included in the calculation of the energy and of the virial, but not of the electrostatic potential at the

ion sites. The resulting TI curves were integrated numerically with the trapezoidal rule. The obtained values for ΔG_{chg}^{raw} are reported in Table SII. ΔG_{cav} was calculated using the GROMOS11 program.[11] Thermodynamic integration (TI)[4] calculations were performed along a scaling parameter $\lambda = 0.0, 0.05, ...0.95, 1.0$ controlling the growth of the van der Waals envelope of the neutral ($q_i = 0$ for all atoms) molecule. Lennard-Jones interactions were modified using a soft-core interaction function[3,12] with a softness parameter of 0.5. Wherever necessary to smoothen the TI curve, additional λ points were included. The TI curves were integrated numerically with the trapezoidal rule. The TI simulations were performed in similar manner as described previously in terms of the number of water molecules and the pressure and temperature coupling. But a pairlist with a molecule-based twin-range cutoff scheme, updated every five time steps of the simulation, was employed. Interactions within a distance of 0.8 nm were computed at each time step and interactions within a distance range of 0.8-1.4 nm were computed along with pairlist updates only. Van der Waals interactions were modeled with the Lennard-Jones potential, truncated based on molecules at a distance of 1.4 nm, and electrostatic interactions were handled with molecule-based truncation and a Barker-Watts reaction field correction[13] relying on a relative dielectric permittivity of 66.6[14] as appropriate for the SPC water model. The obtained values for ΔG_{cav} are reported in Table SII in the supplementary material. ΔG_{cor} was calculated according to the correction scheme for oligoatomic ion hydration[15] for the case of lattice-sum electrostatic interactions,

$$\Delta G_{cor} = \Delta G_{A+B+D} + \Delta G_{C_1} \quad . \tag{6}$$

The first term on the right-hand side of Eq. 6 is a combined correction for artifacts in the solvent polarization arising from artificial periodicity induced by usage of a lattice-sum scheme and a spurious relative dielectric permittivity of the solvent model. It is calculated as[14,15]

$$\Delta G_{A+B+D} = \Delta G_{chg}^{NPBC} - \Delta G_{chg}^{PBC} \quad , \tag{7}$$

where the charging free energies under nonperiodic (ΔG_{chg}^{NPBC}) and periodic (ΔG_{chg}^{PBC}) boundary conditions were computed with the finite-difference Poisson equation solver[16–18] employing Coulombic electrostatic interactions under nonperiodic and periodic boundary conditions, respectively. These calculations were carried out in cubic boxes with an edge length of 3 nm, a grid spacing of 0.02 nm and a threshold of 10^{-6} kJ·mol^{-1} for the convergence of the electrostatic free energy. Relative dielectric permittivities of 78.4 and 66.6 were used for calculations under nonperiodic and periodic boundary conditions, respectively. A van der Waals envelope was used to define the solute cavity, with atomic radii defined as the distances at the minimum of the Lennard-Jones potential between the different solute atoms and the oxygen atom of a SPC water molecule using the Lennard-Jones interaction parameters of the corresponding ion, reduced by 0.14 nm,[19] an estimate for the radius of a water molecule (0.14 nm). Polar hydrogen atoms were treated differently[20,21] and assigned an atomic radius of 0.05 nm. The second term on the right-hand side of Eq. 6 is a correction for the improper boundary conditions of the electrostatic potential induced by usage of a lattice-sum scheme, namely a vanishing average electrostatic potential over the box volume, rather than a vanishing value at infinity. It is calculated as[14,15]

$$\Delta G_{C_1} = -N_A(6\epsilon_o)^{-1} N_w \gamma_w q_I \frac{1}{\langle L \rangle^3} \tag{8}$$

where N_A is Avogadro's constant, ϵ_o is the vacuum permittivity, q_I the full ionic charge, N_w is the number of water molecules in the computational box, $\langle L \rangle$ the average box-edge length and γ_w is the quadrupole moment trace of the employed solvent model, which, for the SPC water model, evaluates to $\gamma_w = 0.0082\ e{\cdot}\text{nm}^2$.[14] The obtained values for ΔG_{cor} (Eq. 6) are reported in Table SII. The parameterization was done by trial-and-error adjustments of the partial charges of the Cl and O atoms until agreement between the experimental $\Delta_s G^{\ominus}$ (Eq. 4) and simulated $\Delta_s G^{\ominus}$ (Eq. 5) was reached.

Ion	$s^{\ominus}(X_g^-)$ [J·mol^{-1}·K^{-1}]	$\Delta_r H^{\ominus}_{ac}(X_g^-)$ [kJ·mol^{-1}]	$\Delta_f H^{\ominus}(HX_g)$ [kJ·mol^{-1}]	$\Delta_f G^{\bullet}(X_{aq}^-)$ [kJ·mol^{-1}]	$\Delta_s G^{\ominus}(X_g^-)$ [kJ·mol^{-1}]
Cl^-	153.4[a]	-1396.0[b]	-92.3[c]	-131.2[c]	-309.4[d,e]
ClO^-	215.7[f]	-1487.8[g]	-76.1[h]	-36.8[c]	-335.0[d,i]
ClO_2^-	257.0[f]	-1402.1[g]	20.9[h]	17.2[c]	-310.6[d]
ClO_3^-	264.3[f]	-1310.4[g]	-10.9[h]	-8.0[c]	-240.7[d]
ClO_4^-	263.0[f]	-1254.8[g]	-0.4[h]	-8.5[c]	-227.1[d]

Table SI: Experimental data used to calculate and compare the parameters for the ions. (a) *Fawcett et al.*;[22] (b) NIST Chemistry WebBook;[23] (c) *CRC Handbook of Chemistry*; (d) Eq. 4; (e) the value reported in *Single-ion solvation: Experimental and theoretical approaches to elusive thermodynamic quantities*[1] is -308.6 kJ·mol^{-1}; (f) *Loewenschuss et al.*;[24] (g) experimental data reported in Table 4 of *Meyer et al.*;[25] (h) data from method W4 reported in Table 3 of *Meyer et al.*;[25] (i) using the experimental values $\Delta_f H^{\ominus}(HClO_g) = -78.7$ or -74.9 kJ·mol^{-1} reported in the *CRC Handbook of Chemistry* and *Meyer et al.*[25] gives $\Delta_s G^{\ominus}(ClO_g^-) = -332.4$ and -336.2 kJ·mol^{-1}, respectively.

Ion	ΔG^{raw}_{chg} [kJ·mol^{-1}]	ΔG_{A+B+D} [kJ·mol^{-1}]	ΔG_{C_1} [kJ·mol^{-1}]	ΔG_{cav} [kJ·mol^{-1}]	$\Delta G^{\ominus}_{std}$ [kJ·mol^{-1}]	$\Delta_s G^{\ominus}$ [kJ·mol^{-1}]
ClO^-	-364.8	-64.7	77.2	7.2	7.95	-337.2
ClO_2^-	-339.8	-64.5	77.2	8.2	7.95	-311.0
ClO_3^-	-258.4	-64.3	77.1	8.9	7.95	-228.8
ClO_4^-	-246.9	-64.2	77.0	9.3	7.95	-216.9

Table SII: Results of the parametrization for the ion series for the gromos 54A7 forcefield.[26] The charge distributions for the ions were as follows. ClO^-: Cl -0.17, O1 -0.83; ClO_2^-: Cl 0.55, O1 -0.775 O2 -0.775; ClO_3^-: Cl -0.1, O1 -0.3, O2 -0.3, O3 -0.3; ClO_4^-: Cl -0.2, O1 -0.2, O2 -0.2, O3 -0.2, O4 -0.2

References

[1] Hunenberger, P.; Reif, M. *Single-Ion Solvation*; RSC Theoretical and Computational Chemistry Series; Royal Society of Chemistry: Cambridge, 2011.

[2] Reif, M. M.; Hünenberger, P. H. *The Journal of chemical physics* **2011**, *134*, 144104.

[3] van Gunsteren, W.; Billeter, S.; Eising, A.; Hünenberger, P.; Krüger, P.; Mark, A.; Scott, W.; Tironi, I. **1996**,

[4] Kirkwood, J. G. *The Journal of Chemical Physics* **1935**, *3*, 300.

[5] Berendsen, H. J. C.; Postma, J. P. M.; van Gunsteren, W. F.; DiNola, A.; Haak, J. R. *The Journal of Chemical Physics* **1984**, *81*, 3684.

[6] Hockney, R. W.; Eastwood, J. W. *Computer Simulation Using Particles*; 1981.

[7] Redlack, A.; Grindlay, J. *Canadian Journal of Physics* **1972**, *50*, 2815–2825.

[8] Nijboer, B. R. A.; Ruijgrok, T. W. *Journal of Statistical Physics* **1988**, *53*, 361–382.

[9] Hummer, G.; Pratt, L. R.; García, A. E. *The Journal of Physical Chemistry* **1996**, *100*, 1206–1215.

[10] Hunenberger, P. H. Lattice-sum methods for computing electrostatic interactions in molecular simulations. Simulation and theory of electrostatic interactions in solution. 1999; pp 17–83.

[11] Schmid, N.; Christ, C. D.; Christen, M.; Eichenberger, A. P.; van Gunsteren, W. F. *Computer Physics Communications* **2012**, *183*, 890–903.

[12] Beutler, T. C.; Mark, A. E.; van Schaik, R. C.; Gerber, P. R.; van Gunsteren, W. F. *Chemical Physics Letters* **1994**, *222*, 529–539.

[13] Barker, J.; Watts, R. *Molecular Physics* **1973**, *26*, 789–792.

[14] Kastenholz, M. A.; Hünenberger, P. H. *The Journal of chemical physics* **2006**, *124*, 124106.

[15] Reif, M. M.; Hünenberger, P. H.; Oostenbrink, C. *Journal of Chemical Theory and Computation* **2012**, *8*, 3705–3723.

[16] Davis, M. E.; Madura, J. D.; Luty, B. A.; McCammon, J. *Computer Physics Communications* **1991**, *62*, 187–197.

[17] Madura, J. D.; Briggs, J. M.; Wade, R. C.; Davis, M. E.; Luty, B. A.; Ilin, A.; Antosiewicz, J.; Gilson, M. K.; Bagheri, B.; Scott, L.; McCammon, J. *Computer Physics Communications* **1995**, *91*, 57–95.

[18] Hunenberger, P. H.; McCammon, J. A. *The Journal of Chemical Physics* **1999**, *110*, 1856.

[19] Ferrara, P.; Caflisch, A. *Proceedings of the National Academy of Sciences of the United States of America* **2000**, *97*, 10780–5.

[20] Reif, M. M.; Kräutler, V.; Kastenholz, M. A.; Daura, X.; Hünenberger, P. H. *The journal of physical chemistry. B* **2009**, *113*, 3112–28.

[21] Kastenholz, M. A.; Hünenberger, P. H. *The Journal of Physical Chemistry B* **2004**, *108*, 774–788.

[22] Fawcett, W. R. *The Journal of Physical Chemistry B* **1999**, *103*, 11181–11185.

[23] Linstrom, P. J.; Mallard, W. G. *Journal of Chemical & Engineering Data* **2001**, *46*, 1059–1063.

[24] Loewenschuss, A.; Marcus, Y. *Journal of Physical and Chemical Reference Data* **1987**, *16*, 61.

[25] Meyer, M. M.; Kass, S. R. *The journal of physical chemistry. A* **2010**, *114*, 4086–92.

[26] Schmid, N.; Eichenberger, A. P.; Choutko, A.; Riniker, S.; Winger, M.; Mark, A. E.; van Gunsteren, W. F. *European biophysics journal : EBJ* **2011**, *40*, 843–56.

Chapter 8

Conclusion

Conclusion

In this work biophysical and biochemical properties of chlorite dismutase (Cld) were determined in order to understand the relationship between structure and function of this peculiar heme enzyme and propose a mechanism of reaction. Since the discovery of chlorite dismutases in perchlorate-reducing bacteria in 1996 (van Ginkel et al., 1996) it was found that Clds are widely distributed among Bacteria and Archaea.

Up to now functional (i.e. chlorite degrading) Clds with two distinct different oligomeric arrangements and subunit structures have been described. In chapter 3 (Hofbauer et al., 2012a) the thermal and conformational stability of two representatives from nitrite-oxidizing bacteria were determined, namely from Clds from pentameric *"Candidatus* Nitrospira defluvii" (NdCld) and dimeric *Nitrobacter winogradskyi* (NwCld). Pentameric NdCld exhibits a very high thermal and a conformational stability. It was demonstrated that the heme stabilizes the overall fold of Cld and that it is released during unfolding. From a biotechnological point of view NdCld is the most promising, because most stable, candidate for further mechanistic studies and enzyme engineering approaches.

Despite the clear differences in protein stability the catalytic properties of NdCld and NwCld are very similar. This mirrors almost identical heme cavities and substrate channel architectures as suggested by the published X-ray structures (Kostan et al., 2010; Mlynek et al., 2011). This is also reflected by almost identical redox potentials and redox thermodynamics, with minor differences in the actual enthalpic and entropic contributions (Chapter 4, Hofbauer et al., 2012b). Also molecular dynamics simulations and calculations of the dimensions of the substrate channels of NdCld and NwCld revealed a high degree of similarity.

Interestingly, NdCld and NwCld show significant differences in their UV-vis and EPR-spectra under identical conditions. While NwCld is present mainly as high-spin species, NdCld shows a larger portion of low-spin at pH 7.0. The high-spin signal of NdCld (as detected by EPR spectroscopy) is composed of a rhombic (5-coordinated high-spin) and an axial (6-coordinated high-spin) contribution, while EPR spectra of NwCld solely show a clear axial high-spin signal. With these sensitive spectroscopic techniques it becomes obvious that the electronic structures of these two enzymes in solution are substantially different compared to the "frozen" structures in X-ray crystallography. The higher amount of high-spin heme in NwCld at pH 7.0 might explain the marginally higher catalytic efficiency compared to NdCld.

In order to get a better functional understanding of the enzyme and the reaction mechanism, variants of NdCld of conserved residues in close proximity to the active site were produced and characterized in detail. On the distal side of the heme there is only one charged residue, namely the positively charged arginine (R173). It was hypothesized that it plays a major role in binding of the negatively charged substrate chlorite. A first investigation on Arg173 variants by Kostan and co-workers (Kostan et al., 2010) showed that the distal arginine is important for the reaction but not fully essential. In chapter 5 (Hofbauer et al.,

2014) a more detailed analysis of four different Arg173 variants suggests that the distal arginine is more important to keep the transiently produced hypochlorite in place, but is negligible for the initial substrate binding. Michaelis-Menten constants of the variants Arg173Ala, R173Q, and even of the negatively charged Arg173Glu were at maximum only three-times higher than that for the wild-type enzyme. This clearly suggests that the anionic substrate binds to the ferric heme iron even in the absence of Arg173. The drastically increased K_m-value of the R173K mutant is due to the low-spin complex that is formed with the distal lysine that hinders the substrate to reach the active site.

On the other hand, the turnover number (k_{cat}) was decreased at least ten-fold for R173A, R173Q, and R173E, meaning that the second part of the reaction cycle, where the proposed transiently produced hypochlorite recombines with Compound I and releases chloride and molecular oxygen, is supported by Arg173. In the turnover of Cld this seems to be the rate-limiting step.

In this study we further created variants, where conserved residues at the proximal heme side were mutated. In chlorite dismutase a histidine is coordinating the heme iron as fifth ligand (His160). Crystal structures revealed a hydrogen-bonding network that connects His160 with a fully conserved glutamate residue (Glu210) and a lysine (Lys141). The imidazolate character of the proximal His160 depends on its H-bonding to Glu210 and Lys141. Additionally, a tryptophan residue (Trp145) is present and forms a hydrogen bond to the proprionate group of the heme in close proximity to Lys141. Perturbation of the proximal H-bonding network changes the imidazolate character of the proximal histidine. As a consequence significant changes of the active site architecture in solution occur as determined by UV-vis spectroscopy and spectroelectrochemical investigations. The crystal structures of the NdCld variants Trp145Phe and Trp145Val suggest a breakage of the H-bond between His160 and Glu210Ala. Variants of the proximal tryptophan in Cld from *Dechloromonas aromatica* (DaCld) showed strongly impaired heme binding properties, leading to a non-functional enzyme (Blanc et al., 2013). This effect is not as dramatic in NdCld but our data clearly suggest that the proximal hydrogen bonding network in Cld is very susceptible to perturbation. Furthermore it is necessary for proper heme incorporation.

Chlorite dismutases suffer from rapid self-inhibition during chlorite degradation. The driving force of this inhibition mechanism was investigated in chapter 6. An off-pathway, involving radical migration from the porphyrin to the proximal tryptophan residues, was originally postulated to cause inhibition in DaCld by Goblirsch and co-workers (Goblirsch et al., 2010). Later activity studies of tryptophan variants of DaCld (Blanc et al., 2013) and NdCld (chapter 5, Hofbauer et al., 2014) proved the inactivation mechanism does not include proximal residues. In the proposed reaction mechanism by Lee and co-workers the substrate, chlorite, binds the ferric enzyme in the reaction sphere and upon heterolytic cleavage of the O-Cl bond, a Compound I intermediate and hypochlorite are transiently formed. The reaction cycle is completed when the anionic hypochlorite attacks the ferryl oxygen (rebound mechanism) thereby producing molecular oxygen, chloride and the protein in its resting state (Lee et al., 2008). First kinetic studies of wild-type Clds and variants indicate that the rate limiting step in the reaction is not the substrate binding and Compound I formation, but rather

the formation of the oxygen-oxygen double bond and the subsequent release of molecular oxygen and chloride. This is also obvious when the pH-dependence of the catalytic parameters for wild-type NdCld was assessed (chapter 6). While the K_m-values are independent of pH, the turnover number is very sensitive to changes of pH and it was speculated whether inactivation by hypochlorite contributes to this phenomenon. Up to now, there was no spectroscopic or other experimental prove of the actual existence of hypochlorite as intermediate species during turnover of Cld. Computational analyses of the reaction of chlorite with heme based on Density Functional Theory (DFT) calculation suggested a homolytic cleavage of the O-Cl bond of chlorite (Keith et al., 2011; Sun et al., 2014) forming a $OCl^{\bullet}$ radical species and a Compound II-like state of Cld. Our studies clearly demonstrate that this proposed mechanism has no relevance for Cld catalysis.

In chapter 6 the influence of hypochlorite traps on the reaction of NdCld with chlorite was elucidated, showing a clear influence on the kinetic parameters. In the presence of the efficient hypochlorite trap methionine the enzyme's lifetime was significantly prolonged and inactivation delayed. This was the first indirect prove that hypochlorite is actually produced in catalysis. However, a small portion of hypochlorite continuously escapes from the reaction sphere and causes damage to the protein matrix and the prosthetic group. As a consequence, Cld becomes irreversibly inactivated. The amount of hypochlorite escaping the active site was roughly quantified and shown to depend on pH as well as the presence of the distal Arg173. These data agree well with the hypothesis that Arg173 is responsible for keeping hypochlorite within the reaction sphere in close proximity to Compound I. The escape of hypochlorite from Compound I was additionally demonstrated by molecular dynamics simulations (Chapter 7). Released hypochlorite oxidatively modifies the protein matrix and forms 3-chloro-tyrosines, a fingerprint of action of hypochlorite. Additionally, the prosthetic group is modified and heme bleaching is observed. Methionine protects Cld from oxidative damage at least to some extent.

In summary, in this work the mechanism of reaction and inhibition of the highly stable pentameric NdCld was investigated. The proposed reaction cycle (see Scheme) includes several steps: (i) Chlorite binding to the ferric heme, (ii) heterolytic cleavage of chlorite forming Compound I and hypochlorite (of which a small portion can escape and promotes damage of Cld) and (iii) recombination of the hypochlorite with Compound I forming O_2, chloride and Cld in its resting state. The only heme cavity residue that participates in this reaction cycle is Arg173. Its main function is to keep hypochlorite in the reaction sphere for the rebound mechanism. Because of the high similarity of the heme cavity architecture (seen in the X-ray structures) of dimeric and pentameric Clds, it is reasonable to assume that all functional Clds follow this reaction cycle.

References

Blanc, B., Rodgers, K. R., Lukat-Rodgers, G. S., and DuBois, J. L. (2013) Understanding the roles of strictly conserved tryptophan residues in O2 producing chlorite dismutases. *Dalton Trans.*, *42*, 3156-3169

van Ginkel, C.G., Rikken, G.B., Kroon, A.G.M., and Kengen, S.W.M. (1996) Purification and characterization of chlorite dismutase: a novel oxygen-generating enzyme. *Arch. Microbiol*., *166,* 321-326

Goblirsch, B. R., Streit, B. R., DuBois, J. L., and Wilmot, C. M. (2010) Structural features promoting dioxygen production by Dechloromonas aromatica chlorite dismutase. *J. Biol. Inorg. Chem*., *15*, 879-888.

Hofbauer, S., Bellei, M., Sündermann, A., Pirker, K. F., Hagmüller, A., Mlynek, G., Kostan, J., Daims, H., Furtmüller, P. G., Djinovic-Carugo, K., Oostenbrink, C., Battistuzzi, G., and Obinger, C. (2012b) Redox thermodynamics of high-spin and low-spin forms of chlorite dismutases with diverse subunit and oligomeric structures. *Biochemistry 51*, 9501-9512

Hofbauer, S., Gysel, K., Bellei, M., Hagmüller, A., Schaffner, I., Mlynek, G., Kostan, J., Pirker, K. F., Daims, H., Furtmüller, P. G., Battistuzzi, G., Djinovic-Carugo, K., and Obinger, C. (2014) Manipulating conserved heme cavity residues of Chlorite dismutase: Effect on structure, redox chemistry and reactivity. *Biochemistry 53*, 77-89

Hofbauer, S., Gysel, K., Mlynek, G., Kostan, J., Hagmüller, A., Daims, H., Furtmüller, P. G., Djinovic-Carugo, K., and Obinger, C. (2012a) Impact of subunit and oligomeric structure on the thermal and conformational stability of chlorite dismutases. *Biochim. Biophys. Acta 1824*, 1031-1038

Keith, J. M., Abu-Omar, M. M., and Hall, M. B. (2011) Computational investigation of the concerted dismutation of chlorite ion by water-soluble iron porphyrins. *Inorg. Chem., 50*, 7928-7930

Kostan, J., Sjoeblom, B., Maixner, F., Mlynek, G., Furtmüller, P. G., Obinger, C., Wagner, M., Daims, H., and Djinovic-Carugo, K. (2010) Structural and functional analysis of the chlorite dismutase from the nitrite-oxidizing bacterium "*Candidatus* Nitrospira defluvii": identification of a catalytically important amino acid residue. *J. Struct. Biol*., *172*, 331-342

Lee, A. Q., Streit, B. R., Zdilla, M. J., Abu-Omar, M. M., and DuBois, J. L. (2008) Mechanism of and exquisite selectivity for O-O bond formation by the heme dependent chlorite dismutase. *PNAS*, *105*, 15654-15659

Mlynek, G., Sjöblom, B., Kostan, J., Füreder, S., Maixner, F., Gysel, K., Furtmüller, P. G., Obinger, C., Wagner, M., Daims, H., and Djinović-Carugo, K. (2011) Unexpected diversity of chlorite dismutases: a catalytically efficient dimeric enzyme from *Nitrobacter winogradskyi. J. Bacteriol*., *193*, 2408-2417

Sun, S., Li, Z. S., and Chen, S. L. (2014) A dominant homolytic O-Cl bond cleavage with low-spin triplet-state Fe(IV)=O formed is revealed in the mechanism of heme-dependent chlorite dismutase. *Dalton Trans., 43*, 973-981

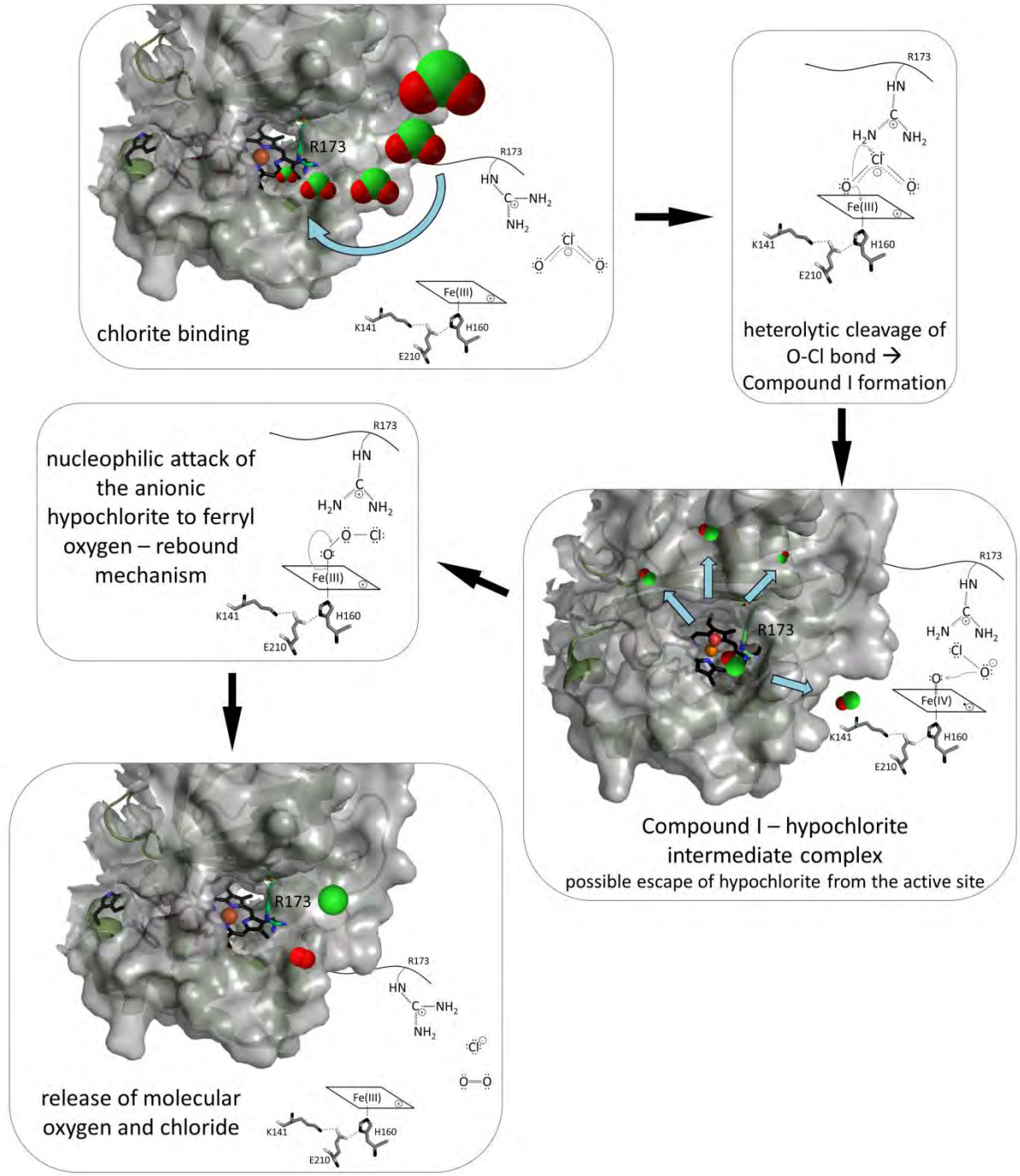

Proposed reaction mechanism of chlorite dismutase. The reaction starts with the spontaneous attack of anionic chlorite at ferric heme *b* (binding of chlorite does not require the distal R173). After formation of the Fe(III)-chlorite complex, heterolytic cleavage of one covalent oxygen-chlorine bond in chlorite leads to the formation of hypochlorite and the redox intermediate Compound I [oxoiron (IV) porphyrin cation radical] (R173 is keeps the transiently produced hypochlorite in the reaction sphere). Finally, upon nucleophilic attack of intermediate anionic hypochlorite at the ferryl oxygen, Compound I is reduced to the resting state and dioxygen and chloride are released.

APPENDIX I

Inactivation of human myeloperoxidase by hydrogen peroxide

Martina Paumann-Page, Paul G. Furtmüller, Stefan Hofbauer, Louise N. Paton, Christian Obinger, Anthony J. Kettle

Research Article

Archives of Biochemistry and Biophysics (2013), 539, 51-62

Archives of Biochemistry and Biophysics 539 (2013) 51–62

Contents lists available at ScienceDirect

Archives of Biochemistry and Biophysics

journal homepage: www.elsevier.com/locate/yabbi

Inactivation of human myeloperoxidase by hydrogen peroxide ☆

Martina Paumann-Page [a,b], Paul G. Furtmüller [b], Stefan Hofbauer [b], Louise N. Paton [a], Christian Obinger [b,*], Anthony J. Kettle [a]

[a] Centre for Free Radical Research, University of Otago Christchurch, Christchurch, New Zealand
[b] Department of Chemistry, Division of Biochemistry, BOKU – University of Natural Resources and Life Sciences, Muthgasse 18, Vienna, Austria

ARTICLE INFO

Article history:
Received 18 June 2013
and in revised form 2 September 2013
Available online 11 September 2013

Keywords:
Myeloperoxidase
Neutrophils
Oxidative stress
Suicide inhibitor
Mechanism-based inhibition
Oxidative modification

ABSTRACT

Human myeloperoxidase (MPO) uses hydrogen peroxide generated by the oxidative burst of neutrophils to produce an array of antimicrobial oxidants. During this process MPO is irreversibly inactivated. This study focused on the unknown role of hydrogen peroxide in this process. When treated with low concentrations of H_2O_2 in the absence of reducing substrates, there was a rapid loss of up to 35% of its peroxidase activity. Inactivation is proposed to occur via oxidation reactions of Compound I with the prosthetic group or amino acid residues. At higher concentrations hydrogen peroxide acts as a suicide substrate with a rate constant of inactivation of $3.9 \times 10^{-3}\ s^{-1}$. Treatment of MPO with high H_2O_2 concentrations resulted in complete inactivation, Compound III formation, destruction of the heme groups, release of their iron, and detachment of the small polypeptide chain of MPO. Ten of the protein's methionine residues were oxidized and the thermal stability of the protein decreased. Inactivation by high concentrations of H_2O_2 is proposed to occur via the generation of reactive oxidants when H_2O_2 reacts with Compound III. These mechanisms of inactivation may occur inside neutrophil phagosomes when reducing substrates for MPO become limiting and could be exploited when designing pharmacological inhibitors.

Introduction

Neutrophils are the predominant white blood cells in circulation. They are highly specialized for their primary function, the phagocytosis and destruction of invading pathogens by antimicrobial proteins and reactive oxidants [1]. When stimulated, neutrophils consume oxygen in a respiratory burst that produces superoxide and hydrogen peroxide [1]. Simultaneously, these white blood cells discharge the abundant heme enzyme myeloperoxidase (MPO)[1] that uses hydrogen peroxide to oxidize chloride, bromide and thiocyanate to the respective hypohalous acids and hypothiocyanite. These oxidants kill ingested bacteria but are also implicated in tissue damage associated with numerous inflammatory diseases [2]. It has been demonstrated that during phagocytosis the amount of extractable neutrophilic MPO decreases while a significant fraction of the soluble enzyme is inactivated [3,4]. The mechanism by which this occurs and its relevance to infection and inflammation have yet to be investigated in detail.

Enzyme inactivation is likely to involve reactions with either hydrogen peroxide or its products because they have the potential to oxidatively modify amino acids and the prosthetic heme group. It has been demonstrated with several heme peroxidases, including horseradish peroxidase [5,6], ascorbate peroxidase [7] and lactoperoxidase [8], that hydrogen peroxide alone can promote irreversible inactivation. There are also reports that MPO is inactivated by hydrogen peroxide in the absence of exogenous electron donors [9,10]. However, the mechanism of inactivation and the effect on its structural integrity have not been investigated.

In this study we aimed to show how hydrogen peroxide affects the activity of MPO and describe the mechanisms involved in enzyme inactivation. We demonstrate that MPO is highly sensitive to inactivation by hydrogen peroxide. Irreversible inactivation of MPO was accompanied by changes in its secondary and tertiary architecture including breakage of covalent heme linkages and disruption of its subunit structure.

* Corresponding author. Address: Department of Chemistry at BOKU – University of Natural Resources and Life Sciences, Muthgasse 18, A-1190 Vienna, Austria. Fax: +43 1 47654 6059.
E-mail address: christian.obinger@boku.ac.at (C. Obinger).

[1] *Abbreviations used:* MPO, myeloperoxidase; Por, porphyrin; TMB, 3,3′,5,5′-tetramethylbenzidine; DTPA, diethylenetriaminepentaacetic acid; cetrimide, alkyltrimethylammonium bromide; FOX, ferrous oxidation of xylenol orange; PVDF, polyvinylidene difluoride; CID, collision induced dissociation; ECD, electronic circular dichroism; DSC, differential scanning calorimetry; GdnHCl, guanidinium hydrochloride.

0003-9861/$ - see front matter © 2013 The Authors. Published by Elsevier Inc. All rights reserved.
http://dx.doi.org/10.1016/j.abb.2013.09.004

Materials and methods

Reagents

Human MPO (lyophilized and highly purified, Reinheitszahl 0.84) was obtained from Planta Natural Products (http://www.planta.at) and the concentration was determined spectrophotometrically with a molar extinction coefficient of 91,000 M^{-1} cm^{-1} per heme [11]. Hydrogen peroxide (30% analytical grade) was purchased from Biolab (Aust) Ltd. and concentrations were determined spectrophotometrically using a molar extinction coefficient of 43.6 M^{-1} cm^{-1} at 240 nm [12]. TMB (3,3′,5,5′-tetramethylbenzidine), xylenol orange, D-sorbitol, diethylenetriaminepentaacetic acid (DTPA), alkyltrimethylammonium bromide (cetrimide), glucose, catalase from bovine liver, bovine superoxide dismutase, glucose oxidase from *Aspergillus niger*, 3-(2-pyridyl)-5,6-diphenyl-1,2,4-triazine-p, p′-disulfonic acid monosodium salt hydrate (ferrozine) and L-ascorbate were purchased from Sigma. Dimethylformamide and ferrous ammonium sulfate were from J.T. Baker.

All spectrophotometric assays were performed on an Agilent 8453 diode array spectrophotometer. For enhanced chemiluminescence Amersham™ ECL Plus Western Blotting Detection System from GE Healthcare was used.

Myeloperoxidase activity assays

The residual peroxidase activity of MPO was determined by measuring its ability to oxidize TMB. MPO (32 nM) in 50 mM sodium phosphate buffer, pH 7.4, and 100 μM DTPA was incubated at various protein to hydrogen peroxide ratios and aliquots were taken over time to assess the decline in peroxidase activity. Superoxide dismutase was added to a separate number of experiments at a concentration of 20 μg/mL to investigate the requirement for superoxide in enzyme inactivation caused by hydrogen peroxide. Residual peroxidase activity was measured by adding a 25 μL aliquot to 850 μL of 200 mM sodium acetate buffer, pH 5.4, containing 0.01% cetrimide, 100 μL of 20 mM TMB in DMF (made fresh each day and kept in the dark) and 25 μL of 8 mM hydrogen peroxide. Reactions were performed at 28 ± 0.5 °C and started by addition of the MPO aliquot. TMB oxidation was followed at 670 nm and initial rates were calculated over the first 60 s of the reaction.

The halogenation activity of MPO was determined under the same conditions as described above with the exception that 10 mM bromide was present in the TMB assay. Under these conditions, bromide was the preferred substrate for MPO and was converted to HOBr, which was responsible for 80% of the oxidation of TMB with the remainder due to direct oxidation by MPO (i.e., peroxidase activity).

Determination and generation of hydrogen peroxide

Consumption of hydrogen peroxide by MPO was measured using ferrous iron-catalyzed oxidation of xylenol orange (FOX assay) [13]. The FOX reagent was composed of 1 mM ammonium ferrous sulfate, 400 μM xylenol orange and 400 mM D-sorbitol in 200 mM H_2SO_4. Each peroxide assay was performed by adding 70 μL of sample to 25 μL FOX reagent while vortexing. The solution was then incubated at room temperature for 45 min in the dark prior to reading the absorbance at 560 nm. The hydrogen peroxide concentration was calculated against a standard curve of the range of 0–5 nM hydrogen peroxide. Samples with concentrations higher than the standard curve range were diluted accordingly in 50 mM phosphate buffer, pH 7.4, before adding to the FOX reagent. This assay was also used to determine the rate at which glucose oxidase and glucose (1 mg/mL) produced hydrogen peroxide in 50 mM phosphate buffer, pH 7.4. The flux of hydrogen peroxide was linear over 60 min and increasing concentrations of glucose oxidase (0.1–2.5 μg/mL glucose oxidase) gave a linear increase in production of hydrogen peroxide (9.4 μM–285.5 μM per h).

Spectral analysis of myeloperoxidase

Spectra of 1.5 μM MPO in 50 mM phosphate buffer, pH 7.4, containing 100 μM DTPA were recorded after reactions were started by adding hydrogen peroxide. To determine how peroxidase or halogenation substrates influenced the degradation of the heme groups of MPO, 200 μM ascorbate or 5 mM bromide with 5 mM methionine, respectively were also added as indicated below. The involvement of superoxide was checked by adding 20 μg/mL SOD to a separate set of reactions.

SDS–PAGE analyses

To follow the impact of hydrogen peroxide on the structural integrity of myeloperoxidase, 1.5 μM MPO in 50 mM sodium phosphate buffer, pH 7.4, and 100 μM DTPA was incubated with 1.5 mM hydrogen peroxide. Aliquots were taken at 5, 10, 25, 40 and 60 min and residual hydrogen peroxide was removed by adding 20 μg/mL catalase. Samples of 15 μL were added to non-reducing and reducing sample loading buffers, respectively (final concentrations: 2% SDS, 10% glycerol, 125 mM Tris–HCl buffer, pH 6.5, and for reducing SDS–PAGE 1% β-mercaptoethanol). Samples were loaded without prior heating and resolved by 8–20% gradient SDS–polyacrylamide gel electrophoresis. Gels were stained with Coomassie Brilliant Blue R-250 for 60 min and subsequently destained. Gels were scanned using ChemiDoc® XRS (Bio-Rad).

Furthermore, 1.5 μM MPO in 50 mM sodium phosphate buffer, pH 7.4, and 100 μM DTPA was incubated with the following hydrogen peroxide: protein ratios: 1:1, 5:1, 10:1, 40:1, 100:1, 167:1, 500:1, 1000:1 and 2000:1 for 2 h at room temperature. Samples were resolved on SDS–PAGE, stained and analyzed as described above.

For detection of intact heme covalently linked to the protein, MPO was incubated with hydrogen peroxide and resolved by SDS–PAGE under the same conditions as described above and subsequently blotted onto a PVDF membrane (100 V, 60 min). Enhanced chemiluminescence (Amersham™ ECL Plus Western Blotting Detection System, GE Healthcare) was used to detect covalently bound and intact heme [14].

Analysis of free iron

Release of free iron from the heme prosthetic group of MPO was measured colorimetrically using ferrozine following a published method but with slight modifications [15]. After buffer exchange with 50 mM sodium acetate buffer, pH 7.4, using a Micro Bio-Spin chromatography column (Bio-Rad) 1.5 μM MPO was treated with 1.5 mM hydrogen peroxide and incubated at room temperature for 2 h. The volume of 1 mL was reduced to dryness and the pellet resuspended in 30 μL water. Ascorbic acid (30 μL of 1.13 mM in 0.2 M HCl) was added and left for 5 min. The protein was then precipitated by adding 30 μL of 11.3% trichloroacetic acid and samples were kept on ice for 5 min followed by a short fast spin at 4 °C. Finally, 36 μL of 10% ammonium acetate was added to the supernatant followed by 9 μL of 6.1 mM ferrozine and the absorbance at 563 nm was measured after 5 min (ε = 28,000 M^{-1} cm^{-1}).

Differential scanning calorimetry

Differential calorimetric (DSC) measurements were performed using a VP-capillary DSC microcalorimeter from Microcal (cell volume: 137 μL), controlled by the VP-viewer program and equipped with an autosampler for 96 well plates. Samples were analyzed using a programmed heating scan rate of 60 °C h^{-1} over a temperature range of 20–110 °C and a cell pressure of approximately 60 psi (4.136 bar). The maximum temperature inside the cuvette was 95 °C. Collected DSC data were corrected for buffer baseline and normalized for protein concentration. The reaction conditions were: 5 μM MPO in 5 mM phosphate buffer, pH 7, in the absence or presence of 500 μM or 5 mM hydrogen peroxide for 60 min). Guanidinium hydrochloride (GdnHCl; 5 mM) was added before measurements were started to avoid non-specific protein aggregation at increasing temperatures.

Microcal origin software was used for data analysis. Heat capacity (C_p) was expressed in kcal mol^{-1} K^{-1} (1 cal = 4.184 J). Data points were fitted to non-two-state equilibrium-unfolding models by the Lavenberg/Marquardt (LM) non-linear least square method.

Electronic circular dichroism spectrometry

Thermal unfolding was also followed by electronic circular dichroism (ECD) spectroscopy (Chirascan, Applied Photophysics, Leatherhead, UK). The instrument was flushed with nitrogen at a flow rate of 5 L min^{-1} and was capable of simultaneous UV–vis and ECD monitoring. The instrument was equipped with a Peltier element for temperature control and temperature-mediated denaturation was monitored between 20 and 95 °C with stepwise increments of 1.0 °C min^{-1}.

Single wavelength scans were performed with instrumental parameters set as follows. Visible ECD at a Soret minimum of 412 nm was performed with 5 μM MPO in 5 mM phosphate buffer, pH 7.0, containing 0.5 M GdnHCl to avoid aggregation at higher temperatures. Samples were monitored in the absence and presence of 100 and 1000-fold excesses of hydrogen peroxide over 60 min. The pathlength was 10 mm, spectral bandwidth 1 nm and the scan time per point was set at 10 s. Far-UV ECD at 222 nm was performed on the same samples with the pathlength set at 1 mm, spectral bandwidth at 3 nm and the scan time per point was set at 10 s.

The fraction α of unfolded protein was calculated according to $\alpha = (\theta_N - \theta)/(\theta_N - \theta_U)$ with θ_N being the ellipticity (in mdeg) at 222 nm of the protein in the native folded state, θ the ellipticity at defined temperature (T), and θ_U being the ellipticity at 222 nm of the completely unfolded state.

Mass spectrometric analyses

To determine which amino acid residues become oxidized during enzyme inactivation, 1.5 μM MPO was incubated with 1.5 mM hydrogen peroxide in 50 mM sodium phosphate buffer, pH 7.4. The treated sample and a control sample were reduced and alkylated prior to trypsin digestion following standard procedures. Changes in the tryptic peptides due to oxidation were then determined by LC-MS/MS at the center for Protein Research, University of Otago, Dunedin. Each sample was analyzed four times using the same instrument settings.

For LC-MS/MS analysis of tryptic peptides samples were reconstituted in 5% (v/v) acetonitrile, 0.2% (v/v) formic acid in water and injected onto an Ultimate 3000 nano-flow HPLC-System (Thermo Scientific, Dionex Co, CA) that was in-line coupled to the nanospray source of a LTQ Orbitrap XL hybrid mass spectrometer (Thermo Scientific, San Jose, CA). Peptides were loaded onto a PepMap100 trap column (Thermo Scientific, Dionex Co, CA) and separated on a PepMapRSLC analytical column (75 μm × 150 mm; Thermo Scientific, Dionex Co, CA) by a gradient developed from 5% (v/v) acetonitrile, 0.2% (v/v) formic acid to 80% (v/v) acetonitrile, 0.2% (v/v) formic acid in water at a flow rate of 400 nL/min.

Full MS in the mass range between m/z 400 and 2000 was performed in the Orbitrap mass analyzer with a resolution of 60,000 at m/z 400 and an AGC target of 5e5. Preview mode for FTMS master scan was enabled to generate precursor mass lists. The strongest five signals were selected for collision induced dissociation (CID)-MS/MS in the LTQ ion trap at a normalized collision energy of 35% using an AGC target of 2e4 and one microscan. Dynamic exclusion was enabled with one repeat counts during 60 s and an exclusion period of 180 s. Exclusion mass width was set to 0.01.

For protein identification MS/MS data were searched against a user defined amino acid sequence database containing the target sequence using the SEQUEST program operated through the Proteome Discoverer software (Thermo Scientific). The search was set up for full tryptic peptides with a maximum of two missed cleavage sites. Carboxyamidomethyl cysteine, oxidation (Cys, Met), dioxidation (Cys, Met), trioxidation (Cys) were selected as variable modifications. The precursor mass tolerance threshold was 10 ppm and the maximum fragment mass error 0.8 Da. Ion chromatograms were compared pair-wise using the SIEVE software (Thermo Scientific). The SIEVE Frame List was filtered for monoisotopic peaks and positive identifications (based on the imported SEQUEST search results). For the analysis of differential modifications the SIEVE Frame List and the Proteome Discoverer Peptide List were both integrated into a relational database (Microsoft Access) and linked by the unique combination of scan number and raw file name.

Results

Kinetics of inactivation of MPO by hydrogen peroxide

Myeloperoxidase was incubated with a given concentration of hydrogen peroxide in the absence of reducing substrate. Then, aliquots were taken and the residual enzyme activity was determined. As there were no differences between the residual halogenation and peroxidase activity, only the latter activity was measured in further experiments. The enzyme was incubated with increasing stoichiometric excesses of hydrogen peroxide and the loss of peroxidase activity was determined over time. These experiments were carried out in the absence of reducing substrates. At low ratios of hydrogen peroxide to MPO (⩽5:1), there was rapid but limited inactivation (Fig. 1A). For example, at ratio of 5:1, approximately 30% of the enzyme's activity was lost within 10 min. No further loss in activity occurred after this time. Interestingly, the rate of inactivation decreased as the ratio of hydrogen peroxide to MPO was increased to 20:1 and then 1000:1 (Fig. 1A and B). Thereafter the rate of inactivation increased with increasing molar ratios of hydrogen peroxide to MPO (Fig. 1B).

When the ratio of hydrogen peroxide to MPO was kept constant at 5000:1 but the concentrations varied, it was evident that the rate of inactivation was dependent on the concentration of hydrogen peroxide (Fig. 1C). As an alternative to this experiment, we also generated a slow flux of hydrogen peroxide with glucose oxidase to maintain a low steady-state concentration of hydrogen peroxide but still expose the enzyme to similar doses of hydrogen peroxide as when we used bolus additions of the substrate. The rate of inactivation of MPO over the first 25 min of reaction was independent of the flux of hydrogen peroxide (Fig. 1D). The extent of inactivation, however, increased with increasing fluxes of hydrogen peroxide. Interestingly, at the lowest flux of hydrogen peroxide (i.e., 0.5 μM/min) inactivation reached a maximum of only about 40% which is similar to that obtained with a bolus addition of 160 nM

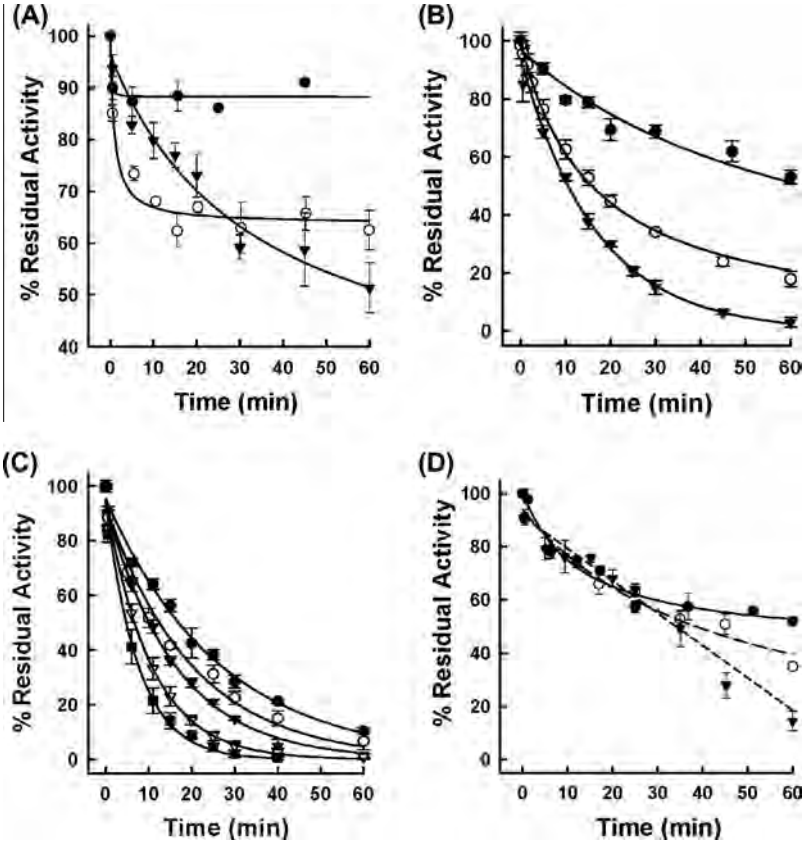

Fig. 1. Loss of peroxidatic activity of myeloperoxidase upon incubation with hydrogen peroxide. (A) Loss of peroxidase activity at low MPO to hydrogen peroxide ratios. 32 nM MPO reacted with hydrogen peroxide at oxidant to protein ratios of (●) 1:1, (○) 5:1 and (▼) 20:1 in 50 mM phosphate buffer, pH 7.4, containing 100 μM DTPA. The residual peroxidase activity of MPO was determined by taking aliquots over time and measuring the TMB peroxidase activity ($n = 2$). (B) 32 nM MPO was incubated with hydrogen peroxide at H_2O_2 to protein ratios of (●) 1000:1 (32 μM H_2O_2), (○) 5000:1 (160 μM H_2O_2), (▼) 10,000:1 (320 μM H_2O_2), in 50 mM phosphate buffer, pH 7.4, with 100 μM DTPA. Aliquots were taken and the residual TMB activitiy of MPO over time was determined ($n = 3$). (C) Loss of peroxidase activity at a constant hydrogen peroxide to protein ratio. MPO was incubated with a 5000-fold stoichiometric excess of hydrogen peroxide at varying enzyme concentrations: (●) 160 μM, (○) 240 μM, (▼) 320 μM, (Δ) 640 μM and (■) 1280 μM H_2O_2 in 50 mM phosphate buffer, pH 7.4, with 100 μM DTPA. MPO concentrations ranged accordingly from 32 to 256 nM. Residual TMB activities over time are presented ($n = 3$). (D) Loss of peroxidase activity when MPO was reacted with a steady flux of hydrogen peroxide. 32 nM MPO reacted with a continuous hydrogen peroxide flux of (●) 33.3 μM/60 min, (○) 153.3 μM/60 min and (▼) 286.6 μM/60 min hydrogen peroxide in 50 mM phosphate buffer, pH 7.4, and 100 μM DTPA. Residual activity over time was determined by the TMB peroxidase activity assay ($n = 2$).

hydrogen peroxide. From these data we conclude that MPO is very susceptible to low concentrations of hydrogen peroxide. Higher concentrations of hydrogen peroxide protect the enzyme from a fast inactivation event but at the highest concentrations a slower inactivation process occurs that is dependent on the concentration of hydrogen peroxide.

Next we determined whether the kinetics of inactivation at high concentrations of hydrogen peroxide conform to the equations developed for mechanism-based inhibitors [16]. Plotting the initial concentration of MPO against the concentration of hydrogen peroxide consumed over 60 min gave a straight line with the slope representing the partition ratio (r) for turnover *versus* inactivation (Fig. 2A). The value obtained indicates that the enzyme turned over 799 times before it was fully inactivated. However, as will be outlined below (see also Fig. 7), each mole of MPO consumes two moles of H_2O_2, if it follows the peroxidase cycle ($r = 400$), and three moles of H_2O_2 are consumed if Compound III is involved in turnover ($r = 266$).

Half-times for inactivation were determined from the data in Fig. 1C and plotted according to Equation (1). From the slope of the secondary plot depicted in Fig. 2B the rate constant for inactivation (k_{in}) was determined to be 3.9×10^{-3} s^{-1} while the dissociation constant for hydrogen peroxide (K') was calculated from the intercept to be 740 μM. It is evident from this analysis that inactivation of MPO conforms to the model proposed for mechanism-based inactivation [15] and hydrogen peroxide can be considered to be a suicide substrate for MPO.

$$[H_2O_2]_0 \times t_{1/2} = [\ln(2\text{-}M)/(1\text{-}M)] \times (K'/k_{in}) + (\ln 2/k_{in}) \times [H_2O_2]_0 \quad (1)$$

where $M = (1 + r) \times [MPO]_o / [H_2O_2]_o$

Spectral analysis of MPO reacting with hydrogen peroxide

MPO has numerous redox intermediates that have distinct absorption spectra [17]. To demonstrate which of these redox intermediates are involved in the turnover and inactivation of the enzyme, absorption spectra were recorded at different molar ratios of hydrogen peroxide to MPO. In these analyses the redox intermediates Compound II and Compound III were distinguished from each other by the ratio of absorbances at 625 and 456 nm (A_{625}/A_{456}), which are 0.17 for Compound II and 0.54 for Compound III [17]. When 1.5 μM MPO was reacted with 60 μM of hydrogen peroxide, A_{625}/A_{456} changed to 0.20 within 5 s, which indicates that the enzyme was almost completely converted to Compound II (Fig. 3A). Compound II subsequently slowly decayed back to the ferric MPO and no more spectral changes could be observed after 120 min. At this time the Soret absorbance at 430 nm was decreased by 6.2 ± 2.8%. Under these conditions all the hydrogen

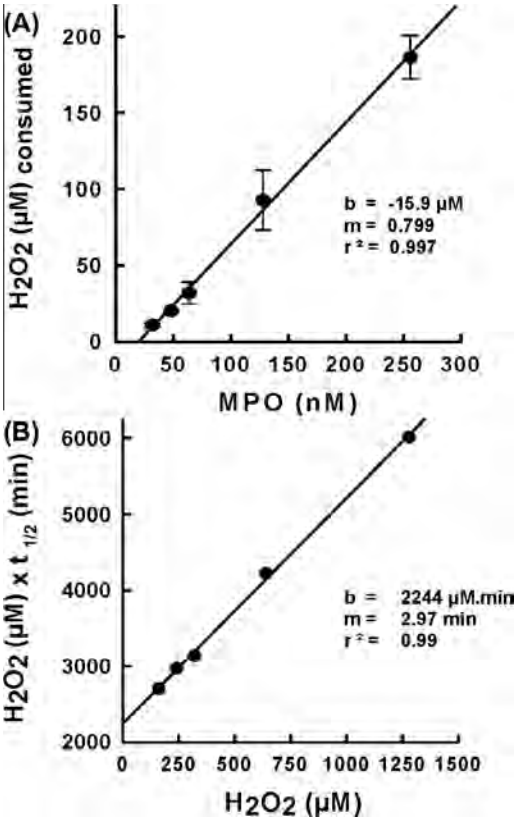

Fig. 2. Mechanistic analysis of inactivation of myeloperoxidase by hydrogen peroxide. (A) Partition ratio for the inactivation of MPO by hydrogen peroxide. Residual hydrogen peroxide concentrations were measured at 60 min using the FOX assay when MPO reacted with increasing hydrogen peroxide concentrations at the constant hydrogen peroxide to protein ratio of 5000:1 in 50 mM phosphate buffer, pH 7.4, and 100 μM DTPA (same conditions as Fig. 1C). (B) Determination of kinetic parameters for the inactivation of MPO by H_2O_2. Half-times of inactivation, $t_{1/2}$, were determined from Fig. 1C and initial concentrations of hydrogen peroxide were used in the secondary plot.

peroxide was consumed within 2 min and the enzyme lost ~10% activity (insets to Fig. 3A). At 250 μM hydrogen peroxide, MPO was also rapidly converted to Compound II but there was a greater loss of the absorbance at 430 nm (19.9 ± 3.2%) (Fig. 3B). Under these conditions all the hydrogen peroxide was consumed within five minutes and the enzyme lost about 30% of its activity (insets to Fig. 3B). With 1.5 mM of hydrogen peroxide, the enzyme was converted to a mixture of about 50% Compound II and 50% Compound III (A_{625}/A_{456} = 0.33), with a subsequent fast decrease in absorbance at 454 nm. At 60 min the loss of absorbance at 430 nm was 78.1 ± 1.3% after which no more spectral changes were observed (Fig. 3C). Under these conditions MPO consumed all hydrogen peroxide and lost most of its activity within 20 min (insets to Fig. 3C).

With all concentrations of hydrogen peroxide, adding 100 μM ascorbate at the end of the reactions did not restore the absorbance at 430 nm. Consequently, because ascorbate readily reduces Compounds I and Compound II [18], it is apparent that the loss of heme absorbance was due to an irreversible oxidative modification and not incomplete conversion of the redox intermediates back to the native MPO.

From these results we conclude that MPO readily consumes hydrogen peroxide in the absence of other reducing substrates. During this process heme absorbance is lost and enzyme activity declines. As the enzyme consumed more hydrogen peroxide, there was greater heme destruction and enzyme inactivation, which was associated with conversion of the enzyme to Compound III.

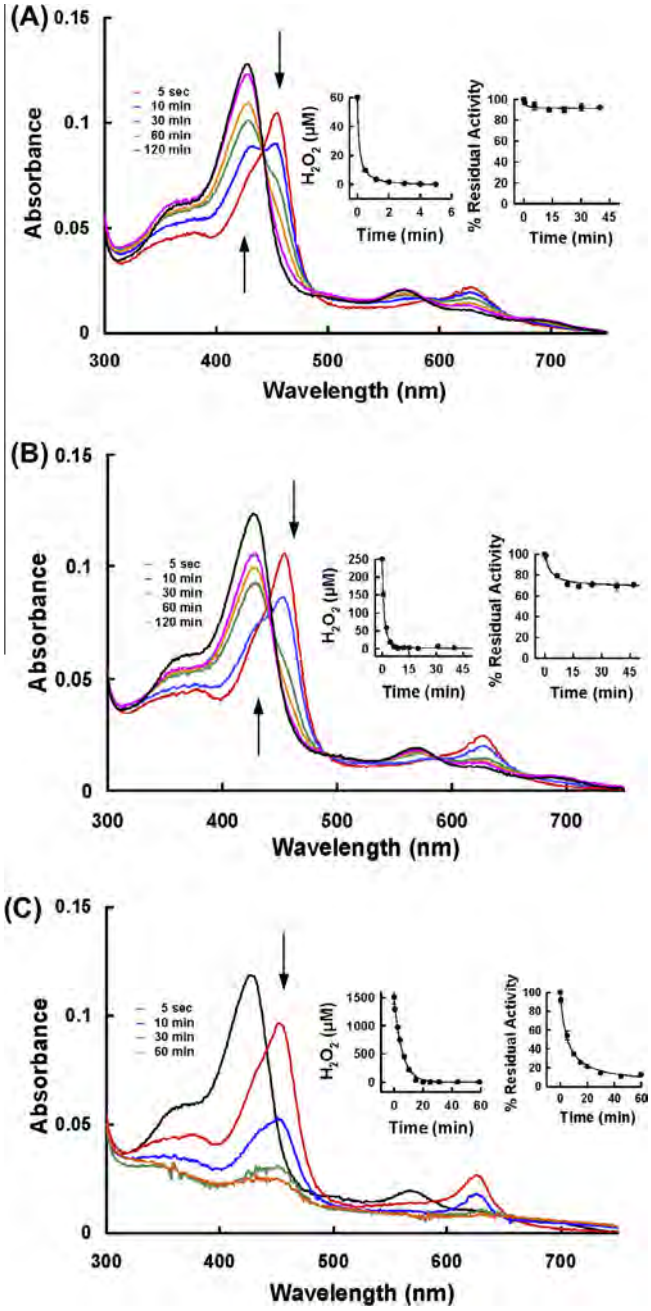

Fig. 3. Spectral analysis of MPO reacting with hydrogen peroxide. 1.5 μM MPO was incubated with 60 μM H_2O_2 (A), 250 μM H_2O_2 (B) and 1.5 mM H_2O_2 (C) in 50 mM phosphate buffer, pH 7.4, 100 μM DTPA. Time resolved spectra were recorded over time. The black spectrum depicts the spectral signature of ferric MPO before addition of H_2O_2, arrows indicate direction of spectral changes. Insets represent consumption of hydrogen peroxide over time as measured by the FOX assay as well as the residual peroxidase activity determined with the TMB-assay.

Protective effect of reducing substrates on loss of heme absorbance

To determine whether reducing substrates protect the enzyme against inactivation by hydrogen peroxide, absorption spectra were recorded under the same conditions as in Fig. 3A–C but in the presence of either ascorbate or bromide plus methionine. Ascorbate is a classical peroxidase substrate that reduces Compound I and Compound II [18] with a single electron whereas bromide is a halogenation substrate that donates two electrons to Compound I and is oxidized to hypobromous acid [17]. Methionine was present in this reaction to scavenge produced HOBr. Addition

of 200 μM ascorbate significantly decreased the loss of Soret absorbance at 430 nm at all concentrations of hydrogen peroxide (Table 1). Compound II was formed in the presence of ascorbate and all the hydrogen peroxide was consumed within a few minutes. Bromide also protected the enzyme but was less effective than ascorbate. In its presence, conversion of Compound II back to native MPO took much longer than with ascorbate (Table 1).

Hydrogen peroxide-mediated changes to the structure of MPO

Treatment of 1.5 μM MPO with 1.5 mM of hydrogen peroxide resulted in the release of approximately 85% of the iron from the protein (Fig. 4A). This result correlated very well with the loss of heme absorbance observed under the same conditions (Fig. 3C) and suggests that the oxidative break down of the heme prosthetic group causes it to release the chelated iron.

The effect of hydrogen peroxide on the overall structure of MPO was analyzed by gel electrophoresis. Chemiluminescence [14] was used to detect changes in the heme content of the protein. Hydrogen peroxide was added to MPO at a 1000:1 ratio and aliquots were taken over time after the reaction was stopped by addition of catalase to remove residual hydrogen peroxide. Under non-reducing conditions untreated MPO ran as one single diffuse band on SDS–PAGE at the expected molecular weight of the MPO homodimer (146 kDa, Fig. 4B top panel, lane 1) consisting of two identical glycosylated heavy chain monomers (58.5 kDa) and two light chains (14.5 kDa). The heavy and light chains are connected via their covalent linkages to the heme prosthetic group. The two monomers are linked via one disulfide bridge to form the dimer. On some gels a faint band of 14.5 kDa was also visible for untreated MPO, indicating that a minor fraction of the light chain can detach from the homodimer under non-reducing conditions (Fig. 4D top panel, lane 1). After reaction with hydrogen peroxide the single band progressively changed into a doublet with a concomitant increase in the appearance of a 14.5 kDa band (Fig. 4B top panel, lanes 2–6) for the light polypeptide chain. The 60 kDa band visible in lanes 2–6 originated from the added catalase. A second identical gel was blotted on a PVDF membrane and enhanced chemiluminescence was used to detect the heme prosthetic group. The strong signal for untreated MPO at 146 kDa (Fig. 4B lower panel, lane 1) decreased over time when the enzyme was treated with hydrogen peroxide (Fig. 4B lower panel, lane 2–6). No chemiluminescence signals appeared at other molecular weights on the membrane after treatment with hydrogen peroxide. These results suggest that the heme was degraded by hydrogen peroxide while there were relatively subtle changes to the protein involving detachment of the light chain from the heme.

Under reducing SDS–PAGE conditions untreated MPO should theoretically run as one polypeptide band of the molar mass of 73 kDa for the monomer consisting of one heavy and one light subunit linked via the heme. Under reducing conditions we observed two additional bands at molar masses of approximately 60 and 14 kDa, as shown in Fig. 4C top panel, lane 1. Taking the above results under non-reducing conditions into consideration, it was concluded that the polypeptide chain at approx. 60 kDa was the heavy chain and the 14 kDa band was the light chain. When MPO was treated with hydrogen peroxide, the intensity of the 73 kDa band of the MPO monomer decreased progressively over time (Fig. 4C, lanes 2–6) with no additional bands appearing. The catalase that was added to stop the reaction ran at the same molar mass as the heavy polypeptide chain. An identical gel run under reducing conditions was blotted onto a PVDF membrane and again the heme prosthetic group was visualized using chemiluminescense. The heme group of untreated MPO showed one strong signal at the molecular weight of 73 kDa (Fig. 4C lower panel, lane 1), which upon treatment with hydrogen peroxide progressively decreased with no additional signals appearing on the blot (Fig. 4C lower panel, lanes 2–6).

MPO was also reacted with increasing hydrogen peroxide concentrations for two hours and subsequently resolved by SDS–PAGE under non-reducing condition (Fig. 4D upper panel). The same fragmentation pattern as described above in both the high and low molar mass regions was observed with increasing concentrations of hydrogen peroxide. The doublet became very apparent from lane 6 (100:1 ratio of hydrogen peroxide to protein). At a ratio of 2000:1 (lane 10) the most prominent high molecular weight band was observed at approx. 120 kDa which correlated well with the molecular weight of the homodimer that has lost both light chains (117 kDa), whereas the second prominent high molecular weight band correlated with the homodimer that has lost one light chain (131.5 kDa). At the same time a strongly increased band for the light chain at 14.5 kDa was observed. The 38 kDa fragment also visible on this gel, was observed only on some of the gels run under the same conditions and was interpreted earlier as a degradation product deriving from a specific cleavage between Met243 (that forms the sulfonium ion linkage at pyrrole ring A) and Pro244 [19]. The heme prosthetic group was detected again using chemiluminescence (Fig. 4D, lower panel). The intensity of the band decreased with increasing concentrations of hydrogen peroxide which became very noticeable from lane 7 (167:1 ratio of hydrogen peroxide to MPO) (Fig. 4D top panel, lanes 7–10). Collectively, these results indicate that as MPO is inactivated by hydrogen peroxide the heme group is destroyed with concomitant release of iron and the light chain becomes detachable from the homodimer under SDS–PAGE conditions as a consequence of the heme destruction.

Hydrogen peroxide-mediated changes to protein unfolding and the thermal stability of MPO

Next we evaluated the impact of hydrogen peroxide treatment on the thermal stability of MPO. With native MPO one single endotherm was obtained that was best fitted by a non-two-state transition with maxima at 84.0 and 88.4 °C which confirms recently published data [20]. Treatment of MPO with a 100-fold excess of hydrogen peroxide resulted in a very similar unfolding pathway (T_{m1} = 83.9 and T_{m2} = 86.5 °C) for the protein (Fig. 5A). This also includes the calculated calorimetric enthalpies for the two transitions (Table 2). With a 1000-fold excess of hydrogen peroxide three transitions were seen with T_{m1} = 75.0 °C, T_{m2} = 85.2 °C and

Table 1
Protective effect of a reducing substrate on the loss of absorbance in the ferric state (430 nm). The absorbance loss of the heme Soret peak (1.5 μM in 50 mM phosphate buffer, pH 7.4) was further investigated under the same conditions as in Fig. 3A–C, with either 200 μM ascorbate or 5 mM bromide plus 5 mM methionine present. The time until no more further spectral changes were observed is shown as Δ time (min).

H_2O_2 (μM)	Without substrate		200 μM ascorbate		5 mM bromide 5 mM methionine	
	Loss $A_{430\ nm}$ (%)	Δt (min)	Loss $A_{430\ nm}$ (%)	Δt (min)	Loss $A_{430\ nm}$ (%)	Δt (min)
60	6.2 ± 2.8	120	4.1 ± 1.5	0.7	9.6 ± 1.0	15
250	19.9 ± 3.2	120	5.5 ± 1.3	1	10.5 ± 1.6	40
1500	78.1 ± 1.3	60	18.1 ± 1.8	2.5	20.7 ± 1.5	60

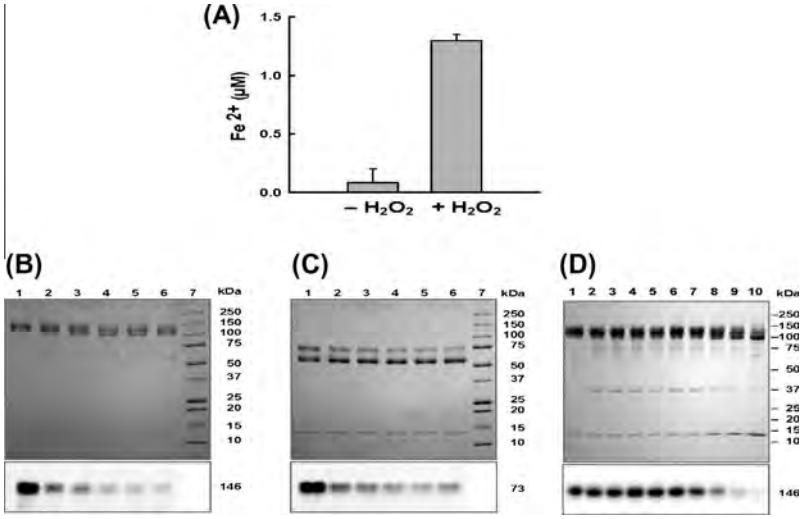

Fig. 4. Structural consequences of myeloperoxidase incubated with hydrogen peroxide. (A) Detection of iron release from the heme prosthetic group. 1.5 μM MPO was reacted with 1.5 mM hydrogen peroxide in 50 mM sodium acetate buffer, pH 7.4, (column 2). Column 1 shows the result for untreated MPO. Ferrozine was used to measure the release of iron from the heme group ($n = 3$). (B, C) SDS–PAGE: Time course of MPO reacted with hydrogen peroxide. Top panels: 1.5 μM MPO was reacted with 1.5 mM of hydrogen peroxide in 50 mM phosphate buffer, pH 7.4, and 100 μM DTPA. 15 μL aliquots were taken at 5 min (lane 2), 10 min (lane 3), 25 min (lane 4), 45 min (lane 5) and 60 min (lane 6) and added to 20 μg/mL catalase to remove remaining hydrogen peroxide. Lane 1: negative control (15 μL of untreated MPO, no catalase added). The samples were run on a 8–20% resolving SDS–PAGE under non-reducing (B) and reducing (C) conditions. Bottom panels: SDS–PAGE run under the same conditions as shown in top panels, blotted onto a PVDF membrane and detection of the heme by chemiluminescence. (D) 1.5 μM MPO was incubated with hydrogen peroxide in 50 mM phosphate buffer, pH 7.4, containing 100 μM DTPA for 2 h at various hydrogen peroxide to MPO ratios; 1:1 (lane 2), 5:1 (lane 3), 10:1 (lane 4), 40:1 (lane 5), 100:1 (lane 6), 167:1 (lane 7), 500:1 (lane 8), 1000:1 (lane 9) and 2000:1 (lane 10). 15 μL aliquots were taken and resolved on a 8–20% SDS PAGE under non-reducing conditions. Lane 1: negative control (15 μL of untreated MPO). Bottom panel: SDS–PAGE run under the same conditions as shown in top panel, blotted onto a PVDF membrane and detection of the heme by chemiluminescence.

T_{m2} = 86.1 °C (Fig. 5A) reflecting protein fragmentation as observed by SDS–PAGE analyses (compare with Fig. 4D, lane 9). In all assays 0.5 M GdnHCl was present to avoid non-specific aggregation during heating, which is confirmed by the fact that the sum of calorimetric enthalpies ($\sum H_m$) were very similar for all fitted transitions (Table 2A) [20].

To gain more information about the hydrogen peroxide-mediated structural changes, unfolding of MPO was also followed by electronic circular dichroism (ECD) spectroscopy in the far-UV as well as in the visible region. The far-UV ECD spectrum of MPO in the native state exhibited two minima at 208 and 222 nm, respectively (not shown) [20], which is typical for its mainly α-helical structure [17,21,22]. Upon heating the protein from room temperature to 70 °C a small fraction of ellipticity was already lost, but melting of the α-helices started above 70 °C (T_m = 76.8 °C) (Fig. 5C) concomitantly with the observed changes in the heme cavity followed at 416 nm (i.e., minimum of Soret ellipticity) (Fig. 5B). Thus unfolding of α-helices followed by ECD suggests a cooperative two-state transition, including loss of the proper heme environment. The conformational stability at room temperature ($\Delta G_{25°C}$) was calculated to be 18.9 kJ mol^{-1} (222 nm) (Fig. 5C and Table 2A). A similar unfolding pathway was seen when MPO was incubated with a 100-fold stoichiometric excess of hydrogen peroxide. Upon incubation of MPO with a 1000-fold excess of hydrogen peroxide the loss of ellipticity in the initial phase was more pronounced and the T_m-value of the main transition was lowered to 73.2 °C (Table 2B). From Fig. 5B it is also evident that incubation of MPO with hydrogen peroxide leads to loss of Soret ellipticity reflecting the loss of Soret absorbance at 430 nm (for comparison see Fig. 3).

Table 2
(A) Calorimetric enthalpy calculated from thermal unfolding experiments (Fig. 5) using differential scanning calorimetry. Conditions: 5 μM human myeloperoxidase in 5 mM phosphate buffer, pH 7.0. (Native enzyme or incubated with 100- or 1000-fold stoichiometric amount of hydrogen peroxide for 2 h. (B) Thermodynamic data of thermal unfolding (calculated from van't Hoff plot) for MPO without and with 100 and 1000 fold excess of H_2O_2 followed by electronic circular dichroism spectroscopy at 222 nm.

	MPO	MPO plus 100 eq H_2O_2	MPO plus 1000 eq H_2O_2
(A)			
ΔH_m (kJ mol^{-1})	–	–	38.5
ΔH_{m2} (kJ mol^{-1})	111.7	104.6	85.0
ΔH_{m3} (kJ mol^{-1})	138.7	135.0	140.3
$\sum \Delta H_m$ (kJ mol^{-1})	250.5	239.6	263.8
	MPO ([θ]222)	MPO 100 eq H_2O_2 ([θ]222)	MPO 1000 eq H_2O_2 ([θ]222)
(B)			
T_m (°C)	76.8 ± 0.1	76.1 ± 0.2	73.2 ± 0.1
ΔH_m (kJ mol^{-1})	261.4 ± 16.7	245.7 ± 18.9	266.7 ± 11.5
ΔS_m (J mol^{-1})	746.8 ± 48.7	703.6 ± 54.3	770.1 ± 33.2
ΔC_p (kJ mol^{-1} K^{-1})	4.88	4.70	5.41
$\Delta G_{25°C}$ (kJ mol^{-1})	18.9	17.4	17.6

Hydrogen peroxide-mediated modifications of amino acid residues of MPO

When MPO was reacted with various hydrogen peroxide concentrations the loss of the heme prosthetic group was detectable by following its absorbance at 430 nm but we could not identify the modified heme products by mass spectrometry. Thus, we focused our attention on modifications of the protein by analyzing tryptic peptides for oxidized sulfur containing amino acid residues. 10 out of 17 methionine residues were oxidized to methionine sulfoxide (two from the light and eight from the heavy chain) as depicted in Fig. 6A and summarized in Table 3. Oxidation of cysteine would not be detected because the sample was reduced and alkylated before digestion. Of the modified methionines only three were surface exposed (i.e., having more than 8 Å^2 surface exposed). Interestingly, many of the surface exposed methionines were not modified (Fig. 6 and Table 3). This suggests that the

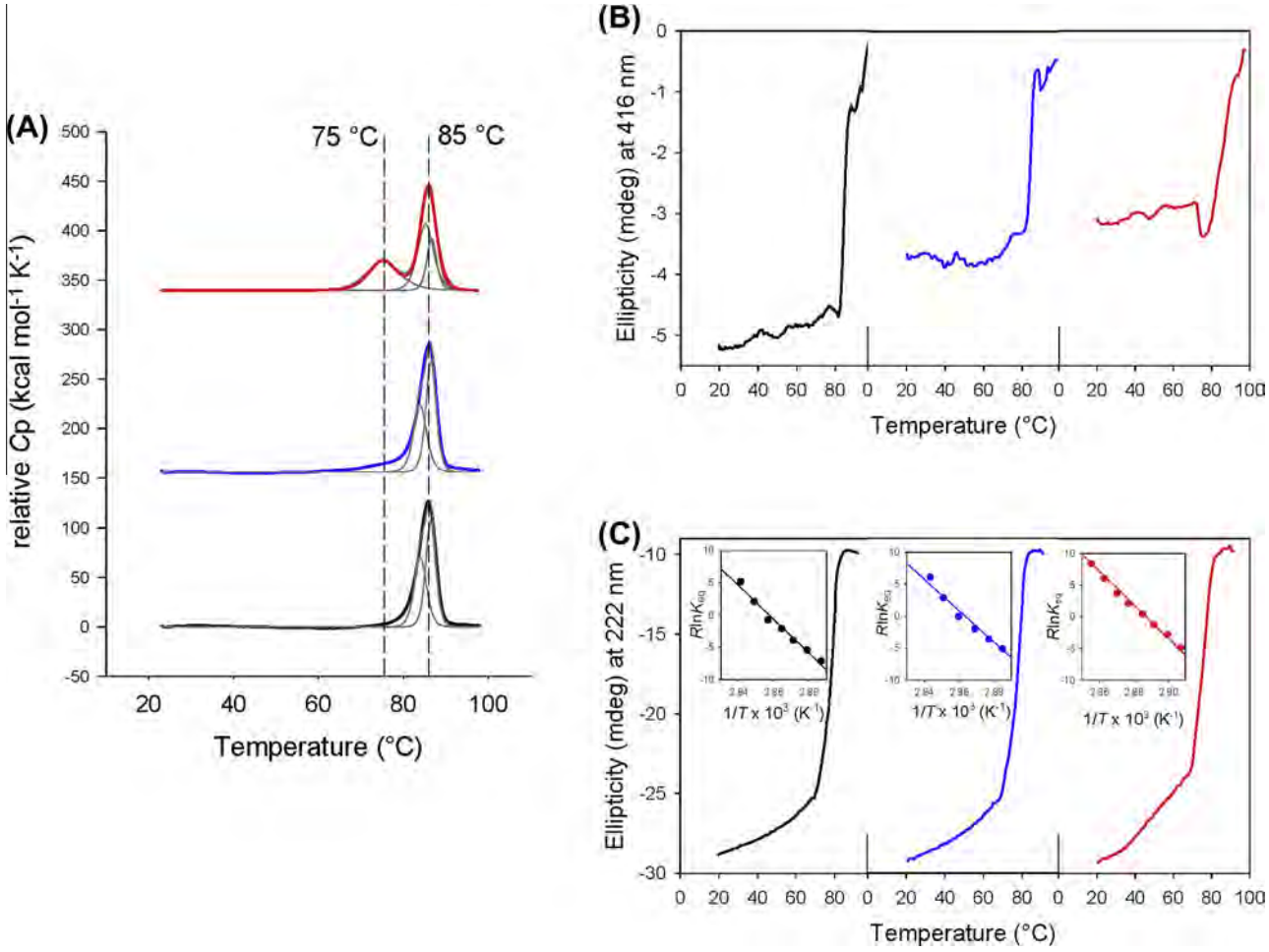

Fig. 5. Thermal stability and unfolding of human myeloperoxidase treated with hydrogen peroxide. (A) Thermal unfolding of leukocyte MPO followed by differential scanning calorimetry. Normalized DSC scans of 5 μM MPO in 5 mM phosphate buffer, pH 7.4, after pre- and post-transitional baseline subtraction in the range of 20–100 °C. Absence of H_2O_2 (black line), incubation with 500 μM H_2O_2 (blue line) and incubation with 5 mM H_2O_2 (red line). Experimental data and fitting to a non-two-state model (thin black lines) are shown. (B) Thermal unfolding followed by circular dichroism at 416 nm. Same conditions as in (A). (C) Thermal unfolding of leukocyte MPO followed by circular dichroism at 222 nm. The insets represent the corresponding van't Hoff plots and linear fits. Same conditions as in (A). (For interpretation of the references to color in this figure legend, the reader is referred to the web version of this article.)

methionine residues did not react directly with hydrogen peroxide but served as scavenger of protein radicals formed inside the protein. The methionine residue that forms the covalent sulfonium ion linkage with the vinyl group on pyrrole ring A (Met243) was not modified.

Discussion

In this investigation we have shown that MPO is exquisitely sensitive to a fast but limited inactivation event mediated by low concentrations of hydrogen peroxide. Higher concentrations of hydrogen peroxide protect against this fast inactivation event but lead to a slower pathway of inactivation in which the heme prosthetic groups are destroyed, and in the process their iron is released and the small polypeptide subunits detach from the heme prosthetic group.

Human myeloperoxidase is a cationic 146 kDa dimer of high conformational and thermal stability [17,20,21,22] with a single disulfide bridge between symmetry-related halves (73 kDa), each of which contains two polypeptides of 14.5 and 58.5 kDa. The heavy polypeptide is glycosylated and contains five intra-chain disulfides whereas the light polypeptide contains only one [21,22]. Each subunit of MPO contains a derivative of protoporphyrin IX in which the methyl groups on pyrrole rings A and C are linked via ester bonds to the carboxyl groups of highly conserved aspartate and glutamate residues [21,22]. In addition, the β-carbon of the vinyl group on pyrrole ring A forms a covalent bond with the sulfur atom of a fully conserved methionine [20,21]. As a consequence, the heme porphyrin ring is considerably distorted from planarity, confering unique spectral and redox properties to MPO [23,24].

The mechanisms of inactivation of MPO by hydrogen peroxide are understandable in terms of the protein's architecture and the redox transformations it undergoes during turnover (Fig. 7). Reaction of hydrogen peroxide with ferric MPO leads to reductive heterolytic cleavage of its oxygen–oxygen bond and oxidation of the enzyme to its Compound I state (Fig. 7; Reaction 1). This form of MPO contains two oxidizing equivalents more than the resting enzyme [17]. Compound I contains an oxoiron (IV) and a π-cation radical on the porphyrin ring. It has high one- and two-electron reduction potentials [25–27], allowing the oxidation of numerous one- and two-electron donors. Compound I is either reduced directly by (pseudo-)halides ($X^- = Cl^-$, Br^-, SCN^-) to the resting state producing hypohalous acids (HOX = HOCl, HOBr, HOSCN) (Reaction 2) or it undergoes one-electron reduction by a typical peroxidase substrate (AH, Reaction 3a) and hydrogen peroxide (Reaction 3b)

to produce Compound II and the substrate radical (A) or superoxide ($O_2^{\bullet-}$ or $HO_2^{\bullet}$), respectively [28]. Finally, Compound II is reduced back to the resting state with either another peroxidase substrate (Reaction 4a) [29] or superoxide (Reaction 4b) [30]. Furthermore, at high concentrations of hydrogen peroxide Compound II can be converted to Compound III (Reaction 5) [31], where ferrous MPO with bound dioxygen exists in equilibrium with ferric MPO with bound superoxide. Compound III slowly decays to ferric MPO and superoxide. Alternatively, it can decay to ferrous MPO which rapidly recombines with dioxygen or reacts with hydrogen peroxide to form Compound II (Reaction 6) [31]. Based on burst phase kinetics for hydrogen peroxide consumption by MPO in the absence of chloride, it has also been proposed that the enzyme has catalatic activity, degrading hydrogen peroxide to oxygen and

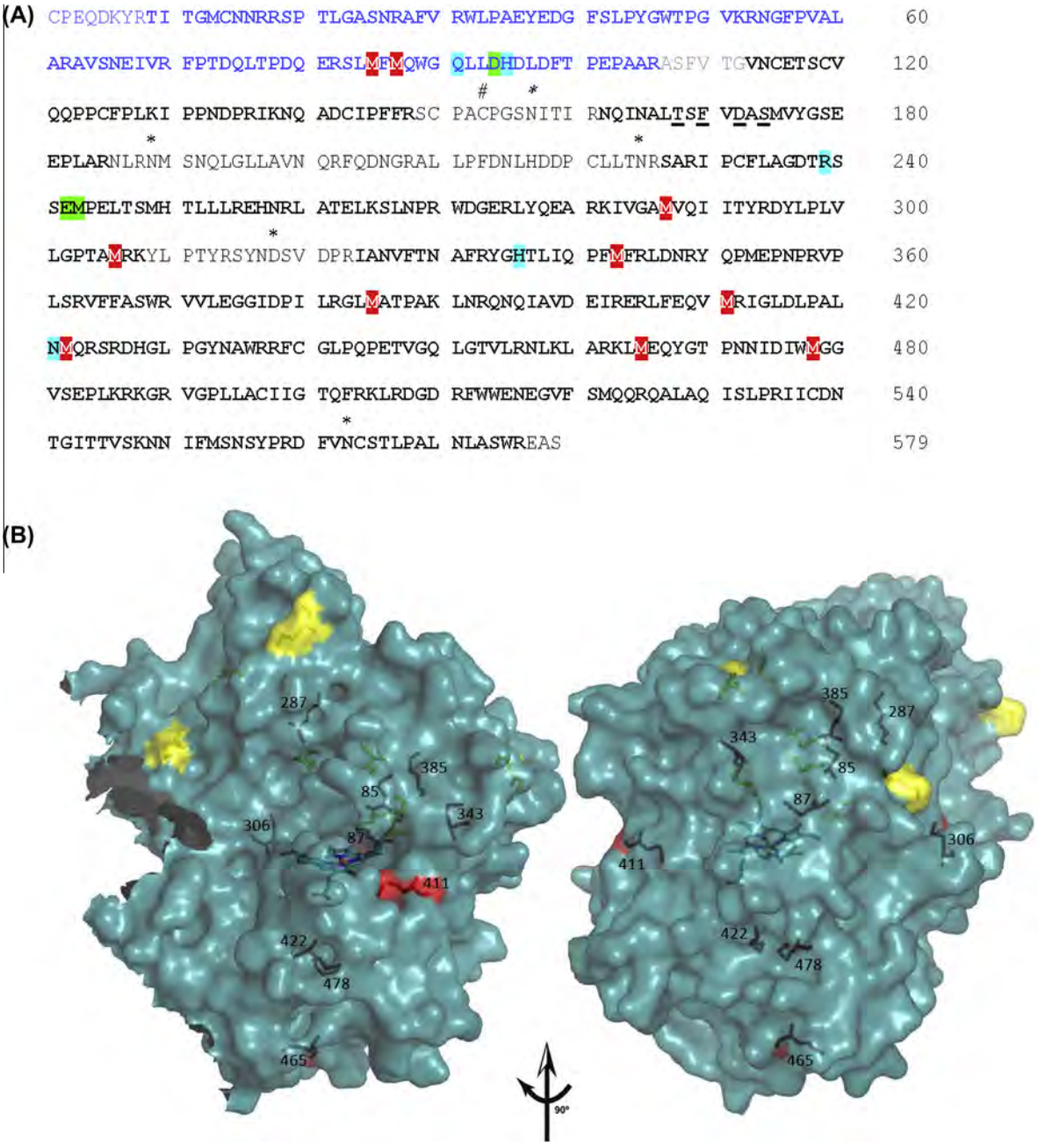

Fig. 6. Modification of amino acids of myeloperoxidase incubated with hydrogen peroxide. (A) LC-MS/MS analysis (amino acid sequence coverage of 86%) and oxidized methionine residues of MPO after treatment with hydrogen peroxide. Mature MPO is a homodimer, each half being composed of a light chain (106 amino acids, blue) and a heavy chain (467 amino acids, black). The small excised hexa-peptide between the light and heavy subunit is depicted in grey. Important catalytic residues are highlighted in turquiose, amino acids involved in the covalent link with the prosthetic group are in green. Glycosylation sites (asparagines, N) are marked by *, the cysteine that forms the disulfide bridge between the subunits is marked by # and ligands of the calcium ion binding site are underlined. The amino acid numbering for MPO is based on the mature protein with the first cysteine in the small polypeptide designated as residue 1. Amino acid sequence coverage by LC-MS/MS is depicted in bold letters, oxidized methionine residues are highlighted in red. (B) 3D structure of the MPO monomer (one light and one heavy chain covalently linked via the heme group) showing the ten oxidized methionine residues which were detected by LC-MS/MS when 1.5 μM MPO was reacted with 1.5 mM of hydrogen peroxide. Surface exposed methionines that were not modified by H_2O_2 incubation are depicted in yellow, oxidized methionines are shown in red. For definition of surface accessibility see Table 4. (For interpretation of the references to color in this figure legend, the reader is referred to the web version of this article.)

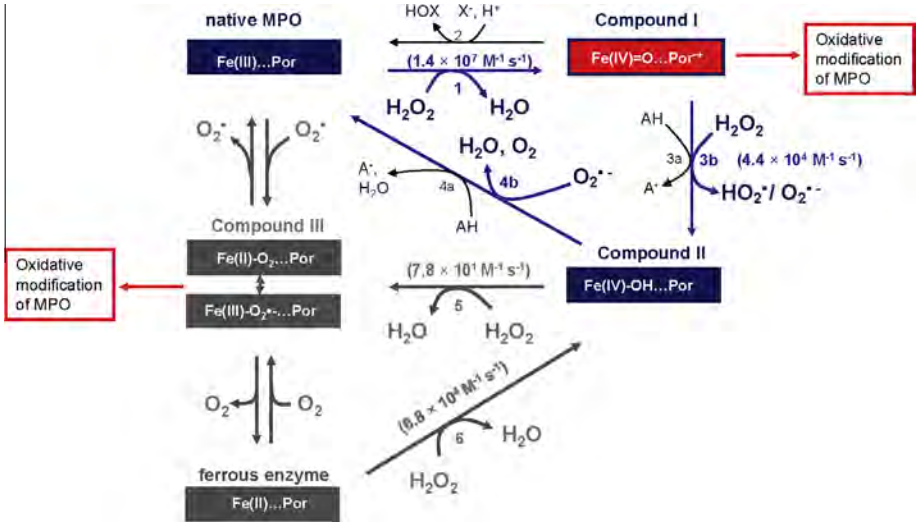

Fig. 7. Proposed reaction scheme for redox interconversion of MPO in the presence of hydrogen peroxide. In the micromolar H_2O_2 concentration range cycling of MPO includes the ferric state, Compound I and Compound II and Reactions 1, 3b and 4b (blue cycle). Compound II accumulates. The strong electrophilicity of Compound I oxidizes the prosthetic group and the protein. Inactivation is suppressed in the presence of one- (Reactions 3a and 4a) and two-electron donors (Reaction 2). In the millimolar concentration range Compound II conversion to Compound III (dark grey intermediates) becomes relevant and cycling of MPO then includes the ferric and ferrous state, Compound I, Compound II and Compound III. The latter intermediate accumulates. Upon reaction of Compound III with excess of hydrogen peroxide reactive oxidants might be formed that destroy the heme and oxidize the protein. (For interpretation of the references to color in this figure legend, the reader is referred to the web version of this article.)

Table 3
LC-MS/MS analysis of oxidized tryptic peptides of MPO when reacted with hydrogen peroxide. 1.5 μM MPO was reacted with 1.5 mM of hydrogen peroxide in 50 mM phosphate buffer pH 7.4. The reduced and alkylated protein was digested with trypsin and peptides were analyzed by LC-MS/MS. Peptides with a signal ratio of treatment *versus* control of ⩾3 and a *p* value of ⩽0.001 are presented.

MPO amino acid #	Identified modified peptide	Oxidized residue on peptide	Charge	m/z Value	Ratio ⩾3 treatment vs control	*p*-value ⩽0.001	SD
M 85 M 87	SLmFmQWGQLLDHDLDFTPEPAAR	M3 M5	3	950.7812	11.36	1.02E-5	2.75
M 287	KIVGAmVQIITYR	M6	3	503.2933	19.68	1.08E-6	4.59
M 306	DYLPLVLGPTAmR	M12	2	731.3934	6.72	5.99E-10	0.85
M 306	DYLPLVLGPTAmRK	M12	2	795.4401	7.06	0.00016	1.41
M 306	KIVGAMVQIITYRDYLPLVLGPTAmRK	M25	4	766.4382	4.30	1.72E-5	1.06
M 343	YGHTLIQPFmFR	M10	2	763.3850	5.06	8.60E-6	0.42
M 343	YGHTLIQPFmFR	M10	3	509.2593	10.82	3.43E-5	1.46
M 343	IANVFTNAFRYGHTLIQPFmFR	M20	4	665.5958	9.76	1.85E-6	3.00
M 385	GLmATPAKLNR	M3	2	594.3316	9.28	2.38E-5	0.57
M 385	VVLEGGIDPILRGLmATPAKLNR	M15	3	817.1353	36.18	7.90E-6	6.39
M 411	LFEQVmRIGLDLPALNmQR	M6 M17	3	759.4016	13.59	0.000266	2.42
M 422	IGLDLPALNmQR	M10	2	678.8680	7.38	1.00E-5	0.53
M 465 M 478	LmEQYGTPNNIDIWmGGVSEPLKR	M2 M15	3	927.4525	16.01	2.76E-5	4.14

water. That is, it acts in an analogous manner to catalase where hydrogen peroxide also reduces Compound I directly in a two-electron reaction to produce dioxygen [32]. However, no evidence for this reaction has been demonstrated using pre-steady-state kinetic measurements [28,33]. All of these redox intermediates are relevant to the physiological activities of MPO because when the enzyme is released by neutrophils into phagosomes or the extracellular environment it reacts with both superoxide and hydrogen peroxide [34,35].

It has been demonstrated that a ten-fold molar excess of hydrogen peroxide over MPO is needed [28] for complete conversion of ferric MPO to Compound I, which is subsequently reduced to Compound II via Reaction 3b. Among heme peroxidases MPO is unique in catalyzing the one-electron oxidation of hydrogen peroxide to superoxide [28]. Compound I is likely to be the crucial redox intermediate in the fast inactivation pathway because there was irreversible loss of peroxidase activity at ratios lower than 10:1. Protection of the enzyme from this fast inactivation event by high concentrations of hydrogen peroxide and reducing substrates, including ascorbate and bromide, can be explained by their reactions with Compound I. Compound I has a very positive reduction potential [25,26] so that in the absence of exogenous electron donors it will promote radical oxidation reactions within the heme group or with the protein moiety.

At higher concentrations of hydrogen peroxide analysis of the loss of peroxidase activity at a constant oxidant to protein ratio conformed to the kinetics expected for mechanism-based inhibition [16]. The calculated partition ratio ($r = 799$), the inactivation rate constant ($k_{in} = 3.9 \times 10^{-3}\ s^{-1}$) and the dissociation constant for hydrogen peroxide ($K' = 740\ \mu M$) suggest that at higher concen-

Table 4
Surface exposure [37] of methionines in human myeloperoxidase. In addition, the distance of the Cα atom of the respectives methionines to the heme iron is given.

Methionine		Molecular surface accessibility (Å^2)			Distance (Cα) to heme iron (Å)
Residue	Oxidized	Total	Backbone	Sidechain	
13	no	17.8993	0.5285	17.3707	26.6
85	yes	0.0000	0.0000	0.0000	14.7
87	yes	1.0485	0.1747	0.8737	10.3
175	no	0.1747	0.0000	0.1747	14.7
190	no	36.5191	9.6475	26.8715	33.1
243	no	0.1747	0.0000	0.1747	10.8
249	no	0.8047	0.1057	0.6990	15.3
287	yes	1.3979	0.0000	1.3979	22.6
306	yes	10.8340	0.1747	10.6593	23.0
343	yes	0.0000	0.0000	0.0000	15.7
353	no	14.6223	0.3495	14.2728	26.9
385	yes	0.0000	0.0000	0.0000	20.0
411	yes	15.8951	5.1581	10.7370	17.1
422	yes	0.0000	0.0000	0.0000	12.3
465	yes	11.4057	2.8131	8.5926	26.1
478	yes	0.0000	0.0000	0.0000	14.2
522	no	48.8422	2.6605	46.1817	37.4
553	no	31.7514	0.9147	30.8367	21.1

trations hydrogen peroxide acts as a very moderate suicide substrate for MPO. A turnover of 799 + 1 molecules of hydrogen peroxide per MPO is followed by irreversible inactivation of the enzyme under the conditions tested. Thus, the mechanism of inactivation under these conditions appears to be different from that at low concentrations of hydrogen peroxide.

Spectral analysis revealed that formation of Compound II was associated with minimal inactivation and heme loss. In contrast, there was extensive degradation of the heme groups and loss of activity when the concentration of hydrogen peroxide was sufficient to convert the enzyme to Compound III (Reaction 5). Previous work with lactoperoxidase suggested that its inactivation by hydrogen peroxide resulted from reaction of the oxidant with either Compound III or the ferrous enzyme to produce reactive oxygen species including singlet oxygen and hydroxyl radical [8,36]. The role of ferrous MPO is questionable since it rapidly binds O_2 or reacts with H_2O_2 forming Compound III or Compound II, respectively. In any case, we found that ten of its methionine residues were oxidized to methionine sulfoxide at high concentrations of hydrogen peroxide. Most of the oxidized methionine residues are located in the interior of the protein whereas the majority of the surface exposed methionine residues were not modified. This result suggests that radical production within the protein was responsible for oxidation of these residues as opposed to their direct reaction of hydrogen peroxide. The protection afforded by bromide and ascorbate can be explained by their ability to promote rapid consumption of hydrogen peroxide via Reactions 3a and 4a and prevent the conversion of Compound II to Compound III.

Although MPO has high thermal and conformational stability [19], the oxidative modification induced by hydrogen peroxide were able to disrupt the proteins structural integrity. This was reflected by loss of absorbance as well as ellipticity at the Soret maximum, which suggests that the heme was degraded. This was confirmed by demonstrating that high concentrations of hydrogen peroxide promote the release of heme iron. Degradation of the heme groups explains why the light polypeptide chains became detached from the heme and subsequently from the protein under SDS–PAGE conditions. These polypeptides are linked to the heme groups via an ester bond with Asp94. Presumably this or an adjacent bond must break when the heme is degraded by hydrogen peroxide. The free iron would also be expected to contribute to further protein damage because it is likely to catalyze site specific Fenton-type reactions with hydrogen peroxide.

Conclusion

We have identified two mechanisms by which hydrogen peroxide can inactivate MPO. The first involves formation of Compound I at low concentrations of hydrogen peroxide where, in the absence of a reducing substrate, the strong electrophilicity of this redox intermediate enables it to oxidize the heme group or protein moiety. Secondly, hydrogen peroxide is likely to react with Compound III to give rise to reactive oxidants that destroy the heme and oxidize the protein. Under normal physiological conditions, such that reducing substrates are always present and the concentration of hydrogen peroxide does not accumulate, these mechanisms of inactivation are unlikely to occur *in vivo*. However, it is within the confines of the neutrophil phagosomes where these mechanisms of inactivation are most likely to operate. The concentration of chloride inside phagosomes has been reported to be approximately 70 mM [38]. If this declines due to its oxidation to hypochlorous acid and the conversion to chloramines [39], then Compound I may be free to oxidize itself. Hydrogen peroxide may also accumulate sufficiently to react with Compound III, which is the predominant form of the enzyme in this compartment [39]. Hypochlorous acid could also contribute to inactivation of MPO within phagosomes after other more abundant targets are quenched. These mechanisms would be reliant on continued activity of the NADPH oxidase which is also susceptible to inactivation [40]. Inactivation via Compound I could be exploited in the search for pharmacological inhibitors of MPO. Inhibitors that bind tightly to the active site of MPO and prevent binding of reducing substrates would make the enzyme susceptible to inactivation by low concentrations of hydrogen peroxide.

Acknowlegements

This project was supported by the Austrian Science Foundation, FWF [FWF-Schroedinger Fellowship J2877-B11 and doctoral program BioToP – Biomolecular Technology of Proteins (FWF W1224)] and a grant from the Health Research Council of New Zealand.

References

[1] S.J. Klebanoff, A.J. Kettle, H. Rosen, C.C. Winterbourn, W.M. Nauseef, J. Leukoc. Biol. 93 (2013) 185–198.

[2] M.J. Davies, C.L. Hawkins, D.I. Pattison, M.D. Rees, Antioxid. Redox Signal. 10 (2008) 1199–1234.
[3] P.P. Bradley, R.D. Christensen, G. Rothstein, Blood 60 (1982) 618–622.
[4] S.W. Edwards, H.L. Nurcombe, C.A. Hart, Biochem. J. 245 (1987) 925–928.
[5] M.B. Arnao, M. Acosta, J.A. del Rio, F. Garcia-Canovas, Biochim. Biophys. Acta 1038 (1990) 85–89.
[6] M.B. Arnao, M. Acosta, J.A. del Rio, F. Garcia-Canovas, Biochim. Biophys. Acta 1041 (1990) 43–47.
[7] N.P. Hiner, J.N. Rodriguez-Lopez, M.B. Arnao, E. Raven, F. Garcia-Canovas, M. Acosta, Biochem. J. 348 (2000) 321–328.
[8] M. Huwiler, H. Jenzer, H. Kohler, Eur. J. Biochem. 158 (1986) 609–614.
[9] A.J. Kettle, C.A. Gedye, C.C. Winterbourn, Biochem. Pharmacol. 45 (1993) 2003–2010.
[10] F.J. Olorunniji, M.O. Iniaghe, J.O. Adebayo, S.O. Malomo, S.A. Adediran, Open Enzym. Inhib. J. 2 (2009) 28–35.
[11] P.G. Furtmüller, U. Burner, C. Obinger, Biochemistry 37 (1998) 17923–17930.
[12] R.F. Beers, I.W. Sizer, J. Biol. Chem. (1952) 133–140.
[13] C. Gay, J.M. Gebicki, Anal. Biochem. 284 (2000) 217–220.
[14] G. Cheng, J.C. Salerno, Z. Cao, P.J. Pagano, J.D. Lambeth, Free Radic. Biol. Med. 45 (2008) 1682–1694.
[15] P. Carter, Anal. Biochem. 40 (1971) 450–458.
[16] S.G. Waley, Biochem J. 227 (1985) 843–849.
[17] P.G. Furtmüller, M. Zederbauer, W. Jantschko, J. Helm, M. Bogner, C. Jakopitsch, C. Obinger, Arch. Biochem. Biophys. 445 (2006) 199–213.
[18] L.A. Marquez, H.B. Dunford, H. Van Wart, J. Biol. Chem. 265 (1990) 5666–5670.
[19] L.T. Taylor, J. Pohl, J.M. Kinkade, J. Biol. Chem. 267 (1992) 25282–25288.
[20] S. Banerjee, J. Stampler, P.G. Furtmüller, C. Obinger, Biochim. Biophys. Acta 1814 (2011) 375–387.
[21] T.J. Fiedler, C.A. Davey, J. Biol. Chem. 275 (2000) 11964–11971.
[22] X. Carpena, P. Vidossich, K. Schroettner, B.M. Calisto, S. Banerjee, J. Stampler, M. Soudi, P.G. Furtmüller, C. Rovira, I. Fita, C. Obinger, J. Biol. Chem. 284 (2009) 25929–25937.
[23] M. Zederbauer, P.G. Furtmüller, S. Brogioni, C. Jakopitsch, G. Smulevich, C. Obinger, Nat. Prod. Rep. 24 (2007) 571–584.
[24] G. Battistuzzi, J. Stampler, M. Bellei, J. Vlasits, M. Soudi, M. Sola, P.G. Furtmüller, C. Obinger, Biochemistry 50 (2011) 7987–7994.
[25] J. Arnhold, P.G. Furtmüller, C. Obinger, Redox Rep. 8 (2003) 179–186.
[26] P.G. Furtmüller, J. Arnhold, W. Jantschko, H. Pichler, C. Obinger, Biochem. Biophys. Res. Commun. 301 (2003) 551–557.
[27] J. Arnhold, P.G. Furtmüller, G. Regelsberger, C. Obinger, Eur. J. Biochem. 268 (2001) 5142–5148.
[28] P.G. Furtmüller, U. Burner, W. Jantschko, C. Obinger, FEBS Lett. 484 (2000) 139–143.
[29] W. Jantschko, P.G. Furtmüller, M. Allegra, M. Livrea, C. Jakopitsch, G. Regelsberger, C. Obinger, Arch. Biochem. Biophys. 398 (2002) 12–22.
[30] A.J. Kettle, R.F. Anderson, M. Hampton, C.C. Winterbourn, Biochemistry 46 (2007) 4888–4897.
[31] W. Jantschko, P.G. Furtmüller, M. Zederbauer, M. Lanz, C. Obinger, Biochem. Biophys. Res. Commun. 312 (2003) 292–298.
[32] A.J. Kettle, C.C. Winterbourn, Biochemistry 40 (2001) 10204–10212.
[33] P.G. Furtmüller, U. Burner, W. Jantschko, G. Regelsberger, C. Obinger, Redox Rep. 5 (2000) 171–176.
[34] C.C. Winterbourn, R. Garcia, A.W. Segal, Biochem. J. 228 (1985) 583–592.
[35] A.J. Kettle, D.F. Sangster, J. Gebicki, C.C. Winterbourn, Biochem. Biophys. Acta 956 (1988) 58–62.
[36] H. Jenzer, W. Jones, H. Kohler, J. Biol. Chem. 261 (1986) 15550–15556.
[37] G. Vriend, J. Mol. Graph. 8 (1990) 52–56.
[38] R.G. Painter, L. Marrero, G.A. Lombard, V.G. Valentine, W.M. Nauseef, G. Wang, J. Leukoc. Biol. 87 (2010) 933–942.
[39] C.C. Winterbourn, M.B. Hampton, J.H. Livesey, A.J. Kettle, J. Biol. Chem. 281 (2006) 39860–39869.
[40] W.M. Nauseef, Immunol. Rev. 219 (2007) 88–102.

APPENDIX II

Mechanism of reaction of chlorite with mammalian heme peroxidases

Christa Jakopitsch, Katharina F. Pirker, Jörg Flemmig, Stefan Hofbauer, Denise Schlorke, Paul G. Furtmüller, Jürgen Arnhold, Christian Obinger

Research Article

Journal of Inorganic Biochemistry (2014), 135, 10-19

Journal of Inorganic Biochemistry 135 (2014) 10–19

Contents lists available at ScienceDirect

Journal of Inorganic Biochemistry

journal homepage: www.elsevier.com/locate/jinorgbio

Mechanism of reaction of chlorite with mammalian heme peroxidases

Christa Jakopitsch [a], Katharina F. Pirker [a], Jörg Flemmig [b,c], Stefan Hofbauer [a], Denise Schlorke [b], Paul G. Furtmüller [a], Jürgen Arnhold [b,c], Christian Obinger [a,*]

[a] Department of Chemistry, Division of Biochemistry, BOKU — University of Natural Resources and Life Sciences, Muthgasse 18, A-1190 Vienna, Austria
[b] Institute for Medical Physics and Biophysics, Medical Faculty, University of Leipzig, Härtelstr 16-18, D-04107 Leipzig, Germany
[c] Translational Centre for Regenerative Medicine, University of Leipzig, Philipp-Rosenthal-Strasse 55, D-04103 Leipzig, Germany

ARTICLE INFO

Article history:
Received 12 December 2013
Received in revised form 19 February 2014
Accepted 19 February 2014
Available online 28 February 2014

Keywords:
Myeloperoxidase
Lactoperoxidase
Chlorite
Hypochlorous acid
Chlorine dioxide
Oxoferin

ABSTRACT

This study demonstrates that heme peroxidases from different superfamilies react differently with chlorite. In contrast to plant peroxidases, like horseradish peroxidase (HRP), the mammalian counterparts myeloperoxidase (MPO) and lactoperoxidase (LPO) are rapidly and irreversibly inactivated by chlorite in the micromolar concentration range. Chlorite acts as efficient one-electron donor for Compound I and Compound II of MPO and LPO and reacts with the corresponding ferric resting states in a biphasic manner. The first (rapid) phase is shown to correspond to the formation of a MPO-chlorite high-spin complex, whereas during the second (slower) phase degradation of the prosthetic group was observed. Cyanide, chloride and hydrogen peroxide can block or delay heme bleaching. In contrast to HRP, the MPO/chlorite system does not mediate chlorination of target molecules. Irreversible inactivation is shown to include heme degradation, iron release and decrease in thermal stability. Differences between mammalian peroxidases and HRP are discussed with respect to differences in active site architecture and heme modification.

1. Introduction

Chlorite ($^{-}$OClO) reacts with a variety of different heme containing enzymes. For example, it was shown to induce the formation of methemoglobin [1] and might act as hydroxylating agent in cytochrome P450 [2]. However, detailed mechanistic studies are only available for two classes of heme enzymes, namely chlorite dismutases and peroxidases. Chlorite dismutases are found in bacteria and archaea [3,4] and convert chlorite to chloride (Cl^{-}) and dioxygen (O_2) with hypochlorous acid (HOCl) as proposed reaction intermediate [5]. During this conversion a covalent O–O bond is formed, a reaction which was so far only observed at photosystem II of oxygenic phototrophic organisms.

Among heme peroxidases, chlorite was shown to be utilized by cytochrome *c* peroxidase [6], chloroperoxidase [7] and horseradish peroxidase (HRP) [8]. Upon reaction with chlorite the enzymes produced halogenating agents but not O_2. Detailed studies were carried out by Hager and co-workers on HRP [9–11]. Recently, by using sequential-mixing stopped-flow spectroscopy, we have reinvestigated this reaction and could demonstrate that HRP mixed with chlorite follows the whole peroxidase cycle [12]. Chlorite mediates the two-electron oxidation of ferric HRP [Fe(III)…Por] to Compound I [Fe(IV) = O…Por$^{\bullet+}$] thereby releasing hypochlorous acid (Reaction 1). Furthermore, chlorite acts as one-electron reductant of both Compound I and Compound II [Fe(IV) = O…Por] forming chlorine dioxide ($^{\bullet}ClO_2$) (Reactions 2 & 3). The HRP mediated reactions are strongly pH dependent, suggesting that chlorous acid (HOClO) is the reacting species [12]. In addition both reaction products also mediate the two-electron oxidation of ferric HRP to Compound I (Reaction 4 & 5) but cannot serve as electron donors for Compounds I or II.

$$[Fe(III)\ldots Por] + {}^{-}OClO \rightarrow \left[Fe(IV) = O\ldots Por^{\bullet+}\right] + HOCl/{}^{-}OCl, H^{+} \quad \text{(Reaction1)}$$

$$[Fe(IV) = O\ldots Por^{\bullet+}] + {}^{-}OClO \rightarrow [Fe(IV) = O\ldots Por] + {}^{\bullet}ClO_2 \quad \text{(Reaction2)}$$

$$[Fe(IV) = O\ldots Por] + {}^{-}OClO \rightarrow [Fe(III)\ldots Por] + {}^{\bullet}ClO_2 + H_2O \quad \text{(Reaction3)}$$

$$[Fe(III)\ldots Por] + HOCl \rightarrow \left[Fe(IV) = O\ldots Por^{\bullet+}\right] + Cl^{-} \quad \text{(Reaction4)}$$

$$[Fe(III)\ldots Por] + {}^{\bullet}ClO_2 \rightarrow [Fe(IV) = O\ldots Por^{\bullet+}] + {}^{\bullet}ClO. \quad \text{(Reaction5)}$$

In this work we have extended this study to human myeloperoxidase (MPO) and bovine lactoperoxidase (LPO). The fact that MPO is involved in the regulation of immune functions [13] and that commercially

* Corresponding author. Tel.: +43 1 47654 6073; fax: +43 1 47654 6059.
E-mail address: christian.obinger@boku.ac.at (C. Obinger).

http://dx.doi.org/10.1016/j.jinorgbio.2014.02.010

available wound healing and immunomodulatory drug solutions like Oxoferin and WF10 contain chlorite as the active principle [14], prompted us to this study.

In contrast to plant-type peroxidases the heme in MPO is covalently attached to the protein via two ester-linkages and a sulfonium ion linkage [15]. These posttranslational modifications significantly modify the spectral and redox properties of this oxidoreductase, e.g. allowing MPO to oxidize chloride to hypochlorous acid that acts as antimicrobial agent in the innate immune system [16]. Additionally, the covalent heme to protein bonds were proposed to protect the heme of MPO from its highly reactive reaction products [17].

Here we demonstrate that – in contrast to horseradish peroxidase (HRP) – human MPO and bovine LPO cannot utilize chlorite to form chlorinating species [6]. Moreover, we show that both peroxidases are very susceptible to chlorite resulting in fast loss of activity accompanied by (almost) complete heme bleaching. We report the first comprehensive study of the reactions of all biological relevant redox intermediates (ferric state, Compounds I & II) of MPO and LPO with chlorite and their potential reaction products. We propose a mechanism of interaction between chlorite and the metalloproteins, discuss the observed differences with plant-type peroxidases as well as the biological relevance of our findings.

2. Material and methods

2.1. Reagents

Standard chemicals and biochemicals were obtained from Sigma-Aldrich Handels GmbH (Vienna, Austria) at the highest grade available. Hydrogen peroxide concentration was determined spectrophotometrically using an extinction coefficient at 240 nm of 39.4 M^{-1} cm^{-1} [18]. The concentration of sodium chlorite (Sigma, 80%) and hypochlorite were determined using the extinction coefficient at 260 nm of 154 M^{-1} cm^{-1} [19] and at 292 nm of 350 M^{-1} cm^{-1} [20], respectively. Highly purified dimeric leukocyte myeloperoxidase of a purity index (A_{428}/A_{280}) of at least 0.85 was purchased as lyophilized powder from Planta Natural Products (http://www.planta.at) and the concentration was determined spectrophotometrically using ε_{428} = 91 000 M^{-1} cm^{-1} per heme [21]. Lactoperoxidase from bovine milk was purchased as a lyophilized powder (Sigma, purity index A_{412}/A_{280} = 0.9). Enzyme concentration was determined by using the extinction coefficient 112,000 M^{-1} cm^{-1} at 412 nm [22]. Horseradish peroxidase type VIa was obtained from Sigma and used without further purification. An extinction coefficient at 403 nm of 102,000 M^{-1} cm^{-1} [23] was used for the determination of protein concentration. Oxovasin was obtained from NUVO Manufacturing GmbH (Wanzleben, Germany). Essentially the same drug is also marketed as Oxoferin™, a term more frequently used in a scientific context, therefore we will also refer to Oxoferin instead of Oxovasin in this study.

2.2. Preparation of chlorine dioxide

Chemically pure, chlorine free chlorine dioxide ($^{\bullet}ClO_2$) solutions were prepared by acidification of sodium chlorite (NaOClO) with sulfuric acid (H_2SO_4) according to $4\,NaOClO + 2\,H_2SO_4 \rightarrow 2\,^{\bullet}ClO_2 + HCl + HOClO_2 + 2\,Na_2SO_4 + H_2O$ [12]. In detail, 100 mL sodium chlorite (2.5% $^{w}/_{w}$) was acidified with 10 mL sulfuric acid (10% $^{v}/_{v}$). Sulfuric acid was added in 1 mL portions with 5 min intervals. Formed gaseous $^{\bullet}ClO_2$ was removed from the reaction flask by a nitrogen flow, purified by bubbling through a gas scrubbing tower containing 100 mL sodium chlorite solution (2.5% $^{w}/_{w}$) and, finally, recovered by absorbing in 100 mL chilled deionized water in an amber reagent bottle. The concentration of $^{\bullet}ClO_2$ was determined using an extinction coefficient at 359 nm of 1230 M^{-1} cm^{-1} [24]. The obtained stock solution (≈42 mM) was immediately aliquoted in Eppendorf tubes and stored in the dark at −30 °C. After thawing the stock solution was kept in the dark on ice and was stable for about 4 h. More diluted solutions were prepared immediately before use and the concentrations were determined simultaneously to the measurements.

2.3. In gel activity staining

For in-gel heme staining MPO samples (10 μg) were separated using SDS-PAGE electrophoresis under non-reducing conditions. Gels were incubated with a mixture of 6.3 mM 3,3,5,5,-tetramethylbenzidine (TMB) in methanol (3 parts) and 0.25 M sodium acetate at pH 5.0 (7 parts) for 1 h in the dark. Activity staining was started by adding hydrogen peroxide at a final concentration of 30 mM [25].

2.4. Activity assays

Monochlorodimedon (MCD) is a substrate often used to study halogenation reactions. Upon chlorination to dichlorodimedon (DCD) it loses its absorbance at 290 nm [26]. Monochlorodimedon (100 μM) and various amounts of chlorite were dissolved in 100 mM phosphate buffer, pH 5.0, and the reaction was started by addition of MPO or LPO.

For the determination of the inhibitory effect of chlorite on the chlorination activity of MPO assays contained additional hydrogen peroxide (100 μM) and chloride (100 mM). In this case the reaction was started either with MPO (100 nM) or hydrogen peroxide. The latter case resulted in a preincubation of MPO with both chloride and chlorite for 1 min.

Additionally, the inhibitory effect of chlorite on the chlorination activity was measured by continuously monitoring hydrogen peroxide concentration polarographically with a platinum electrode covered with a hydrophilic membrane and fitted to the Amperometric Biosensor Detector 3001 (Universal Sensors, Inc., U.S.A.). Again the reaction was started by adding either MPO (100 nM) or hydrogen peroxide (100 μM) after one minute. All reactions were performed at 25 °C.

As a further method to study the inhibitory effect of chlorite on MPO we used aminophenyl fluorescein (APF) which specifically detects the halogenating enzyme activity [27]. Briefly, 10 nM MPO was preincubated with 0–500 μM chlorite in phosphate buffered saline (PBS), pH 7.4, at 37 °C for 1 min. All samples also contained 10 μM APF. The enzymatic activity was started by adding 25 μM H_2O_2 via an injector device. The HOCl-derived oxidation of APF was followed for 30 min at 37 °C by measuring the fluorescence intensity at 522 nm (excitation at 488 nm). All measurements were performed in a fluorescence microplate reader Tecan Infinite 200 PRO, Switzerland.

2.5. Circular dichroism and electron paramagnetic resonance spectroscopy

Circular dichroism spectra (CD) were recorded using a Chirascan CD spectrophotometer (Applied Photophysics, UK). In the far-UV region an enzyme concentration of 2 μM and a cuvette with a path length of 1 mm was used. For measurements in the Soret region (300 nm–500 nm) the enzyme concentration was 5 μM and the path length of the cuvette was 1 cm.

Samples for electron paramagnetic resonance (EPR) measurements were prepared using 100 μM MPO in 100 mM phosphate buffer, pH 5. After addition of chlorite in 5- and 10-fold excess, respectively, 5% glycerol was added as cryoprotectant and 100 μL of the reaction solution were immediately transferred into a quartz EPR tube (4 mm OD) and frozen in liquid nitrogen. Before measurement, the tube was degassed with Ar while the sample was kept frozen on dry ice.

EPR measurements were carried out at 10 K on an EMX continuous wave (cw) spectrometer (Bruker, Germany), operating at X-band (9 GHz) frequencies, equipped with a high sensitivity resonator and a helium cryostat from Oxford Instruments (ESR900). EPR spectra were recorded under non-saturating conditions using 2 mW microwave power, 100 kHz modulation frequency, 1 mT modulation amplitude, 20 ms conversion time and 20 ms time constant and 4096 data points. Simulations of high-spin Fe(III) spectra were carried out using the

software EasySpin [28] and consist of a weighted sum of simulations of the individual high-spin intermediates.

2.6. Transient state kinetics

Transient-state measurements were made using the SX.18 MV stopped-flow spectrophotometer and PiStar-180 circular dichroism spectrometer (Applied Photophysics, UK) equipped with a 1 cm observation cell. Calculation of pseudo first-order rate constants (k_{obs}) from experimental time traces was performed with a SpectraKinetic work station (Version 4.38) interfaced to the instruments. Second-order rate constants were calculated from the slope of the linear plot of the pseudo first-order rate constants versus substrate concentration. To follow spectral transitions, a Model PD.1 photodiode array accessory (Applied Photophysics, UK) connected to the stopped-flow machine together with XScan diode array scanning software (Version 1.07) was utilized.

2.7. Differential scanning calorimetry

Differential scanning calorimetric (DSC) measurements were performed using a VP-capillary DSC microcalorimeter from Microcal (cell volume: 137 μL), controlled by the VP-viewer program and equipped with an autosampler for 96 well plates. Samples were analyzed using a programmed heating scan rate of 60 °C h^{-1} over a temperature range of 20 °C to 110 °C and a cell pressure of approximately 60 psi (4.136 bar). Collected DSC data were corrected for buffer baseline and normalized for protein concentration. The reaction conditions were: 5 μM MPO in 100 mM phosphate buffer pH 5.0 in the absence or presence of 25 μM chlorite and different incubation times. Reactions were stopped by addition of 4 mM cysteine. Guanidinium hydrochloride (GdnHCl; 5 mM) was added before measurements were started to avoid non-specific protein aggregation at increasing temperatures.

Microcal origin software was used for data analysis. Heat capacity (C_p) was expressed in kcal mol^{-1} K^{-1} (1 cal = 4.184 J). Data points were fitted to non-two-state equilibrium-unfolding models by the Lavenberg/Marquardt (LM) non-linear least square method.

3. Results

The plant-type model peroxidase HRP is able to use chlorite instead of hydrogen peroxide as two-electron oxidant of the ferric state, thereby forming Compound I and hypochlorous acid [12], which is known to chlorinate various target molecules like MCD. In contrast, as already observed by George [6], no chlorinating species could be detected in the reaction between MPO with chlorite. Upon re-evaluation of this reaction we could confirm that the system MPO/chlorite is unable to chlorinate MCD (not shown). This significant discrepancy between plant-type peroxidases and their mammalian counterparts prompted us to perform a more comprehensive study on (i) the interaction of chlorite with all relevant redox intermediates of MPO and LPO as well as on (ii) the impact of chlorite on their structural integrity.

3.1. Reaction of ferric MPO and LPO with chlorite

Upon reaction of chlorite with ferric MPO the heme absorbance in the Soret region rapidly decreased. Fig. 1A and B depict the spectral changes upon addition of 200 μM chlorite to 2 μM ferric MPO at pH 5.0. The reaction was biphasic (inset to Fig. 1A), with the first rapid phase (Fig. 1A) leading directly (isosbestic points at 445 nm, 490 nm, 595 nm and 660 nm) to an intermediate state within 60 ms. This state (gray spectrum in Fig. 1A) exhibited a decreased absorbance at the Soret maximum as well as a shoulder around 455 nm (isosbestic point at 445 nm), which was more pronounced at higher chlorite concentrations. Concomitant spectral changes at higher wavelengths in the visible region included absorbance decrease at 570 nm and increase at 625 nm

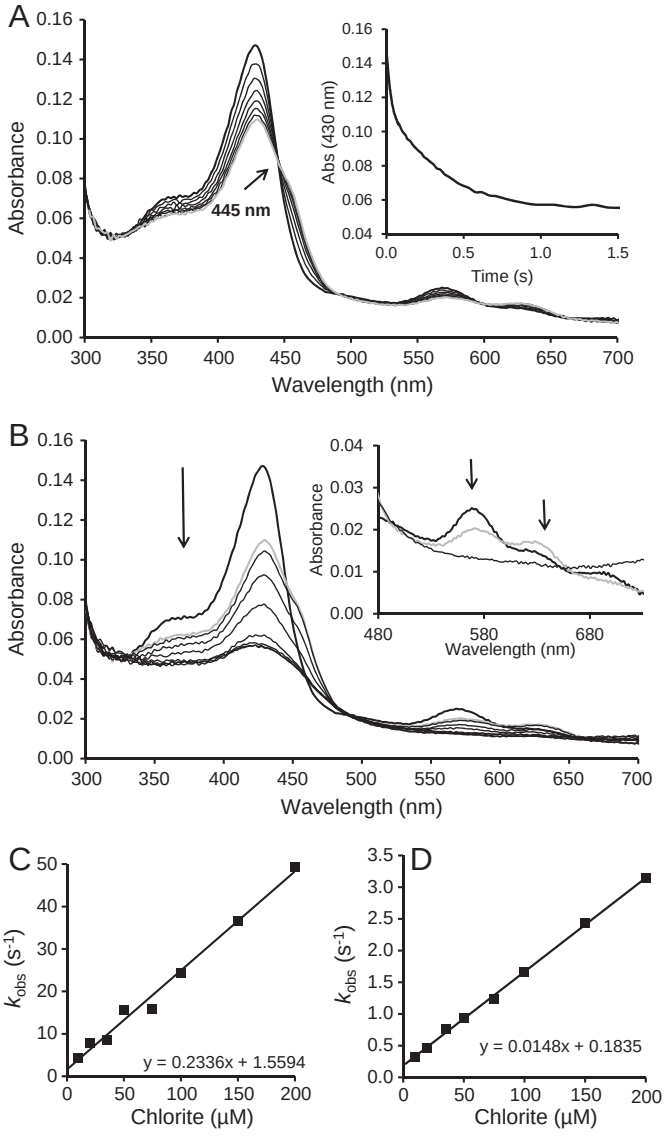

Fig. 1. Reaction of ferric MPO with chlorite. Assay: 2 μM MPO with 200 μM chlorite in 100 mM phosphate buffer, pH 5.0. (A) Spectral changes observed within the first 60 ms. Black spectrum, ferric MPO; and gray spectrum, intermediate observed after 60 ms. The inset shows the corresponding biphasic time trace at the Soret maximum for the first 1.5 s. (B) Continuation of reaction in (A). Gray spectrum corresponds to gray spectrum in (A). Subsequent spectra (black) were taken at 80 ms, 170 ms, 350 ms, 710 ms, 1.5 s and 10 s, respectively. For orientation the spectral features of ferric MPO (bold black) are included. (C) Plot of the pseudo-first-order rate constants against chlorite concentration for the fast phase of the reactions. (D) Plot of the pseudo first-order rate constants against chlorite concentration for the second slower phase.

(isosbestic points at 492 and 593 nm). The second and slower phase (Fig. 1B) was characterized by a continuous loss of absorbance in the whole spectral region between 300 and 650 nm.

Upon fitting of this biphasic reaction by using a double exponential equation apparent bimolecular rate constants were calculated. Both phases were dependent on the concentration of chlorite. Fig. 1C and D show the resulting plots of the respective pseudo-first order rate constants against substrate concentration yielding second order rate constants of 2.3×10^5 M^{-1} s^{-1} (fast reaction) and 1.5×10^4 M^{-1} s^{-1} (slow reaction) at pH 5.0. Both reactions strongly depended on the pH. The second-order rate constants at pH 4.0 were roughly one order of magnitude higher compared to pH 5.0 (1.5×10^6 M^{-1} s^{-1} and 8.4×10^4 M^{-1} s^{-1}), whereas at pH 7.0 rate constants of 4.6×10^4 M^{-1} s^{-1} and 3.1×10^3 M^{-1} s^{-1}, respectively, were obtained.

Fig. 2A shows an overlay of the spectrum of 1 μM ferric MPO at pH 5 (black line) and the final absorbance spectrum after reaction with 50 μM chlorite (gray line). Heme bleaching at the Soret band was accompanied by a substantial increase in absorbance in the region between 650 and 850 nm and the appearance of maxima at 700 nm and 754 nm (inset to Fig. 2A). To our knowledge these spectral features have never been reported so far for MPO and most probably indicate heme destruction and the formation of an inactive form similar to the P670 species in HRP [29]. Fig. 2B shows a typical time trace of the reaction of 2 μM MPO with 1 mM chlorite at pH 5.0 followed at 720 nm. The reaction was monophasic and could be fitted using a single exponential equation and the plot of the pseudo-first order rate constants against chlorite concentration yielded a straight line (Fig. 2C). From the slope an apparent second order rate constant of 4.8×10^3 M^{-1} s^{-1} could be calculated. Again this reaction was pH dependent with 9.1×10^4 M^{-1} s^{-1} and 1.5×10^3 M^{-1} s^{-1} at pH 4.0 and 7.0, respectively. These rate constants were similar to those obtained for the slow phase of the biphasic reaction depicted in Fig. 1 and might reflect modification and destruction of the prosthetic group.

In order to probe the nature of the initial binding complex (the transition with clear isosbestic points, Fig. 1A) between ferric MPO and chlorite, EPR spectroscopy was performed. Fig. 3A shows the spectrum of 100 μM ferric MPO in 100 mM phosphate buffer, pH 5.0, reflecting a predominantly rhombically distorted high-spin form with some small contributions of less rhombicity. Similar spectra were recorded previously [30]. Already upon preincubation of MPO with a very low excess of chlorite (5-times stoichiometric excess) the rhombicity significantly changed, indicating a rearrangement around the heme center towards axial symmetry (Fig. 3B). Since formation of a low-spin species was not detected, chlorite seemed to act as high-spin ligand. This became

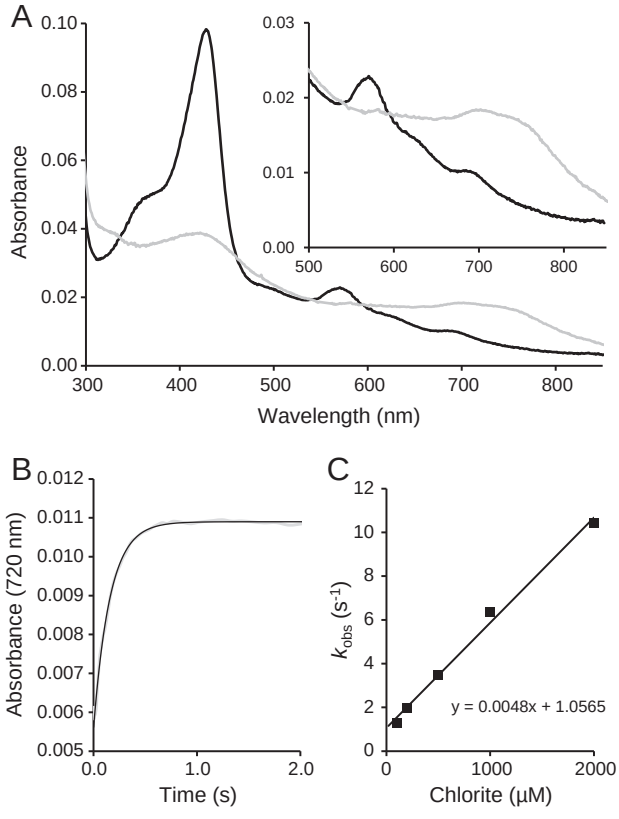

Fig. 2. Kinetics of heme degradation. (A) Comparison of spectral features of 1 μM ferric MPO (black) with the spectral features obtained upon reaction of 1 μM MPO with 50 μM chlorite (gray) at pH 5.0. (B) Time trace at 720 nm and single exponential fit for the reaction of 2 μM MPO with 1 mM chlorite at pH 5.0. (C) Plot of the obtained pseudo-first-order rate constants against chlorite concentration.

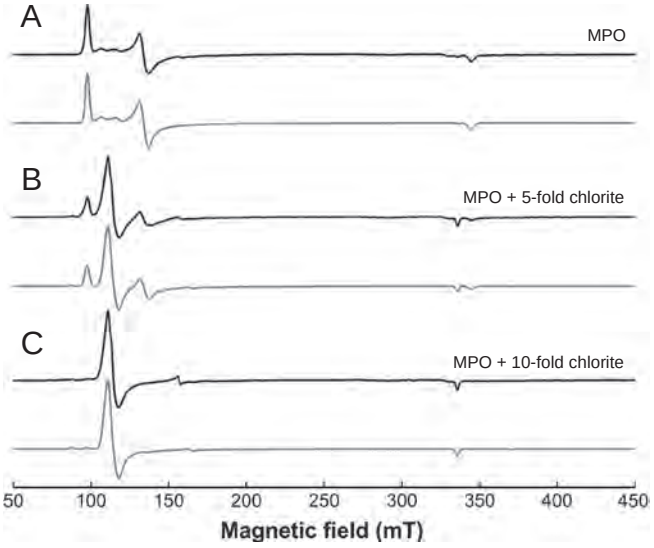

Fig. 3. EPR analysis of the interaction of MPO with chlorite. Experimental cw EPR spectra (black) and simulation (gray) of (A) 100 μM ferric MPO in 100 mM phosphate buffer, pH 5.0, (B) 100 μM MPO after addition of 5-fold chlorite and (C) 100 μM MPO after addition of 10-fold chlorite. The spectra were recorded at 10 K and the samples contained 5% glycerol.

further evident by preincubation of MPO with a higher (10-fold) excess of chlorite (Fig. 3C). Here, the rhombically distorted high-spin forms disappeared almost completely leading to a predominantly axial signal. Table 1 shows the simulation parameters of the individual high-spin forms as well as their rhombicity and intensity fraction based on the simulation. Again, a low-spin species could not be detected. Moreover, with increasing chlorite concentrations the intensity at $g = 4.3$ increased slightly (compare Fig. 3A and C) reflecting the release of non-heme Fe(III).

Next we tested another member of the vertebrate peroxidase subfamily [31], namely bovine LPO, in its interaction with chlorite. Lactoperoxidase was also unable to utilize chlorite in MCD chlorination (data not shown) and was even faster inactivated by chlorite than MPO. The reaction between LPO and chlorite was again biphasic (Supplemental Fig. 1). Upon mixing of 1 μM ferric LPO with 100 μM chlorite at pH 5.0, a rapid spectral transition occurred within the first 20 ms (isosbestic point at 425 nm), resulting in a decrease in absorbance of the Soret band which was accompanied by a small red shift of the Soret maximum (Supplemental Fig. 1A). This fast transition was followed by a slower reaction leading to a further loss of absorbance in the Soret region within 400 ms (Supplemental Fig. 1B). Interestingly, and in contrast to MPO, this second transition showed an isosbestic point at 448 nm before heme bleaching occurred. The loss of absorbance at the Soret maximum and the charge transfer bands during heme

Table 1
EPR simulation parameters from individual high spin forms of MPO with chlorite (HS — high-spin, R — rhombicity, I — relative intensity, E/D — rhombic to axial contribution).

	HS compounds*	g_x^{eff}	g_y^{eff}	g_z^{eff}	E/D	R (%)	I (%)
Ferric MPO	HS1	5.000	6.660	1.945	0.040	12	94
	HS2	5.700	6.300	1.995	0.013	4	6
Ferric MPO +	HS1	4.100	7.650	1.945	0.079	22	4
5-fold chlorite	HS2	5.000	6.880	1.945	0.040	12	50
	HS3	5.750	6.200	1.998	0.006	3	45
	HS4	5.890	6.050	1.998	0.003	1	2
Ferric MPO +	HS1	4.100	7.650	1.945	0.079	22	8
10-fold chlorite	HS2	5.000	6.880	1.945	0.040	12	5
	HS3	5.750	6.200	1.998	0.006	3	84
	HS4	5.890	6.050	1.998	0.003	1	4

* Minimum number of high-spin compounds used for simulation.

bleaching was accompanied by a broad increase of absorbance in the range of 600–850 nm with two clear peaks with maxima at 650 nm and 730 nm (Supplemental Fig. 1E).

Analysis of the time traces at 412 nm and double exponential fitting yielded bimolecular rate constants of 2×10^6 M^{-1} s^{-1} (fast transition) and 7.7×10^4 M^{-1} s^{-1} (slower transition) at pH 5.0 (Supplemental Fig. 1C & D). Both rates were significantly faster compared to MPO. Again this reaction was pH dependent. At pH 7.0 both rate constants were about one order of magnitude lower (1.1×10^5 M^{-1} s^{-1} and 4×10^3 M^{-1} s^{-1}, respectively).

3.2. Influence of cyanide and chloride on heme bleaching mediated by chlorite

Cyanide is known to bind directly to the Fe(III) center of heme peroxidases [32]. Ferric MPO (2 μM) was incubated with 10 mM cyanide resulting in the formation of a low-spin complex, characterized by a red shift of the Soret band of MPO to 455 nm and formation of a prominent peak at 635 nm (black spectrum in Fig. 4A). Upon addition of chlorite to the cyanide complex of MPO no spectral changes were observed even at high chlorite concentrations and prolonged measurements (Fig. 4A, gray trace, final concentration 500 μM chlorite). No heme bleaching was observed. This suggests that the presence of cyanide hampers the attack of the heme iron and/or the prosthetic group by chlorite.

Since chloride acts both as high-spin ligand and substrate of MPO [33], we have also probed the effect of chlorite on the MPO-Cl^- complex. At pH 5.0 the spectrum of the latter shows a Soret maximum at 435 nm and a Q-band at 574 nm. Myeloperoxidase was incubated with 100 mM chloride at pH 5.0 before chlorite was added. Fig. 4B shows the spectral changes of the reaction between 2 μM MPO-chloride complex and 200 μM chlorite. In contrast to cyanide the presence of chloride did not protect MPO from heme bleaching. However, compared to native MPO clear differences were observed. The reaction was slower and monophasic (Fig. 4C). The absence of a shoulder at 455 nm as well as of an absorbance increase at 625 nm (compared to Fig. 1A) suggests that the presence of chloride had an influence on the velocity of the formation of the (high-spin) MPO-chlorite complex but not on the final heme degradation. The presence of chloride did slow down binding of chlorite and the reaction lost its biphasic behavior. Heme bleaching was still evident from the observed increase of absorbance in the long wavelength range (600–850 nm). This hypothesis is underlined by the fact that the rate constant of absorbance loss at 430 nm of 2.5×10^3 M^{-1} s^{-1} (Fig. 4D) corresponded well to the rate of absorbance increase at 720 nm, i.e. 4.8×10^3 M^{-1} s^{-1} (see also Fig. 2C).

For HRP we could demonstrate, that chlorine dioxide (besides chlorite) mediates Compound I formation [12]. By contrast, neither ferric MPO nor ferric LPO reacted with chlorine dioxide at pH 5.0 and 7.0. No heme bleaching was observed and the spectral features of both enzymes remained unchanged (data not shown).

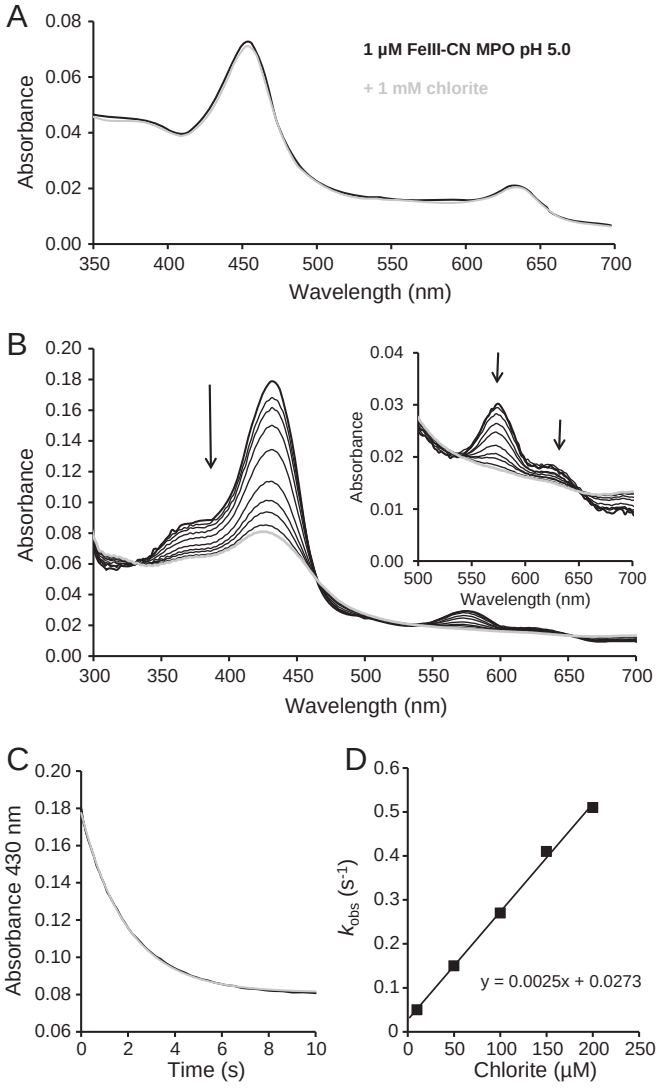

Fig. 4. Impact of ligands on the interaction of MPO and chlorite. (A) 2 μM ferric MPO was preincubated with 10 mM cyanide prior to mixing with 500 μM chlorite (final enzyme concentration 1 μM) at pH 5.0. First spectrum collected after 1.3 ms (black) corresponds to the low-spin complex of MPO. Even 10 s after mixing with chlorite no changes in the spectral features were detected (gray spectrum). (B) 4 μM ferric MPO at pH 5.0 was pre-incubated with 100 mM chloride prior to mixing with 200 μM chlorite (final enzyme concentration 2 μM) at pH 5.0. First spectrum was taken after 5 ms (bold), subsequent spectra at 163 ms, 317 ms, 592 ms, 1.1 s, 2.1 s, 3.1 s, 4.1 s, 6.2 s and 10 s (gray spectrum). The inset shows an enlargement of the visible region from 500 to 700 nm for the same reaction. (C) Time trace at 430 nm (black) including single-exponential fit (gray) for the reaction in (B). (D) Plot of pseudo-first-order rate constants versus chlorite concentration.

3.3. Reactions of Compound I and Compound II of MPO and LPO with chlorite

In the next step the reaction of preformed MPO Compound I with chlorite was investigated by multi-mixing stopped-flow spectroscopy. In contrast to ferric MPO, Compound I reacted very fast with chlorite forming Compound II, which was further converted back to ferric MPO (Fig. 5). Fig. 5A depicts the spectral changes of the reaction between 2 μM MPO Compound I and 20 μM chlorite at pH 5.0. Compound II was formed rapidly (Soret maximum at 455 nm and a dominant peak at 625 nm). The first recorded spectrum 1.3 ms after mixing (black bold spectrum) already showed a significant amount of Compound II and the reaction was completed within 15 ms (gray spectrum). From the monophasic time traces at 455 nm a bimolecular rate constant of 1.2×10^7 M^{-1} s^{-1} was calculated (Fig. 5B and C). The rate decreased with increasing pH, i.e. 1.7×10^6 M^{-1} s^{-1} at pH 7.0.

Compound II was not stable but reacted back to ferric MPO dependent on the chlorite concentration (Fig. 5D is a continuation of Fig. 5A) within 700 ms (isosbestic points at 441 nm, 490 nm, 585 nm and 670 nm). Exact determination of the bimolecular rate constant was not possible due to the fact that excess of chlorite immediately reacted with any formed ferric enzyme resulting in heme bleaching. Estimated values for Compound II reduction were 1.4×10^5 M^{-1} s^{-1} at pH 5.0 and 3×10^4 M^{-1} s^{-1} at pH 7.0, respectively.

Similarly, Compounds I and II of LPO were probed in their reactivity with chlorite. Clear monophasic transitions (without heme bleaching during these distinct redox transformations) were observed. Supplemental Fig. 2A shows the reaction between 2 μM Compound I and 5 μM chlorite to Compound II (Soret maximum at 428 nm and two peaks at 536 nm and 566 nm) at pH 7.0. The bimolecular rate constant was calculated to be 5.8×10^6 M^{-1} s^{-1} at pH 7.0. The spectral features obtained in these reactions did not resemble a pure Compound II but did

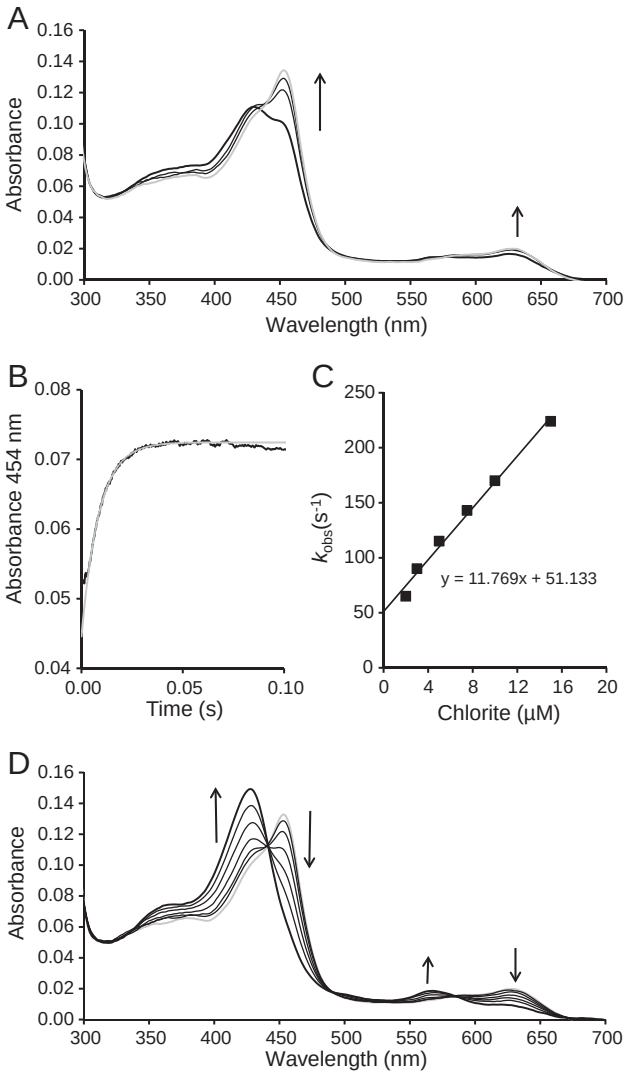

Fig. 5. Reactions of MPO Compounds I and II with chlorite. (A) 2 μM MPO Compound I was pre-formed with a 10-fold excess of hydrogen peroxide (pH 5.0) and – after a delay time of 20 ms – chlorite at a concentration of 20 μM was added. First spectrum (bold) was taken at 1.3 ms, subsequent spectra at 4 ms, 6 ms and 15 ms (gray spectrum). (B) Plot of pseudo-first-order rate constants for Compound I reduction versus chlorite concentrations. (C) Time trace at 454 nm and single-exponential fit for the reaction of 1 μM MPO Compound I with 5 μM chlorite. (D) Continuation of reaction in (A) showing the reduction of Compound II by chlorite. Gray spectrum corresponds to Compound II (15 ms, as in A) and subsequent spectra were taken at 100 ms, 200 ms, 300 ms, 500 ms and 700 ms (black bold spectrum).

already contain a shoulder caused by the formation of ferric LPO due to the reaction of Compound II with chlorite.

Finally, Compound II of LPO (pre-formed by mixing of 8 μM LPO with 12 μM hydrogen peroxide and 40 μM tryptophan in the aging loop and setting a delay time of 2 s) [34] was directly converted to ferric LPO by chlorite with a rate constant of 4.4×10^4 M^{-1} s^{-1} at pH 7.0 (Supplemental Fig. 2B). However, as already observed with MPO, ferric LPO was not formed completely as it reacted immediately with excess chlorite leading to heme destruction.

3.4. Impact of chlorite on the overall halogenation activity of MPO

As mentioned at the beginning, the system of MPO/chlorite (in contrast to HRP/chlorite) was not able to promote monochlorodimedon chlorination, suggesting that hypochlorous acid was not formed or at least could not leave the heme cavity or immediately reacted with the heme or neighboring amino acids of the protein. Hypochlorous acid is well known to mediate Compound I formation of MPO [35] as well as to promote degradation of the heme group [36]. Thus, in order to exclude a role of HOCl in the observed heme bleaching reaction mediated by chlorite, we have probed the impact of 10 mM methionine on the inactivation process. Methionine is small enough to enter the substrate channel and it reacts very fast with HOCl [37]. However, with both MPO and LPO, the presence of methionine did not prevent heme bleaching (data not shown). Similarly addition of taurine, another very efficient trap for hypochlorous acid, showed no effect on the spectral transitions.

Next, the inhibitory effect of chlorite on the chlorination activity of MPO was determined. At pH 5.0 the effect was investigated both spectrophotometrically (monitoring the chlorination of MCD to DCD at 290 nm) and polarographically (monitoring consumption of hydrogen peroxide).

In order to exclude a possible impact of MCD as potential one-electron substrate for MPO Compounds I and II on the reaction, the effect of chlorite was in addition determined fluorimetrically (monitoring the chlorination of APF at pH 7.4). The reactions were started by addition of either MPO or hydrogen peroxide, in the latter case MPO was preincubated with chlorite for 1 min.

Independent of the method used the inhibitory effect was stronger when MPO was preincubated with chlorite and the reaction was started with hydrogen peroxide. A concentration of ~15 μM of chlorite resulted in a loss of 50% activity (Fig. 6A & B) when MPO was preincubated with chlorite. When the reaction was started with native MPO much higher concentrations of chlorite (40–50 μM) were necessary to obtain 50% inhibition (Fig. 6C & D). These observations underline that only MPO in its ferric state is susceptible to degradation by chlorite. Similar to high-spin (chloride) or low-spin (cyanide) ligands the substrate hydrogen peroxide binds to the sixth heme position and protects or at least delays inactivation by chlorite.

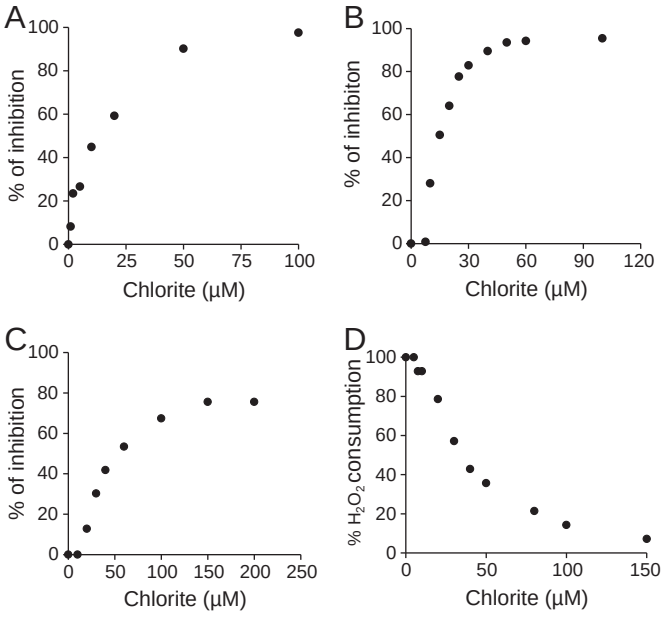

Fig. 6. Inhibition of chlorination activity of MPO by chlorite. Activity was monitored either by APF chlorination fluorimetrically (A), monochlorodimedon (MCD) chlorination spectrophotometrically (B, C) or by monitoring hydrogen peroxide consumption polarographically (D). In (A) and (B) MPO was incubated with various concentrations of chlorite for one minute and the reaction was started by adding hydrogen peroxide. In (C) and (D) the reaction was started by adding native MPO to the reaction mixture. For detailed reaction conditions see Material and methods.

3.5. Effect of chlorite on the structural integrity of MPO

Chlorite-mediated heme destruction could readily be detected by in-gel activity heme staining after samples were run on a non-reducing SDS-PAGE. Human MPO (10 μg) was mixed with increasing concentrations of chlorite (Fig. 7A; lane 2–5: 0, 50, 200 and 500 μM chlorite, respectively) at pH 5.0 and loaded on the gel followed by activity staining. Addition of chlorite decreased the color development in a concentration dependent manner (Fig. 7A), proofing the loss of active heme.

On a separate gel the same amount of MPO and chlorite were run on a non-reducing SDS-PAGE and stained by Coomassie (Fig. 7B). Myeloperoxidase predominantly ran as a dimer (lane 2) but upon mixing with chlorite a second protein band at ~14 kDa appeared, which corresponds to the light chain of MPO. The more chlorite was added to MPO, the more pronounced was this band (Fig. 7B; lanes 3–5). Additionally, diffuse protein bands with high molar masses were formed (lane 5), indicating either protein aggregation or crosslinked multimeric states of MPO.

For comparison, Fig. 7C depicts the SDS-PAGE of the same sample preparations under reducing conditions [50 mM dithiothreitol (DTT) was added to the samples]. Here, two prominent bands of MPO appeared, corresponding to its heavy (60 kDa) and light chains (14 kDa). No differences between untreated and chlorite-treated samples were detected indicating that the chlorite dependent decrease in heme activity staining was not due to loss of protein.

To further evaluate the effect of chlorite on the secondary structure composition of MPO CD spectroscopy in the far-UV region was performed. Fig. 8A shows identical CD spectra of 2 μM native MPO (pH 5.0) and 2 μM MPO after treatment with 1 mM chlorite at 25 °C. The CD spectra consisted of two minima at 208 and 222 nm, which are typical for a mainly α-helical structure. Even upon longer incubations of MPO with this huge excess of chlorite (500-times) only a very slight loss of ellipticity was observed. Obviously, chlorite did not have any impact on the overall secondary structure composition of MPO at room temperature.

Next we investigated the effect of chlorite on the heme ellipticity in the Soret region at room temperature. Ferric MPO showed a negative ellipticity with a minimum around 412 nm in the Soret region (Fig. 8B, black line). Upon binding of moderate (20-times) excess of chlorite the signal changed dramatically resulting in alteration of the sign of ellipticity (Fig. 8B, gray line). This indicates that (i) the heme was still attached to MPO under these conditions (free heme does not show an CD signal) and (ii) that upon chlorite binding the interaction of the prosthetic group and its (asymmetric) protein environment was significantly modified [38]. By contrast, simultaneous measurements of the Soret maximum at 430 nm by UV–vis spectroscopy showed an almost complete loss of absorbance in this region (Fig. 8C).

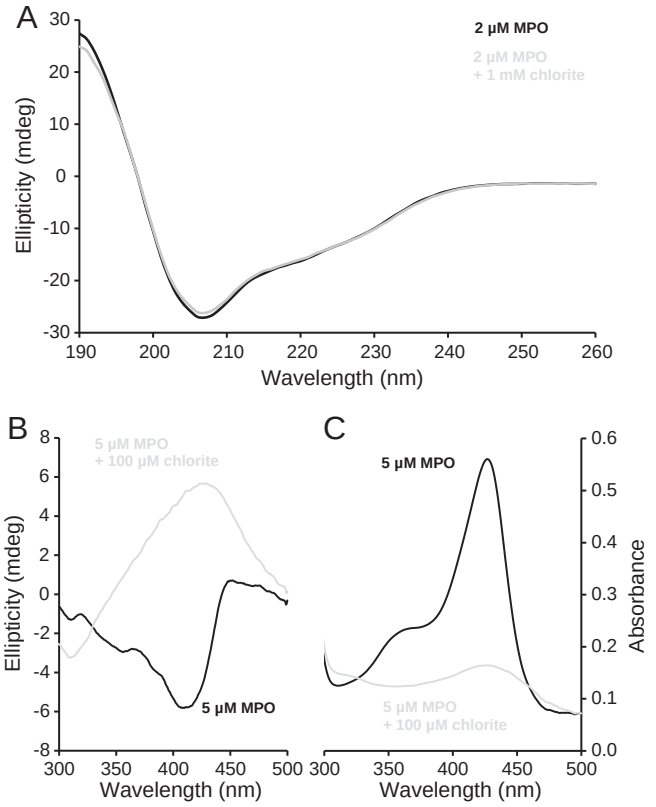

Fig. 8. Circular dichroism analysis. (A) Far-UV CD spectra of native MPO (black) MPO incubated with chlorite (gray) at pH 5.0. Protein concentration: 2 μM; and chlorite concentration: 1 mM. Path length: 1 mm. (B) CD spectra in the Soret region of native MPO and chlorite treated MPO at pH 5.0. Protein concentration: 5 μM; and chlorite concentration: 100 μM. Path length: 1 cm (C) Corresponding absorbance spectra of native MPO and chlorite treated MPO. Conditions as in (B).

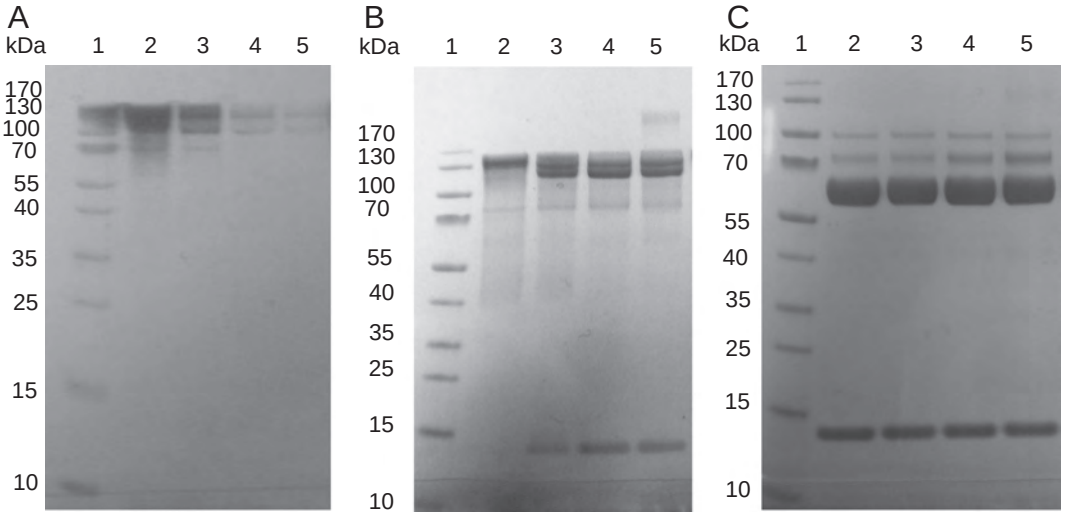

Fig. 7. SDS-PAGE analysis of MPO incubated with chlorite. (A) Non-reducing SDS-PAGE. Bands were visualized by in-gel heme staining. (B) Non-reducing SDS-PAGE. Protein bands were visualized by Commassie staining. (C) Reducing SDS-PAGE. Protein bands were visualized by Commassie staining. Lane 1, marker; lane 2, 10 μg MPO; lane 3, 10 μg MPO + 50 μM chlorite; lane 4, 10 μg MPO + 200 μM chlorite; and lane 5, 10 μg MPO + 500 μM chlorite.

Finally, calorimetric studies of the effect of chlorite on the thermal unfolding of MPO were performed. Fig. 9 shows the DSC profile of MPO in 100 mM phosphate buffer, pH 5.0. One slightly asymmetric endotherm was obtained with a maximum at T_m of 87 °C. Deconvolution of data suggests a non-two-state unfolding and two transitions at 84.5 and 87.5 °C. Upon incubation with a 5-time stoichiometric excess of chlorite for 1 min (stopping the reaction by 4 mM cysteine) a completely different unfolding pattern was obtained that clearly reflected loss of structural integrity and a diminished thermal stability. Satisfactory fitting was only possible by supposing of at least three intermediate states with calculated T_m values at 87.5, 84.5 and 73.0 °C, respectively. At longer incubation times or higher excess of chlorite, the T_m values shifted to lower temperatures and the endotherms became broad and flat (data not shown).

3.6. Comparison of chlorite with chlorite-based drugs in interaction with MPO

The drug substance OXO-K993 (NUVO Research Inc., Mississauga, Canada), also referred as tetrachlorodecaoxygen anionic complex [i.e. $(Cl_4O_{10})_n$ with molar mass of 301.8 for n = 1] contains 4.25% chlorite, 1.9% chloride, 1.5% chlorate, 0.7% sulfate and sodium ions as cationic species in an aqueous solution [14]. A sterile, pyrogen-free, aqueous 10% (w/v) solution of OXO-K993 is applied under the name WF10 for intravenous infusion in patients with chronic-inflammatory diseases [39–41]. Another 55-fold diluted formulation derived from OXO-K993 is Oxoferin™ that is topically applied as a wound-healing agent [42,43].

Here we applied Oxoferin to test the effects of this drug solution upon interaction with MPO. The chlorite content in Oxoferin is reported to be 12.3 mM [44]. To test if the additives lead to any differences in reactivity the direct reaction of human ferric MPO with this drug was investigated. The reaction of MPO with Oxoferin showed similar kinetics and finally resulted in heme bleaching (Supplemental Fig. 3). The reaction was biphasic with calculated rate constants of $3.9 \times 10^5\ M^{-1}\ s^{-1}$ and $2.3 \times 10^4\ M^{-1}\ s^{-1}$ (pH 5.0), respectively. Thus, with respect to reactivity towards MPO in terms of heme bleaching and kinetics, Oxoferin is indistinguishable from a pure chlorite solution.

4. Discussion

In the present study, we have demonstrated remarkable differences in the reaction of the mammalian peroxidases MPO and LPO with chlorite in comparison to the plant-type model peroxidase HRP. In the latter, chlorite acts as both a two-electron oxidant for the ferric enzyme forming Compound I as well as a one-electron donor for Compound I and Compound II. Two reaction products are formed, hypochlorous acid and chlorine dioxide, and both can mediate chlorination reactions. By contrast, the system MPO/chlorite is unable to perform chlorination reactions.

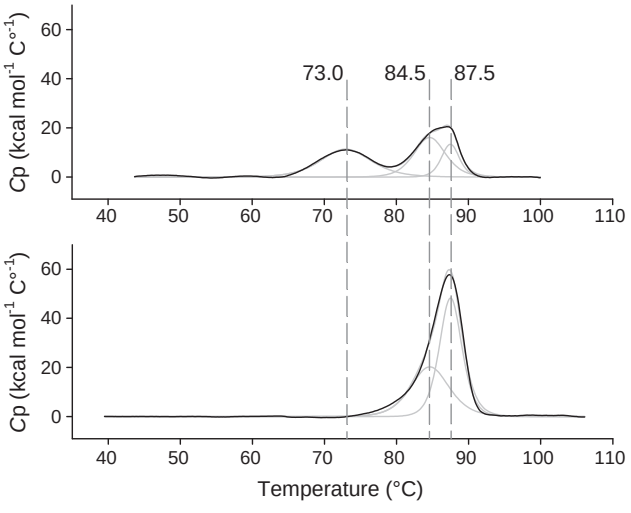

Fig. 9. Effect of chlorite on the thermostability of myeloperoxidase. Normalized DSC scans of 5 μM MPO in the absence (lower panel) or presence of 25 μM chlorite in 100 mM phosphate buffer, pH 5.0. Experimental data (black lines) and fitting to non-two-state models (gray lines) are shown.

The main difference between the mammalian peroxidases and HRP concerns the interaction of chlorite with the ferric resting state. Chlorite is well known to oxidize ferric HRP to Compound I by abstracting two electrons [12]. The standard reduction potential for the couple Compound I/ferric HRP can be calculated from data given in ref. [45] to be 0.92 V at pH 7. This value is lower than the potential for the couple ClO_2^-/HOCl, H_2O being 1.08 V at pH 7 [46], indicating the thermodynamic feasibility of HRP oxidation by chlorite. Under slightly acidic conditions, this oxidation becomes more favorable because of the divergent pH dependencies of both redox couples. The potential of the couple Compound I/ferric HRP increases by 0.59 V per decreasing pH unit, while a corresponding increase of 0.88 V is found for the couple ClO_2^-/HOCl, H_2O.

However, chlorite was unable to oxidize ferric LPO or MPO to Compound I. Instead of this, both peroxidases were inactivated by chlorite due to heme degradation. The standard reduction potentials of the redox couple Compound I/ferric enzyme are higher than for HRP at pH 7 with 1.16 V for MPO [47] and 1.09 V for LPO [34]. Considering the abovementioned pH dependencies of redox couples, an oxidation of at least ferric LPO to Compound I by chlorite can be expected at lower pH values. However, our results clearly revealed that even at pH 5 neither LPO nor MPO were oxidized by chlorite. Thus in addition, differences in the heme structure and the surrounding protein are apparently responsible for divergent chlorite effects with ferric MPO and LPO in contrast to ferric HRP. The most striking structural difference in the active site between HRP and the mammalian peroxidases is that in the latter two the heme is covalently attached to the protein (Fig. 10). The 1- and 5-methyl groups of heme pyrrole rings A and C are modified in both LPO and MPO allowing them to form ester linkages with the carboxyl group of a conserved aspartate and glutamate. In addition, in MPO a sulfonium linkage between the ß-carbon of the vinyl ring of pyrrole ring A and the sulfur atom of methionine 243 is formed [15]. Besides these heme modifications also the residues on the distal side of the heme differ between HRP and MPO/LPO. In plant-type peroxidases the triad histidine, arginine and phenylalanine is conserved, whereas the most prominent distal residues in mammalian peroxidases are histidine, arginine and glutamine, respectively (Fig. 10).

Chlorite rapidly binds at the active site forming a high-spin complex (MPO: $4.6 \times 10^4\ M^{-1}\ s^{-1}$ and LPO: $1.1 \times 10^5\ M^{-1}\ s^{-1}$ at pH 7.0) as demonstrated by (i) UV–vis stopped-flow spectroscopy, (ii) EPR-spectroscopy, and (iii) the impact of cyanide and chloride on this reaction. After binding of chlorite heme degradation occurred (MPO: $1.5 \times 10^3\ M^{-1}\ s^{-1}$ and LPO: $4.0 \times 10^3\ M^{-1}\ s^{-1}$ at pH 7.0) leading to loss of Soret absorbance and partial iron release. New absorbance bands in the region 600–800 nm indicate the formation of heme degradation product(s). The pH-dependence of both reactions (chlorite binding and heme bleaching) suggests that apparently HOClO, the protonated form of chlorite, is the reactive species. The pK_a value of HOClO is 1.72 [48].

In contrast to the ferric state, Compounds I and II of MPO and LPO are able to oxidize chlorite in a one-electron step as was previously observed for HRP [12]. However, rate constants for these transitions are much higher for MPO and LPO than for HRP in the pH range from 4 to 7. For all three peroxidases, these rate constants increase with decreasing pH. In addition to structural aspects determining the binding of chlorite near the heme, thermodynamic considerations play also a role in this divergent behavior. The standard reduction potential of the couple ClO_2/ClO_2^- has a value of 0.934 V and is independent of pH at pH values higher than 2 [49]. The reduction potential for the couple

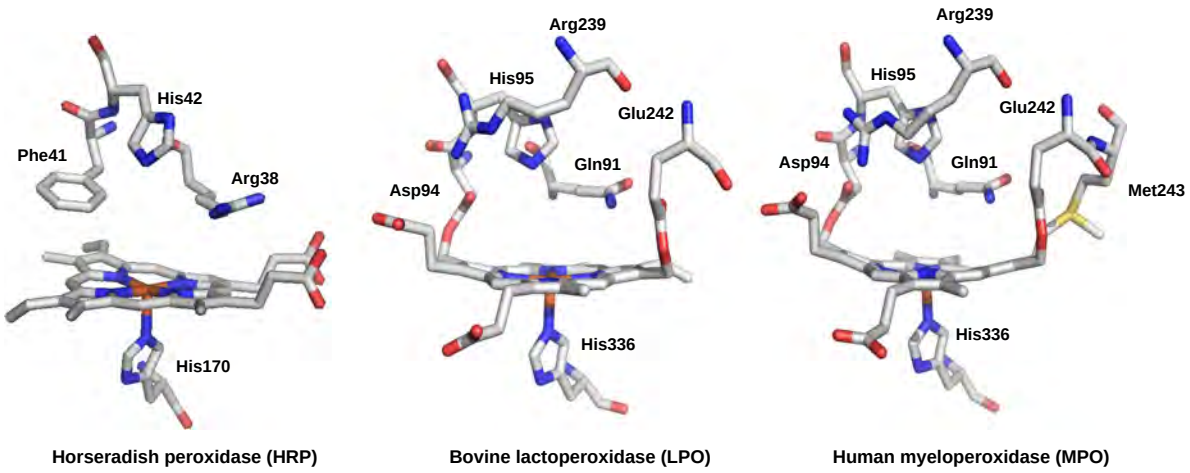

Fig. 10. Active site structure of HRP, bovine LPO and human MPO. The figures were constructed using the coordinates deposited in the Protein Data Bank. Accession codes: 1ATJ (HRP), 1CXP (MPO) and 2GJM (LPO).

Compound I/Compound II for HRP can be calculated to be 0.91 V at pH 7 [12]. The corresponding $E^{\circ\prime}$ values for MPO and LPO at pH 7 are significantly higher, namely 1.35 V [50] and 1.14 V [34], respectively, reflecting better oxidation capacities for chlorite oxidation compared to HRP. For the couples Compound II/ferric enzyme the $E^{\circ\prime}$ values for MPO and LPO are 0.97 V [50] and 1.04 V [34], respectively, at pH 7. These values are slightly higher than the corresponding value for HRP being 0.93 V [12].

During one-electron oxidation of chlorite by Compound I/II chlorine dioxide has to be formed as a reaction product. This was demonstrated in the HRP-mediated transitions monitored by the increase of absorbance of ClO_2 at 359 nm. In the MPO/chlorite or LPO/chlorite systems ClO_2 could not accumulate since the reaction cycle is interrupted at the ferric state, which is immediately attacked by the excess of chlorite resulting in heme bleaching. Thus, neither HOCl (two-electron reduction product of chlorite) nor sufficient amounts of ClO_2 (one-electron oxidation product) could be formed which easily explains the absence of chlorination activity. We could also demonstrate that ClO_2 is unable to mediate heme degradation upon addition to ferric MPO.

Upon interaction with MPO chlorite destroys the structural integrity of MPO. Activity staining in SDS-PAGE, UV–vis- and EPR-spectroscopy clearly demonstrated that chlorite causes heme degradation, partly by release of free iron. Although the overall secondary composition of MPO was not affected as determined by far-UV ECD spectroscopy, the conformational and thermal stability was decreased and the light chain detached from the protein in SDS-PAGE under non-reducing conditions. This can easily be explained by the fact that in native MPO the prosthetic group (together with a Ca^{2+}-ion) crosslinks the light and heavy chains [51]. Upon degradation of the prosthetic group the two polypeptides fall apart under denaturing conditions.

Comparing effects of pure chlorite with the chlorite-containing drug Oxoferin, we observed nearly identical kinetics of its interaction with the relevant redox intermediates. Oxoferin also mediated heme bleaching. Thus, concerning the interaction with heme in MPO, chlorite is really an active compound in the OXO-K993-derived drug solution Oxoferin. To what extent the interaction of the chlorite-containing drugs Oxoferin and WF10 with MPO are responsible for the observed therapeutic effects of these drugs, remains unknown. As shown here, chlorite is able to inactivate MPO and LPO irreversibly with the ferric state representing the susceptible redox intermediate. Inactivation included heme degradation and iron release. Recently 2-thioxanthines were also described as potent irreversible inactivators of MPO [52,53]. However, kinetic analysis, mass spectrometry and X-ray crystal structures revealed that these inhibitors become oxidized by MPO and, finally, covalently attached to the heme prosthetic groups thereby blocking the entrance to the heme cavity. Being dependent on hydrogen peroxide 2-thioxanthines are typical mechanism-based inhibitors, whereas chlorite competes with H_2O_2 for binding to ferric MPO.

Data about potential chlorite actions under pathological conditions like cardiovascular diseases, where MPO is known for their adverse effects [54,55], are lacking. In therapeutic use, other possible chlorite effects are modulation and stimulation of immune responses [56], activation of macrophage functions [40], the stimulation of killer cell cytotoxicity [57], methemoglobin formation [44] and formation of chlorine dioxide. The later species has strong anti-microbial properties [58] and can be also derived from one-electron oxidation of chlorite by Compounds I and II of MPO or LPO. At inflammatory sites, the likelihood for the aforementioned chlorite activity might be increased considering enhanced levels of hydrogen peroxide at these sites. Taken together, chlorite can principally cause a number of divergent effects upon its application. Which effects under strong pathological conditions dominate needs to be further specified.

Abbreviations

MPO	human myeloperoxidase
LPO	bovine lactoperoxidase
HRP	horseradish peroxidase
MCD	monochlorodimedon
APF	aminophenyl fluorescein
CD	circular dichroism
DSC	differential scanning calorimetry

Acknowledgments

This project was supported by the Austrian Science Fund (FWF P25270-B22), by the German Federal Ministry of Education and Research (BMBF 1315883), and by the Sächsische Aufbaubank from a funding of the European Regional Development Fund (ERDF). S.H. was supported by the PhD program BioToP — Biomolecular Technology of Proteins (FWF W1224).

Appendix A. Supplementary data

Supplementary data to this article can be found online at http://dx.doi.org/10.1016/j.jinorgbio.2014.02.010.

References

[1] C.L. French, S.S. Yaun, L.A. Baldwin, D.A. Leonard, X.Q. Zhao, E.J. Calabrese, J. Appl. Toxicol. 15 (1995) 167–174.
[2] E.G. Hrycay, J.A. Gustafsson, M. Ingelman-Sundberg, L. Ernster, FEBS Lett. 56 (1975) 161–165.
[3] C.G. van Ginkel, G.B. Rikken, A.G. Kroon, S.W. Kengen, Arch. Microbiol. 166 (1996) 321–326.
[4] G. Mlynek, B. Sjoblom, J. Kostan, S. Fureder, F. Maixner, K. Gysel, P.G. Furtmuller, C. Obinger, M. Wagner, H. Daims, K. Djinovic-Carugo, J. Bacteriol. 193 (2011) 2408–2417.
[5] A.Q. Lee, B.R. Streit, M.J. Zdilla, M.M. Abu-Omar, J.L. DuBois, Proc. Natl. Acad. Sci. U. S. A. 105 (2008) 15654–15659.
[6] P. George, J. Biol. Chem. 201 (1953) 413–426.
[7] S. Shahangian, L.P. Hager, J. Biol. Chem. 256 (1981) 6034–6040.
[8] P.F. Hollenberg, T. Rand-Meir, L.P. Hager, J. Biol. Chem. 249 (1974) 5816–5825.
[9] W.D. Hewson, L.P. Hager, J. Biol. Chem. 254 (1979) 3182–3186.
[10] W.D. Hewson, L.P. Hager, J. Biol. Chem. 254 (1979) 3175–3181.
[11] S. Shahangian, L.P. Hager, J. Biol. Chem. 257 (1982) 11529–11533.
[12] C. Jakopitsch, H. Spalteholz, P.G. Furtmuller, J. Arnhold, C. Obinger, J. Inorg. Biochem. 102 (2008) 293–302.
[13] J. Arnhold, J. Flemmig, Arch. Biochem. Biophys. 500 (2010) 92–106.
[14] M.S. McGrath, J.O. Kahn, B.G. Herndier, Curr. Opin. Investig. Drugs 3 (2002) 365–373.
[15] R. Fenna, J. Zeng, C. Davey, Arch. Biochem. Biophys. 316 (1995) 653–656.
[16] P.G. Furtmuller, M. Zederbauer, W. Jantschko, J. Helm, M. Bogner, C. Jakopitsch, C. Obinger, Arch. Biochem. Biophys. 445 (2006) 199–213.
[17] L. Huang, G. Wojciechowski, P.R. Ortiz de Montellano, J. Biol. Chem. 281 (2006) 18983–18988.
[18] D.P. Nelson, L.A. Kiesow, Anal. Biochem. 49 (1972) 474–478.
[19] C.S. Furman, D.W. Margerum, Inorg. Chem. 37 (1998) 4321–4327.
[20] R. Floris, R. Wever, Eur. J. Biochem. 207 (1992) 697–702.
[21] P.G. Furtmuller, W. Jantschko, G. Regelsberger, C. Jakopitsch, N. Moguilevsky, C. Obinger, FEBS Lett. 503 (2001) 147–150.
[22] K.G. Paul, P.I. Ohlsson, in: K.M. Pruitt, J.O. Tenuovo (Eds.), The lactoperoxidase system, chemistry and biological significance, Marcel Dekker, New York, 1985, pp. 15–30.
[23] H.B. Dunford, Heme Peroxidases, Wiley VCH, New York, 1999.
[24] T. Chen, Anal. Chem. 39 (1967) 804–813.
[25] P.E. Thomas, D. Ryan, W. Levin, Anal. Biochem. 75 (1976) 168–176.
[26] L.P. Hager, D.R. Morris, F.S. Brown, H. Eberwein, J. Biol. Chem. 241 (1966) 1769–1777.
[27] J. Flemmig, J. Zschaler, J. Remmler, J. Arnhold, J. Biol. Chem. 287 (2012) 27913–27923.
[28] S. Stoll, A. Schweiger, J. Magn. Reson. 178 (2006) 42–55.
[29] B. Chance, Arch. Biochem. 21 (1949) 416–430.
[30] H. Hori, R.E. Fenna, S. Kimura, M. Ikeda-Saito, J. Biol. Chem. 269 (1994) 8388–8392.
[31] M. Zamocky, C. Jakopitsch, P.G. Furtmuller, C. Dunand, C. Obinger, Proteins 72 (2008) 589–605.
[32] B.G. Bolscher, R. Wever, Biochim. Biophys. Acta 788 (1984) 1–10.
[33] A.R. Bakkenist, J.E. de Boer, H. Plat, R. Wever, Biochim. Biophys. Acta 613 (1980) 337–348.
[34] P.G. Furtmuller, J. Arnhold, W. Jantschko, M. Zederbauer, C. Jakopitsch, C. Obinger, J. Inorg. Biochem. 99 (2005) 1220–1229.
[35] P.G. Furtmuller, U. Burner, W. Jantschko, G. Regelsberger, C. Obinger, Redox Rep. 5 (2000) 173–178.
[36] D. Maitra, F. Shaeib, I. Abdulhamid, R.M. Abdulridha, G.M. Saed, M.P. Diamond, S. Pennathur, H.M. Abu-Soud, Free Radic. Biol. Med. 63 (2013) 90–98.
[37] D.I. Pattison, M.J. Davies, Chem. Res. Toxicol. 14 (2001) 1453–1464.
[38] M.C. Hsu, R.W. Woody, J. Am. Chem. Soc. 93 (1971) 3515–3525.
[39] S.P. Raffanti, W. Schaffner, C.F. Federspiel, R.B. Blackwell, O.A. Ching, F.W. Kuhne, Infection 26 (1998) 202–207.
[40] V. Veerasarn, W. Boonnuch, C. Kakanaporn, Gynecol. Oncol. 100 (2006) 179–184.
[41] N. Yingsakmongkol, P. Maraprygsavan, P. Sukosit, J. Foot Ankle Surg. 50 (2011) 635–640.
[42] J. Hinz, H. Hautzinger, K.W. Stahl, Lancet 1 (1986) 825–828.
[43] M.S. McGrath, V. Kotelja, Pathobiology. 67 (1999) 277–281.
[44] E. Habermann, B. Muller, Klin. Wochenschr. 67 (1989) 20–25.
[45] Y. Hayashi, I. Yamazaki, J. Biol. Chem. 254 (1979) 9101–9106.
[46] I.R. Epstein, K. Kustin, J. Phys. Chem. 89 (1985) 2275–2282.
[47] J. Arnhold, P.G. Furtmuller, G. Regelsberger, C. Obinger, Eur. J. Biochem. 268 (2001) 5142–5148.
[48] I. Fabian, G. Gordon, Inorg. Chem. 30 (1991) 3785–3787.
[49] U.K. Kläning, K. Sehested, J. Holcman, J. Phys. Chem. 89 (1985) 760–763.
[50] P.G. Furtmuller, J. Arnhold, W. Jantschko, H. Pichler, C. Obinger, Biochem. Biophys. Res. Commun. 301 (2003) 551–557.
[51] T.J. Fiedler, C.A. Davey, R.E. Fenna, J. Biol. Chem. 275 (2000) 11964–11971.
[52] J. Ward, S.N. Spath, B. Pabst, P.A. Carpino, R.B. Ruggeri, G. Xing, A.E. Speers, B.F. Cravatt, K. Ahn, Biochemistry 52 (2013) 9187–9201.
[53] A.K. Tidén, T. Sjögren, M. Svensson, A. Bernlind, R. Senthilmohan, F. Auchère, H. Norman, P.O. Markgren, S. Gustavsson, S. Schmidt, S. Lundquist, L.V. Forbes, N.J. Magon, L.N. Paton, G.N. Jameson, H. Eriksson, A.J. Kettle, J. Biol. Chem. 286 (2011) 37578–37589.
[54] T.K. Rudolph, S. Wipper, B. Reiter, V. Rudolph, A. Coym, C. Detter, D. Lau, A. Klinke, K. Friedrichs, T. Rau, M. Pekarova, D. Russ, K. Knoll, M. Kolk, B. Schroeder, K. Wegscheider, H. Andresen, E. Schwedhelm, R. Boeger, H. Ehmke, S. Baldus, Eur. Heart J. 33 (2012) 1625–1634.
[55] C. Nussbaum, A. Klinke, M. Adam, S. Baldus, M. Sperandio, Antioxid. Redox Signal. 18 (2013) 692–713.
[56] T. Giese, M.S. McGrath, S. Stumm, H. Schempp, E. Elstner, S.C. Meuer, Cell. Immunol. 229 (2004) 149–158.
[57] L. Kuhne, M. Konstandin, Y. Samstag, S. Meuer, T. Giese, C. Watzl, J. Biomed. Biotechnol. (2011) 436587.
[58] C.J. Volk, R. Hofmann, C. Chauret, G.A. Gagnon, G. Ranger, R.C. Andrews, J. Environ. Eng. Sci. 1 (2002) 323–330.

Supplementary Information:

Mechanism of reaction of chlorite with mammalian heme peroxidases

Christa Jakopitsch[1], Katharina F. Pirker[1], Jörg Flemmig[2,3], Stefan Hofbauer[1], Denise Schlorke[2], Paul G. Furtmüller[1], Jürgen Arnhold[2,3] and Christian Obinger[1]*

[1]Department of Chemistry, Division of Biochemistry, BOKU - University of Natural Resources and Life Sciences, Muthgasse 18, A-1190 Vienna

[2]Institute for Medical Physics and Biophysics, Medical Faculty, University of Leipzig, Härtelstr. 16-18, D-04107 Leipzig, Germany

[3]Translational Centre for Regenerative Medicine, University of Leipzig, Philipp-Rosenthal-Strasse 55, D-04103 Leipzig

*corresponding author: +43-1-47654 6073; fax: +43-1-47654 6059;

Email:christian.obinger@boku.ac.at

Keywords: myeloperoxidase, lactoperoxidase, chlorite, hypochlorous acid, chlorine dioxide, Oxoferin

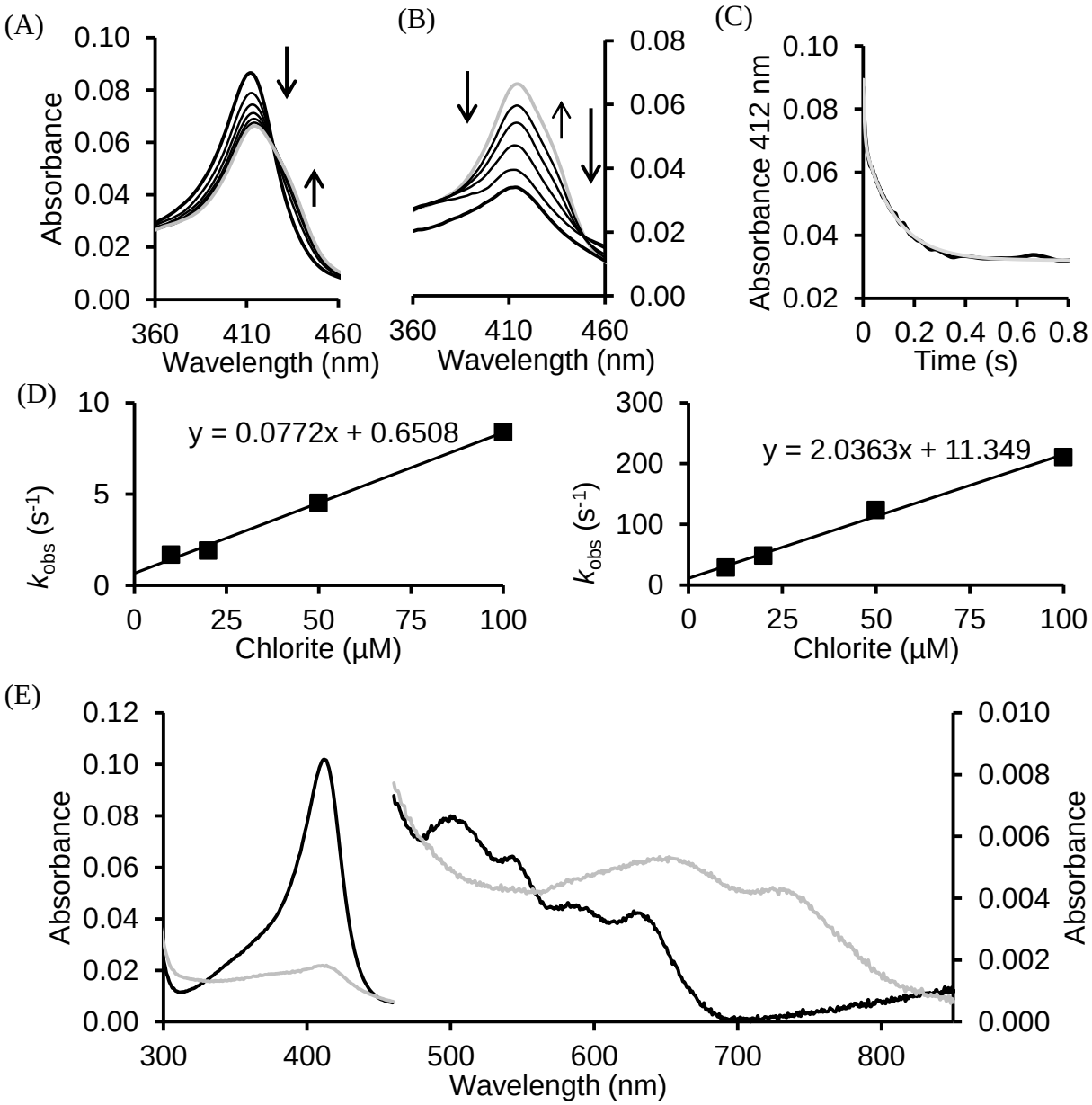

Figure S1: **Reaction of ferric LPO with chlorite**. (A) Spectral changes obtained by mixing 1 μM ferric LPO with 100 μM chlorite at pH 5.0. First observed spectrum was taken at 1.3 ms after mixing, subsequent spectra at 4 ms, 6 ms, 9 ms, 11 ms, 14 ms and 16 ms (grey spectrum). (B) Continuation of reaction in (A). The grey spectrum taken at 16 ms corresponds to the grey trace in (A). Subsequent spectra were taken at 42 ms, 68 ms, 117 ms, 200 ms and 2 s (black spectrum). (C) Time trace and double-exponential fit obtained at 412 nm for the reaction in (A). (D) Plot of the pseudo-first-order rate constants for the reaction of ferric LPO *versus* chlorite concentration (left panel: first phase and right panel: second phase). (E) Overlay of 1 μM native bovine LPO and LPO incubated with 50 μM chlorite for two minutes (grey spectrum) in 100 mM phosphate buffer, pH 5.0.

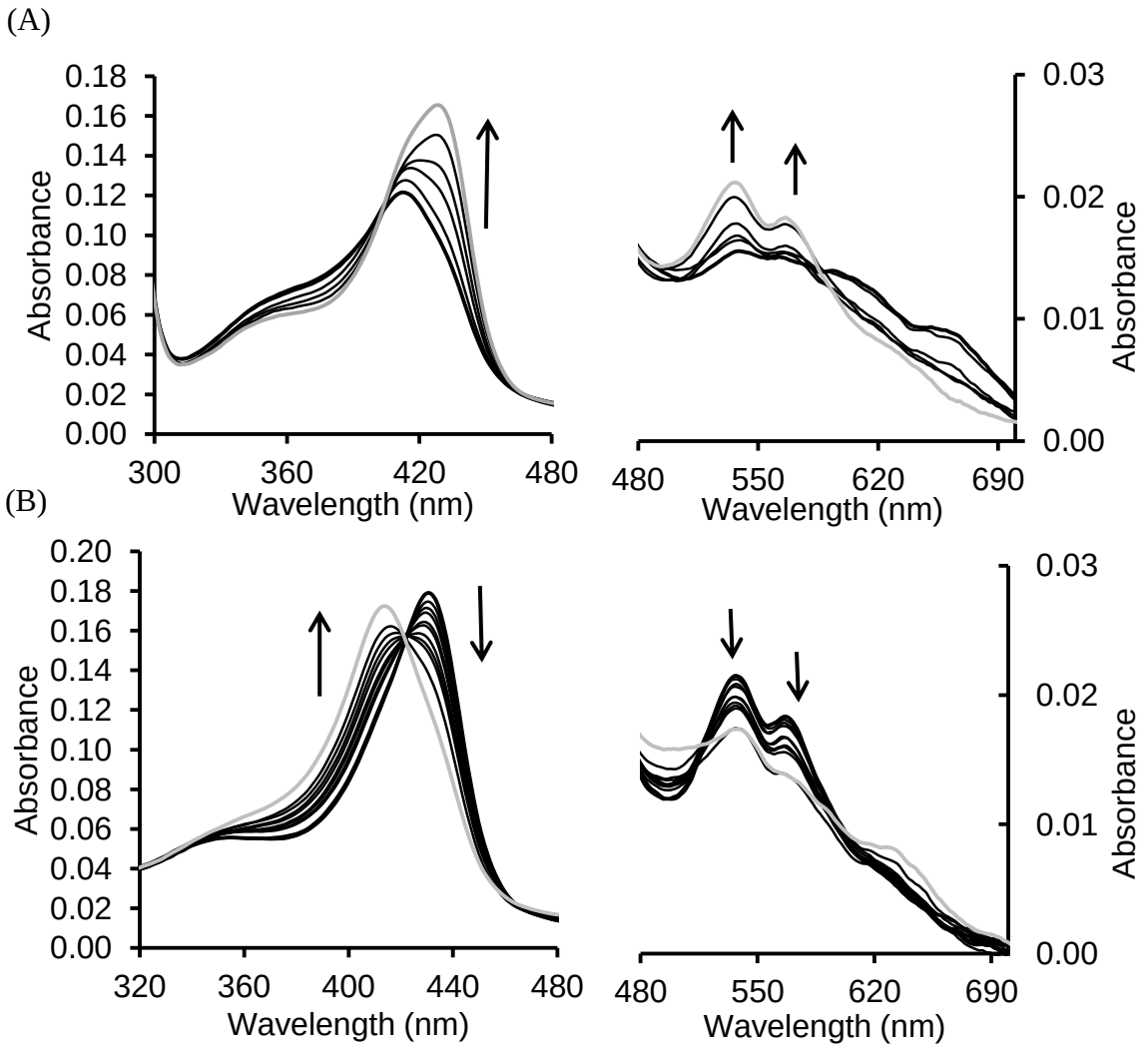

Figure S2. **Reactions of Compounds I and II of LPO with chlorite**. (A) Reaction of LPO Compound I with chlorite. 2 µM LPO Compound I was pre-formed by mixing 4 µM ferric LPO with 40 µM hydrogen peroxide and after a delay time of 80 ms chlorite (final concentration: 5 µM) was added. First spectrum recorded 5 ms after mixing (bold black), subsequent spectra were taken at 27 ms, 78 ms, 160 ms, 330 ms and 820 ms (grey spectrum, respectively. Conditions: 100 mM phosphate buffer, pH 7.0. (B) Reaction of LPO Compound II with chlorite. 2 µM LPO Compound II was pre-formed by mixing 8 µM ferric LPO with 12 µM hydrogen peroxide and 40 µM tryptophan and after a delay time of 2 s chlorite was added. Final concentrations: 2 µM LPO Compound II, 50 µM chlorite. First spectrum at 4 ms (bold black), subsequent spectra at 30 ms, 150 ms, 200 ms, 280 ms, 330 ms, 430 ms, 500 ms, 580 ms, 760 ms and 1.2 s (grey spectrum). Conditions: 100 mM phosphate buffer, pH 7.0.

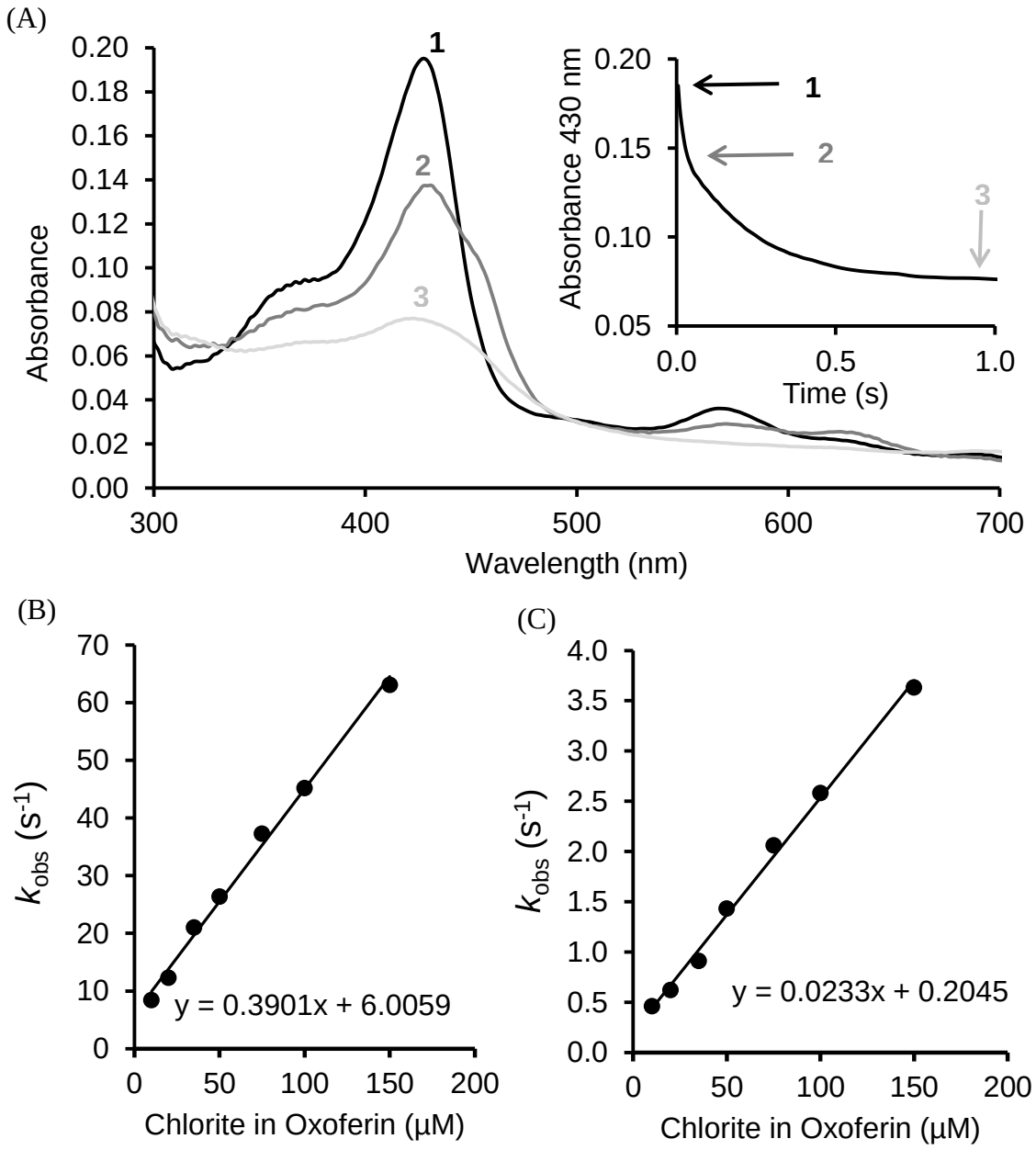

Figure S3. Reaction of MPO with Oxoferin. (A) Intermediates formed in the reaction of 2 µM ferric MPO in 100 mM phosphate buffer, pH 5.0 with Oxoferin (200 µM chlorite content). 1, ferric MPO; 2, spectrum obtained 50 ms after mixing; 3, final spectrum after 1 s after mixing. The inset shows the time trace at 430 nm for this reaction. (B) Plot of pseudo-first-order rate constants against chlorite concentration in Oxoferin for the initial phase of the reaction. (C) Plot of pseudo-first order rate constants against chlorite concentration in Oxoferin for the second phase of the reaction.

Acknowledgements

I thank Christian Obinger and Paul Furtmüller for giving me the opportunity to do my PhD thesis in the Protein Biochemistry Group under their supervision. I want to thank everyone involved in the doctoral program BioToP, especially Christa Jakopitsch, for creating perfect conditions to do a PhD-thesis. A very special “thank you” goes to all members of the BioB working group, who were responsible that I felt comfortable and supported during the entire time of my thesis by creating a joyful atmosphere in the lab and in the office. Further, I want to thank Gianantonio Battistuzzi and Giulietta Smulevich for the opportunity to work in their labs for two months each and for their outstanding hospitality during those research visits.

After all, I truly want to thank Andrea for always supporting me, being there for me, and making my life amazingly happy. I am also happy and thankful for the support provided throughout my whole life by my parents and my brothers.